THE ORIGIN OF SEAMOUNT VOLCANISM IN THE NORTHEAST INDIAN OCEAN

Rajat Taneja

Department of Earth and Planetary Sciences

Macquarie University

MACQUARIE UNIVERSITY

A thesis submitted in fulfilment of the requirements for the degree of Doctor of Philosophy (PhD)

August, 2014

Table of Contents

List of Figures

List of Tables

Abstract

The Northeast Indian Ocean formed during the breakup of Australia and India at 155 Ma, and spreading continued along the Wharton Ridge until 43 Ma. The region encompasses the Christmas Island Seamount Province, which comprises of at least ~50 seamounts distributed over a region of 2000 km east-west by 500 km north-south. In addition to the submerged seamount, the seamount province also contains two sub-aerially exposed island groups, the Cocos (Keeling) Archipelago, and Christmas Island.

The evolutionary history of the intraplate region and the oceanic-continental margins surrounding the seamount province has been constrained by interpretation of magnetic and gravity anomalies, ocean drilling, and dredged samples. Recent work in the region has suggested the Christmas Island Seamount Province contains a recycled continental lithosphere component. However the ultimate formation mechanism for this disseminated seamount province is not well understood.

This study undertakes a geophysical investigation of the area, including gravity modelling, oceanic subsidence modelling, and flexure modelling, to constrain the lithospheric characteristics, and loading and subsidence ages of these submerged seamounts. We coupled our observations with paleomagnetic analysis, and integrate our results with seismic tomography models, and plate reconstructions. The study also undertakes a geochemical and $^{40}Ar/^{39}Ar$ geochronological analyses on the volcanic rocks from Christmas Island to constrain source characteristics, and the duration and age of volcanism at Christmas Island.

The crustal structure of the Cocos (Keeling) Islands and Christmas Island, constrained by gravity modelling, suggests a ~2100 m thick limestone cover overlays the submerged basaltic surface at Cocos (Keeling) Island. Modelling has revealed a deeper basaltic core underneath the centre of the islands, followed by a 5 - 7 km thick gabbro layer, extending down to depth

of 15 - 18 km. The last exposure ages calculated from age-depth subsidence modelling highlights that the older seamounts formed in the east, and seamount ages young towards the west, and this agrees with the seafloor ages. The last exposure ages of these seamounts are comparable with radiometrically determined ages by Hoernle et al. (2011), while the loading ages suggests they formed on very young oceanic crust. $^{40}Ar/^{39}Ar$ geochronology has yielded an Eocene (43 - 37 Ma) and a Pliocene (5 - 4 Ma) age for Christmas Island. Although no geochronological dating exists for the oldest volcanic core of the island, this study has been able to propose a loading age of the island between 88 – 75 Myrs using lithospheric flexural modelling. Paleomagnetism of Christmas Island basalts have suggested a paleolatitude between $-43.5\,^{\circ}{}^{+9.0}_{-11.2}{}^{\circ}$, suggesting a position further south than Christmas Island's reconstructed position in the Eocene (~30°S), and a paleolatitude of 13°S ± 11° for the volcanic activity in the Pliocene. The Pliocene position of the island is consistent with plate reconstructions models and backtracking of the island using plate motions rates. Seismic tomography models support a low velocity zone underneath the reconstructed position of the seamount province, which may have been an important component in the formation of the seamount province. These tomographic models also conform with upwelling mantle flow models calculated in the East Indian Ocean.

Geochemical analyses of volcanic rocks from Christmas Island have a trace element pattern that is similar to OIB's. Intermediate Pb ($^{206}Pb/^{204}Pb$, 18.7874-18.9725 and $^{207}Pb/^{204}Pb$, 15.5585-15.6417) and Nd ($^{143}Nd/^{144}Nd$, 0.512684-0.512798) isotopic ratios for the Eocene phase of volcanism point towards an enriched (EM-2) type composition that is inherited from continental (or recycled sediment) contamination. In addition, the Eocene phase has a distinct Indian Ocean DUPAL anomaly signature. This suggests a mixing of sources contributed to the volcanics, including a lower-mantle DUPAL contribution, and an upper mantle continental lithosphere signature - a possible remanent of Gondwana dispersal. The Pliocene

phase of volcanism on Christmas Island is a product of melt rising through flexure-induced cracks, produced in response to changing lithospheric stresses at the flexural fore-bulge as the lithosphere subducts. The Pliocene phase has sampled both EM-1 (from Hoernle et al., 2011, $^{206}Pb/^{204}Pb$, 17.8498-17.8692 and $^{207}Pb/^{204}Pb$, 15.4550-15.5481) and EM-2 (this study) type composition suggesting that older material is still present underneath the lithosphere.

Declaration

This research contained in this thesis is based on the work carried out at Department of Earth and Planetary Sciences, Macquarie University, with assistance from CSIRO, North Ryde, for paleomagnetism, Western Australian Argon Isotope Facility, Department of Applied Geology and John de Laeter Centre, Curtin University of Technology, Perth for $^{40}Ar/^{39}Ar$ geochronology and Laboratoire de Geologie de Lyon, France for producing the isotope results. All interpretation, and analyses was carried out at Macquarie University. Proof reading of the thesis was undertaken both in-house, and commercially by an external agency.

This work is an original piece of work conducted by me from the start of this project in February 2010 and any help received has been acknowledged. Background knowledge within this thesis has been duly acknowledged all through.

Additionally, work carried out within this research was presented in various conferences and have been attached in appendices at the end. This thesis has not been submitted elsewhere for a higher degree to any other institution or a university.

Rajat Taneja
6th August 2014

Notes on Thesis Format

This thesis is presented in "Thesis by Publication" format. The initial three chapters introduce the project, describe the background, and introduce the methodology and approaches. Chapters 4 - 6 constitute the results, and are presented in the form of published or submission-ready papers. Two of these chapters are published and one is ready for publication in reputed peer reviewed journals. Due to these chapters being presented in paper format, repetition and duplication will occur which is unavoidable. The three papers have been formatted according to guidelines required by the journals. For continuity within these papers, Figures and Tables have been included within text and they follow a central thesis numbering theme. Each paper has its own figure and table numbering system but are prefixed by the chapter number, 1.1; 1.2; 2.1; 3.1 and so on. The same goes for Tables as well.

Numeral page number starts from Chapter 1 and continues up to references and appendices. Initial introductory pages (Table of Content, Acknowledgement, etc.) follow Roman numeral system.

Appendices have been attached at the end of the thesis after the references, though these are mentioned in relevant chapters. For example, the appendix to Chapter 6, has been number according to its chronological order, after the appendix of Chapter 5.

Chapters 7 and 8 present an overview and synthesis of this research, and discussion of its implications, followed by final conclusions.

Contribution towards papers

Chapter 4 (Paper 1): Published in Marine Geophysical Research (in-press but available online).

Geophysical Investigation: 95% of the result section (including gravity modelling, GPlates reconstruction, seismic tomography analyses, and subsidence and flexural modelling) and

discussion was done by me. My contribution towards writing the paper is 90%. For the rest of it I was assisted by my supervisor.

Chapter 5 (Paper 2): Published in Gondwana Research (in-press but available online)

Geochronology and Paleomagnetism: Field sampling at Christmas Island was done by me with assistance from my supervisor. Laboratory analyses including sawing the drilled core and running the samples in the lab was done by me with introductory assistance from Phil Schmidt. Around, 85 % analyses and discussion was done by me with assistance from co-authors. I ran two samples for Geochronology at Western Australian Argon Isotope Facility, Curtin University of Technology, when I visited the university, while the rest were run by the lab staff. I have 85% contribution towards analysing the results including age plateaus. My contribution towards writing both the parts of this paper is between 85 to 95%.

Chapter 6 (Paper 3): Geochemistry: I was helped by my supervisor during the field trip for sample collection at Christmas Island, while preparation of samples, including, sawing, grinding, and preparation of glass disc was done by me. Sample preparation for isotopes analysis and results were solely produced at the Laboratoire de Geologie de Lyon, France. Analyses of results and discussion was mostly done by with 10% contribution from co-authors. My contribution towards writing the paper is 90 - 95%, with 5 - 10% help from co-authors including my supervisor. This paper is being submitted to Chemical Geology.

Acknowledgment

I would like to thank first and foremost my supervisor A/Prof. Craig O'Neill for giving me this opportunity and believing in me I could do this. I very much appreciate the kind support, encouragement and knowledge granted on to me all through this project. There were difficulties and hardships but your guidance help the boat sail through easily. I must acknowledge you for an amazing company while on the field trip to Cocos (Keeling) Island and Christmas Island and the wonderful time spent at the CKI pub and Golden Bosun at CI.

I would also like to thank my secondary supervisor A/Prof. Tracy Rushmer for her constant encouragement and directions in helping me with geochemistry, constant meetings, clearing my confusions time and again and going through endless excel based graphs.

I would also like to thanks Dr. Phil Schmidt, CSIRO, for letting me use the paleomagnetic laboratory at CSIRO, North Ryde. Your constant help both at CSIRO and at the geophysics lab at Macquarie University has provided valuable input. Paleomagnetic analyses would not have reached its conclusion if I was not helped by Dr. Mark Lackie. I thank him for long enduring help every second day on paleomagnetic techniques. I really appreciate your help in answering my infinite questions be it in your office or while you were teaching. Many thanks to Prof. Simon Turner for great help with geochemistry and isotopic analyses. Your scientific inputs multiple number of times, reading the geochemical manuscripts, amongst your busy schedule is highly appreciated. Alongside, I would like to thank A/Prof. Fred Jourdan, Curtin Institute of Technology for running the geochronology samples and making me understand the techniques in such an easy and simple way that is unforgettable. Discussions with you while at Curtin, Macquarie, IGC, or at AGU have been very positive and enriching be it regarding work or as a friendly advice towards career opportunities. Last but not the least, I wish to thank Dr Mark Lackie, Prof. Simon Turner, A/Prof. Doritt Jacobs,

and other academics and colleagues for proof reading the entire thesis number of times. I thank you all.

A special thanks to my family in Australia, Rohan Mehrotra and Twisha Mehrotra, surviving here would have been full of hardships had you not tolerated me all the while. Your help for everything, including, crashing on the bed every weekend, amazing home cooked dinner, BBQ'ing and hiking has been much needed support in completion of this thesis and surviving Down Under.

A special thanks Elyse Schinella, who started this journey at the same time. It's been a wonderful experience to have a colleague and friend like you. Thanks for all the encouragement, gossips, discussion all through this journey and making life in the "grey demountable" for two years, a lot easier. Special thanks to Shahid Ramzan, your support and encouragement in the last six months has been very kind and helpful, especially when I had someone to vent out in my native language.

Last but not the least, a special thanks to everyone in the geophysics lab, fellow post graduate students Soumaya, Eileen, and Raul who have constantly offered advice on research, skills, encouragement. In addition, Hons. Students, Cam, Rusty, Sam, Alex, Cait, and Vicki who have spent countless hours in the geophysics lab during hot summer and cold winter from early morning up to late evenings.

Lastly, a special thanks to my family members and friends, your constant support and wishes have helped me survive the challenges and hardships.

Chapter 1: Introduction

The Indian Ocean region is dominated by numerous oceanic islands, submerged seamounts, guyots, large igneous provinces, age progressive volcanic chains, and hotspots, many of whose origin is well understood and well constrained through geophysical modelling and geochemical analyses (Houtz et al., 1977; Norton and Sclater, 1979; Cande and Mutter, 1982; Müller et al., 1993; Frey et al., 2000; Antretter et al., 2002; Duncan, 2002). Sampling from these oceanic islands, and drilling and dredging in the case of submerged seamounts or large igneous provinces have been instrumental in constraining their evolution and source characteristics (Duncan, 1978; Weis et al., 1989; Gautier et al., 1990; Duncan, 1991; Weis et al., 1991; Storey et al., 1995; Mahoney et al., 1996). Geochemical analyses along with geophysical investigations have often complemented each other in developing models for their origin and tectonic structure. More specifically, geochemical isotopic analysis has been used with high resolution gravity, bathymetric, magnetic, and seismic data for the Kerguelen hotspot track including the Ninetyeast Ridge, Kerguelen Island, and the Broken Ridge; Reunion hotspot and its volcanic trail; and the Marion hotspot track to comprehend their age progressive tracks and volcanic field associated with ridge jumps (Mutter and Cande, 1983; Fisk et al., 1989; Duncan et al., 1989; Peng and Mahoney, 1995; Mattielli et al., 1996; Dyment, 1998; Frey et al., 2000; Georgen et al., 2001; McDougall et al., 2001; Antretter et al., 2002; Wallace et al., 2002; Lénat et al., 2009).

The Indian Ocean is the third largest ocean in the world (after the Pacific and Atlantic Ocean) and is surrounded by Africa, the Indian subcontinent, Southeast Asia, Australia, and Antarctica. The East Indian Ocean that lies east of the Ninetyeast Ridge and hosts one of the largest disseminated volcanic provinces in the Indian Ocean Basin. This province is located in the northern East Indian Ocean, while the southern East Indian Ocean mostly comprises of flat abyssal plain, and the Broken Ridge. The seamount province is referred as the Christmas Island Seamount Province (CHRISP, Hoernle et al., 2011) or the Northeast Indian Ocean Seamount Province. It is bounded by the Java Trench in the north, the Ninetyeast Ridge in the west, and the North West Shelf of Australia in the east (Figure 1.1). While, there is a morphological similarity with the submerged seamounts found across the ocean floor; the size and orientation of the province and the distribution of seamounts raises numerous questions about the mechanism of their origin. Unfortunately, this seamount province has remained understudied in terms of geological research in the past. Though the region contains two sub-aerially exposed island groups, namely, the Cocos (Keeling) Archipelago and Christmas Island, there is a dearth of literature pertaining to their mechanism of origin. Very recently, Hoernle et al. (2011) conducted a dredging expedition within the seamount province. They used geochemical analyses and $^{40}Ar/^{39}Ar$ geochronology on dredged volcanic samples to develop a model for their formation, which, to date has not been tested.

The Cocos (Keeling) Islands is a small archipelago that comprises of 27 islands with a total land area of 14 km^2. It was first discovered in 1609 and was settled by John Clunies-Ross as a private residence in 1814-1816. It was formally declared part of the British Dominions in 1857 by Captain Freemantle of the HMS Juno. Cocos (Keeling) Island was the focus of research by Charles Darwin who formulated his famous theory of coral atoll formation while on his voyage aboard the HMS Beagle in 1836 (Darwin, 1842). In 1955, the islands that were under the British Dominion became a territory of Australia.

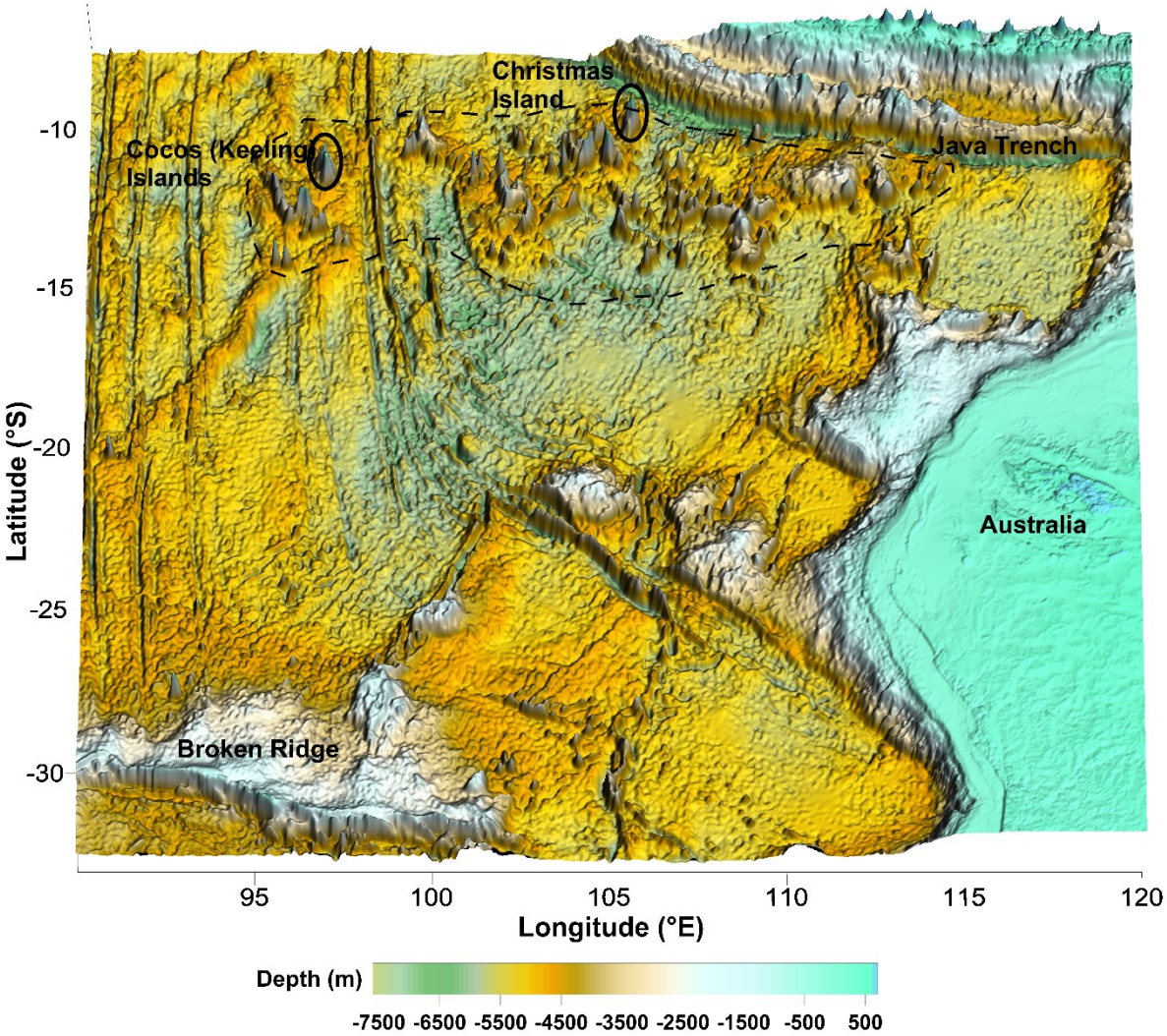

Figure 1.1: Bathymetry map of the Northeast Indian Ocean showing the seamount province and the general ocean floor morphology (Smith and Sandwell, 1997). The geographical boundary of the seamount province is outlined in a black dashed line. Christmas Island and the Cocos (Keeling) Islands (circled in black) are the two sub-aerially exposed islands. Other physiographic features are marked in Figure 2.1.

Similarly, Christmas Island is well known for its diverse flora and fauna including the annual red crab migration (O'Dowd and Lake, 1991), and its economy has been primarily supported by phosphate mining. The first landing at the island was reported in 1688 by William Dampier. The island was annexed by the British in June 1888 following discovery of its huge phosphate deposits. During World War II it was briefly annexed by the Japanese and formally became part of Australia in 1958.

The Indo-Australian Plate extends from the Himalayas in the north, to the Macquarie Island in the southeast. The northern boundary of the plate is subducting below the Eurasian Plate at the Sunda and Java Trench. The Indian side of the plate, at ~70 Ma, prior to the collision of India and Eurasia moved at 8-10 cm/yr and later, at ~40 Ma, its velocity slowed down to 2-4 cm/yr (Molnar and Tapponnier, 1977). Australia and Antarctica moved very slowly initially in the Late Cretaceous (chron 34) at the rate of <1 cm/yr, but later gained velocity to about 2 cm/yr in Early Eocene (chron 23), and accelerated to 4.5 cm/yr in the Middle Eocene (chron 20) (Cande and Mutter, 1982). Australia is now moving a north-easterly direction at 7 cm/yr (Tregoning et al., 1994). The difference in the rate of motion of the Indian side (continent-continent collision) and Australian side (subduction margin) of the Indo-Australian Plate is resulting in torsional rotation within the plate (Cloetingh and Wortel, 1986). This has led to deformational stresses within the once intact rigid plate (Deplus et al. 1998) and the intraplate zone of deformation has now been labelled as the Capricorn Plate (Royer and Gordon, 1997). Sea floor spreading rates, earthquake focal mechanism, orientation of fracture zones (Yue et al. 2012), and space geodetic kinematic modelling by Gordon et al. (2008) provide enough evidence towards a deformed plate (Capricorn Plate, Royer and Gordon, 1997) within the Indo-Australian Plate.

Deformational stresses have resulted in increased seismicity in the region, and the most notable earthquakes of the region include a 7.9 M_w (June 2000) earthquake southwest of Cocos (Keeling) Island (Robinson et al., 2001; Abercrombie et al., 2003), a 5.4 M_w (Sept. 2006) earthquake striking off the coast of Christmas Island, and 8.6 - 8.2 M_w (April 2012) twin earthquakes produced due to strike-slip faulting off north-western Sumatra (Yue et al., 2012). Earthquakes of large magnitude are known to occur at subduction margins, but the April 2012 twin earthquakes were one of the largest strike slip earthquake ever recorded (Yue et al., 2012). Besides these, there are numerous other minor earthquakes within the intraplate region that

occur frequently on either side of the Ninetyeast Ridge with different stress axis suggesting a complex and distinct tectonic regime on either side of the Ninetyeast Ridge (Deplus et al., 1998).

1.1: Mechanisms of intraplate volcanism

Submarine volcanism predominantly occurs at plate margins, typically at mid ocean ridges, or volcanic arcs. However, many locations within rigid tectonic plates, continental and oceanic, have recorded large volumes of volcanism in the form of igneous provinces (Coffin and Eldholm, 1994; Mahoney and Coffin, 1997; Todal and Edholm, 1998). Submarine volcanism in an intraplate oceanic region has been ascribed to convective upwellings from the lower mantle, as first proposed by Morgan (1971). These upwellings, rising from the deep mantle or the core mantle boundary (CMB), typically have a bulbous head and a narrow tail (Griffiths and Campbell, 1990). Courtillot et al. (2003) categorised the mantle plume hotspots in three categories, the first type originating from the deep mantle and having an age progressive character. The second and third type were described as secondary plumes, arising from the top of super plumes and those produced due to extensional stresses in the oceanic lithosphere, respectively (Courtillot et al., 2003). Numerous regions within the Pacific, Indian, and the Atlantic Ocean owe their existence to plume related hotspots (DePaolo and Manga, 2003; Courtillot et al., 2003; Montelli et al., 2004; Lei and Zhao, 2006). As a lithospheric plate moves across near stationary hotspots they leave a trail of linear volcanic islands and the Hawaii – Emperor Island chain (Clague and Jarrard, 1973; Molnar and Atwater, 1973; McDougall and Duncan, 1980; Duncan and Clague, 1985), the Kerguelen Island and its expressions in the form of the Rajmahal Traps and the Ninetyeast Ridge (Mahoney et al., 1983; Duncan, 1991; Klootwijk et al., 1992; O'Neill et al., 2003), and the linear tracks left by the Reunion and

Marion hotspots are a few examples (Fisk et al., 1989; Peng and Mahoney, 1995; Mahoney et al., 2002; O'Neill et al., 2003).

In contrast to this mantle plume mechanism, intraplate volcanism may also occur due to small scale convection (King, 2007) or cracking of the lithosphere (Forsyth et al., 2006). Flexure induced volcanism was reported in the northwest Pacific Ocean by Hirano et al. (2001) rising through lithospheric cracks produced by the flexural bulge of the subducting lithosphere. This style of volcanism leads to low volume knolls that are of the order of 2 – 3 km in diameter and rising only a few hundred meters above the sea floor (Fujiwara et al., 2007). Hirano et al. (2006) are of the opinion, that such a mechanism could produce volcanism elsewhere in the ocean basins. Much earlier, "hotlines in the mantle" was suggested as a mechanism by Bonatti and Harrison (1976) for the formation of the Easter Island volcanic chain as opposed to a stationary hotspot. Gans et al. (2003) suggested uneven thermal contractions under young lithosphere as another cause for volcanism within intraplate regions. Leaking transform faults, and weak zones below the lithospheric plates in regions susceptible to decompressional melting could also lead to intraplate oceanic seamount trails (Koppers et al., 2003).

As a result of multiple causative mechanisms for intraplate volcanism, a debate has arisen amongst the pro-mantle plume proponents and anti-mantle plume proponents (King and Anderson, 1995; Anderson, 2000; Natland and Winterer, 2005; Forsyth et al., 2006; Ballmer et al., 2013), who espouse alternate mechanisms. There are thousands of seamounts and volcanic ridges scattered around the ocean floor whose origin cannot be justified and constrained by a single existing intraplate mechanism and quite often there is a debate on the origin of most of these, for instance, the Pukapuka Ridge (Sandwell et al., 1995; Gans et al., 2003). Therefore, it is essential to integrate complementary analytical approaches and datasets in constraining complex formation mechanisms. Quite often, this is achieved by adopting seismic, gravity, and other geophysical techniques to provide sub-surface constraints along

with geochemical analyses to develop models for intraplate volcanism and such an approach has been adopted here.

Earlier work on Christmas Island volcanism has been documented by Andrew (1900), Trueman (1965), and Barrie (1967), however, these authors did not discuss any mechanism for the origin of the island. Due to the time gap since these previous works, there is a need to use modern scientific analytical techniques and a conceptual framework to better understand the region and constrain the mechanism of its origin. More recently, Hoernle et al. (2011) dredged the seamount province and the two island groups in the region, and proposed geochemical models involving recycling of subcontinental lithospheric mantle as a possible mechanism for the origin of the seamount province. They dredged volcanic samples within the seamount province including Christmas Island and Cocos (Keeling) Islands, and have yielded ages in the range of 136 – 47 Ma with older ages in the east and younger in the west. This age progression does not conform to that expected from volcanism over a stationary hotspot. Hoernle et al. (2011) conceptual model for the formation of CHRISP has issues with dynamic plausibility. The entrapment of continental material in the model proposed by Hoernle et al. (2011) does not conform to observed flow calculations of the Indian Ocean mantle flow (Steinberger and O'Connell, 1998; Steinberger, 2000; O'Neill et al., 2003). Such a complex setting warrants an integrated approach in understanding the geodynamic possibilities for the formation of CHRISP.

1.2: Research objective

The objective of this study is to constrain formational mechanism of the CHRISP by utilising an integrated geophysical, geochemical, and geochronological approach. The main objective are listed below:

- Constrain the last sub-aerial exposure age of different flat-topped seamounts within CHRISP using subsidence modelling, and calculate the elastic lithospheric thickness of the lithosphere to determine its age at the time of loading using lithospheric flexural modelling.
- Constrain the origin of the seamount province using published seismic imaging tomography models.
- Reconstruct the paleomagnetic history of Christmas Island using paleomagnetic analysis of drilled core samples and estimate the paleoposition of Christmas Island within the Northeast Indian Ocean.
- Understand the relation of intraplate seismicity with the region's evolution, especially, since the intraplate region is undergoing intense deformational stresses.
- Determine the absolute date and duration of the volcanism at Christmas Island using $^{40}Ar/^{39}Ar$ geochronology.
- Understand the source characteristics of exposed volcanic rocks from Christmas Island using major and trace element, and isotopic analyses to suggest a mechanism for its formation, and develop a geochemical evolution model for the province.

1.3: Research scope and approach

- Modelling the gravity signature of the ocean floor and seamounts is carried out to constrain the depths of different layers beneath the seamount. This is done using Encom's 3D gravity and magnetism modelling tool ModelVision. For this, the study uses global gravity model of Smith and Sandwell (2009). This aids in constraining the thickness of the crustal layers, and estimating the thickness of the limestone cover on Cocos (Keeling) Island and its subsidence history.

- Using subsidence modelling of the oceanic lithosphere, the study constrains the time since the last sub-aerial exposure of the seamounts, which roughly approximates to the time of their origin. Depth to basalt at Cocos (Keeling) Island derived from gravity modelling is then combined with subsidence modelling to determine its last sub-aerial exposure age. Lithospheric flexural modelling aids in constraining the mechanical properties of the lithosphere and determine the age of the lithosphere when the seamount loaded the lithosphere.

- $^{40}Ar/^{39}Ar$ geochronology of volcanic samples from Christmas Island is undertaken to determine the age and duration of volcanism exposed on the island. These ages will test the dates mentioned previously in the literature by Trueman (1965), Barrie (1967), and Hoernle et al. (2011) and are complementary to subsidence modelling and elastic flexure modelling.

- Reconstructing the paleoposition of Christmas Island using paleomagnetic analysis and existing plate reconstruction models to assist in recreating the dynamic evolution of the volcanism within the region. This is done especially for the basaltic rocks from Christmas Island by comparing its paleoposition with previous reconstruction models. Combining the paleoposition with existing mantle seismic tomography models can then

be used to constrain the source characteristics and origin of this submarine volcanic province.

- Major and trace element analyses are used to constrain the tectonic setting. Isotopic analyses of Christmas Island volcanic rocks can aid in source characterisation, and identification of mantle heterogeneities responsible for volcanism at Christmas Island.

This thesis is presented in a "Thesis by Publication" format and comprises of eight chapters. Chapter 1 to 3 provides theoretical underpinning for the research work, where Chapter 1 introduces the project, and Chapter 2 presents background material and the geodynamic history of the Northeast Indian Ocean. Chapter 3 is on methodology and presents methodological and analytical approaches used in this study. Chapters 4 to 6 constitute the results and are presented in form of published or submission ready papers. As self-contained research papers there occurs some duplication and repetition with Chapter 2 and 3, and also amongst the papers. Since these have to be presented as individual papers, and not just as results section of a thesis, some repetition and duplication is unavoidable. Chapter 7 presents a final discussion for the thesis. This chapter discusses alternate models proposed for intraplate volcanism, and evaluates whether they could lead to the formation of Christmas Island Seamount Province. Chapter 8 presents the final conclusions.

Chapter 2: Background

The NE Indian Ocean is a complex region with a rich tectonic history. Formed during the breakup of India and Australia at ~155 Ma (Sager et al., 1992; Heine and Müller, 2005), the spreading history of the region culminated with the cessation of spreading at the Wharton Ridge at ~43 Ma (Liu et al., 1983). The region is bounded by the Ninetyeast Ridge – formed by the Kerguelen hotspot – to the west, and the NW shelf of Australia to the east (Figure 2.1). The collision of India with Eurasia affected the stress state of the Indo-Australian plate, and culminated with the development of a diffuse plate boundary in this region – called the Capricorn Plate (Royer and Gordon, 1997). It hosts a large zone of disseminated seamounts and volcanic islands – the NE Indian Ocean Volcanic/Seamount Province also called Christmas Island Seamount Province (CHRISP). Recently, a scientific expedition dredged some volcanic samples in the seamount province, and Hoernle et al. (2011) proposed the province formed due to the convective recycling of continental lithosphere. This seamount province is unusual, as it is neither a narrow linear trail of age progressive volcanics consistent with a conventional mantle plume model (Morgan, 1971), nor is it aligned with the fracture zones of the ocean floor.

This chapter reviews background information and published literature relevant to the Northeast Indian Ocean, especially, its physiographic divisions and evolution. This chapter is divided into three main sections, each section divided into several sub sections. The first section presents a brief introduction to the geographical divisions of the Northeast Indian Ocean. This section

also introduces the prominent features of the region, such as the CHRISP, and its two sub-aerially exposed expressions, the Cocos (Keeling) Islands, and Christmas Island.

The second section discusses the evolution of the western margin of Australia as it rifted from Greater India and its subsequent dispersal from Gondwana. Much of this tectonic history has been reconstructed utilising data collected during geophysical surveys (e.g. seismic reflection and marine magnetic data collection), or drilling operations in the ocean floor (e.g. DSDP Leg 22, 26 and 27 (Larson, 1975; Larson et al., 1978) and ODP Leg 123 (Sager et al., 1992)). More recently, satellite derived bathymetry and gravity data have been used for identification of features such as fracture zones, and hotspot trails, that aid in constraining the margins of tectonic plates (Royer and Sandwell, 1989; Smith and Sandwell, 1997; Sandwell and Smith, 2009).

There is voluminous literature that deals with the tectonic fabric, and evolution of the Indian Ocean in general, and the Northeast Indian Ocean in particular. The tectonism of the Indian Ocean was examined by Veevers (1971), Wiens et al. (1985), Neprochnov et al. (1988), Royer and Sandwell (1989), Royer and Gordon (1997), Robinson et al. (2001), Abercrombie et al. (2003), and DeMets and Royer (2003). The papers by Liu et al. (1983), Powell et al. (1988), Royer et al. (1989), Veevers et al. (1991), Müller et al. (1998, 2000a, 2000b, 2001), Heine and Müller (2005), and Seton et al. (2012) deal with the evolution of the western margin of Australia following the breakup of Gondwana. More recently, Gibbons et al. (2012) found Late Jurassic (~153 Ma) crustal slivers within the Cretaceous (95 Ma) seafloor that provided additional constraints on the northern margin of Greater India.

In the third section, deformation within the intraplate region, and the formation of an incipient plate boundary is briefly discussed. Earthquake focal mechanisms within the intraplate region are different on either side of the Ninetyeast Ridge, and therefore, the ridge acts as a mechanical barrier with distinct deformation patterns on either side of it (Deplus et al., 1998).

2.1: Location and physiographic divisions of the Northeast Indian Ocean

The area of study lies within the Northeast Indian Ocean that is bounded by the Ninetyeast Ridge in the west, the Sunda Trench and Java Trench in the north, and by Australia in the east as shown in Figure 2.1. It lies between the equator, and 15°S latitude within the Indo-Australian Plate, which is moving north-northeast at an average rate of 7 cm/year (Tregoning et al., 1994). The plate is subducting underneath the Java-Sunda Trench causing small to large magnitude earthquakes that range from shallow to deep along the trench axis. The M_w 9.3 (December, 2004), earthquake that struck off the coast of Sumatra producing a massive tsunami (Lay et al., 2005; Ghobarah et al., 2006; Stein and Okal, 2007) is one such example.

The crustal age of the ocean floor in the region follows a trend that youngs towards the west, with a maximum age of 154 Ma in the east, and around 46 Ma in the west (Gibbons et al., 2012). Most of the ocean floor comprises flat abyssal plains with a few isolated seamounts and guyots (Smith and Sandwell, 1997). These seamounts can be divided into those with rounded/conical peaks and those with flat-tops. The flat-tops of these seamounts indicate these were exposed to erosion and weathering while they were above sea-level (Hess, 1946; Winterer, 1998).

The northern part of the NE Indian Ocean is dotted with seamounts that extend east-west between 10° to 15°S latitudes and are orthogonal to the direction of plate motion (Smith and Sandwell, 1997). The seamount zone is dissected by numerous north-south trending faults and fracture zones. The Investigator Ridge is a prominent example that strikes along 98°E longitude. The region is divided into a series of abyssal plains and ocean basins (Larson et al., 1978).

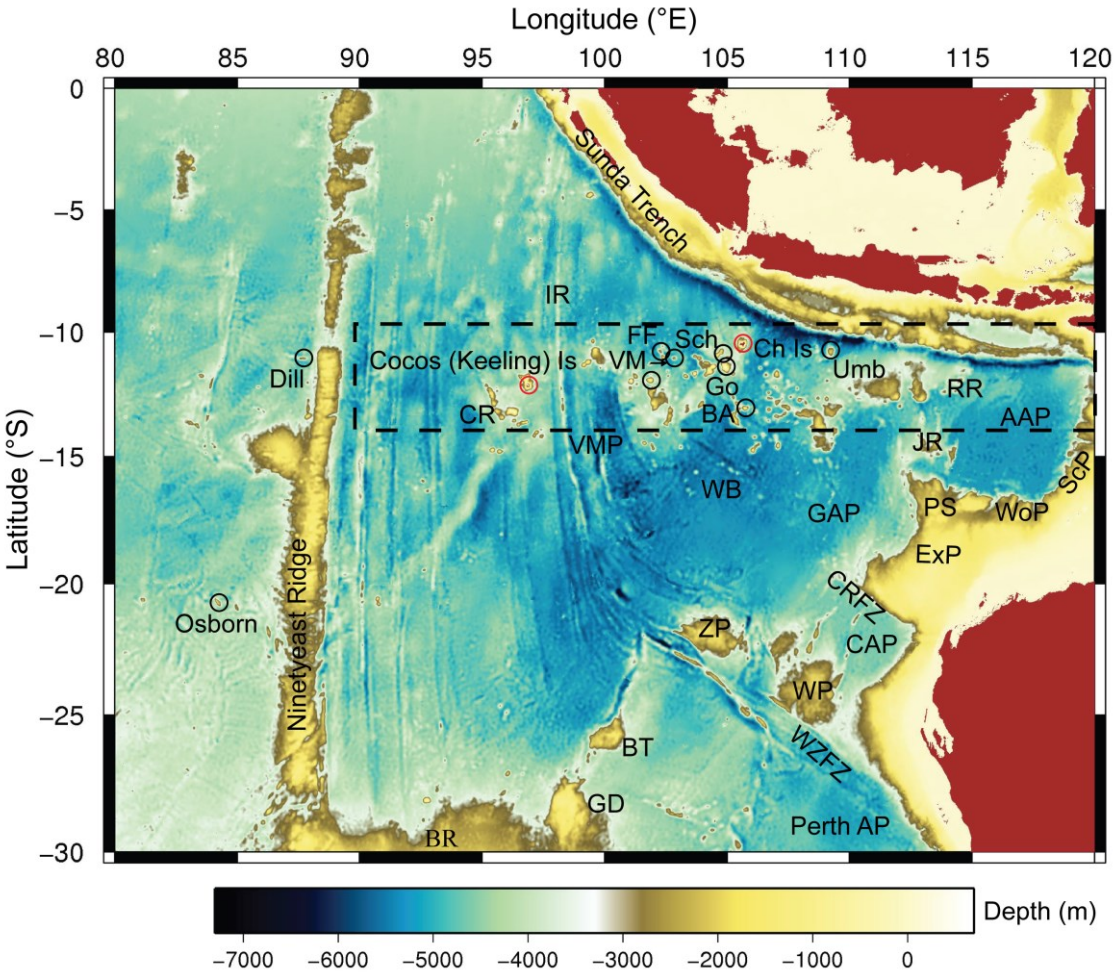

Figure 2.1: Bathymetric map of the East Indian Ocean (Smith and Sandwell, 1997). AAP, Argo Abyssal Plain; GAP, Gascoyne Abyssal Plain; CAP, Cuvier Abyssal Plain; Perth AP, Perth Abyssal Plain; RR, Roo Rise; JR, Joey Rise; ScP, Scott Plateau; ExP, Exmouth Plateau; WoP, Wombat Plateau; PS, Platypus Spur; WRFZ, Wallaby Zenith Fracture Zone; CRFZ, Cape Range Fracture Zone; WP, Wallaby Plateau; ZP, Zenith Plateau; IR, Investigator Ridge; BR. Broken Ridge; WB, Wharton Basin; VMP, Vening-Meinesz Province; Ch Is, Christmas Island. Prominent seamounts are circled (black) and include Vening Meinesz (VM), Shcherbakov (Sch), Umbgrove (Umb), Golden Bo'Sunbird (Go), Flying Fish (FF), Bartlett (BA), Batavia (BT) and Gulden Draak (GD). Black dashed rectangle is shown as a 3D bathymetry map in Figure 2.3.

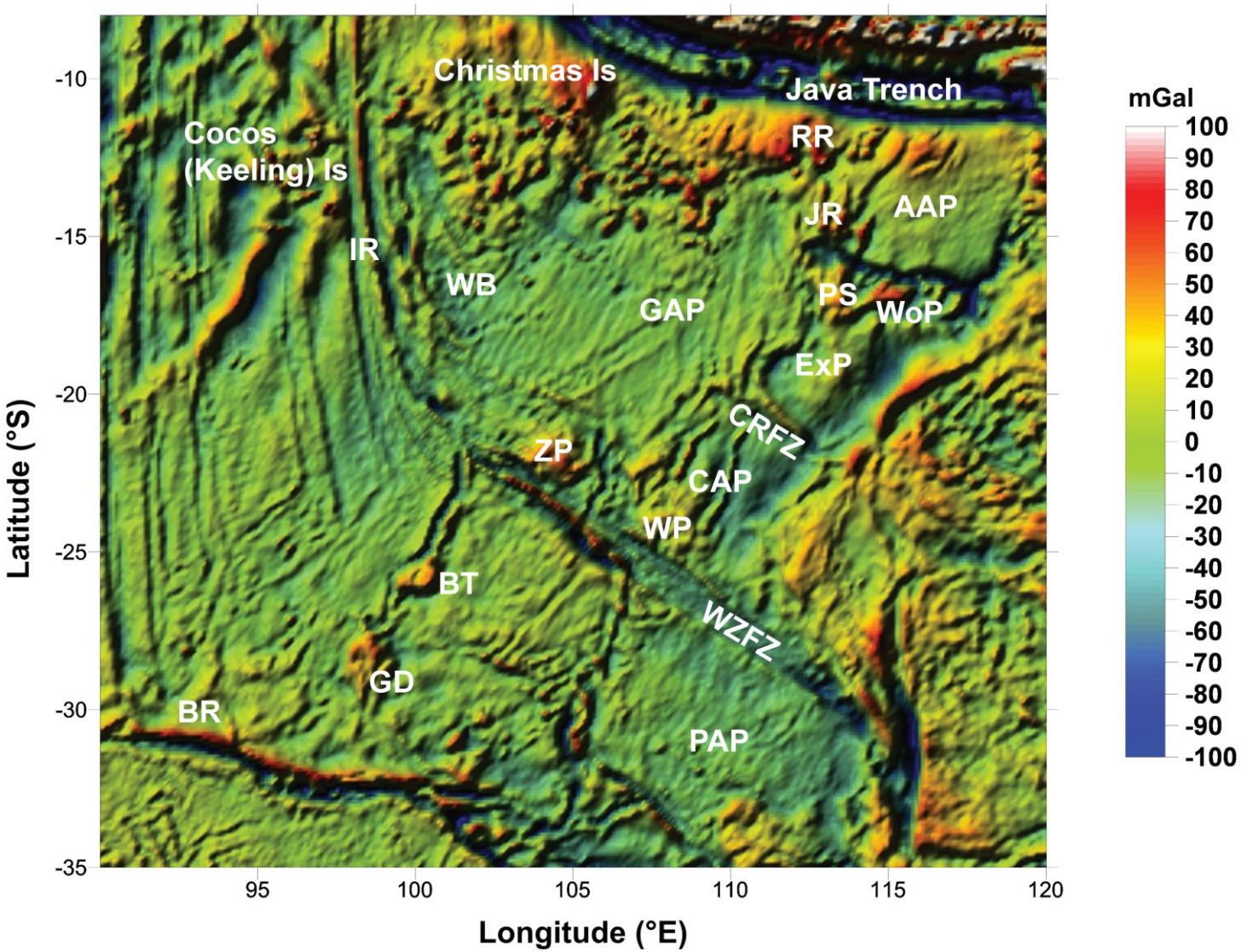

Figure 2.2: 3D surface gravity map (Sandwell and Smith, 2009) of the East Indian Ocean showing the physiographic divisions. AAP, Argo Abyssal Plain; GAP, Gascoyne Abyssal Plain; CAP, Cuvier Abyssal Plain; PAP, Perth Abyssal Plain; RR, Roo Rise; JR, Joey Rise; ExP, Exmouth Plateau; WoP, Wombat Plateau; PS, Platypus Spur; WP, Wallaby Plateau; WB, Wharton Basin; ZP, Zenith Plateau; BR, Broken Ridge; IR, Investigator Ridge; WRFZ, Wallaby Zenith Fracture Zone, CRFZ, Cape Range Fracture Zone; BT, Batavia; GD, Gulden Draak.

These include the Argo Abyssal Plain, Gascoyne Abyssal Plain, Cuvier Abyssal Plain, and the Wharton Basin. The seamount province also includes two sub-aerially exposed volcanic islands, the Cocos (Keeling) Archipelago and Christmas Island. The following sub-sections will discuss the tectonic features and physiographic divisions in more detail, beginning with the western margin of Australia, and followed by the other tectonic divisions that collectively form the Northeast Indian Ocean.

2.1.1: Western Australian Margin

The western margin of Australia was developed following the separation of Australia from Greater India during its dispersal from Gondwana starting in the Late Jurassic (Veevers, 1971; Heirtzler et al., 1978; Veevers et al., 1991; Sager et al, 1992; Heine and Müller, 2005). On its oceanic side it is flanked from north to south, by the Argo, Gascoyne, Cuvier, and Perth Abyssal Plains (Figure 2.1). The North West Shelf occupies the region between the Argo Abyssal Plain and the north-western edge of Australia.

The North West Shelf is a 2400 km long passive margin that extends from the Arafura Sea in northern Australia down south along the continental landmass up to the Exmouth Plateau (Heine and Müller, 2005). It has undergone multiple extensional and compressive events in its evolutionary history in the Late Palaeozoic and Early Mesozoic (Heine and Müller, 2005).

The identification of magnetic anomalies within the abyssal plains indicates these represent ~155 Ma old oceanic floor (Sager et al., 1992, Heine and Müller, 2005). The oceanic character of the Argo and Gascoyne Abyssal Plains have been recognized by Powell and Luyendyk (1982), Fullerton et al. (1989), Veevers and Li (1991), and Veevers et al. (1991). Drilling expeditions by DSDP, Leg 22 (McDougall, 1974), Leg 26 (Rundle et al., 1974) and ODP Leg 123 (Gradstein and Ludden, 1991) have also encountered oceanic basement in the abyssal plains of the Northeast Indian Ocean. The Argo Abyssal Plain (~600 km x km located west of

the North West Shelf) contains the oldest magnetic anomalies of the region at 155 Ma (Sager et al., 1992), and the Gascoyne, Cuvier, and Perth Abyssal Plain contain Early Cretaceous magnetic anomalies (Heirtzler, 1978; Fullerton et al., 1989; Sager et al., 1992; Heine and Müller, 2005). This Mesozoic magnetic record provides evidence of rifting between India and Australia in the Late Jurassic/ Early Cretaceous (Mihut and Müller, 1998; Stagg et al., 1999). Heine and Müller (2005) have worked extensively around the western coast of Australia and identified 155 – 153.1 Ma old anomalies on the eastern margin of Argo Abyssal Plain close to the continental regions of the Exmouth Plateau and Rowley Terrace. The Argo Abyssal Plain opened up during this time (Late Jurassic) eventually leading to the separation of Greater India and the western margin of Australia.

Magnetic anomaly interpretation is a pre-requisite for decoding and understanding the evolutionary history and sea-floor spreading that separated Australia from Greater India. However, lack of older magnetic anomalies in the region posed problems for their identification and interpretation. The anomalies adjacent to the continental margins of Australia are currently subducting beneath the Java Trench, posing a problem for Mesozoic reconstruction histories (Hall, 2012). Where present, these anomalies follow a N70°E trend that is different from the trend observed in the other abyssal plains of the region (Heirtzler at al., 1978). Subduction in the north consumed most of the older Mesozoic seafloor (Hall, 2012) and intraplate volcanism to the west of the Argo Abyssal Plain disturbed the inherent fabric of these anomalies making their interpretation difficult (Heine and Müller, 2005). Nevertheless, as part of a research cruise in the region, Gibbons et al. (2012) documented unexpected slivers of Jurassic seafloor (153 Ma) within much younger Cretaceous seafloor and suggested reconstruction models constraining the northern extent of Greater India during the Jurassic.

2.1.2: Wharton Basin

Wharton Basin is a vast expanse of ocean basin (145,000 km^2) within the Northeast Indian Ocean intraplate region bounded by the Sunda-Java Trench in the north, Gascoyne Abyssal Plain and Roo Rise in the east, the Broken Ridge in the south and the Ninetyeast Ridge in the west. This region consists of abyssal depths in the range of 5000 to 6000 m below sea-level (Smith and Sandwell, 1997). Based on its bathymetric characteristics, the Wharton Basin can be divided into two parts (Figure 2.1), northern and southern (Naini, 1973). The northern region of the Wharton Basin is dominated by scattered but densely populated submerged volcanic seamounts, plateaus and contains within itself the two exposed islands, the Cocos (Keeling) Archipelago and Christmas Island (Smith and Sandwell, 1997). The southern region of the basin is both flatter and deeper, extending down towards Broken Ridge in the south (Heezen and Tharp, 1966). The sedimentation rate in the Wharton Basin is quite low because of the basin's isolation from any major sediment source, and also because the Ninetyeast Ridge acts as an obstruction to sediments from the Bay of Bengal (Naini, 1973). The Investigator Ridge bisects the Wharton Basin into east-west components. Towards the west of the ridge are the Cocos (Keeling) Islands and the Cocos Rise, whereas towards the east greater seamount province and Christmas Island are situated (Figure 2.1).

Old inactive faults and fracture zones, oriented north-south, are a characteristic features of the Wharton Basin that are being reactivated (Abercrombie et al. 2003). Associated with these ridges are the occurrences of "deeps" that can exceed 7000 m (Carpenter and Ewing, 1973). A recent M_w 7.9 (June 2000) earthquake, 200 km southeast of the Cocos (Keeling) Island in the vicinity of the Investigator Ridge (Abercrombie et al., 2003) or the trough associated with it (Robinson et al., 2001), suggests reactivation of some of the fracture zones as the Indo-Australian Plate collides with the Eurasian Plate. The magnetic anomalies in the region have been studied in detail by Sclater and Fisher (1974), Larson et al. (1978), Liu et al. (1983),

Müller et al. (1998), and more recently by Gibbons et al. (2012). The Early Cretaceous magnetic anomalies are oriented parallel to the fracture zones observed in the region. The bends in the fracture zones after 100 Ma have been attributed to a change in spreading direction from northwest-southeast to north-south (Müller et al., 2000b, Matthews et al., 2012). Powell et al. (1988) suggested this event occurred at 96 Ma, and Müller et al. (1998) believes this event has important implications as it led to tectonic reactivation, and subsidence of the order of 200 to 550 m, in the North West Shelf.

Spreading in the eastern Wharton province ceased at magnetic anomaly C20, but prior to this, India, Australia, and Antarctica were moving relative to each another from 90 to 43 Ma (Liu et al., 1983). Following the cessation of this spreading, India and Australia became a single rigid plate (Liu et al., 1983) which was dated to be ~45 Ma. Müller et al. (2000) then revised this date following developments in Geomagnetic Polarity Time Scale by Cande and Kent (1995) to 43 Ma. Recently, Seton et al. (2012) in their study on oceanic and continental reconstruction have stressed that the activity of the Wharton Ridge ceased at 43 Ma, and following the closure of the Wharton Ridge, the combined plate moved northwards, with spreading accommodated by the Southeast Indian Ridge.

Jacobs et al. (2014) have revisited the Wharton Basin to understand its age, structure and evolution. Since most of the Mesozoic anomalies have now been subducted under the trench (as discussed in Section 2.1.1) they analysed the plate kinematic evolution of the region between India and Australia using a two plate (India-Australia) and three plate (India-Australia-Antarctica) reconstruction from 84 Ma to 38 Ma. They re-modelled some of the magnetic anomalies and interpreted them as Chron 18 (38 Ma) and Chron 15 (35) if a reduced spreading is considered. On the basis of re-modelling magnetic anomalies, they suggested that the Wharton Ridge spreading centre ceased between 38 Ma – 36.5 Ma.

2.1.3: Investigator Ridge

This is a roughly 1800 km long ridge that trends north-south and is one of the most characteristic features of the seamount province. It can be seen prominently in bathymetric maps (Smith and Sandwell, 1997) as a continuous linear ridge that extends from 18°S to 7°S. North of this, it becomes patchy and broken before subducting underneath Sumatra (Figure 2.1 and Figure 2.2). The fractures and faults in the vicinity of the ridge range from as deep as 5000 m to as shallow as 2500 m. The Ridge divides the region into eastern and western sections; the oceanic crust towards the east is much older and contains the oldest volcanic phase, while in the west the seafloor ages and seamount volcanism is younger (Hoernle et al., 2011). The ridge offsets oceanic floor of similar age by 900 km as determined through the proposed location of the C33 (79 - 74 Ma) magnetic anomaly. Larson et al. (1978) studied the region around the ridge calculating the ages on either side, and suggested that crust on the west was formed after the change in motion between the Indian and Australian Plates at 80 – 110 Ma. Sclater and Fisher (1974) have referred to the Investigator Ridge as the Investigator Fracture Zone, noting it trends north-south from near the Sunda Trench up to 20°S, and offsets magnetic anomalies in the region. Larson et al. (1978) noted that a change in spreading direction occurred between 110 and 80 Ma that produced a clockwise rotation of 55°. They suggested that the original transform offset was represented by the Wallaby Fracture Zone, and the later offset was accommodated by the Investigator Fracture Zone. Robinson et al. (2001) and Abercrombie et al. (2003) believe that the ridge and other parallel linear topographic highs either side of it are being reactivated due to compressional stresses within the deformed intraplate region as its northern margin subducts underneath the Sumatra Trench.

2.1.4: Christmas Island Seamount Province

The seamount province lies east of the Ninetyeast Ridge within the Wharton Basin and extends to the Roo Rise and the Argo Abyssal Plain in the east. It is bisected by numerous north-south oriented fracture zones, including the Investigator Ridge. In addition to the fracture zones, the region is home to considerable number (~50) of small and large seamounts, inactive volcanic cones most of which rise up to 3000 m from the ocean floor, and two sub-aerially exposed islands. The submerged volcanic province that extends east-west and is 1500 to 1700 km long between latitudes 10°S and 15°S.

Prominent seamounts in the region include Vening Meinesz (VM), Shcherbakov (Sch), Umbgrove (Umb), Golden Bo'Sunbird (Go), Flying Fish (FF) and Bartlett (BA), among others (Figure 2.1). Umbgrove seamount (Figure 2.3) is of particular interest due to the fact that it lies very close to the Java Trench. As seamounts approach and impinge upon a subduction zone, they may lead to the growth of an accretionary wedge, and influence plate-boundary dynamics, and regional tectonism (Dominguez et al., 2000). The Dill and Orborn seamounts occur to the west of Ninetyeast Ridge, and the Batavia and Gulden Draak volcanic plateaus are in the southern Wharton Basin (Figure 2.1). Additionally, understanding the two exposed islands is of considerable significance as these are the sole exposed representatives of the submarine intraplate volcanic event. Unfortunately, no volcanic rocks are exposed on Cocos (Keeling) Islands, which is a coral atoll, to depths of nearly 2400 m below sea-level (Hoernle et al., 2011).

Volcanic rocks can be found at Christmas Island, in the form of basaltic exposures spread sporadically along the coastline, and in few cases inland (Trueman, 1965; Barrie, 1967). Recent dredging expedition by Hoernle et al. (2011) have documented similar exposure along the Island. Hoernle et al. (2011), in addition, dredged a number of seamounts within the CHRISP, and analysed them using incremental step heating $^{40}Ar/^{39}Ar$ geochronology. They yielded ages in the range of 136.2 ± 1.7 – 46.7 ± 0.2 Ma that shows a westward younging trend. The Eastern

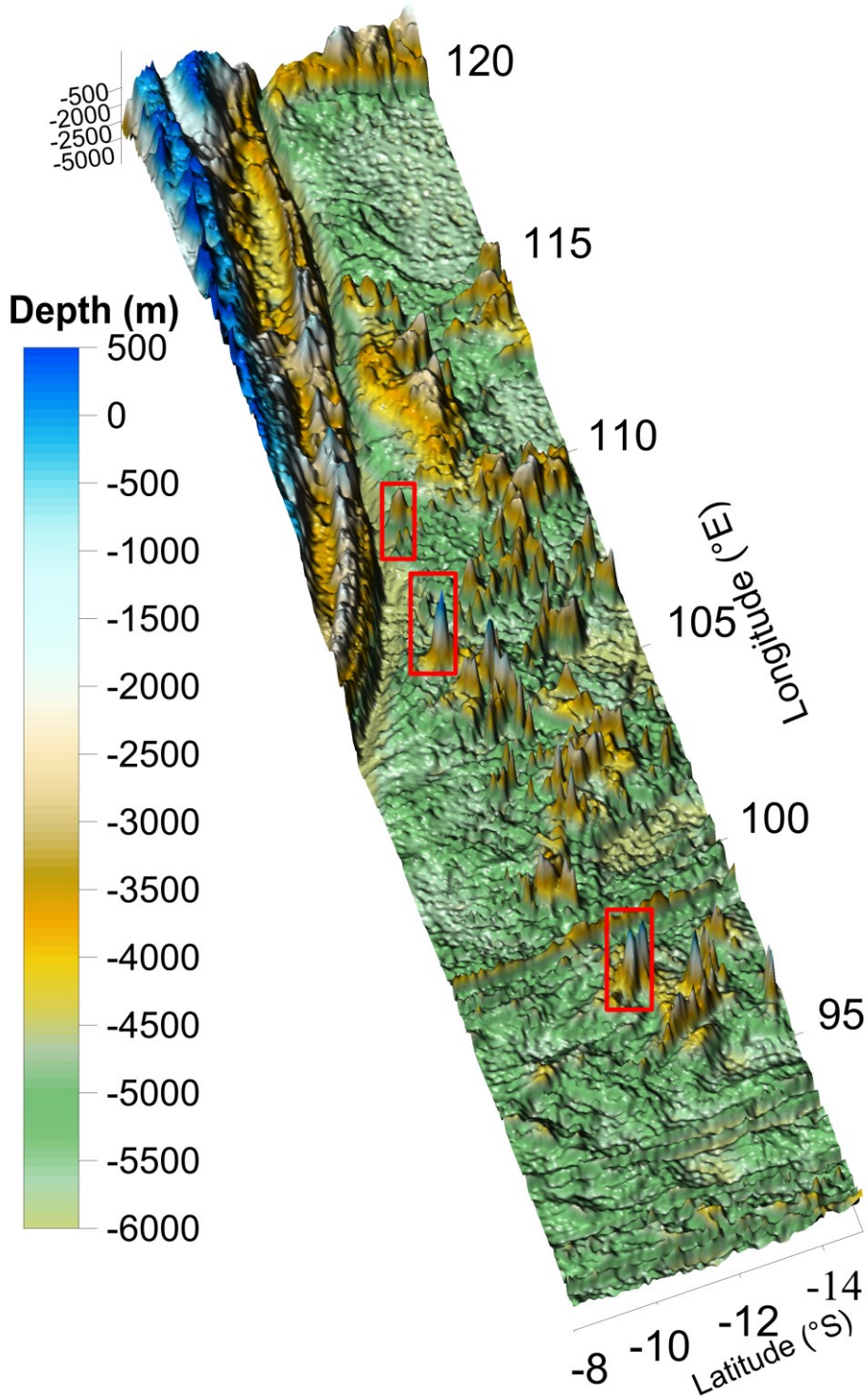

Figure 2.3: 3D bathymetry map (Smith and Sandwell, 1997) of the seamount province of the Northeast Indian Ocean. Red boxes show (from the top to bottom), the Umbgrove seamount, Christmas Island, and the Cocos (Keeling) Archipelago, other seamounts are shown in Figure 2.1. Viewed from NW.

Wharton Basin contains ages in the range of 115.9 ± 3.8 Ma – 94.3 ± 0.3 Ma, while the Vening-Meinesz province is between 95.6 ± 1.4 - 63.5 ± 0.3 Ma. Additionally, they conducted Sr, Nd, Hf, and high-precision Pb isotopic studies of volcanic rock, suggesting recycling of continental lithosphere was involved in the formation of the seamount province. They also dredged Cocos (Keeling) Islands and Christmas Island and analysed them using geochronological methods that will be discussed in the following sub-sections.

2.1.4.1: Cocos (Keeling) Archipelago

The Cocos (Keeling) Archipelago is a coral atoll that is located approximately 3000 km north-west of Perth. It is a group of twenty seven coral islands with total land area of around 14 km^2. The archipelago was the type example of a Coral Atoll in Darwin's seminal work on their formation (Darwin, 1842), after he visited these islands during his voyage on HMS Beagle in 1836 (Darwin, 1842). The Archipelago consists of two main groups of islands, North Keeling Island and the South Keeling Islands. North Keeling is a small island, 25 km north of the main archipelago and is one of the smallest national parks in Australia. The South Keeling Islands, however, constitute the main coral atoll. They comprise of the West, Home, Direction, Prison, Horsburgh, and South Islands (Figure 2.4). The two inhabited islands within the archipelago are the West and the Home Islands with a total population of ~600. The highest elevation can be found at South Island rising 11 m above sea-level and consists of mostly wind-blown sand dunes (Woodroffe & Falkland, 1997). The atoll of South Keeling is 11 km wide along an east-west direction and around 13 km north-south. It is shallower in the south, where the channels open to the ocean and can be exposed during low tide. They are approximately 15 m deep in the north opening towards Horsburgh Island (Searle, 1994).

Woodroffe and Falkland (1997) discussed the surface morphology of the island, in the context of a subsiding coral atoll over an underlying volcanic basement. They further state that the

surface morphology of the island has been affected by sea-level changes and accompanying sediment movement. The island consists of predominantly Holocene sediments comprising sand, mud, coral, biogenic matter and fossils underlain by Pleistocene Limestone (Woodroffe et al., 1991). The limestone unit is however, not exposed, but drilling operations primarily for groundwater exploration and to study the coral reef, have encountered it at a depth of 8 - 13 m (Woodroffe et al., 1991).

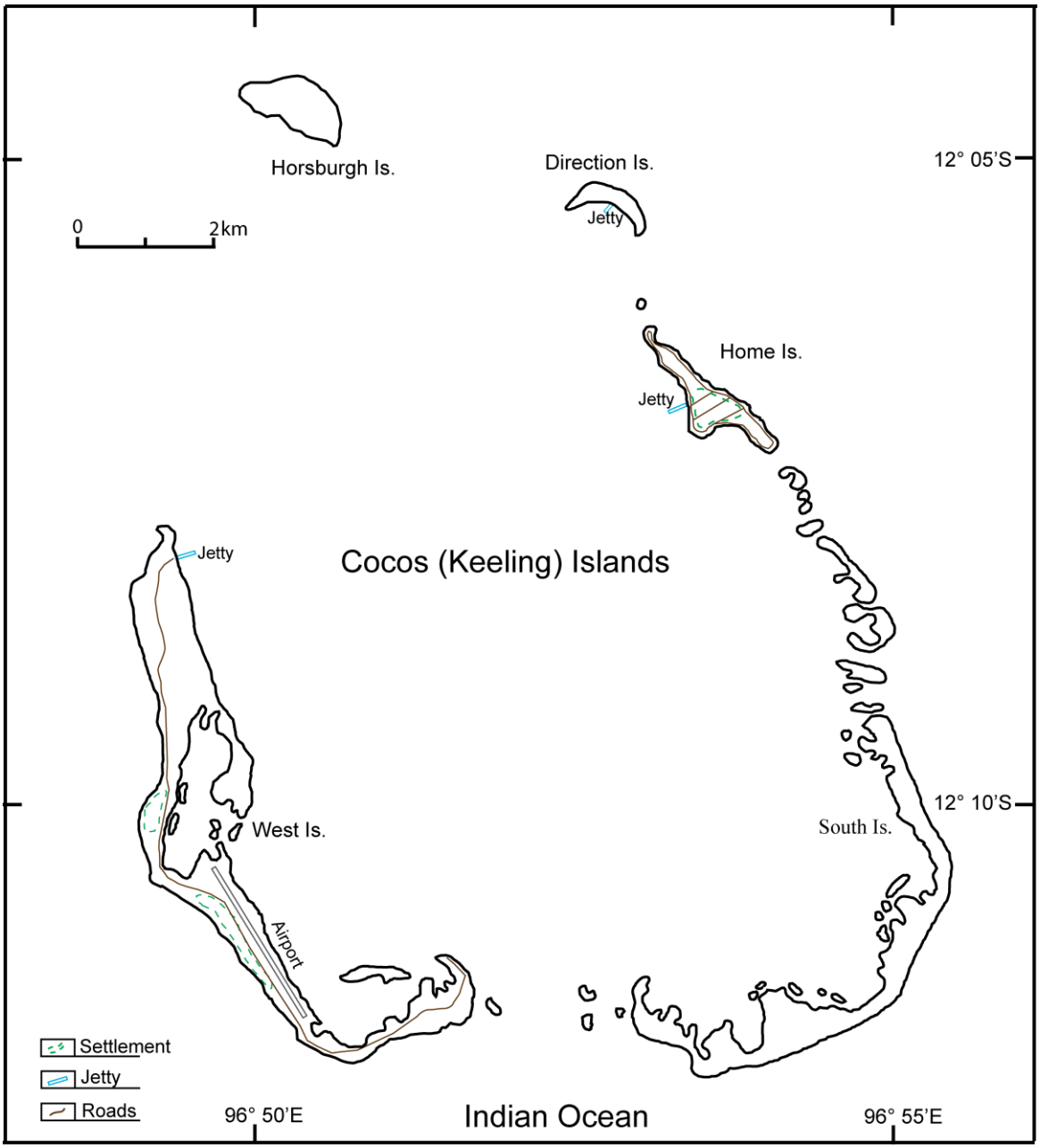

Figure 2.4: Map of Cocos (Keeling) Island showing the group of 27 islands and prominent roads and settlement in the West and Home Islands. Map modified from Woodroffe (2005).

Although most of the boreholes were concentrated on the inhabited region of the islands, drilling on the other islands have encountered similar lithologies at similar depths (Woodroffe et al., 1991). Seismic surveys conducted on the island by Searle (1994) have indicated a reflector at depths of 22 - 24 m within the centre of the lagoon. In addition, Woodroffe et al. (1994) calculated a gradual subsidence rate of the atoll in the range of 0.08 - 0.12 mm/yr based on the depth of the Pleistocene Limestone and sea-level changes.

The volcanic basement/outcrop is nowhere exposed on the island and has not been mentioned in any seismic survey or literature dealing with Cocos (Keeling) Island. Hoernle et al. (2011), however, dredged volcanic rocks from a depth of 2400 - 3100 m below sea-level and have dated these using incremental heating $^{40}Ar/^{39}Ar$ geochronology. Hoernle et al. (2011) have yielded ages of 56 ± 0.2 Ma and 55.6 ± 0.2 Ma for Cocos (Keeling) Island, and 47.0 ± 0.2 Ma south of the archipelago.

2.1.4.2: Christmas Island

Christmas Island is the second sub-aerially exposed limestone-capped volcanic island within the seamount province, and is roughly "T" shaped (Figure 2.5). It is 2500 km northwest of Perth and 350 km south of the Java Trench with a maximum elevation of ~350 m. The island has historically been a large phosphate producer, which is the principle industry and a major export commodity of the island (O'Dowd and Lake, 1989). It also hosts a dense tropical forest with a diverse and unique floral and faunal assemblage, including the terrestrial red crab which migrate en-masse from the jungle to coast each year. Mining operations on the island are currently restricted as large regions of the island are now a National Park. Sydney's Dale on the western coast of the island is one such natural habitat that has been declared as a protected habitat, and 580 hectares of it declared as an important wetland in 2002 in the Ramsar Convention of Wetlands (Butcher and Hale, 2010). Geoscience Australia recently produced

updated maps of the island from which mass-movement features are visible. The shoreline of the island has been influenced strongly by four major erosional features and many landslides have been reported in the northern, south-eastern, and western side of the island, while the eastern side is dominated by rocky seafloor (AusGeo News, 2009).

Most of the literature available for Christmas Island deals with the flora and fauna of the Island (O'Dowd and Lake, 1989; O'Dowd and Lake, 1991). In addition, there are a few reports by the Bureau of Mineral Resources and the Phosphate Mining Company but they concentrate mostly on the island's principal economic deposit. There are, however, some works on the Christmas Island by Rivereau (1965), Barrie (1967), Polak (1976), and Pettifer and Polak (1979) that are primarily geomorphological, or geophysical surveys carried out mainly for locating groundwater aquifers and to study the karst topography.

Pioneering geological work on the volcanic exposures and limestone caves including karst topography was done by Andrew (1900), Trueman (1965), Barrie (1967) and, Grimes (2001). Previous literature documents three stages of volcanic activity at Christmas Island, the oldest event forming the core of the Island occurred during the Late Cretaceous, a second one in the Eocene, and the most recent in the Pliocene (Trueman, 1965; Grimes, 2001). Earlier work had documented the oldest volcanic series within some inland caves that are inferred from stratigraphic and faunal correlations and interbedded limestone units (Trueman, 1965; Grimes, 2001). These caves, however, are now utilised by the island's water authority, and the outcrops are submerged. The intermediate series of Eocene volcanics is found at various locations across the island and has been classified into two units, lower and upper (Trueman, 1965). These are overlain by Late Oligocene to Mid Miocene "Upper Carbonate Series" that are mainly limestone sequences with minor dolomites (Andrew, 1900).

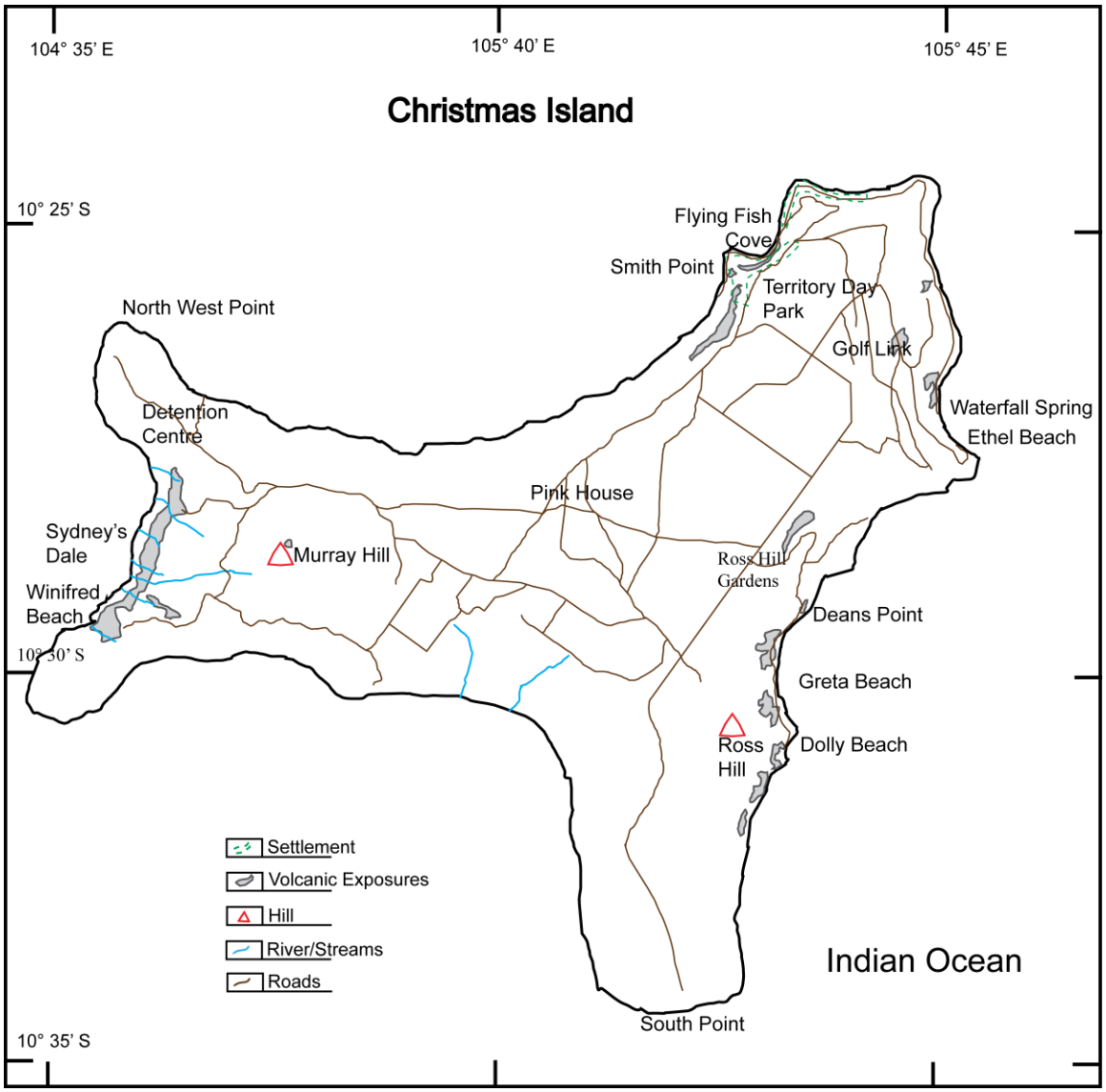

Figure 2.5: Map of Christmas Island showing principal volcanic exposures across the island. Map redrawn from Trueman (1965). Roads re-drawn from map provided by the Christmas Island National Park. Volcanic exposures were re-drawn from a GIS file provided by the Christmas Island National Park and have been confirmed by visual observations as in-situ volcanic outcrops during sampling.

The volcanism on the island was rejuvenated in the Pliocene in the form of dykes and minor volcanic vents (Grimes, 2001). Baxter and Weeks (1984) reported that volcanism in the Pliocene was accompanied by faulting near the Murray Hill region. The Pliocene event is exposed in the central region of the island and is influenced by heavy phosphatisation. Hoernle et al. (2011) dredged volcanic rocks around Christmas Island and analysed them using $^{40}Ar/^{39}Ar$ geochronology yielding two cluster of ages, an older sequence of 43.6 ± 0.4 Ma to 37.0 ± 0.6 Ma and a younger series of 4.31 ± 0.14 Ma to 4.52 ± 0.18 Ma. While older samples were both dredge and land samples, the younger samples were land samples.

2.2: Evolution and Opening up of the Northeast Indian Ocean

This section briefly discusses the evolution of the Northeast Indian Ocean following the initiation of a spreading centre between Greater India and Australia and their subsequent separation since the Late Jurassic. Gondwana reconstructions are problematic due to the lack of identified Mesozoic magnetic anomalies, which in some cases have been subducted at the Java Trench, or have been incorporated into the Eurasian lithosphere (Müller et al., 1998; Hall, 2012). Closer to India they are covered by sediments in the Bay of Bengal (Eagle and König, 2008). Major tectonic events along the western margin of Australia and the changing stress regime during the Mesozoic and Cenozoic , particularly at 43 Ma, have played a key role in the evolution of the region (Deplus et al., 1998; Veevers et al., 2000; Whittaker et al., 2007). Three events off the west coast of Australia have played an important role in shaping up the margins and tectonism of the region. These include: separation of Argo Land from Australia (~160 Ma) (Veevers and Cotterill, 1976); separation of India from Australia-Antarctica (118 Ma) (Liu et al., 1983); and propagation of the South East Indian Ridge (SEIR) separating Australia and Antarctica (Cande and Mutter, 1982). The complicated evolution of the region around Australia was addressed by Veevers (1971), Veevers et al. (1991), Sager et al. (1992), Müller et al. (1998, 2000a), Krishna and Rao, (2000), Ramana et al. (2001), Heine and Müller (2005), Gaina et al. (2007), Whittaker et al. (2007), Desa et al. (2009), and Gibbons et al. (2013). The reconstruction models described by Veevers et al. (1991) and Müller et al. (1998) are based on palaeo-geographic and paleomagnetic studies, the identification of magnetic anomalies, and the linearity and location of fracture zones aided by satellite derived gravity data (Veevers et al. 1991; Williams et al. 2012). The evolutionary history of the Northeast Indian Ocean, off the north-western margin of Australia has been divided into two sections. These include: a) the Late Jurassic to Late Cretaceous, when the major evolution took place; and b) the Late Cretaceous to Paleocene onwards, when the activity concentrated more in the

southern and eastern margins. This present section will concentrate on the western margin of Australia, as it the focus of this study, while the eastern and northern margins of Australia are very briefly discussed.

2.2.1: Late Jurassic – Late Cretaceous: Evolution along the western margin of Australia

Reconstruction models suggest Greater India, Australia and Antarctica were in contact in the Late Jurassic (~160 Ma), and there is a good fit along their margins (Veevers et al. 1991; Müller et al. 1998; Müller et al. 2000a). The Lhasa block separated from Greater India in the Triassic, around the Norian (Metcalfe, 1996; Metcalfe, 2002). This was followed by the rifting of smaller blocks from the Northwest Australian margin that included Argoland and SW Borneo (also called as the Banda block, Hall 2009; Metcalfe, 2011). The two blocks later accreted with SE Sundaland following their northward journey leading to the opening of the Ceno-Tethys (Metcalfe, 1996; Metcalfe, 2011; Metcalfe, 2013). The initial rifting in this region instigated with a southward propagation ridge after the breakup between Argo Land and Northwest Australia that occurred at about 156 Ma (Heine and Müller, 2005) (Figure 2.6). Veevers (1988) believes that Argo Land represents a slender continental block or sliver. These were series of first steps amongst the rifting events that took place along the western margin of Australia (Larson, 1975; Heirtzler et al., 1978; Sager et al., 1992). Heine and Müller (2005) and later Seton et al. (2012) in compilation of studies suggested that a NW-SE oriented rifting of the West Burma (also called as the Banda block by Hall, 2011) block at ~156 Ma separating it from the Northwestern margin of Australia. Once spreading started alongside the northwest margin of Australia, Argo Land started to drift away northwest, relative to Australia at a rate of ~160mm/yr (Müller et al., 1998) and created the Argo Abyssal Plain and the Jurassic crust of the present day seamount province (Gibbons et al., 2012).

A reorganisation of the spreading margin causing the northwards movement of Argoland around 136 Ma underwent a steep rotation reaching the western margin of Australia and forming a triple junction. Around 132 Ma, a spreading ridge developed further south, along the west margin of the Gascoyne and Cuvier Abyssal Plain (Heine and Müller, 2005). Fullerton et al. (1989) recognised magnetic lineations trending N30°E, while in the Argo Abyssal Plain they trend at N70°E. The magnetic anomalies are much older in the north (Late Jurassic), and younger (Early Cretaceous) in the south, suggesting seafloor spreading started in the north and later moved southwards (Fullerton et al., 1989). Gibbons et al. (2013) also suggested that Late Jurassic seafloor spreading might have reached south into the Cuvier Abyssal Plain, but is not preserved.

On the basis of some of the oldest magnetic anomalies in the abyssal plains a continuous dispersal along the western margin was suggested (Fullerton et al, 1989). This spreading ridge later continued further south leading to the breakup between Greater India and Australia (Metcalfe, 1996; Müller et al., 2000a) starting at 136 Ma in the northwest and reaching the southern tip of India at 126 Ma (Gibbons et al. 2012). The separation of Greater India resulted in the formation of abyssal plains along the western Australian margin. These began with the Perth Abyssal Plain (~136 Ma), the Gascoyne (~135 Ma), and lastly the Cuvier (~133 Ma), which formed through a series of ridge jumps (Gibbons et al. 2012).

As Greater India migrated from the western margin of Australia, and its subsequent rifting from the South Greater India and Antarctica, the Greater India block left various partially fragmented continental blocks behind, due to ridge jumps (Gibbons et al., 2012). The Wallaby Plateau is one such block that transferred to the Australian Plate via a ridge jump at ~127 Ma, while the Zenith Plateau is another block that transferred from the Indian Plate to the Australian Plate around 124 Ma (Gibbons et al., 2012). Gibbons et al. (2012), however, discussed that further

set of ridge jumps transferred a Late Jurassic sliver back to the Indian Plate, and then finally on to the Australian Plate at reconstruction intervals of 100 and ~95 Ma respectively.

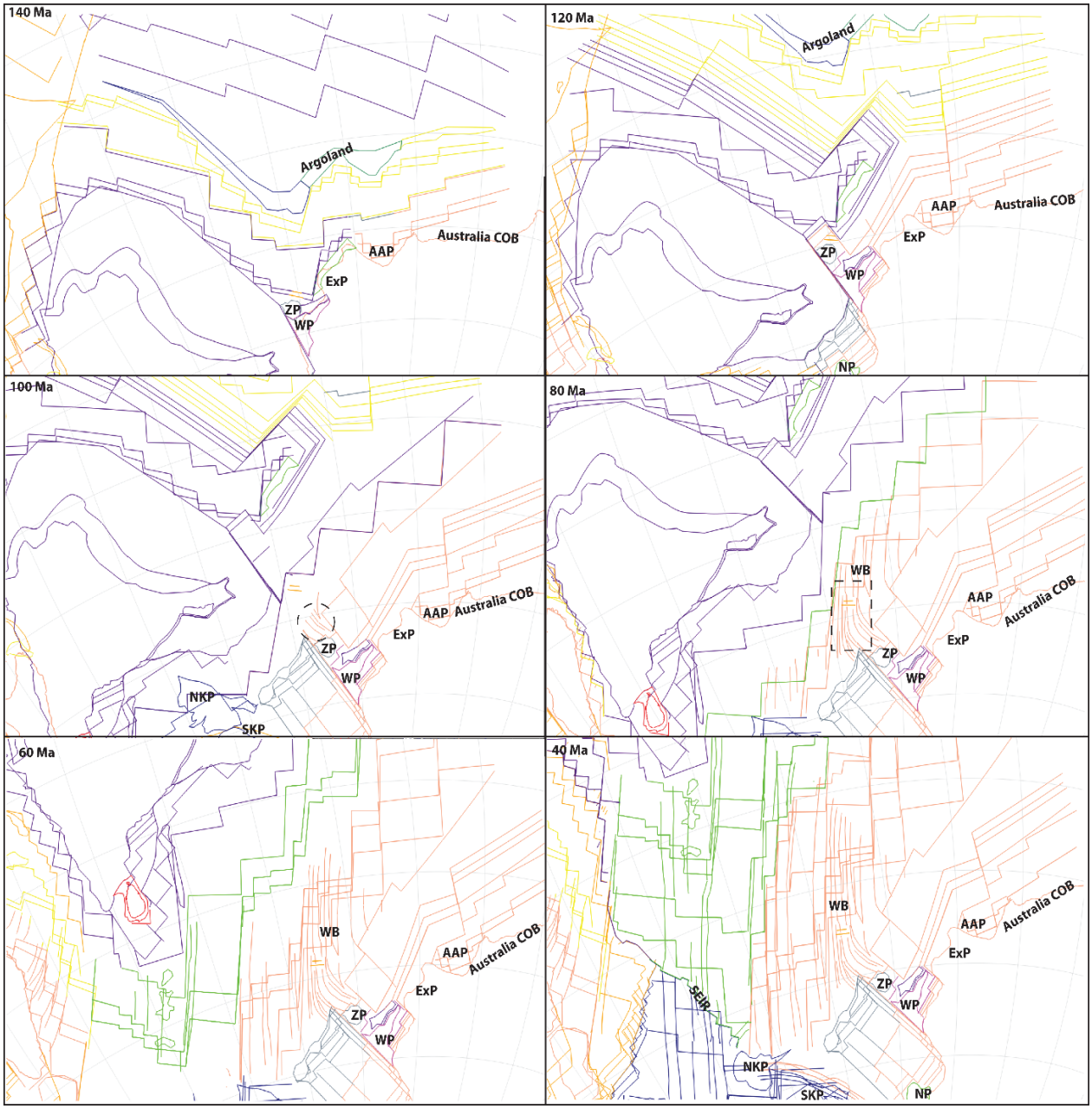

Figure 2.6: Plate reconstruction model for the Northeast Indian Ocean and adjoining region of Western Australia. Dashed circle (100Ma) and dashed rectangle (80 Ma) represent the change in orientation of fracture zones in Wharton Basin before and after the 100 Ma spreading direction event. AAP, Argo Abyssal Plain; ExP, Exmouth Plateau; ZP, Zenith Plateau; WP, Wallaby Plateau; WB, Wharton Basin; NP, Naturaliste Plateau; NKP, North Kerguelen Plateau; SKP, South Kerguelen Plateau. Tectonic plates and ocean floor fabric is colour coded; pink, Australia; green, India; blue, Antarctica. Plate reconstruction model adapted from Gibbons et al. (2012).

Seafloor spreading in the Perth Abyssal Plain continued further south and west into the Enderby Basin as a continuous ridge system (Whittaker et al. 2013). This formed a triple junction that was associated with the spreading in the Perth Abyssal Plain, the Enderby Basin, and the ridge between Australia- Antarctica (Gaina et al. 2007, Seton et al. 2012; Whittaker et al. 2013). Ramana et al. (2001) identified a younger sequence of Mesozoic magnetic anomalies (M11-M0) in the Enderby Basin, East Antarctica, with half spreading rates similar to those in the Bay of Bengal. They concluded that the two basins were contemporary to each other and that the breakup of India from Antarctica occurred before ~134 Ma. Later on, Gaina et al. (2003) identified new magnetic anomalies in the Enderby Basin and suggested that the Elan Bank detached from India ~ 124 Ma, after which it became a part of the Antarctica Plate (contemporaneous with spreading in Perth Abyssal Plain). Whittaker et al. (2013) reconstructed the evolutionary history between Australia and Antarctica starting at ~136 Ma, which involved rifting between India and the Perth Abyssal Plain, and India and Antarctica. The spreading system from the Perth Basin to the Enderby Basin continued up to ~115 Ma, when a ridge jump transferred the Elan Bank to the Antarctic Plate at ~115 Ma (Gibbons et al. 2013).

Krishna and Rao (2000) identified a number of abandoned spreading centres both east and west of the Ninetyeast Ridge within the Northeast Indian Ocean. They proposed that the abandoned ridges east of the Ninetyeast Ridge undertook number of jumps southwards and maintained continuity with the Wharton Ridge. These abandoned ridges, between the 86°E and 90°E fracture zones, transferred parts of oceanic crust from the Antarctic Plate to the Indian Plate repeatedly at different ages (Krishna and Rao, 2000). Desa et al. (2009) identified marine magnetic anomalies in the Northeast Indian Ocean, between the 86°E fracture zone and the Ninetyeast Ridge that documented fossil spreading ridges and extra oceanic crust within the Indian Plate which, were transferred from the Antarctic Plate by southern ridge jumps.

One of the characteristic features of the Northeast Indian Ocean are the north-south fracture zones present in the Wharton Basin, such as the Investigator Ridge. Magnetic anomaly interpretations in the Gascoyne and Cuvier Abyssal Plains demonstrate northwest-southeast trending fracture zones as opposed to north-south trending fracture zones in the Wharton Basin (Powell et al., 1988; Müller et al., 1998). Larson et al. (1978) were the first to recognise magnetic anomalies near the Investigator Ridge and found that spreading underwent a 55° change in direction. Müller et al. (1998, 2000a) explained this on the basis of a change in spreading direction from northwest-southeast to a more north-south orientation around 100 Ma. Major reorganisation (due to closure of subduction east of Australia) occurred in the Indian Ocean ~100 Ma (Müller et al., 2000b; Matthews et al., 2012; Gibbons et al., 2012; Whittaker et al., 2013) and is reflected as curved fracture zones in the Wharton Basin and in the Enderby Basin as the Kerguelen Fracture Zone (Gibbons et al. 2013). Matthews et al. (2012) discussed that this reorganisation occurred between the Cretaceous Normal Superchron (CNS), and its age of 110.8 – 110 Ma can still be determined using relative dating, interpolation between magnetic anomalies, and seafloor ages constrained by ocean drilling programs. Changes in plate reorganisation and intra-plate stresses resulted in renewed lithospheric thinning around 100 Ma (Müller et al., 2000b). Extensional plate deformation and changes in plate kinematics point towards the subduction of a spreading ridge north of Australia at around 61 Ma (Müller et al., 2000b). Beyond this much of the tectonic evolution occurred around the southern and eastern margin as discussed in the following section.

2.2.2: Late Cretaceous to Paleocene onwards: Evolution along the southern and eastern margin with minor events in the west

Spreading had started close to the southeast section of the east coast in the Tasman Sea around the Late Cretaceous (90 Ma). Gaina et al. (1998a) worked on the reconstruction events east of Australia and suggested a thirteen-piece micro continental block evolutionary history for the region. These continental blocks separated from Australia via multiple tectonic events, both extensional and strike-slip (Gaina et al., 1998a). Prior to spreading, the early evolutionary history consisted of rifting events between Australia and East Tasman Plateau (Gaina et al., 1998a). At chron 27, sea floor spreading propagated further north into the northern Tasman Sea and then into the Coral Sea (Gaina et al., 1999). The oblique compressional events, following subsequent changes in the absolute motion of the Pacific Plate and/or collision of India with the Eurasian Plate, resulted in the cessation of sea-floor spreading along the eastern margin of Australia (Gaina et al., 1999) at chron 24 (52 Ma). While spreading along the southern margin progressed, the northward motion of Australia increased from 0.8 cm/yr to 3.0 cm/yr (Royer and Rollet, 1997). Eventually, the Southeast Indian Ridge developed, and with the cessation of spreading at the Wharton Ridge at ~43 Ma (Liu et al., 1983) or 38 – 36.5 Ma (Jacob et al., 2014), the once-separate Indian and Australian plates became one rigid plate (Liu et al., 1983).

At 43 Ma, various tectonic events took place that left their mark on the evolutionary history of the Australian margin. The Kerguelen Plateau and Broken Ridge separated, spreading in the Wharton Basin ceased (Liu et al., 1983) and a significant part of Wharton Basin lithosphere has subducted the Sumatra subduction zone since then (Singh et al. 2011), there was an increase in subsidence in the northern Australian margin, a low angle transform margin developed along the Papua New Guinea margin, and renewal of subduction along the northeast margin of Australia (Müller et al., 2000a). Major reorganisations events in the Pacific Ocean due to

subduction of Izanagi - Pacific spreading ridge led to changes in Pacific Plate motion from northwest to north (Whittaker et al., 2007). Increased slab-pull north of Australia due to the subduction of the Wharton Ridge led to major change in the reorganisation of the Australia Plate motion from northwest to north around 50 Ma (Whittaker et al., 2007).

2.3: An incipient plate- the Capricorn Plate

The Indian and the Australian Plates have undergone significant transformations in terms of plate motion and dynamics since its breakup from Gondwana and its subsequent northward journey as described in the previous section. Since the amalgamation of the Indian Plate and the Australian Plate at ~43 Ma (Liu et al., 1983; Seton et al., 2012), India has collided with the Eurasian Plate and slowed down, but Australia is still moving NNE at 7 cm/yr (Tregoning, 1994). The result is a continental collision at the northern end of the Indo-Australian Plate, and a subduction zone at its eastern end (Weissel et al., 1980; Cloetingh and Wortel, 1985). Cloetingh and Wortel (1985) discovered that there is considerable net resistance to the Indian Plate at the Himalayas collision front and elsewhere along the convergent margin. This change in tectonic setting along the northern margin and the relative motion of the two continental landmasses is causing torsional stresses within the centre of the plate (Cloetingh and Wortel, 1986).

Due to inconsistency in plate motion data for the Southeast Indian Ridge, Southwest Indian Ridge, and the Central Indian Ridge, in addition to increased seismicity and misfit within plate models, Royer and Gordon (1997) suggested internal deformation within the Indo-Australian composite plate system. This deformed region of the Indo-Australian Plate extends from the Central Indian Ocean, spanning across the Ninetyeast Ridge up to the North West Shelf of Australia (Figure 2.7).

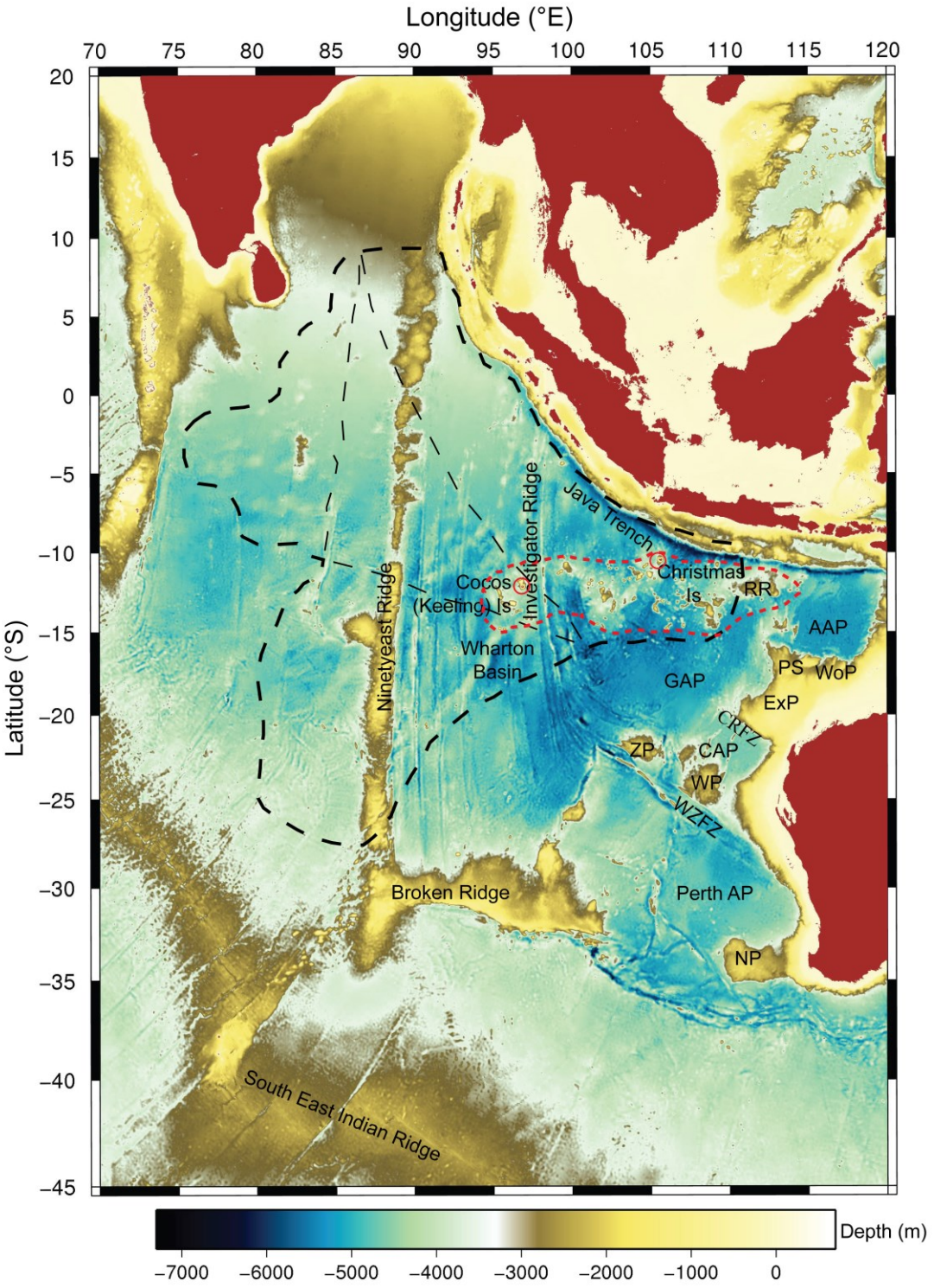

Figure 2.7: Bathymetric map (Smith and Sandwell, 1997) of the eastern Indian Ocean showing the boundary of Capricorn Plate (Royer and Gordon, 1997; thick dashed black line), and Indian, Australian, and Capricorn component plates separated by diffused oceanic plate boundaries (thin dashed lines). Also shown are the physiographic features of the Northeast Indian Ocean. AAP, Argo Abyssal Plain; GAP, Gascoyne Abyssal Plain; CAP, Cuvier Abyssal Plain; Perth AP, Perth Abyssal Plain, RR, Roo Rise; ScP, Scott Plateau; WoP, Wombat Plateau; PS, Platypus Spur; ZP, Zenith Plateau; WP, Wallaby Plateau, WRFZ, Wallaby Zenith Fracture Zone, CRFZ, Cape Range Fracture Zone; NP, Naturaliste Plateau; ExP, Exmouth Plateau, dashed red line represents the boundary of the seamount province and red circles are the two sub-aerially exposed islands.

The deformed margin within the once rigid Indo-Australian Plate has been called the Capricorn Plate (Royer and Gordon, 1997; Gordon, 2009). The deformation on either side of the Ninetyeast Ridge is distinct. Towards the west, folds and east-west oriented reverse faults are common, whereas, on the east of the ridge, left lateral strike slip faulting is prevalent along a north-south trending fracture zone (Deplus et al., 1998). The Ninetyeast Ridge, thus, acts as a natural mechanical barrier separating deformation pattern in the two areas (Deplus et al., 1998).

The Investigator Ridge is a prime example of the numerous parallel north-south trending fracture zones in the region (Sclater and Fisher, 1974; Larson et al., 1978). Most of the fracture zones are located between the Ninetyeast Ridge and the Investigator Ridge (98°E), as the region to its east is dominated by the seamount province (Figure 2.7). Performing plate reconstructions amongst the Indian, Australian and Capricorn Plates, Royer and Gordon (1997) discussed the 100-300 km long wavelength gravity undulations that reflect the variations in topography and described them as fold and thrust mountain ranges analogous to those on the continents. Using high-level seismicity and sea-floor mapping, Deplus et al. (1998) provided evidence that these "aseismic" ridges are in fact continually reactivated.

The change in the collision pattern from the west towards the east; oblique across the Sumatra Trench and frontal along the Java Trench, leads to the rotation of compressive stresses that are north-south in the central Indian Ocean and northwest-southeast in the eastern part (Cloetingh and Wortel, 1986). The compressional axis of most of these earthquakes is located within the north-south fracture zones. Geodetic studies undertaken by Gordon et al. (2008) have provided qualitative evidence in support of the differential movement of the Capricorn Plate relative to both the Indian and Australian component plates.

Abercrombie et al. (2003) believes that the fossil fracture zones in this part of the deformed plate are being reactivated by the current stress field causing rupture and leading to large earthquakes in the intraplate region. The Wharton Basin earthquake of M_w 7.9, (June 2000), one of the largest shallow strike slip earthquakes recorded is the result of such a high stress regime (Abercrombie et al., 2003). The event resulted in aftershocks that were recorded for the following three days, with intermittent seismic activity until October 2000 (Robinson et al., 2001; Abercrombie et al., 2003).

Chapter 3: Methodology

To understand the complexities of the Indo-Australian Plate and the evolution of the CHRISP, this study uses a number of geophysical, geochemical and geochronological analytical methods. To begin with, this research uses different geophysical techniques like gravity modelling, seafloor subsidence modelling, flexural modelling and seismic tomography. This research also utilises paleomagnetic analysis to study the paleomagnetic field locked within the rocks while they were emplaced as sub-aerial representatives of intraplate volcanism in the Christmas Island Seamount Province. Reconstruction models are then overlaid on regional seismic tomography models to determine their relationship with low velocity zones underneath the Northeast Indian Ocean.

Since Christmas Island is the only exposed island to have recorded the volcanic events giving rise to the province, dating the volcanic rocks to determine the age and duration becomes crucial in understanding not just the island's but the igneous province's evolution as well. Hence, select batches of samples from Christmas Island were dated using high resolution $^{40}Ar/^{39}Ar$ geochronology at the Western Australian Argon Isotope Facility, Curtin University of Technology, Perth, Western Australia.

Finally, geochemical analyses were carried out on the same set of rocks to constrain source composition and thereby establish the evolution of the seamount province, by taking Christmas Island as a type example. For this, the research relies heavily on major and trace elemental analysis carried out at Macquarie University and in collaboration with the University of

Wollongong. In addition, Nd, Hf and Pb isotopes were analysed at Ecole Normale Supérieure de Lyon.

This chapter begins with an overview on the field trip and sample collection at Christmas Island. Thereafter it describes various geophysical methods employed in this study, followed by an overview of the $^{40}Ar/^{39}Ar$ geochronology, laboratory techniques and methodology. Finally, the geochemical analytical techniques used for the analyses of major, trace elements, and isotopes are described.

3.1: Sample Collection

Sampling was carried out at Christmas Island during a field visit in November, 2010. Prior to the field trip, careful planning and extensive review studies were conducted to locate potential sites for both hand sample collection and rock drilling. A GIS map of volcanic exposures was provided by the Christmas Island National Park (integrated and depicted in Figure 3.1). All volcanic exposures depicted by the Christmas Island National Park GIS map were visited and sampled. Sydney's Dale and Winifred Beach had very limited volcanic exposures. Previous authors have sampled volcanic rocks in the central regions of the Island near Murray Hill (Grimes, 2001), but during field work only minor dykes that were heavily phosphatised were found, but no fresh in-situ outcrops were observed. Hand specimens were used for geochemical and geochronological analysis, while drilled samples were used for paleomagnetic analysis. Volcanic samples were selected from 26 different locations, and it was ensured during the course of sample collection that only freshest, least-weathered samples were picked. Visual examination of hand specimen, general site conditions, and examination using a hand lens helped differentiate fresh samples from the heavily weathered ones. Due to the onset of red crab migration in November certain sections of roads were blocked, therefore, this involved trekking for a significant part of the field trip. Sampling of the island was divided into east,

west and north sections. While traversing across the southern part of the island, no volcanic outcrops were found, although a heavily weathered dyke altered by phosphatisation was found in the central region around the Murray Hill.

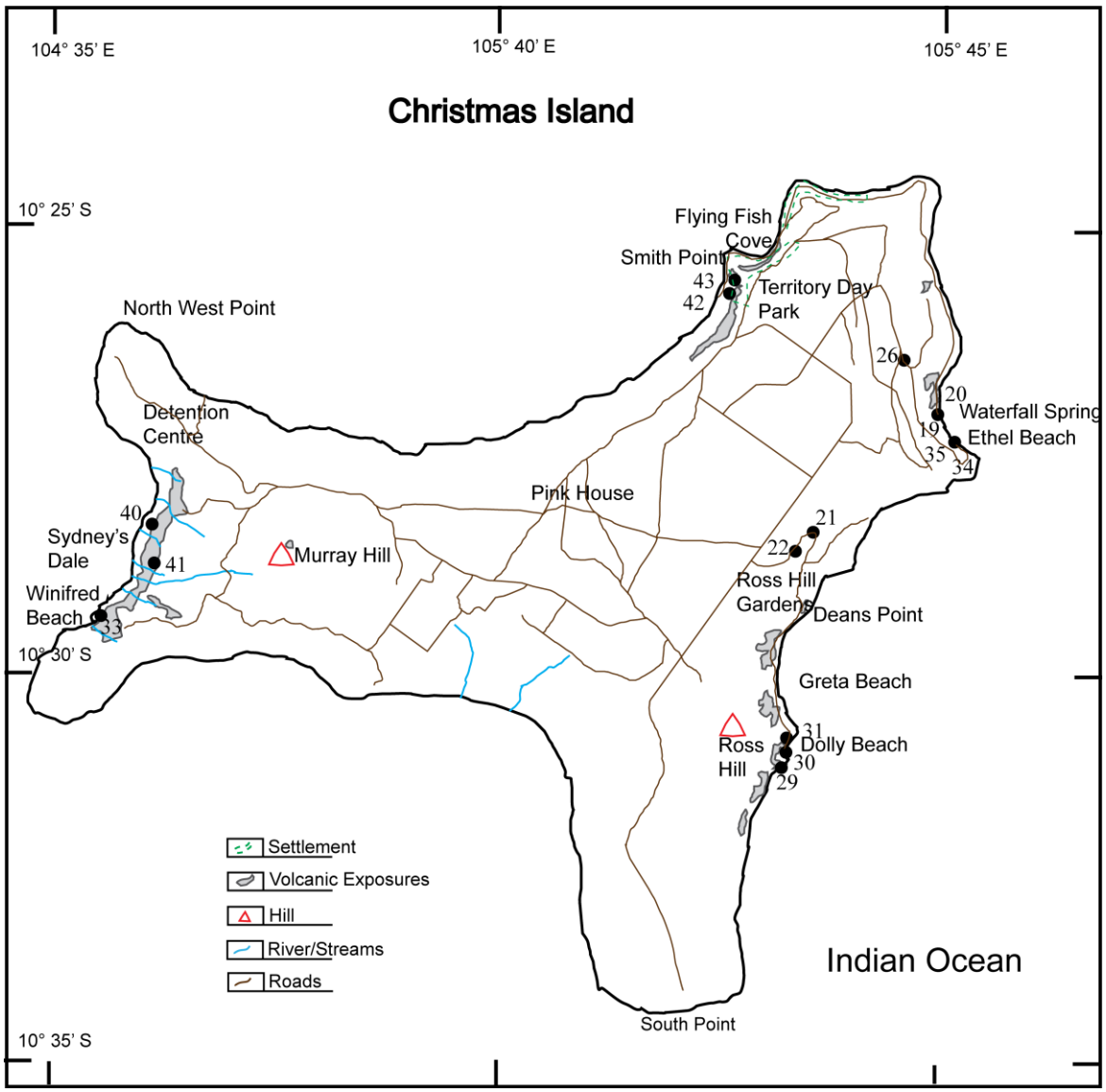

Figure 3.1: Map of Christmas Island showing prominent volcanic exposure and volcanic sampling sites. Major roads and volcanic exposures were re-drawn from maps provided by the Christmas Island National Park. Exposure at Murray Hill in the form of dyke was heavily phosphatised and no fresh in-situ samples were collected.

Prominent sampling sites of the island (Figure 3.1) were:

- North: Territory Day National Park, near the phosphate conveyor belt around Flying Fish Cove.

- East: Waterfall Spring opposite to the Christmas Island resort; Ethel Beach 300 m south of Waterfall Spring; Dolly Beach; Ross Hill Gardens; Ross Hill Water Pump; region around Linkwater and Golfcourse Casino Road. The first three sites are in-situ and along the coast, while the latter three sites outcrop inland.
- West: Sydney's Dale along the creek occurring as volcanic pebbles and Winifred Beach was an in-situ site. Both of these sites were under a thick canopy of tropical forest.

Of the above-mentioned sites, selected least weathered and freshest available in-situ samples were chosen for geochemical and geochronological analyses and four in-situ sites were drilled for paleomagnetic investigations. Dolly Beach on the east coast contains a basaltic dyke protruding though the shore sands containing phenocrysts of olivine and pyroxenes in a feldspar (plagioclase) rich groundmass, which also contained pyroxenes and opaque oxides. The exposed outcrop is approximately 10 x 10 m in extent.

Waterfall Spring on the east coast occurs as a 3 - 5 m^2 outcropped volcanic exposure. In addition, volcanic exposures are visible on the steep cliff ~7 m in height facing the Christmas Island Resort. Visual observations suggest the outcrop to continue along the eastern face of the outcrop towards the shoreline. The outcrop at Ethel Beach is accessible only during low tide and is a 1 x 2 m wide exposure at the base of the cliff and appears to be an extension of the exposures outcropping at Waterfall Spring. The outcrops at Ethel Beach and Waterfall Spring are vesicular, predominantly composed of pyroxene, and some olivine. The groundmass is rich in feldspars (plagioclase) and opaque minerals. Field observations and previous literature suggests these to be exposed volcanic outcrops, while some might be dykes. They are not windows of volcanic exposure through the limestone. The two sites on the west coast (Winifred Beach, and Sydney's Dale) are under a thick canopy of tropical forest. Furthermore, the sampling sites on the west coast occurs at a higher elevation, in contrast to those on the east coast which are located at the shore. Much of Christmas Island is part of a dense tropical forest

without roads or access tracks, and certain areas have undergone phosphate strip mining. This led to limited access to many parts of the island and thus greatly affecting sampling. In addition, due to construction activity in the north, the area near the Smith Point Walking Trail was not accessible and this limited sample collection around the northern part of the island.

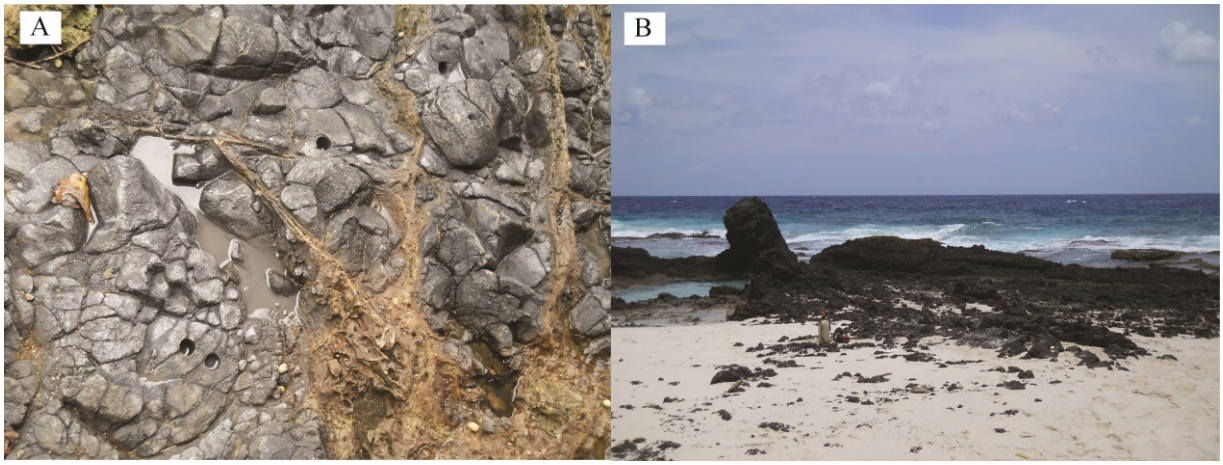

Figure 3.2: Outcrop photographs during sample collection at Christmas Island, A, Waterfall Spring; B, Dolly Beach. Scale: A, Drill holes are 2.2 cm in diameter; B, Paleomagnetic drill water container is 0.5 m in height and the width of vertical volcanic exposure is 1.5 m.

Figure 3.3: Orientation of a sun compass while taking drilled core samples for paleomagnetic interpretation at Waterfall Spring. Dr. Craig O'Neill measuring the orientation of the drilled core.

Drilled rock cores were obtained using a water cooled two stroke powered motor drill as shown in Figure 3.2 (B). Samples were drilled in the field and oriented with the aid of a magnetic and a sun compass as described by Butler (1992) and McElhinny and McFadden (2000). The compass consists of a sun dial and a magnetic needle on a horizontal disc pivoted to a cylinder. By keeping the disc horizontal and fixing the cylinder along the length of the drill, the inclination (dip) of the drill can be ascertained as seen from Figure 3.3. Core measuring 3 to 5 cm in length with a fixed diameter of 2.2 cm were obtained from drilling.

The three sites on the east coast and one on the west coast (Winifred Beach) were drilled for paleomagnetic analysis. These four sites and two additional sampling locales, Sydney's Dale and Flying Fish Cove, were analysed for $^{40}Ar/^{39}Ar$ geochronology and geochemistry. Sydney's Dale was not drilled for paleomagnetic analysis as it is a protected natural habitat and 580 hectares of this habitat are declared as an important wetland in 2002 Ramsar Convention of Wetlands (Butcher and Haler, 2010). Vertical drilling was performed using a portable hand drill, and exposures on the cliff at Waterfall Spring could only be accessed with a scaffolding, therefore no samples were obtained from the cliff. Nevertheless, a comprehensive field work was performed on the Island, and samples were collected from all accessible sites.

3.2: Geophysical Techniques

3.2.1: Locating submerged seamounts

As oceanic crust moves away from a mid-oceanic ridge spreading centre, it cools, contracts, and becomes dense, leading to subsidence of the seafloor (Sclater et al., 1971). Geomorphic features, such as seamounts and oceanic islands, exposed above sea-level, eventually subside and sink as well in response to this seafloor subsidence (Paulay and Edward, 1990). Once below sea-level, coral reefs begin to form and, if subsidence rates are low enough, they may keep in pace with the subsidence. Higher subsidence rates may exceed coral growth rates, resulting in

the island eventually sinking, with a flat sedimentary sequence as its top (Winterer, 1998). Accretion of coral reef over a subsiding volcanic island was first explained by Darwin (1842) for the South Keeling Atoll of the Cocos (Keeling) Archipelago. With respect to the present sea-level, Woodroffe et al. (1991) suggested a subsidence rate of 0.08 mm/yr for Cocos (Keeling) Island, but due to variation in paleo sea-level, a rate of 0.12mm/yr has also been suggested. Flat-topped seamounts indicate sub-aerial exposure and can be found scattered in the seamount province. Similar seamounts with flat sedimentary sequences underlain by basaltic rocks have been found for the Corner and Cruiser seamounts in the North Atlantic Ocean (Tucholke and Smooth, 1990).

The study has used global bathymetry and gravity data available by Smith and Sandwell (1997) from Scripps Institution of Oceanography to locate these seamounts. These are 1 arc minutes "netcdf" format grids that comprise ship-track and satellite derived data to form a global coverage file and are available free to the public domain. These grid files can be plotted as bathymetry maps using Generic Mapping Tools (GMT, Wessel and Smith, 1991) to produced post script (PS) vector files as compared to Google Earth, where the data cannot be downloaded but only visualised.

The first step in our approach was to identify and characterise the seamounts in the 1500 km by 600 km CHRISP. Numerous bathymetry and gravity profiles were constructed and seamounts and volcanic guyots were identified from this data. Once these volcanic features were found, they were then separated into those with rounded peaks (also called conical seamounts, Dominguez et al. 1998) and flat tops. Numerous seamounts and submarine volcanic edifices present within the region can be seen clearly on the map. These flat-topped features indicate that erosive and weathering processes were once active while the seamounts were exposed above sea-level (Hess, 1946; Winterer and Metzler, 1984). Hess (1946) first documented that flat topped seamounts were a truncated feature of volcanic origin that

underwent erosion. Winterer and Metzler (1984) dredged coral reefs of Mid Pacific Mountains of the central Pacific Ocean, and concluded that these were formed on subsiding seamounts that grew to form atolls. Winterer (1998) surveyed and drilled Cretaceous guyots from the Pacific Ocean concluding that the surface morphology of these features results from erosional processes active on the seamount while it was sub-aerial. Two such flat top and rounded peak seamounts are shown in Figure 3.4.

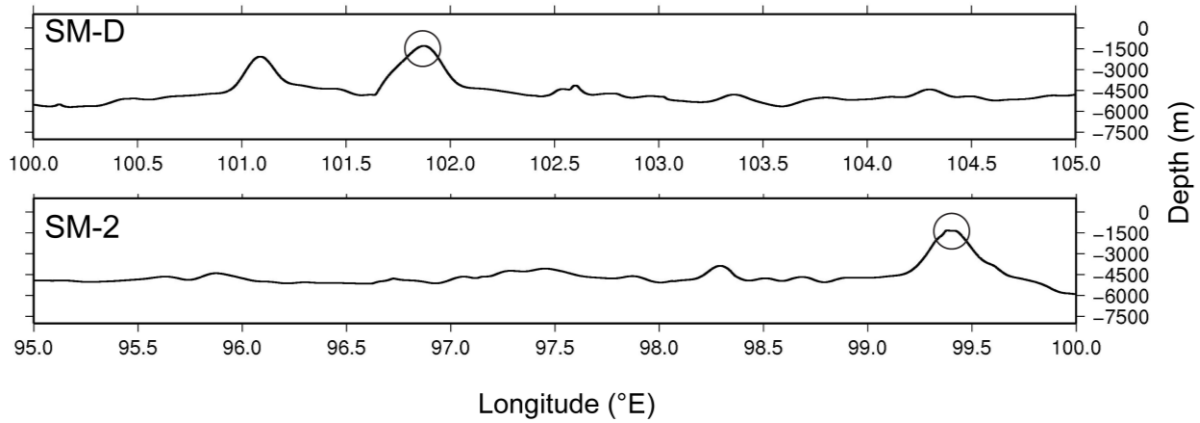

Figure 3.4: Bathymetry profiles of selected seamounts located in the Northeast Indian Ocean. Top, rounded/conical topped seamount SM-D (seamount left of SM-D is the impression of SM-C); bottom, flat top seamount, SM-2.

3.2.2: Gravity Modelling

Ocean floor bathymetry is as varied as the topography of the continents. Changes in the bathymetry of the ocean floor leads to variation in gravitational responses. In many instances, the variations in the bathymetry of a region is obscured due to sediments. Gravity anomaly maps in such cases are often used to delineate surface features that are hard to distinguish or unlikely to be identified from conventional bathymetric and topographic maps. Due to the high density of marine features (for example, seamounts with density of 3.0 g/cm^3) they are easily identifiable underneath lighter sediments. Within the Northeast Indian Ocean, fracture zones on either side of the Investigator Ridge, and the Cape Range Fracture Zone, are rather more apparent in the gravity anomaly map (Chapter 2, Figure 2.2) than in bathymetric maps.

Gravity profiles extracted from binary grids representing distance and gravity response were used to model the crustal structure of the oceanic lithosphere beneath the seamounts and islands. This helps in constraining the thickness and depth of various crustal layers underneath the island. For this, 2D data was imported into the geophysical modelling software ModelVision V.8, developed by Pitney Bowes, Inc (Encom). ModelVision is a 3D potential field modelling tool used for a wide variety of geological and geophysical analysis. Ideally, it would have been best to collect high resolution gravity data at Cocos (Keeling) Island and Christmas Island. This was, however, not possible in this project, as Cocos (Keeling) Island is a coral atoll and the land strips at its periphery are not wide enough to produce a long and sufficiently high quality gravity grid, if a terrestrial survey was conducted. Additionally, a marine survey using ships or (airborne gravitometry) data collection was beyond the scope of this research. Christmas Island, on the other hand, is covered by a dense tropical forest, with extensive historical mining operations across the island, and this limited the scope for collecting high resolution geophysical data.

The regional gravity response of the Cocos (Keeling) Island, and Christmas Island was modelled to determine the island's crustal structure. East – west gravity profiles across the island show a maximum gravity anomaly of roughly 170 mGal for Cocos (Keeling) Island and ~300 mGal for Christmas Island. For Cocos (Keeling) Islands a 220 km long profile was selected and modelled. Similarly, Christmas Island was modelled along a 220 km traverse in an east-west direction (a representative raw modelling file is shown in Figure 3.5).

XYZ formatted ASCII data, consisting of distance (m) and gravity anomaly values in mGal, was imported into Modelvision to produce an observed gravity profile of the island. In addition, bathymetric profile of the island was loaded into the modelling software. The crustal structure of the ocean floor was then modelled by assembling polygonal bodies, each representing a known crustal layer, to produce a calculated gravity profile that matched with

the observed gravity curve. During the entire modelling exercise, it was ensured that the surface of the first crustal layer matched as accurately as possible with the bathymetric profile of the island.

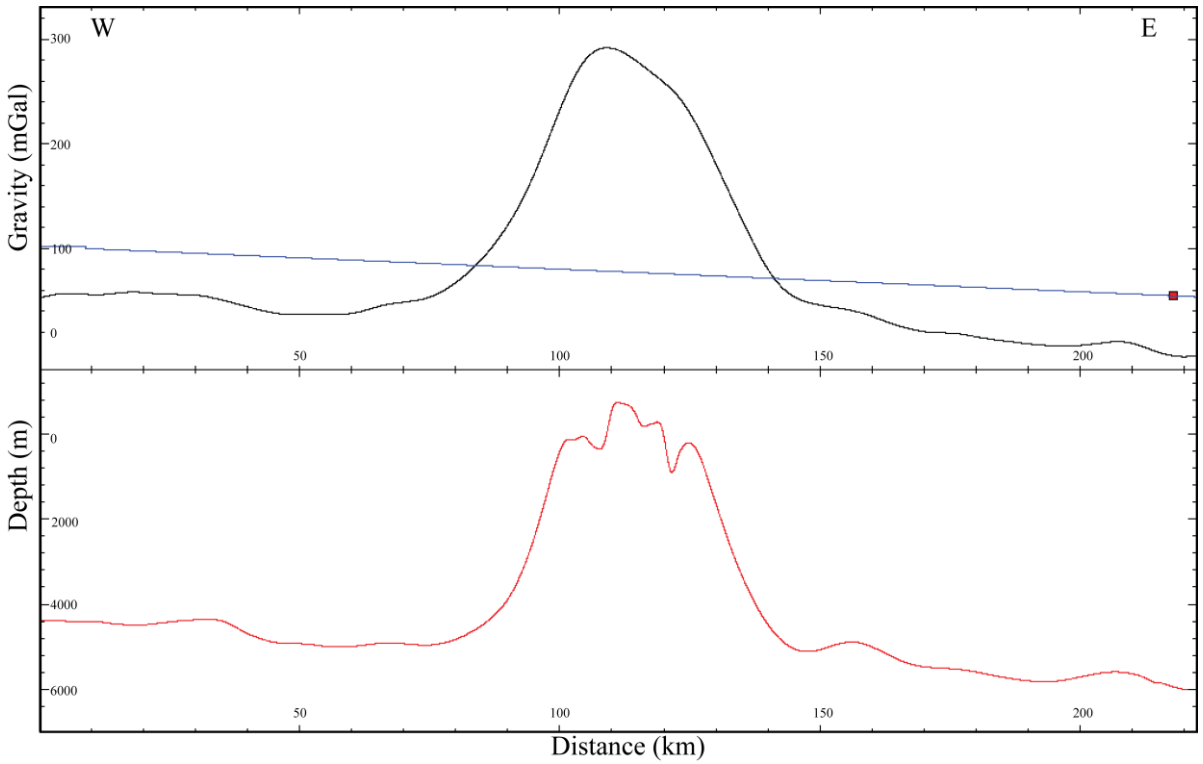

Figure 3.5: A profile of the observed free air gravity (top, black line, in mGal) across Christmas Island imported into ModelVision. Blue line represents the regional anomaly. Bottom: bathymetry profile (red line) of the island. X-axis is in kilometres. Gravity data is from Sandwell and Smith (2009), and the bathymetry data is from Smith and Sandwell (1997).

For modelling, a simple (three layer) crustal structure of the ocean floor consisting of basalt, gabbro, and mantle was assumed. This is based on the work of Shurbet and Worzel (1955), Watts et al. (1975), Miles (1982), Watts et al. (1985), and Weigel and Grevemeyer (1999) who have used both gravitational modelling and seismic techniques to study the lithospheric structure beneath various islands and seamounts. Davy and Wood (1994) have pointed out the similarity and correlation amongst the satellite derived gravity data and basement interpretation done through seismic surveys. Lack of any deep seismic data within the seamount region adds to the inability of using multiple data sets for constraining the model at higher resolution and map-out any limestone or volcanic sub-layers. Nevertheless, a best possible approach was

followed to correctly constrain the crustal structure. The gravity signature was modelled laterally over 200 km in linear profile to avoid any edge effect at the boundaries of our modelling domains. Due to lack of basement maps or sub-crustal constraints the models were subjected to variation in crustal thickness and densities to test sensitivities, and as pointed out by Davy and Wood (1994) the variation in the layers can be of the order 2 – 4 km.

3.2.3: Flexure of the lithosphere and age at the time of loading

The load exerted by the island on the oceanic lithosphere can lead to its flexure and bending directly below the load producing a bulge upwards on either side (Walcott, 1970; Watts and Cochran, 1974, Watts, 2001) as seen diagrammatically in Figure 3.6. This elastic nature of the lithosphere is often used to determine the mechanical properties of the lithosphere that depend on the age of the lithosphere at the time of loading (Watts, 1978; Bodine et al., 1981). Turcotte and Schubert (2002) used this relationship to calculate the elastic lithosphere thickness for the Oahu Island in the Hawaiian seamount chain. The distance (X_b) from the centre of the load to the crest of arch is used to determine the elastic lithospheric thickness using the formulae:

$$F = X_b/\pi \quad 3.1$$

$$4D = F^4\,(\rho_m - \rho_w)g \quad 3.2$$

$$12\,D\,(1-\nu^2) = E\,T_e^3 \quad 3.3$$

Where, X_b is the distance between the centre of the load to the centre of the crest, F is flexural parameter, D is flexural rigidity, T_e is elastic lithospheric thickness, E is the Young's Modulus (70 GPa), ν is Poisson's ratio (0.25), ρ_m (3.3 g/m^3), ρ_w (1.03 g/m^3) the density of the material and water respectively, g is acceleration due to gravity (9.81 m/s^2). These values are those adopted by Turcotte and Schubert (2002), and are characteristic for oceanic lithosphere modelling.

Since the flexural rigidity is proportional to the 4th power of flexural parameter, determining D can provide information on the thickness of the lithosphere in the region at the time of loading (Watts et al., 1975).

Knowing the T_e of the lithosphere for the seamount acting as a load, the age of the lithosphere at the time of loading can be calculated by using Bodine et al.'s (1981) model for effective elastic thickness for loads in the interior of plate, which is given by:

$$T_e = a * age^{\frac{1}{2}} \quad 3.4$$

Where, a=4.3 ± 0.5 (dry) and 3.3 ± 0.5 (wet) and age is the age of the lithosphere at the time of loading. The age of the seamount can be constrained, if the age of the oceanic crust below the seamount is known. For this, the age of the seamount is calculated by subtracting the age of the lithosphere at the time of loading from the age of the seafloor on which the seamount is loaded as discussed by Watts and Ribe (1984).

The results, as discussed by Watts and Ribe (1984), show an increase of elastic lithospheric thickness (T_e) with increased age at the time of loading. Thus, loads placed on young oceanic crust have lower T_e as compared to those formed on older crust (Watts, 1978). Watts's (1978) approach, where the elastic lithospheric thickness was bounded by the 300° C - 600° C isotherm of Parsons and Sclater's (1977) cooling plate model, also predicts that as the plate becomes old, it cools and becomes stiffer with respect to loading. It has been argued by Bodine et al. (1981) that the central core of the load within the region may undergo brittle behaviour while the surrounding lithosphere flexes elastically.

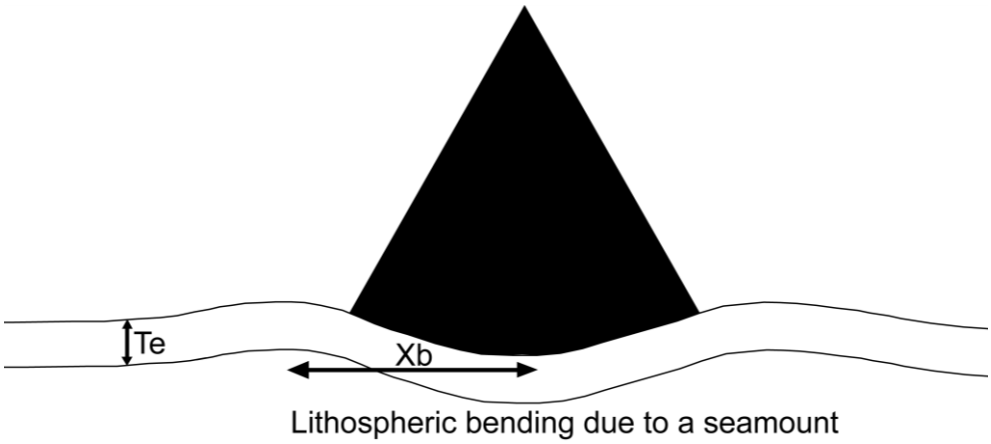

Figure 3.6: Schematic diagram re-drawn from Turcotte and Schubert, (2002) of lithospheric bulging produced due to the load (seamount). X_b is the distance between the centre of the load and the crest formed due to the load, T_e is the thickness of the elastic lithosphere.

Lithosphere approaching a subduction zone undergoes flexure and responds in a similar way as under a point load, by behaving elastically (Walcott, 1970; Watts and Talwani, 1974; McAdoo et al., 1978). This leads to bulging upwards of the lithosphere on the seawards side of the subducting plate (Walcott, 1970; Watts and Talwani, 1974; Turcotte and Schubert, 2002). This has been observed in the south-west Pacific Ocean islands like Niue Island, where the reef structure is above sea-level where, this uplift has been attributed to the island riding the bulge produced by the flexure at the Kermadec Trench (Dubois et al., 1975). Such a bending often leads to brittle fracturing on its seaward side as in the case of Hokkaido Rise in northwest Pacific Ocean (Hirano et al., 2001, 2006). The Indo-Australian Plate in the region is undergoing subduction south of the Java and Sunda Trench, and the flexure produced can be seen schematically in Figure 3.7. A northeast-southwest bathymetry profile passing through Christmas Island, perpendicular to the Sunda Java Trench, was extracted from the global bathymetry data (Smith and Sandwell, 1997) using GMT (Wessel and Smith, 1991) to determine the flexural bulge produced in case of the Indo-Australian Plate subducting underneath the Eurasian Plate.

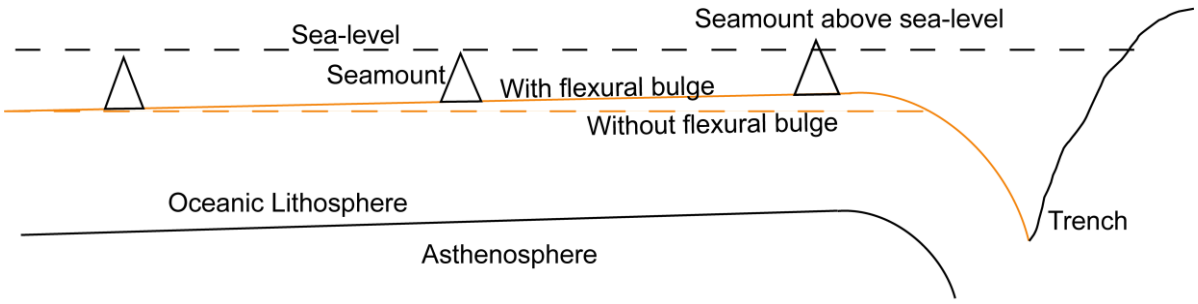

Figure 3.7: A schematic diagram (modified from Watts (2001)) depicting the flexure of the oceanic lithosphere as the subducting slab approaches the trench (Watts and Talwani, 1974). Solid orange line represents the flexure of lithosphere as it rises before subducting, dashed orange line represents the lithosphere if there was no flexure from the subducting slab. A seamount initially submerged will rise above sea-level as the seamount rides the flexural bulge, a case represented by some seamounts in the region.

3.2.4: Subsidence of the oceanic lithosphere with time

The ocean floor is studded with around 25 million seamounts that rise anywhere up to 100 m above the ocean floor, and more than a 100,000 that rise more than 1 km from the ocean floor globally (Wessel et al., 2010). Detailed bathymetric mapping of oceanic seamounts can provide age constraints via subsidence modelling, which, in under-sampled areas, can complement traditional geochronology.

As the lithosphere moves away from a mid-ocean ridge towards a subduction zone, it cools, contracts, increases in density, and subsides (Sclater et al., 1971). There are several models that explain the relationship between the depth of a moving lithosphere and its age. Sclater et al. (1971) showed the attributes of heat flow with time and the depth should be similar irrespective of ocean basin. A simple cooling plate model predicted a linear relationship between the depth and square root of the age of ocean floor, though this trend does not hold for ages greater than 80 Myrs. Parsons and Sclater (1977) put forward a revised cooling plate model for the North Pacific and North Atlantic Ocean floor where the subsidence of the ocean floor is proportional to the square root of the age, and for larger ages it follows a negative exponential relation (Heestand and Crough, 1981).

In the cooling half-space model the thickness of the oceanic crust increases proportionally to the square root of its age but there is no heat flux associated with it at the base of the lithosphere (Turcotte & Oxburg, 1967; Parker & Oldenburg, 1973). Crough (1975) and Kono & Yoshii (1975), later modified the cooling half space model by using a non – zero flux at the base of the lithosphere. These relationships were further modified by Parsons and Sclater (1977) who documented a break in the linear relation between 60 and 80 Ma. They argued that for ages up to 80 Myrs, the sea floor reaches a depth of 6400 m and hence behaves as a cooling plate. Hillier and Watts (2005) customised the cooling plate model for the Pacific Ocean and suggested a relationship with the square root of time (of the plate) up to 85 Ma. Beyond this the depth flattens, and levels out at 6.1 km. The relationship is described by:

$$z = 61230 - 3010^{(-0.026t)} \quad 3.5$$

where z (m) is the depth, and t is time (in Myrs).

As the depth of these submerged seamounts and the age of the underlying oceanic crust are known, the time when these features were exposed and above sea-level can be ascertained if a relationship between age and depth can be assumed (Tucholke and Smoot, 1990). Using an age-depth relation proposed by Tucholke and Vogt (1979), this study constrains the apparent age of seamounts formed at sea-level, and modifies Tucholke & Smoot's (1990) model of oceanic subsidence in the Northeast Indian Ocean as follows:

$$(5900 - d_{sm}) = 2500 + 350 * t^{\frac{1}{2}} \quad 3.6$$

$$t = \left\{\frac{(5900 - d_{sm}) - 2500}{350}\right\}^2 \quad 3.7$$

Where, 5900 m is the average depth of the seafloor for the region; d_{sm} is the depth of the seamount; t is the age in Myr. There is a general uncertainty in the depth of a given location in satellite derived dataset, which here is of the order 100 – 200 m, and is implicit in age

calculation. It can produce age uncertainties in the range of ± 4 Ma for a seamount at 1200 m below sea level, and ±2 Ma for 2700 m bsl. The age obtained from the relation above is subtracted from the age of the ocean crust, to get the age when the seamount was last sub-aerially exposed, which approximates to the age of origin of the seamount. The oceanic crustal age model by Müller et al. (2008) was used to obtain seafloor ages for positions occupied by seamounts. For this, it is assumed that there is no other process acting to uplift or thermally reset the crust (Tucholke and Smoot, 1990). Tucholke and Smoot (1990), however, discuss the issue of thermal uplift but argue that it is compensated by the load induced subsidence. The constant 350 in Equation 3.5 has been argued by Sclater et al. (1975) and Tucholke and Vogt (1979) to provide reliable age estimates for features formed at sea-level.

Verhoef and Collette (1985) have used age-depth back-tracked subsidence models to constrain the maximum ages of seamounts in the Great Meteor seamount chain and concluded an age range between 37 - 23 Ma. Tucholke and Smoot (1990) modelled the age-depth subsidence for the Corner Seamounts in the North Atlantic and indicated their formation around 80 - 76 Ma on crust floor with an age of 99 – 80 Ma, while Duncan (1984) calculated an age of 75 – 70 Ma for the Corner Seamounts. Müller et al. (1999, 2008) used the back-tracked age by Tucholke and Smoot (1990) in their plate reconstruction models of Atlantic Ocean signifying the relevance of this technique.

3.2.5: Seismic tomography and plate reconstruction

Seismic tomography is a technique used to image the interior of the Earth three dimensionally by using seismic waves generated primarily from earthquakes. The changes in seismic wave velocities have been used to understand upper and lower mantle heterogeneities, and, more specifically, to constrain hotspot conduits structure (e.g. Ritsema et al., 1999; Zhao, 2004; Montelli et al., 2004, 2006). Similarly, the subduction of oceanic lithosphere beneath continents and island arcs has also been distinguished using seismic tomography (Kárason and van der Hilst, 2000; Conrad and Gurnis; 2003; Hafkenscheid et al., 2006; Nolet et al., 2006). It is generally much easier to image and model plate boundaries and subduction zones than, anomalies in oceanic plate interiors (Grand, 2002). This is due to great distance from the seismically active areas, and lack of receiver coverage on most oceanic plates (Nolet et al., 2007). The location of an anomaly, and its coverage by seismic stations, and distance from them is a great limitation in the resolution of localised seismic low velocity zones. In the case of the Indian Ocean this problem is significant, as the nearest landmass is either 350 km to the north or 1700 km to the southeast from Christmas Island, and much further away from Christmas Island's reconstructed position in the Eocene, which is where resolution of mantle anomalies is needed.

This study used three different seismic tomography models as shown in Figure 3.8. Two of these (SAW24B16, Mégnin and Romanowicz, 2000); S20RTS, Ritsema et al., 1999) are global 2° resolution models with 8 depth slices extending up to the core mantle boundary at 2800 km, while the third (TX2000, Grand, 2002) has a 4° resolution. These models use a variety of inversion techniques, and they have been used by other workers in their comparative studies (Courtillot et al. 2003, O'Neill et al. 2003; Nolet et al. 2007) and are freely available. These seismic tomography grids are in netCDF binary format, compatible and viewable with GEON IDV (Integrated Data Viewer). GEON IDV is a graphical interface-based visualisation tool

developed by UNAVCO that can produce coloured scale plots, contour maps and 3-D visualisation maps (for ex. Figure 3.8). The depth slices or vertical profiles can be exported into raster format, these are then imported and overlayed in Gplates (Boyden et al., 2011). Gplates is licensed under a GNU public license, making it freely available and can be downloaded from http://www.gplates.org. It is used here to facilitate the reconstruction of Gondwanaland since the Late Cretaceous, and understand the evolutionary history of the western margin of Australia as it separated from Greater India. Separation and rifting of large-scale continental blocks can have important ramifications, an example is the creation of upper mantle heterogeneities with differential stretching during rifting events (O'Reilly et al., 2009; Coltorti et al., 2010). The relationship of these mantle complexities with the seamount province, within the upper and lower mantle, can be ascertained by integrating seismic tomography with reconstruction models.

Reconstruction models from Müller et al. (2008), Seton et al. (2012), and Gibbons et al. (2012) are available from http://www.gplates.org, and have been used to recreate the evolutionary history of the region from 140 Ma up to the present. Seton et al.'s (2012) plate reconstruction model incorporates the most up to date global reconstructions and is based on the moving hotspot model of O'Neill et al. (2005). Global rotation files (.rot file), coastlines (.gpml) and global polygon (.gpml) essential for reconstruction were downloaded from http://www.gplates.org. These gpml files are loaded as feature files and overlayed on a bathymetry map of the region. Seamounts and islands within the seamount province are then digitised and assigned to a plate ID. These models are overlayed on seismic tomography slices to constrain the seamount reconstruction history, with observed anomalies within the shallow and deep mantle.

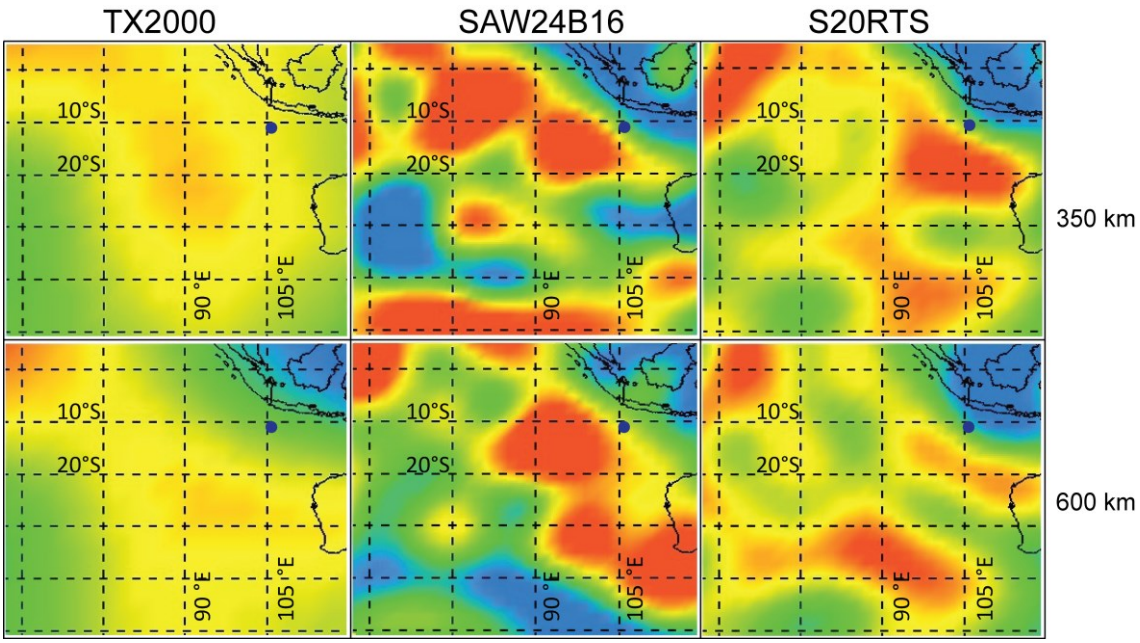

Figure 3.8: Examples of seismic tomography depth slices for the East Indian Ocean. Top, 350 km depth; bottom, 600 km depth. Seismic tomography models TX2000 is from Grand (2002), SAW24B16 from Mégnin and Romanowicz (2000), and S20RTS from Ritsema et al. (1999). Blue circle represents the present position of Christmas Island.

3.2.6: Seismicity

To ascertain the ongoing tectonism of the region, earthquake data since 2000 was downloaded from USGS Global Earthquake Search measuring more than M_w 3 (http://earthquake.usgs.gov/earthquakes/eqarchives/epic/). Data for a total of 27536 earthquakes was downloaded within the geographical limits of 5°S to 40°S latitude and 70°E to 150°E longitudes. Regions with high seismicity within the intraplate region and near the subduction zone were overlayed on PS vector file displaying bathymetry.

3.2.7: Paleomagnetic laboratory techniques

Paleomagnetism is a study of the Earth's magnetic field recorded and stored permanently within a rock body as it forms and cools past the Curie Temperature. Paleomagnetic studies, thus have wide ranging applications in determining plate motion rates, hotspot motion, sea floor spreading, and age determination and geomagnetic field variations. Magnetisation

recorded in a rock body is determined by measuring the Natural Remanent Magnetisation (NRM) acquired by a body when it is cooled (Butler, 1992). This remanent magnetism may consist of a primary magnetic component, and is also often associated with a later secondary magnetisation. The primary magnetisation is acquired initially when the rock was formed and may represent all of, or only partial, remanence. Primary NRM is acquired in a rock in three main ways: thermally, during cooling from higher temperatures (thermoremanent magnetisation); chemically, from the growth of ferromagnetic minerals (chemical remanent magnetisation); or by accumulation of magnetic sediments (detrital remanent magnetisation) (Butler, 1992). In most cases, the primary magnetisation is a partial component of the NRM, it signifies that secondary magnetic events have overprinted on the primary magnetism.

These auxiliary magnetic characters can be acquired, in geological time, due to secondary processes, for example, exposure to high temperatures or the presence of a weak magnetic field (Butler, 1992). In some instances, metamorphism of the rock body can induce alteration due to chemical reactions thereby leaving secondary or later stage magnetic imprints. The aim of undertaking a paleomagnetic investigation is to separate the NRM into primary and secondary components using a combination of demagnetisation techniques. Paleomagnetic studies are then based either on constraining the primary magnetic component acquired during rock emplacement or formation, or in understanding the processes leading to secondary magnetism (Butler, 1992).

In this section, the procedure and methodology undertaken for paleomagnetic analysis is described. As mentioned in Section 3.1, in-situ sample collection was carried out in the field by drilling the outcrop using a hand drill for paleomagnetic investigation. The drilled cores obtained from the field measured 3 to 5 cm. Ideally, a minimum of six samples from each site distributed along the exposure with enough spacing is recommended to gain statistically sound results, but due to limited outcrop availability or accessibility only 3 to 5 cores could be

obtained. These cores were then cut into 2.2 cm individual core samples using a diamond saw at Macquarie University.

Once the samples were cut into required dimensions, progressive demagnetisation was undertaken to isolate the primary magnetisation from secondary magnetisation acquired during the sample's geological history. A set of these samples from all four sampling locations were first demagnetised using an alternating-field (AF) progressive (Figure 3.10 B) demagnetiser (Model 2G600). Later, another separate set of selected samples were thermally demagnetised using a MMTD80 programmable thermal demagnetiser (Figure 3.10 C) at CSIRO (Commonwealth Scientific and Industrial Research Organisation), North Ryde. Remanence magnetisation is measured at each increasing step of AF, or thermal demagnetisation in a zero magnetic field space. Multiple measurements ensure consistency and homogeneity in calculating the remanent magnetisation. The oven within the demagnetiser consists of four layers of mu-metal shielding with a residual field of less than 10 nT. It is capable of heating up to 80 one-inch samples automatically. A 2G Enterprise three-axis cryogenic magnetometer (Model 755) was used to measure remanent intensities. AF demagnetisation was carried out in 14 demagnetisation steps with increments of 1 - 3 mT up to 5 mT, and thereafter, in increments of 5 - 10 mT up to maximum of 70 mT. Selected samples underwent thermal demagnetisation from 200° C in increments of 50° C up to 500° C, thereafter in increments of 5 - 20° C up to 570° C. A Sapphire Instruments S12B susceptibility instrument was used for measuring magnetic susceptibilities.

A typical output obtained from demagnetisation is presented in Figure 3.9. As can be seen from Figure 3.9, the first step before demagnetisation was to determine the remanence (natural remanent magnetisation) using a progressive demagnetiser (Model 2G600). The samples were then demagnetised in the steps mentioned previously and an output file consisting of

demagnetisation step, declination, inclination, intensity (mA/m) and error is obtained. The equipment used for this is shown in Figure 3.10.

After demagnetisation, the vector directions are described in terms of Declination and Inclination. Declination refers to the horizontal demagnetisation direction, with respect to the true north and lies between 0° and 360°. Inclination, on the other hand, is the vertical angle with a horizontal plane. It is between +90° and -90°, positive representing the northern hemisphere and negative representing the southern hemisphere. These three dimensional vector information can be depicted two dimensionally using a stereonet diagram (Butler, 1992). However, paleomagnetic data can be most faithfully represented using orthogonal projection diagrams called Zijdervald diagrams (Zijderveld, 1967).

```
Rem2Asc VB Programme Output

File is c:\2G\xmas2.rem
  Creation data 08-10-2011

xis      rajcraigxmas2010

Todays date is 08-10-2011
20a1  field corrected
 step     dec     inc          int      error          date/time
nrm    92.0    -55.7       1343.068     4.0
0mT    358.8    -56.0        1350.838     3.0
1mT    359.2    -55.7        1324.189     4.0
2mT    0.1    -55.8       1294.402     4.0
5mT    0.5    -57.1       1225.346     4.0
10mT    0.5    -63.2        993.694     4.0
15mT    2.2    -68.5        778.047     4.0
20mT    4.7    -71.6        630.610     4.0
25mT    7.7    -73.3        525.380     4.0
30mT    11.7    -74.4        443.240     4.0
35mT    14.9    -75.3        383.726     4.0
40mT    16.9    -75.7        347.156     4.0
50mT    21.9    -76.9        273.276     4.0
60mT    22.8    -77.8        223.320     4.0
70mT    19.0    -78.6        183.117     4.0

20b1  field corrected
 step     dec     inc          int      error          date/time
nrm    248.4    -51.9        9969.173     2.0
0mT    8.9    -52.7       9898.363     3.0
1mT    10.3    -53.4        9842.133     3.0
2mT    9.5    -53.8       9829.333     3.0
5mT    9.0    -55.6       9569.229     2.0
10mT    10.0    -63.1        8965.138     2.0
15mT    10.6    -66.0        7877.650     2.0
20mT    10.9    -66.8        6671.864     2.0
25mT    11.1    -67.3        5795.726     2.0
30mT    11.3    -67.9        5098.454     3.0
35mT    11.5    -68.4        4560.102     3.0
40mT    11.8    -68.8        4208.686     3.0
50mT    12.2    -70.0        3548.818     3.0
60mT    12.4    -70.9        3019.620     3.0
70mT    12.5    -71.8        2574.814     3.0

20c1  field corrected
 step     dec     inc          int      error          date/time
nrm    280.9    -55.1        1097.972     2.0
0mT    23.2    -57.2       1015.621     2.0
```

Figure 3.9: A screen shot of the output from AF-demagnetisation conducted at CSIRO, North Ryde on the drilled samples from Christmas Island. Thermally demagnetised samples are first heated in the oven and magnetisation is then measured in 2G. The output for thermal demagnetisation is similar to that shown above, except that it presents temperature steps instead of magnetic intensity step.

Figure 3.10: Paleomagnetic laboratory setup at CSIRO (North Ryde) showing the computer (A), operating the AF-demagnetiser (Model 2G600) (B), and the thermal demag (MMTD80) furnace (C) at temp 500° C. For AF-Demagnetisation, drilled sample is put in the long black tube at one end of the AF-demagnetiser, while the computer reads the values. For thermal demagnetisation, samples are first thermally heated in the furnace (C) and then the value is read in the AF-Demagnetisation machine (B).

The demagnetisation steps with their inclinations and declinations are plotted two dimensionally, displaying both directional and intensity vectors on a single diagram. Interpretation of demagnetisation was done by preparing visually identifiable univectorial decay vectors on orthogonal vector plots to determine the polarity and direction. This is helpful in identification of the primary magnetic component, also called the Characteristic Remanent Magnetisation (ChRM), differentiating it from secondary components. Principal Component Analysis (PCA) was used in calculating mean directions and mean intensity of ChRM (Kirschvink, 1980). Fisherian analysis has been used for calculating mean inclinations (I_m) and declination (D_m) for each site. These have been described in Butler (1992) and will be briefly discussed here:

The Fisher distribution function $P_{dA}(\Theta)$ is the probability per unit area for locating the direction with an angular confidence area that is centred at an angle Θ. The direction is thus distributed across the probability function as:

$$P_{dA}(\theta) = \frac{\kappa}{4\pi \sinh(\theta)} \exp(\kappa \cos(\theta)) \qquad 3.8$$

Where, Θ is the angle from the true direction; $P_{dA}(\Theta)$ is the probability density function; and κ is the precision parameter. Taking ξ as the azimuth angle about a true mean direction, the probability of finding the direction angular within an angular area dA is,

$$P_{dA}(\theta)dA = P_{dA}(\theta) \sin(\theta)\, d\theta d\xi \qquad 3.9$$

Normalising the distribution in equation 3.9 gives,

$$P_{d\theta}(\theta) = \int_{\xi=0}^{2\pi} P_{dA}(\theta)DA = 2\pi P_{dA}(\theta) \sin(\theta)\, d\theta$$

$$= \frac{\kappa}{2 \sinh(\kappa)} \exp(\kappa \cos\theta) \sin\theta d\theta \qquad 3.10$$

In paleomagnetism the direction of magnetisation is described by the Declination (D) and the Inclination (I) of the sample. Computing the mean direction is achieved by calculating the individual unit vectors as:

$$l_i = \cos I_i \cos D_i; \quad m_i = \cos I_i \sin D_i; \quad n_i = \sin I_i \tag{3.11}$$

Where, I_i and D_i are the inclination and declination, respectively of the i vector and l_i, m_i and n_i are the cosines of the I vector in north, east and down direction respectively. The direction cosines of the l, m and n mean direction is thus given by:

$$l = \frac{\sum_{i=1}^{N} l_i}{R}; \; m = \frac{\sum_{i=1}^{N} m_i}{R}; \quad n = \frac{\sum_{i=1}^{N} n_i}{R} \tag{3.12}$$

Where R is the resultant vector, given by:

$$R^2 = \left(\sum_{i=1}^{N} l_i\right)^2 + \left(\sum_{i=1}^{N} m_i\right)^2 + \left(\sum_{i=1}^{N} n_i\right)^2 \tag{3.13}$$

The mean inclination, and mean declination are then calculated form Equation 3.12 and 3.13 to give:

$$D_m = \tan^{-1}\left(\frac{m}{l}\right) \quad \text{and } I_m = \sin^{-1}(n) \tag{3.14}$$

The confidence limit of calculating the mean direction is expressed as angular radius from the calculated mean. The angle $\alpha_{(1-p)}$ within the unknown true means at the confidence level (1-p) is calculated as:

$$\cos \alpha_{1-p} = 1 - \frac{N-R}{R}\left\{\left(\frac{1}{p}\right)^{\frac{1}{N-1}} - 1\right\} \tag{3.15}$$

The most standard confident limit of finding the direction is denoted as

$$\alpha_{95} = 140^\circ/\sqrt{\kappa N} \tag{3.16}$$

The Zijdervald diagrams and PCA analyses were carried out using an in-house Microsoft Windows compatible program developed by Phil Schmidt at CSIRO, North Ryde. Fisherian statistics including I_m, D_m, paleolatitude (λ), α_{95} and precision parameter k, were calculated using freely available Paleomagnetic Tools (PMAGTOOL) V 4.2a developed by Mark Hounslow, Lancaster University.

A principal aim of paleomagnetic investigation within the scope of this research it to determine the magnetic polarity of the volcanic exposure from Christmas Island and determine its correlation with the geomagnetic polarity time scale (GPTS). The existence of multiple episodes of volcanism at the island further aids in constraining the position of the island; something which has not been done previously.

To achieve this, the paleolatitude of the island was calculated by using mean inclination (I_m) of the site by a simple relation,

$$\tan I_m = 2\tan\lambda \qquad 3.17$$

Where λ is the latitude of the paleosite.

3.3: $^{40}Ar/^{39}Ar$ Geochronology

$^{40}Ar/^{39}Ar$ is a dating technique that uses two Argon isotopes to determine an age for geological events like, solidification of magma, intrusion of dykes, etc. This method always requires irradiation with neutrons in a nuclear reactor. Although this technique is a modification of the conventional K-Ar dating technology, it is much more complex and has surpassed its predecessor due to its greater precision and suitability for a broad range of geological conditions, as mentioned above. In addition, $^{40}Ar/^{39}Ar$ requires a single relatively small quantity of sample to measure both Ar isotopes as a proxy for K, whereas in the conventional K-Ar dating, separate samples are needed, thus requiring a large quantity of sample to work

on. The following sections provide a brief introduction to $^{40}Ar/^{39}Ar$ technique relevant as per the scope of this research and is drawn from the review work done by Renne (2000, 2006) and Kelly (2002).

3.3.1: K-Ar dating

To understand $^{40}Ar/^{39}Ar$ dating it is essential to review the basics of the K-Ar dating technique, as the former is a modification of the latter. Potassium (K) exists as three isotopes, ^{41}K:^{40}K:^{39}K in 6.73:0.011:93.25 proportions respectively. Argon, on the other hand, exists as ^{40}Ar, ^{38}Ar, ^{36}Ar with 99.60:0.06:0.33 respectively (Nier, 1950). Lee et al. (2006) re-determined the percentage abundances of atmospheric argon ^{40}Ar, ^{38}Ar, and ^{36}Ar to be 99.6035 ± 0.0004, 0.0629 ± 0.0001, and 0.3336 ± 0.0004. ^{40}K, with a half-life of 1.25 Ga, decays to ^{40}Ar with an electron capture. In a closed system, the amount of radiogenic Ar produced from ^{40}K increases over time. It can also decay to ^{40}Ca by β^- emission. Although the concentration of radiogenic ^{40}K to non-radiogenic K is very low, potassium is a major constituent of minerals present in rocks, and so its concentration is sufficient enough to produce significant radiogenic ^{40}Ar.

The rate of decay of a radioactive mineral at any time is proportional to the number of radioactive atoms present, in this case, ^{40}K atoms, giving the relationship:

$$\frac{dN}{dt} = -\lambda N \qquad 3.18$$

Where λ represents the total decay of ^{40}K, and is the sum of decay constant for β- emission and electron capture.

The fundamental age equation for K-Ar system is:

$$t = \frac{1}{\lambda}\ln\left[1 + \left(\frac{^{40}Ar^*}{^{40}K}\right)\left(\frac{\lambda}{\lambda e}\right)\right] \qquad 3.19$$

Where, $^{40}Ar^*$ is radiogenic ^{40}Ar, and λe is the partial decay constant for ^{40}K to ^{40}Ar using electron capture. It should be noted that $^{40}Ar^*$ here is defined as radiogenically produced from the decay of ^{40}K and should not be confused with ^{40}Ar obtained from other natural sources. As the decay constant for the above equation is well known, if the ratio of $^{40}Ar^*/^{40}K$ is determined, the age can be easily calculated. The concentration of these is determined separately and this requires a significantly large quantity of sample to ensure representative sampling. This is a limitation of the K-Ar technique. Mostly, determining the concentration of ^{40}K involves measurement of total K and calculating ^{40}K using a homogeneous isotopic composition as discussed above.

To determine the percentage of $^{40}Ar^*$, the amount of total ^{40}Ar ($^{40}Ar(t)$) is first calculated and then corrected for the non-radiogenic part (initial ^{40}Ar, $^{40}Ar(i)$ present in the sample). The total ^{40}Ar is determined using a "tracer" (usually ^{38}Ar) added to the Ar from the sample so that ^{40}Ar relative abundances of the two isotopes can be calculated.

$$^{40}Ar^* = {}^{40}Ar(t) - {}^{40}Ar(i) \qquad 3.20$$

The correction of ^{40}Ar (i) involves assuming all non-radiogenic ^{40}Ar is atmospheric and is proportional to $^{40}Ar/^{36}Ar = 295.5$ and is substituted in the above equation to give:

$$^{40}Ar^* = {}^{40}Ar(t) - 298.56 * {}^{36}Ar \qquad 3.21$$

Another limitation of this technique as discussed by Renne (2006) is the mobility of K and Ar and their susceptibility to redistribution during weathering and reheating. Loss of Ar if K is fixed leads to spuriously young ages, whereas if Ar is fixed and K is lost, old ages are produced.

3.3.2: $^{40}Ar/^{39}Ar$ dating

As mentioned in the Section 3.3, the $^{40}Ar/^{39}Ar$ method is a modification over the limited K-Ar method. In the $^{40}Ar/^{39}Ar$ method, K is measured by neutron activation of ^{39}K to ^{39}Ar which is produced by neutron absorption, and proton emission, in a nuclear reactor. The half-life of this radioactive ^{39}Ar (also mentioned as $^{39}Ar_k$ produced from ^{39}K) is 269 years; hence there is little or no chance of any background ^{39}Ar.

The amount of ^{39}Ar produced during irradiation in a nuclear reactor is given by:

$$^{39}\mathrm{Ar} = {}^{39}\mathrm{K}.\Delta\int \sigma(\varepsilon)\varphi(\varepsilon)\mathrm{d}(\varepsilon) \qquad 3.22$$

Where ^{39}K: the original amount of ^{39}K present in the sample; Δ: the duration of the irradiation; σ: neutron capture cross section; ε: neutron energy; φ: the neutron flux.

To solve for the complicated neutron flux parameter *(*φ), J (the neutron fluence parameter) is introduced. J is calculated in the same irradiation process, and involves comparing a standard of known age, along with the unknown sample, that have experienced the same neutron fluence. The standards used in the irradiation process should be roughly the same age as the unknown and their age should have been accurately determined previously using other age techniques. Therefore:

$$\mathrm{J} = \left(\frac{^{39}\mathrm{K}}{^{40}\mathrm{K}}\right)\left(\frac{\lambda}{\lambda\mathrm{e}}\right)\Delta\int \sigma(\varepsilon)\varphi(\varepsilon)\mathrm{d}(\varepsilon) \qquad 3.23$$

Substituting in the equation 3.19 and rearranging, we get

$$\left(\frac{^{40}\mathrm{Ar}*}{^{40}\mathrm{K}}\right) = \mathrm{J}.\left(\frac{^{40}\mathrm{Ar}*}{^{39}\mathrm{Ar}}\right).\left(\frac{\lambda}{\lambda\mathrm{e}}\right) \qquad 3.24$$

And the age equation therefore is:

$$\mathrm{t} = \frac{1}{\lambda}\ln\left[1 + \mathrm{J}.\left(\frac{^{40}\mathrm{Ar}*}{^{39}\mathrm{Ar}}\right)\right] \qquad 3.25$$

During the irradiation process, several other elements are produced in addition to ^{39}Ar. These interfering reactions produce argon from Ca, K and Cl and must be corrected for to obtain accurate ages. The most important interferences produced from Ca are the two argon isotopes ^{36}Ar and ^{39}Ar. ^{36}Ar is also produced from ^{35}Cl indirectly, as it changes to ^{36}Cl on absorbing a neutron. ^{36}Cl is radioactive and decays to ^{36}Ar with a half-life of 3.01 $x10^5$ years. These corrections further produce uncertainties within the calculated ages and can depend on some factors like the duration of the irradiation process and the chemical composition of the unknown sample involved. Further detail regarding correction techniques will be skipped here but can be found in Dickin (2005).

3.3.3: $^{40}Ar/^{39}Ar$ geochronological laboratory procedure

The $^{40}Ar/^{39}Ar$ analyses were performed at the Western Australian Argon Isotope Facility at Curtin University, operated by a consortium consisting of Curtin University and the University of Western Australia. As mentioned in Section 3.1 six locations were selected from Christmas Island for $^{40}Ar/^{39}Ar$ dating. From these locations, freshest available samples were chosen and the unaltered, 600 – 800 μm-size groundmass was separated out. A Frantz magnetic separator was used for separating the groundmass material, followed by careful hand picking under a binocular microscope. Selected groundmass material (consisting of homogenous unoxidised pyroxene and plagioclase) was then leached in diluted HF for 1 minute and thoroughly rinsed with distilled water in an ultrasonic cleaner.

Samples were loaded into six large wells of 1.9 cm diameter and 0.3 cm depth aluminium disc. Fish Canyon sanidine (FCs) was used as a neutron fluence monitor in small wells that bracketed the larger wells occupied by the samples. The age of FCs is 28.305 ± 0.036 Ma (1σ) and was established by Renne et al. (2010). Cd-shielded discs were irradiated for 2 hours in the Hamilton McMaster University nuclear reactor (Canada) in position 5C. The mean J-values

computed from standard grains within the small pits range from 0.00068800 ± 0.00000220 to 0.00071000 ± 0.00000099 determined as the value and standard deviation of J-values of the small wells for each irradiation disc. An air pipette was used to monitor mass discrimination and provided a range from 1.004492 ± 0.29 to 1.006127 ± 0.38 (%1σ) per dalton (atomic mass unit) relative to an air ratio of 298.56 ± 0.31 (Lee et al., 2006). The correction factors for interfering isotopes were $(^{39}Ar/^{37}Ar)_{Ca} = 7.30x10^{-4}$ (± 11%), $(^{36}Ar/^{37}Ar)_{Ca} = 2.82x10^{-4}$ (± 1%) and $(^{40}Ar/^{39}Ar)_{K} = 6.76x10^{-4}$ (± 32%). The samples were analysed 6 – 8 months after irradiation.

To ensure a homogenously distributed temperature, the samples were step-heated using a 110 W Spectron Laser Systems, with a continuous Nd-YAG (IR; 1064 nm) laser rastered over the sample for 1 minute. Two SAES AP10 getters and one GP50 getter and a liquid nitrogen condensation trap were used as part of the stainless steel extraction line to purify the resultant gas. Ar isotopes were measured in static mode using a MAP 215-50 mass spectrometer (resolution of ~450; with a sensitivity of $4x10^{-14}$ mol/V), with a Balzers SEV 217 electron multiplier mostly using nine to ten cycles of peak-hopping. The data acquisition from the instruments was conducted with the Argus program written by M.O. McWilliams that ran under a LabView environment. The raw data was processed using ArArCALC software (Koppers, 2002) and the ages were calculated using the decay constants suggested by Renne et al. (2010). Blanks were observed after every three to four steps and the concentration of typical ^{40}Ar blanks range from 1 x 10^{-16} to 2 x 10^{-16} mol. Ar isotopic data corrected for blank, mass discrimination and radioactive decay are given in Appendix 1, Table 1. Individual errors are given at 1σ level in Appendix 1, Table 1. For determination of the plateau, this study adopted the criterion that at least 70% of ^{39}Ar must be included in the plateaus. The plateau for determination of ages should be distributed over a minimum of three consecutive heating steps at a 95% confidence level with a probability of fit (P) of at least 0.05. Plateau ages are

calculated using the mean of all the plateau steps and given at the 2σ level, each weighted by the inverse variance of their individual analytical error. When a plateau can't be defined, mini-plateaus are defined that include between 50% and 70% of ^{39}Ar. Integrated ages with 2σ level are determined by calculating the total amount of gas released for each Ar isotope. Inverse isochrons include the maximum number of steps with a probability of fit ≥ 0.05. The final age calculation includes all estimated uncertainties.

3.4: Geochemical Analytical Techniques

3.4.1: Major and Trace Elements

Only the freshest samples possible (first eliminated through visual observations, and later through petrographical examination) were analysed for major and trace elements at Macquarie University. Any weathering or staining, if present, was removed using a diamond saw. The fresh rock was crushed into small pieces (usually within the range of 1 - 5 cm) by using a hydraulic press fitted with tungsten carbide plates. In order to prevent cross contamination, the press was cleaned thoroughly with 100% ethanol between samples. Approximately 50 grams of crushed sample was then reduced to a fine powder in a tungsten carbide mill. Again, to prevent any contamination with previous samples, the mill was thoroughly cleaned with ethanol and Milli-Q (18 Mohm) water between each sample. Loss of ignition was measured by comparing the weights of the powders before and after heating to 1050°C for 1.5 hours. For major element analysis glass disks were prepared using 2.5 g of lithium tetraborate/metaborate flux and ammonium iodide wetting agent, mixed with 0.4 g of powdered sample. This mixture was heated to 1000° C in a furnace for ~15 minutes, and press-quenched into 30 mm glass disks. Major element analysis was undertaken on a SPECTRO XEPOS energy dispersive XRF spectrometer machine in the Department of Geosciences, University of Wollongong. Lower limit of detection are presented in Appendix 2, Table 1. Bulk Rock ICP-MS analyses were

conducted at the Geochemical Analysis Unit (GAU), located in the Australian Research Council (ARC) National Key Centre for Geochemical Evolution and Metallogeny of Continents (GEMOC), at Macquarie University, Australia. Powdered samples were weighed to approximately 0.1 grams and placed in Teflon beakers and then digested with concentrated HNO_3 (nitric acid) and Hf. Precisely measured spikes of an internal standard (containing ^{6}Li, ^{75}As, ^{103}Rh, ^{115}In, ^{209}Bi) were added to the samples. The samples were measured on an Agilent 7500cs ICP-MS Octopole reaction system, which uses a self-aspiring nebuliser. HNO_3 was initially run three times as a rinse, and followed by a method blank measurement to provide background counts. A series of external calibration standards (BCR-2a) and reference samples (BIR-1 and BHVO-2) were used at the start and end of all runs. Results from BCR-2a, BIR-1, and BHVO-2 are presented in Appendix 2, Table 2.

3.4.2: Nd, Hf, Pb Isotopes

A select group of samples (including those used for paleomagnetism and geochronology and others) were sent to the Ecole Normale Supérieure de Lyon (ENSL) for analysis of Nd, Hf and Pb isotope compositions. They were leached and digested in Savillex beakers and Hf, Nd, and Pb separated using ion-exchange chromatography and their isotope compositions measured using the Nu Plasma HR MC-ICP-MS at ENSL according to the chemistry and mass spectrometry protocols of Blichert-Toft and Albarède (2009) and references therein.

Chapter 4: Geophysical Investigation*

Mar Geophys Res
DOI 10.1007/s11001-014-9229-5

ORIGINAL RESEARCH PAPER

Constraining the age and origin of the seamount province in the Northeast Indian Ocean using geophysical techniques

Rajat Taneja · Craig O'Neill

Received: 8 January 2014 / Accepted: 23 June 2014

4.1: Abstract

The breakup of the western margin of Australia from Greater India started around 155 Ma and progressed southwards. After the separation, the interceding intraplate region experienced large volumes of submarine volcanism, extending over 100 Myrs. The Christmas Island Seamount Province (CHRISP, as it has been dubbed) lies south of the Java-Sunda Trench, and contains numerous submerged volcanic seamounts, and two sub-aerially exposed island groups - Cocos (Keeling) Islands, and Christmas Island. While recent geochronological investigations have shed light on the diverse eruption ages of the volcanics of this region, some islands/seamounts have demonstrated protracted volcanic histories, and it is not clear how the volcanic loading, tectonic subsidence, and subsequent emergence history of the islands relates to these discrete volcanic episodes. This study utilises a number of geophysical techniques to determine the crustal structure, loading and subsidence history, and last sub-aerial exposure age for the

* This is a published paper in Marine Geophysical Research and includes comments from the thesis reviewers.

CHRISP. The study shows that flexural and subsidence modelling are reliable techniques in constraining the age of the seamounts when geochronological techniques are not possible.

Utilising regional gravity signatures, we model the crustal structure underneath the Cocos (Keeling) Island, and constrain the thickness of the limestone cover between 900 to 2100 m. Using age-depth subsidence curves for oceanic lithosphere, the time since these seamounts were exposed above sea-level was determined, and a trend in exposure ages that youngs towards the west is observed. Two episodes of volcanism, of different origin, have been recorded at Christmas Island. The younger phase in the Pliocene is a manifestation of flexure induced cracks produced in the lithosphere as it rides the subduction fore-bulge, whereas a low velocity seismic zone rising from the lower mantle, and tectonic reorganization, may be associated with the older Eocene volcanic phase, as well as much of the rest of the province. Our modelling also supports the existence of an older, undated volcanic core to Christmas Island, based on the loading ages from flexural modelling.

4.2: Introduction

4.2.1: The Northeast Indian Ocean

The Indian Plate and the-Australian Plate have undergone major transformation and evolution since its breakup from Gondwana in the Late Jurassic to Early Cretaceous, and its subsequent motion northwards in the Cenozoic after the onset of spreading at the Southeast Indian Ridge (Veevers, 1971; Heirtzler et al., 1978; Johnson et al., 1980; Liu et al., 1983; Mihut and Müller, 1998; Müller et al., 2000; Gibbons et al., 2012; Seton et al., 2012; Whittaker et al., 2013). The Indo-Australian Plate collided with the southern margin of the Eurasian Plate at ~57 Ma (Leech et al., 2005) or ~34 Ma (Aitchison et al., 2007), consuming most of the older Tethyan oceanic crust north of Gondwana and Greater India, resulting in a convergent plate margin at its

northern boundary (Weissel et al., 1980; Cloetingh and Wortel, 1985) and forming the present day Indian Ocean. South of the Sunda-Java subduction zone lies the Northeast Indian Seamount Province (also called Christmas Island Seamount Province, CHRISP), bounded by the Ninetyeast Ridge in its west, and the North West Shelf, and the Australian landmass to its east. Within this region lies numerous (~50) submarine seamounts, submerged guyots, other volcanic features, and two sub-aerial volcanic islands as shown in Fig 4.1. A recent cruise by Hoernle et al. (2011) shed some light on CHRISP by geochemical and geochronological analyses on dredged volcanic rocks from the submerged volcanic seamounts.

Though there have been few geophysical investigations within the region (Naini, 1973; Larson, 1975; Larson, 1977; Liu et al., 1983), none have constrained the timing and the origin of CHRISP using geophysical techniques. Royer et al. (1989), Müller et al. (1998, 2000), Seton et al. (2012), Gibbons et al. (2012), and Gibbons et al. (2013) have discussed the evolutionary history of the Northeast Indian Ocean, but the relationship of the region's geodynamic history, and the seamount province is unclear.

The Indian and the Australian Plates have undergone intense transformation since the dispersal of Gondwanaland in the Mesozoic, and its collision with the Eurasian Plate in the Cenozoic. The Mesozoic breakup of Gondwanaland is problematic due to a lack of identified Mesozoic magnetic anomalies in the offshore eastern India and Antarctica (Müller et al., 1998). In addition, crust in proximity to Greater India and the western margin of Australia has been consumed at the Sunda Trench and/or accreted to the Eurasian lithosphere (Müller et al. 1998; Hall 2012). Earliest work on the dispersal of the Indian and the western Australian margins have been dealt in great detail by Veevers and McElhinny (1976), Veevers et al. (1991), Sager et al. (1992), Müller et al. (1998), Müller et al. (2000), Krishna and Rao (2000), Gaina et al. (2003), Gaina et al. (2007), Desa et al. (2009), and Whittaker et al. (2013). Müller et al. (1998) computed plate motion models for the Indian and Australia Plates, which was later extended

by Müller et al. (2000), Heine and Müller (2005), and more recently by Gibbons et al. (2012). Gibbons et al. (2012) constrained the tectonic evolution of West Australian margin, and suggested a series of ridge jumps in the Early Cretaceous, supported by the identification of a sliver of old seafloor (153 Ma) within the much younger Cretaceous (95 Ma) ocean floor.

Though the characteristic features of the region are the seamounts, the most unique feature of this submarine volcanic province is the non-linearity of the seamounts and volcanic edifices. The seamount province lies within the latitudes 10°S to 15°S and longitude 95°E to 115°E spreading over 1,000,000 km^2 (Fig 4.1). Several models have been proposed regarding the formation of intraplate islands and seamounts. A convective plume rising from the lower mantle or the core mantle boundary (Morgan, 1971) may result in ocean island basaltic eruptions, and have been implicated in the formation of the Ninetyeast Ridge (due to the Kerguelen plume; Luyendyk and Rennick, 1977; Duncan, 1978; Davies et al., 1989; Duncan, 1991; Frey and Weis, 1995; Mattielli et al., 1996; Duncan, 2002). This seamount province, however, is a broad east-west extending zone of isolated seamounts, rather than a linear chain, and displays a broad younging age progression towards the west (Hoernle et al., 2011). The classical model of plate motion above a fixed hotspot would produce a north-south linear volcanic chain (Morgan, 1971). The east-west extent of the broad zone of volcanism is inconsistent with a localised hotspot. In addition, the region is dominated by north-south trending parallel fracture zones, like the Investigator Ridge (trending along 98°E), that are perpendicular to the east-west trending seamount zone. A number of these fault and fracture zones are believed to be active and responsible for recent earthquakes, for instance, M_w 7.9, Wharton Basin 2000 (Abercrombie et al., 2003).

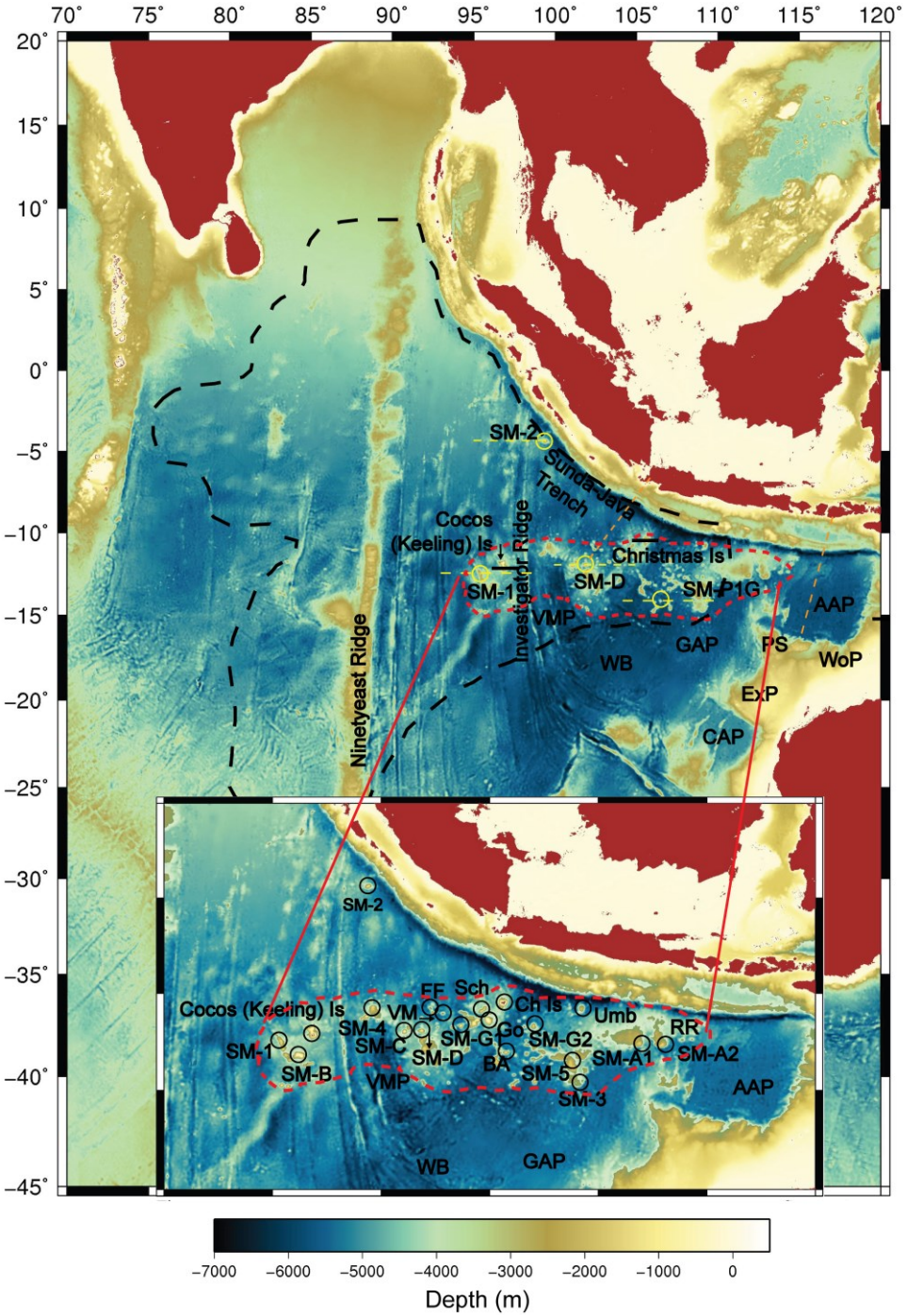

Fig 4.1: Bathymetric map (Smith and Sandwell, 1997) of the East Indian Ocean showing the boundary of the Capricorn Plate and the physiographic features of the seamount province. AAP, Argo Abyssal Plain; GAP, Gascoyne Abyssal Plain; CAP, Cuvier Abyssal Plain; RR, Roo Rise; WB, Wharton Basin; VMP, Vening Meinesz Province; WoP, Wombat Plateau; PS, Platypus Spur; ExP, Exmouth Plateau; Ch Is, Christmas Island. Seamounts are FF, Flying Fish Cove; Go, Golden Bo'Sunbird; VM, Vening Meinesz; Sch, Shcherbakov; Umb, Umbgrove; BA, Bartlett. Red dashed line represents the boundary of seamount province. Black dashed line represents the Capricorn Plate boundary (Royer and Gordon, 1997). Transects for seamounts (dashed yellow line) and profiles across the trench (dashed orange line) are shown in Fig 4.2. Black solid line across Cocos (Keeling) Island and Christmas Island are gravity profiles used for gravity modelling.

Seismic tomography imaging has aided numerous OIB investigations in constraining their origin from mantle depths or the CMB (Grand et al., 1997; Zhao, 2001; Courtillot et al. 2003; DePaolo and Manga, 2003; Grand, 2002; Montelli et al., 2004; Lei and Zhao, 2006). Various authors have presented tomographic models on a regional scale and highlighted prominent anomalies around intraplate volcanic settings such as Hawaii, East Africa, Iceland, Crozet, and the Azores (Grand et al., 1997; Mégnin and Romanowicz, 2000; Montelli et al., 2004, 2006; Nolet et al., 2007). Montelli et al. (2004) used finite frequency tomography to constrain plume conduits beneath 32 hotspots around the world. They documented three plumes within the Eastern Indian Ocean; a plume below the Cocos (Keeling) Archipelago with a depth of <1000 km and a radius of 200 km constrained from P wave anomalies, or a >1400 km depth with a radius of 300 km from S wave anomalies; a second deep plume down to 1900 km depth in the East Indian Ocean; and a third plume starting from the base of the mantle South of Java (radius of 300 km). Mégnin and Romanowicz's (2000) seismic model has also documented a low velocity zone south of Java at a depth of 350 km which can be seen down to a maximum depth of 1000 km, further below it is weak and fades away.

The aim of this study is to constrain the tectono-volcanic evolution of the Christmas Island Seamount Province, using a variety of geodynamic and geophysical techniques which constrain the age of the seamounts when conventional geochronology is impossible, due to a lack of samples, as in the case of many submerged seamounts or coral atolls. This study also examines the crustal structure of the two sub-aerial islands, and constrains the time since the submerged seamounts were last sub-aerially exposed. In addition, we undertake flexural studies of these seamounts to constrain their elastic characteristics, and estimate the age at which the elastic lithosphere was volcanically loaded. We conclude by integrating a model of the province with observed deep mantle anomalies in published seismic tomography models.

4.2.2: Christmas Island Seamount Province

The seamount province lies east of the Ninetyeast Ridge within the Wharton Basin, bisected by the Investigator Ridge (Fig 4.1). The seamounts within the region can be divided into those with rounded peaks (described as conical peaks by Dominguez et al. (1998)) and those with flat tops (Fig 4.2). Within the province are two sub-aerially exposed island groups; the Cocos (Keeling) Archipelago, and Christmas Island. Other seamounts that are submerged below the sea-level are, for example, Vening Meinesz, Shcherbakov, Umbgrove, Golden Bo Sunbird, and Flying Fish (Fig 4.1). Hoernle et al. (2011) conducted a dredging expedition in the Christmas Island Seamount Province and dated volcanic samples using incremental heating $^{40}Ar/^{39}Ar$ geochronology. They yielded ages in the range of 136.2 ± 0.17 and 47.0 ± 0.2 Ma. Older ages have been recorded in the east, in the Argo Abyssal Plain, and younger ages in the west, south of Cocos (Keeling) Islands. The Eastern Wharton Basin contains ages in the range of 115.9 ± 3.8 Ma – 94.3 ± 0.3 Ma, while the Vening-Meinesz province is between 95.6 ± 1.4 - 63.5 ± 0.3 Ma. Using geochemical analysis, Hoernle et al. (2011) proposed that the seamount province was formed at the mid-ocean ridge, and it exhibits an enriched geochemical signature that was formed through shallow recycling of delaminated continental lithosphere.

The Cocos (Keeling) Archipelago is located on the western end of the seamount zone ~1200 km southwest of Jakarta. Consisting of twenty seven islands, it is comprised of both the North Keeling Island and the South Keeling Archipelago. Previous drilling and seismic studies on the island have encountered Pleistocene Limestone at depth of 8 – 13 m that is overlain by biogenic mud and sand deposits (Woodroffe and Falkland, 1997). There are, however, no reports of any volcanic exposure on the island. Hoernle et al. (2011) dredged volcanic rocks at a minimum depth of 2400 m below sea-level, and yielded ages of 56.0 ± 0.2 Ma and 55.6 ± 0.2 Ma, and an age of 47.0 ± 0.2 Ma, south of the island near the Cocos Rise.

Christmas Island is situated in the central region of the seamount zone, southwest of the Java Trench. The island now sits on the fore-bulge of the Indo-Australian Plate, which is subducting at the Java Trench. The island is estimated to be rising at around 140 mm per thousand years (Woodroffe, 1988) and has been subjected to sea-level fluctuation in the recent past (Grimes, 2001). Christmas Island recorded three stages of volcanic activity (Grimes, 2001), of which two are presently exposed (Andrew, 1900; Trueman, 1965; Hoernle et al., 2011; Taneja et al., 2014). The oldest of these purportedly occurred in the Late Cretaceous (e.g. Grimes, 2001), followed by a second stage in the Eocene, and finally the latest in the Pliocene (Hoernle et al., 2011). The Eocene phase of volcanism (Lower Volcanic Sequence, LVS) occurred between 44 – 37 Ma, and the Pliocene event (Upper Volcanic Sequence, UVS) between 4.5 - 4.2 Ma (Hoernle et al., 2011; Taneja et al., 2014). While the oldest episode is now not exposed, earlier reports have documented it at the base of (now inaccessible) fresh water caves (Grimes, 2001). Pliocene volcanism has been accompanied by faulting in the central region of the island – represented as dykes, tuffs and vents in the Murray Hill region, associated with local slip-fault planes and fractures (Grimes, 2001).

4.3: Geophysical techniques for constraining the age of seamounts and mechanism of CHRISP

To understand the dynamics and the lithospheric structure of the Indo-Australian Plate, this study utilises a number of geophysical techniques, including gravity modelling, seafloor subsidence modelling, flexural modelling, and seismic tomography, to determine the loading history of Christmas and Cocos (Keeling) Islands.

4.3.1: Locating submerged seamounts

Seamounts, oceanic islands, and guyots, subside as the crust on which they were emplaced ages with time (Paulay and Edward, 1990; Grigg and Jones, 1997). Coral reefs may develop on the subsiding seamounts if the rate of subsidence is less than the upwards growth rate of coral (Darwin, 1842; Winterer, 1998), which is the case for older oceanic lithosphere. Erosion of the island's surface topography prior to submergence tends to flatten its upper surface, and this erosional contact is often manifested as flat-topped seamounts in bathymetry data (Hesse, 1973; Karig et al., 1970).

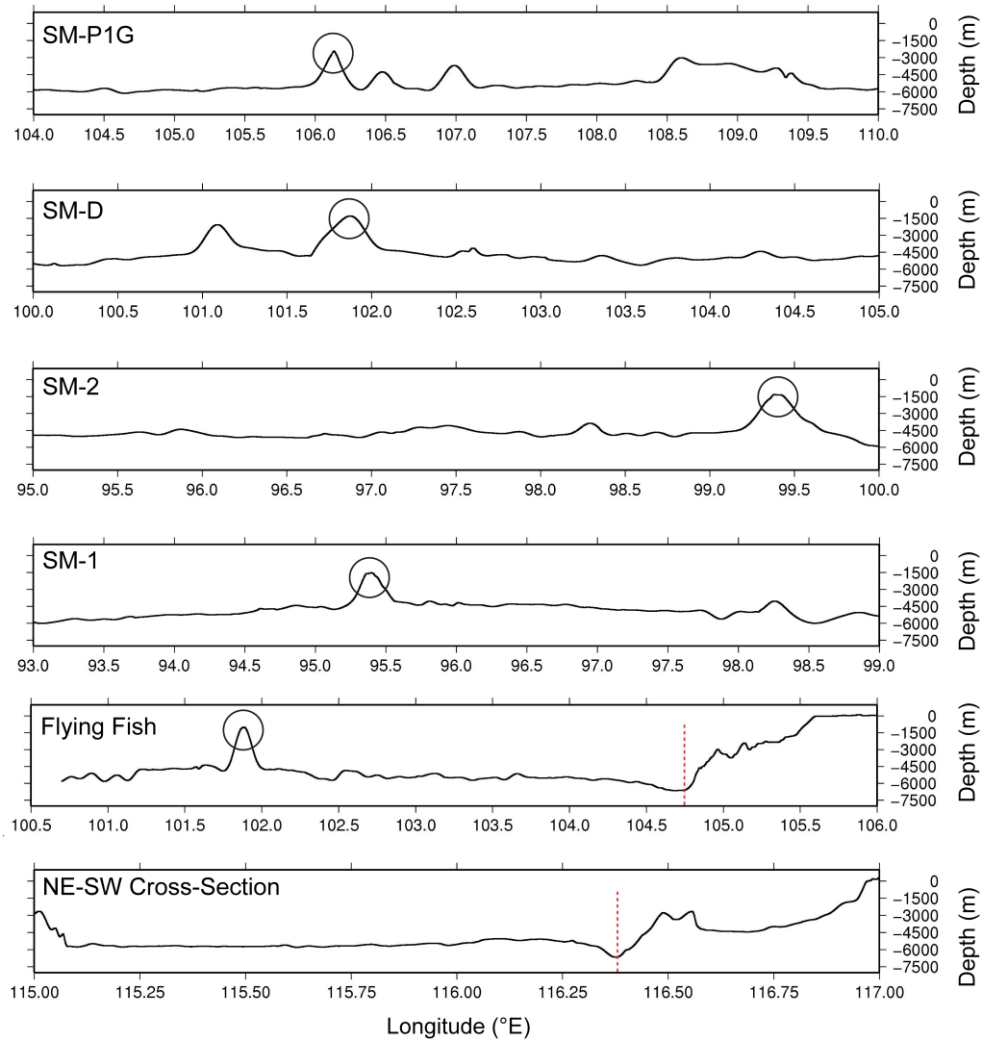

Fig 4.2*:* Bathymetry profiles of selected seamounts located in the Northeast Indian Ocean. SM-P1G (14.2° S, 106.2°E), Sharp peak seamount; SM-D (11.9°S, 101.8°E), rounded/conical topped seamount; SM-2 (4.4°S, 99.4°E) and SM-1 (12.5°S, 95.4°E) are flat top seamounts. West-East transects of the seamounts (SM-P1G, SM-D, SM-2, and SM-1) pass through their centre marked by circle on Fig 4.1. Flexural bulge of the subducting lithosphere can be seen in the bottom two profiles that are perpendicular to the Java Trench. Red dashed line represents the location of the trench.

The first step in this study was to locate flat-topped seamounts within the CHRISP. We used global bathymetry (Smith and Sandwell, 1997), and free-air gravity data (Sandwell and Smith, 2009) to map the distribution of seamounts, and construct bathymetric and gravity profiles across them using GMT (Wessel and Smith, 1991). These seamounts were then separated into those with rounded peaks (also called conical seamounts, Dominguez et al. (1998)) and those with flat tops. Some of the sharp peaked, flat topped, and conical peaked seamounts found in the region are shown in Fig 4.2.

4.3.2: Gravity Modelling

Gravity signatures help determine the crustal structure of the seamounts and islands, due to their excess mass as compared to surrounding ocean floor (Walcott, 1970b; Watts et al., 1975; Watts, 1978; Davy and Wood, 1994). While currently there is no model for the subsurface crustal structure of the CHRISP seamounts, Watts et al. (1975) and Watts et al. (1985) produced a gravity model for the Great Meteor Seamount, in the Northeast Atlantic, and the Hawaii-Emperor seamount chain, respectively, using a combination of different densities that can be used to model CHRISP's seamounts.

This study models the regional gravity response of the South (Keeling) Island, and Christmas Island to determine their crustal structure, and constrain the thickness of individual layers. 200 km east – west gravity profiles passing through the centre of the islands (Fig 4.1 and Fig 4.3) were selected for modelling using Pitney Bowes modelling software Modelvision. Publically available 1-minute gravity and bathymetry datasets (Smith and Sandwell, 1997; Sandwell and Smith, 2009) were imported into Modelvision to produce an observed gravity and bathymetry profile of the islands. The crustal structure of the ocean floor was then modelled by creating polygons representing individual layers to produce a calculated gravity profile that matches

with the observed gravity curve. During this process it is ensured that the top surface of the first crustal layer matches with the bathymetric profile of the island.

A range of density values were used for each crustal layer. The density values were measured for limestone and volcanic samples collected from the Cocos (Keeling) Islands, and Christmas Island, respectively. Limestone density ranges between 1.3 - 2.1 g/cm^3, while volcanic samples vary from 2.6 g/cm^3 (Ross Hill Gardens) and 2.8 g/cm^3 (Winifred Beach), to a maximum of 2.9 g/cm^3 (Dolly Beach). Models presented by previous workers for the Great Meteor Seamount (Watts et al., 1975) and the Hawaiian Islands (Watts et al., 1985) provide constraints on the thickness of basalt and gabbro layers in an equivalent setting. Knowing suitable density ranges, number of layers, and starting depths, the crustal structure of the seamounts were constrained, as discussed in Section 4.4.1.

4.3.3: Flexure of the lithosphere and age at the time of loading

Oceanic lithosphere, when under the influence of a load due to a seamount or an oceanic island, undergoes flexure (Walcott, 1970a; Watts and Cochran, 1974). As a seamount grows by volcanic eruptions, the lithosphere bends under the added weight and the curvature of the response is determined by the flexural rigidity of the lithosphere, and the elastic lithospheric thickness (T_e) (Watts, 2001; Watts and Ribe, 1984). The elastic lithospheric thickness is determined by calculating the distance between the centres of the load to the crest of bulge, X_b using the formulae:

$$F = X_b / \pi \quad 4.1$$

$$4D = F^4 \left(\rho_m - \rho_w \right) g \quad 4.2$$

$$12\, D\, (1 - \nu^2) = E\, T_e^3 \quad 4.3$$

Where, X_b is the distance between the centre of the load to the centre of the crest, E is Young's Modulus (70 GPa), T_e is elastic lithospheric thickness, D is flexural rigidity, F is flexural parameter, g is acceleration due to gravity (9.81 m/s^2), ν is Poisson's ratio (0.25), and ρ_m (3.3 g/m^3), and ρ_w (1.03 g/m^3) the density of the material and water respectively (Turcotte and Schubert, 2002).

The above method calculates the elastic lithospheric thickness given the morphology of flexure, while, we also calculate the age of the lithosphere at the time of loading from the T_e derived in Equation 4.3 using Bodine et al.'s (1981) model for loads in the interior of plate. The relationship between elastic lithospheric thickness and age is given by:

$$T_e = a * age^{\frac{1}{2}} \quad 4.4$$

Where, a=4.3 ± 0.5 (dry), and 3.3 ± 0.5 (wet), and age is the age of the lithosphere at the time of loading (Myrs). With time, the elastic lithospheric thickness increases, therefore loads associated with low T_e were placed on relatively young lithosphere while those with higher T_e values were emplaced on older lithosphere (Watts et al., 1980). The elastic lithospheric thickness generally follows the 300° - 600° C isotherms of the lithosphere cooling model by Parsons and Sclater (1997).

Lithosphere subducting under an oceanic trench experiences a flexure on its seaward side (Walcott, 1970a; Chapple and Forsyth, 1979; Watts, 2001), and undergoes uplift that is broad, around a 200 – 300 km in length, and less than a kilometre in height (Melosh, 1978). An oceanic island (e.g. Christmas Island) or a seamount (e.g. Golden Bo'Sunbird) will begin to shallow as it proceeds toward the bulge, and the submarine feature may eventually be sub-aerially exposed.

The lithospheric flexure associated with a subduction forebulge may result in minor volcanism. Hirano et al. (2001, 2006) documented 6 Ma alkali basalts from the toe of the Japan Trench

that were suggested to have been formed on the seaward side of the flexure. Flexural stresses in the lithosphere may produce cracks due to extensional fracturing that may facilitate the ascent of partial melts from the upper mantle (Hirano et al., 2001). Melt produced in such cases may appear on the surface as low volume knolls or petit spot volcanism (Hirano et al., 2006). Parts of the CHRISP are in a similar tectonic setting to the Hokkaido forebulge (Hirano et al., 2001), and this mechanism may be relevant to the Sunda forebulge. To assess this, profiles of the ocean floor are produced perpendicular to the trench and passing through Christmas Island. These are used to ascertain the scale of the flexural bulge, and the location of brittle fracturing on the seaward side, to examine if such cracking could produce volcanism at Christmas Island.

4.3.4: Ocean floor subsidence with age

As the lithosphere moves away from a mid-ocean ridge towards a subduction zone, it cools, contracts, increases in density, and eventually subsides (Parson and Sclater, 1977). A seamount or an oceanic island loaded on the lithosphere will subside with the same age-depth relationship as the lithosphere (Parson and Sclater, 1977). Exposed seamounts or islands will usually have a sedimentary cover on top, as in the case of South (Keeling) Island in the Cocos (Keeling) Archipelago, reflecting its ongoing subsidence history (Hess, 1946, Winterer 1998). While drilling surveys, and geochronology can constrain the age and history of these seamounts, age-depth subsidence models can be used in the case of under-sampled areas. The approach we use is to constrain the current depths, using Smith and Sandwell (1997) bathymetry dataset, for flat top seamounts within the CHRISP, and backtrack their subsidence history, using their local seafloor age to the time when they were sub-aerially exposed. This approximates their time of origin (Tucholke and Smoot, 1990), and provides a complementary constraint to traditional geochronology in that it can date seamount submergence, as opposed to the age of volcanism, provided the age of underlying ocean crust is known. Modifying the age-depth relation

proposed by Tucholke and Smooth (1990) and using it for the Northeast Indian Ocean, we constrained the age of last sub-aerial exposure by:

$$(5900 - d_{sm}) = 2500 + 350 * t^{\frac{1}{2}} \quad 4.5$$

$$t = \left\{\frac{(5900 - d_{sm}) - 2500}{350}\right\}^2 \quad 4.6$$

Where, d_{sm} is the depth of the seamount; t is the age of the lithosphere at the time of loading in Myr; and the average depth of the seafloor in the region is ~5900 m. Vogt and Tucholke (1979) believe that the constant 350 provides credible estimates for the ages of features that are formed at sea-level. The age obtained from the above equations is subtracted from the age of the ocean crust, to get the date when the seamount was last sub-aerially exposed. We have used oceanic crustal age model by Müller et al. (2008) to extract seafloor ages for locations occupied by the seamounts. While doing this, Tucholke and Smoot (1990) assume no other process acted that might have lead to uplift or thermally reseting the oceanic crust. The age of the ocean crust falls within the Cretaceous Normal Superchron (CNS) for the interval between 120 – 83.5 Ma for which there are only three magnetic isochrons, and hence poorly constrained. Matthews et al. (2012) explains that this difficulty is overcome by relative dating methods, interpolation between magnetic isochrons and seafloor spreading rates, geochronology dating of IODP cores, and biostratigraphy. The uncertainties in the age of magnetic isochrons are associated with dating techniques and the age is then interpolated between the isochrons. Müller et al. (2008) produced colour coded grids of seafloor ages and the uncertainties in sea-floor ages is within 0.1 - 3 Ma for the seafloor formed during Cretaceous Normal Superchron.

4.3.5: Seismic Tomography and plate reconstruction

Seismic tomography is used to image the interior of the Earth by using seismic wave's traveltimes (Nolet et al., 2007). While many different global tomography models have been produced, this study uses three models that have documented anomalies of different intensities

in the East Indian Ocean (TX2000, (Grand, 2002); SAW24B16, (Mégnin and Romanowicz, 2000); and S20RTS, (Ritsema et al., 1999). These models use a variety of inversion techniques, are publically available data, and the comparison of three tomography models eliminates any bias towards a particular model and its inversion techniques. The resolution of these models is an issue as the region is devoid of sufficient receivers and will be dealt in the following sections. Global plate models (Seton et al., 2012) in Gplates are overlain on seismic tomographic depth sections, and are reconstructed back in time to correlate the CHRISP with known deep mantle seismic anomalies. The Gplates model incorporates the most recent reconstructions of the region (Heine and Müller, 2005; Gibbons et al., 2012; Seton et al., 2012) and is based on the moving hotspot model of O'Neill et al. (2005).

4.4: Results

4.4.1: Gravity Modelling

A simple three layer crustal structure of the ocean floor consisting of basalt, gabbro, and mantle was used as the basis for the gravity models, based on the work of Shurbet and Worzel (1955), Watts et al. (1975), Miles (1982), Watts et al. (1985), and Weigel and Grevemeyer (1999).

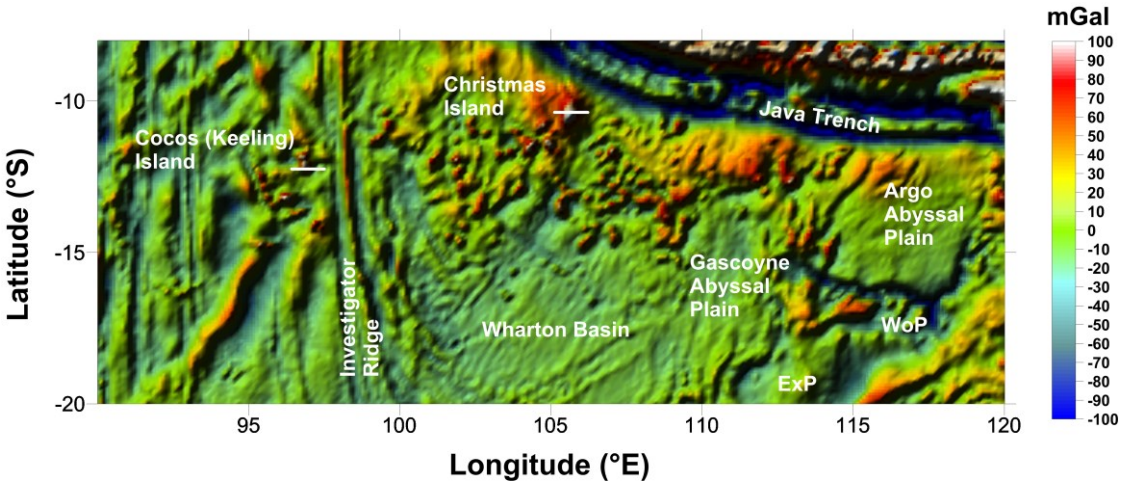

Fig 4.3: Gravity anomaly map (Sandwell and Smith, 2009) of the Northeast Indian Ocean. White solid lines through the Cocos (Keeling) Island and Christmas Island are gravity profiles used for gravity modelling in Fig 4.4. Names of other features are same as in Fig 4.1.

Cocos (Keeling) Island is a coral atoll that is composed primarily of well-lithified, porous Pleistocene Limestone overlain by Holocene sediments (Woodroffe and Falkland, 1997) and

below which should lie the volcanic core of the island. This combined sedimentary unit forms the top layer of the model and gravity modelling constrains the thickness of the limestone cover and depth to basalt at Cocos (Keeling) Island. Representative gravity models for Cocos (Keeling) Island and Christmas Island are shown in Fig 4.4 and location of the profiles are marked on Fig 4.1 and Fig 4.3. The thickness of the limestone on Cocos (Keeling) Island is around 1350 m using a limestone density of 1.7 g/cm^3, and 1500 m for a density of 1.85 g/cm^3. If fixed densities for limestone, gabbro and mantle are assumed (see Table 4.1), and the density of the basalt varied, we observe that the depth of limestone cover increases with increased basaltic densities. For the range of plausible density combinations for these units, we observe that the limestone at Cocos (Keeling) Island may extend from 900 m to 2100 m below sea-level. Although there is no volcanic exposure at Cocos (Keeling) Island, recent dredging by Hoernle et al. (2011) has yielded volcanic rocks at 2400 m below sea-level.

The thickness of the second (basaltic) layer was modelled to be around 2 - 3 km thick, and is underlain by 3 - 5 km of gabbro. However, Davy and Woods (1994) have suggested slightly variable thicknesses for these units in the surrounding oceanic crust. The excess mass of the island above the ocean floor adds additional load on the lithosphere and flexes the overlying low-density basalt and gabbro layers to depths of 13 and 19 km respectively. Further modelling of shallow anomalies at the two islands is not possible due to lack of high resolution data (since the datasets used here are regional), and geological cross section or stratigraphic column that provides constraints on thickness and lateral extent of different lithological units.

Table 4.1: Change in limestone thickness and crustal structure thickness with changing basaltic densities. L, Limestone; B, Basalt; G, Gabbro; M, Mantle; B, Background.

	Density (g/cm^3)	**Depth to base (m)**	**Density (g/cm^3)**	**Depth to base (m)**	**Density (g/cm^3)**	**Depth to base (m)**	**Density (g/cm^3)**	**Depth to base (m)**	**Density (g/cm^3)**	**Depth to base (m)**
L	1.80	900	1.80	1100	1.80	1300	1.80	1800	1.80	2100
B	2.80	13700	2.85	14500	2.90	16400	2.95	17500	3.00	17900
G	3.10	16000	3.10	16600	3.10	18500	3.10	19050	3.10	20000
M	3.30		3.30		3.30		3.30		3.30	
B	2.88		2.88		2.88		2.88		2.88	

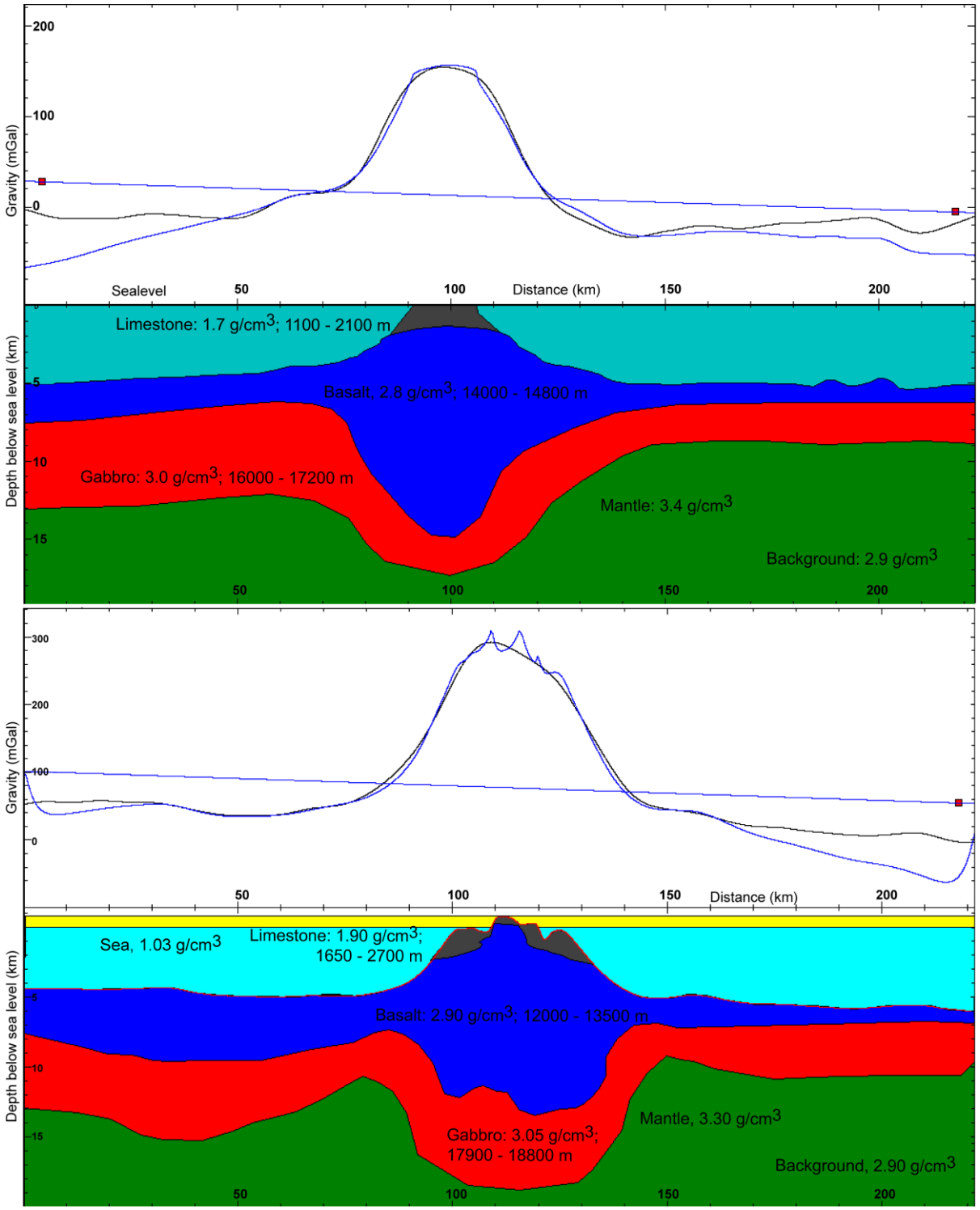

Fig 4.4: Gravity Modelling for Cocos (Keeling) Island (top), and Christmas Island (bottom) along a west-east profile, x-axis distance in km; positive y axis, mGal; negative y axis depth below sea-level. Depth range of each layer is the maximum depth to which it extends into the lithosphere. Black and blue line represents observed and calculated gravity anomaly, and straight blue line represents regional component. Red square is used to change the regional component as per modelling parameters. Background represents the material that comprises most of the feature, which in this case is basalt and can slightly vary as per modelling parameters. Yellow polygon (bottom) represents air column from sea-level up to maximum elevation (360 m) of Christmas Island.

4.4.2: Plate Flexure and age at the time of loading

T_e was calculated by measuring X_b for the two sub-aerially exposed islands. Since the region contains numerous seamounts in the vicinity, the flexure produced by the island is over ridden by these neighbouring seamounts, posing problems in calculating X_b. The profile of the lithosphere perpendicular to the Java Trench is shown in Fig 4.2, where the flexural uplift due to subduction underneath the trench is clearly visible. In some cases, the deformation within the region, or dynamic tomography, has obscured their flexural signature, but for some seamounts the flexure is apparent on one side of the seamount (Fig 4.6). Therefore, in some instances the age of the lithosphere at the time of loading cannot be constrained, but in other seamounts, a loading age can be calculated by modelling their flexural rigidity.

Using the aforementioned elastic lithospheric thickness relation (Equation 4.3), we calculate a T_e of 21 - 23 km for Cocos (Keeling) Islands, and 17 - 20 km for Christmas Island (Table 4.2 and Fig 4.5). Most of the seamounts are at a sufficient distance from the crest of the flexure (e.g. Flying Fish seamount is far away from the flexure as shown in Fig 4.2) to experience any uplift from the subduction, but Christmas Island (at the crest), Shcherbakov, possibly SM-G2, and the Umbgrove seamount, (which has passed the flexural bulge and is now subducting) could have experienced some uplift due to the rise associated with the bulge.

In addition to the two sub-aerially exposed islands, elastic lithospheric thickness was determined for other seamounts (Table 4.2) and their bathymetric profiles are shown in Fig 4.6. An example of flexure being affected by neighbouring seamounts is presented in the case of seamounts SM-C and SM-D, which are very close to each other, while the Shcherbakov seamount is influenced by a rise towards its east.

Table 4.2: Elastic lithospheric thickness for Cocos (Keeling) Island, Christmas Island, and rounded and flat topped seamounts in the region computed using Equation 4.3.

	Xb (m)	F (m)	D (N m)	T_e (km)
Cocos (Keeling) Island -12.16°S	190000	60509	7.46E+22	22.9
Cocos (Keeling) Island -12.18°S	180000	57324	6.01E+22	21.3
Christmas Island -10.50°E	150000	47770	2.90E+22	16.7
Christmas Island-10.40°E	170000	54140	4.78E+22	19.7
SM-C	150000	47770	2.90E+22	16.7
SM-D	140000	44585	2.20E+22	15.2
SM-B	125000	39808	1.40E+22	13.1
Shcherbakov	75000	23885	1.81E+21	6.6
Bartlett	160000	50955	3.75E+22	18.2
SM-1	110000	35031	8.38E+21	11.0
SM-3	80000	25477	2.35E+21	7.2
SM-4	150000	47770	2.90E+22	16.7
SM-5	70000	22292	1.38E+21	6.0

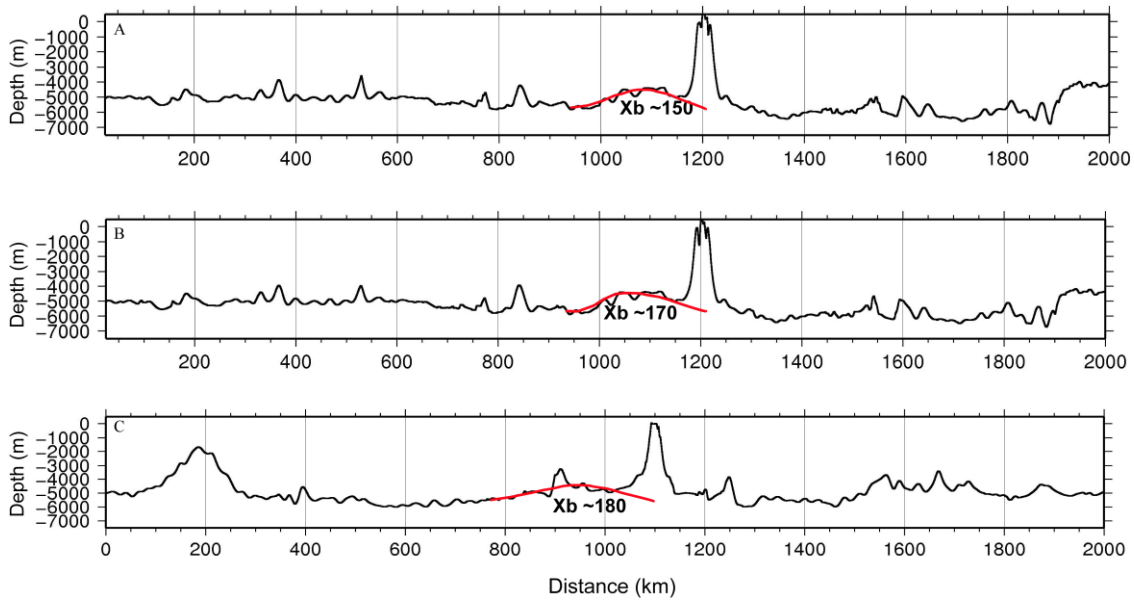

Fig 4.5: West to East bathymetry transects and the associated flexure for A, Christmas Island along 10.50°S; B, Christmas Island along 10.40°S; C, Cocos (Keeling) Island along 12.18°S. The flexure on the eastern side of Christmas Island is obscured as it approaches the subduction margin and the associated flexural bulge. The Cocos (Keeling) Island is affected by features towards the east, and the Investigator Ridge.

The age of lithosphere at the time of loading is calculated using the relation suggested by Bodine et al. (1981) as discussed in Section 4.3.3 Equation 4.4. As per that model, the features that have a low T_e are emplaced on relatively younger lithosphere whereas those with high T_e are formed on older lithosphere. Christmas Island is riding the lithospheric bulge, which has obscured the inherent flexure caused due to volcanic loading. For Christmas Island on an oceanic crust of 105 Ma, the age of the lithosphere at the time of loading was 30 Myrs to 17.5 Myrs which gives an age for the seamount in the range of 87.5 to 75.2 Ma. For Cocos (Keeling) Island, which is on 67.7 Ma old crust, the age of the lithosphere at the time of loading was 44 to 26 Myrs, giving a seamount age of 41.5 to 23.3 Ma (Table 4.3).

Similarly, T_e, for the Shcherbakov and Bartlett seamounts have yielded low to intermediate values of 6.6 and 18.2 km. These seamounts were formed on oceanic crust of 90.0 and 110 Ma, constraining the age of lithosphere at the time of loading to 4.0 - 2.4 Myrs and 30.4 - 17.9 Myrs, respectively. This gives us an age of the seamount in the range of 87.6 - 86.0 Ma for Shcherbakov and 92.1 - 79.6 Ma for Bartlett. The flexural rigidity (D) of Shcherbakov is lower than that of Bartlett with a value of 1.8×10^{21} N m and 3.7×10^{22} N m, respectively. The larger D of Bartlett is a measure of the stiffness of the lithosphere as compared to Shcherbakov, a fact consistent with the older age of the lithosphere of Bartlett.

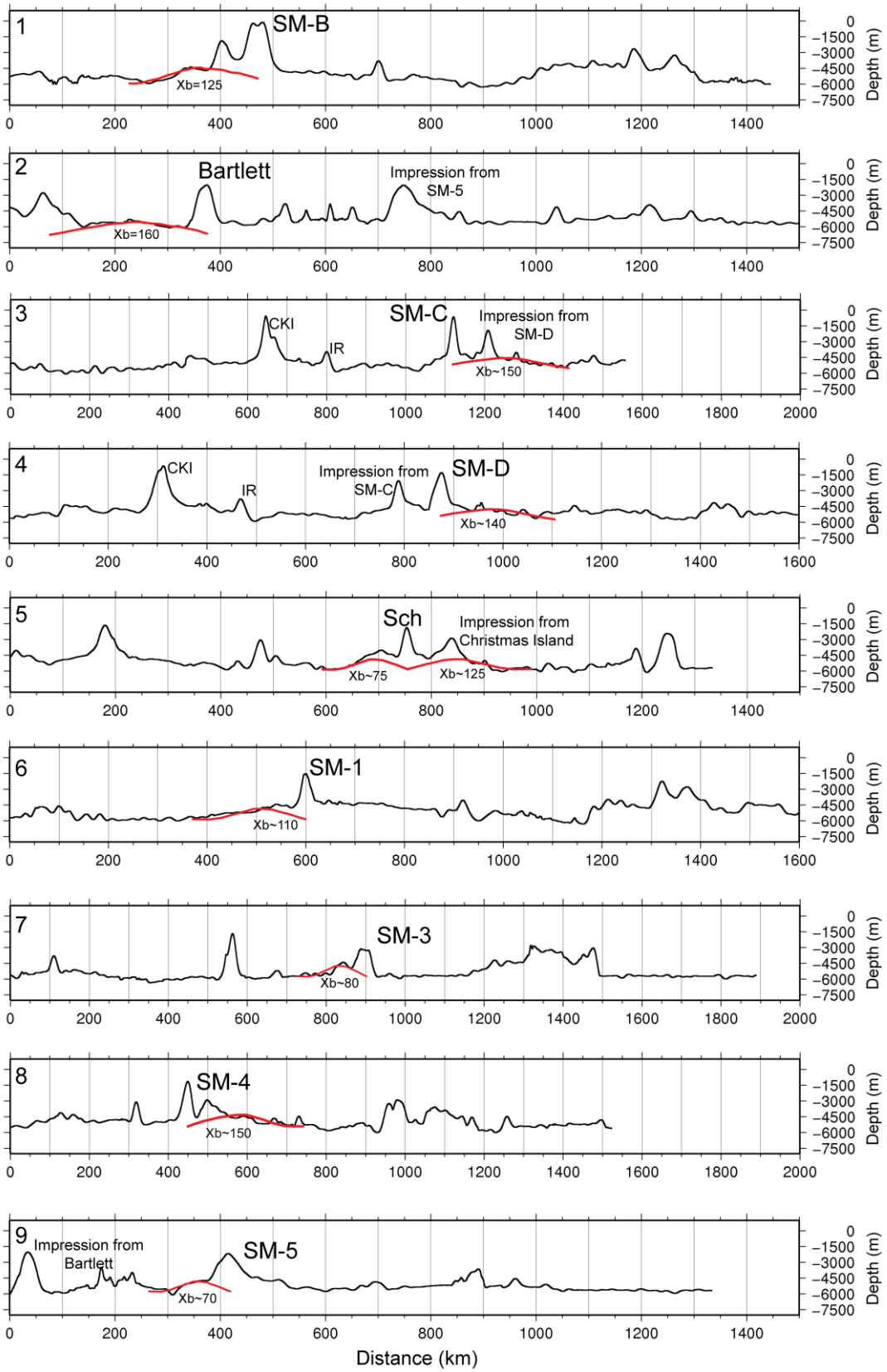

Fig 4.6: Seamounts within the Northeast Indian Ocean and their bathymetric profiles and plate flexure. Note the closeness of seamounts and the resulting interference caused in their bathymetry and flexure. For example (1), SM-B has a small seamount to its west obscuring its apparent flexure; (2), Bartlett seamount has a pronounced conical top but the flexure is not obvious; (3), SM-C and (4), SM-D; (5), Shcherbakov seamount is affected by the flexure of neighbouring Christmas Island to the east. Some of the seamounts, SM-1, SM-3, SM-5 have a very small elastic lithospheric thickness.

Similarly, SM-B formed on young oceanic crust of 56 Ma age, and the age of the lithosphere at the time of loading was 15.8 - 9.3 Myr, yielding an age of the seamount between 46.7 - 40.2 Ma. This age is roughly consistent with the age of 47 Ma obtained by Hoernle et al. (2011) for the seamount (Fig 4.7). Flat topped seamounts SM-3 and SM-4 formed on 124.0 and 85.0 Ma oceanic crust, yielding an age at the time of loading around 4.8 - 2.8 Ma and 25.6 - 15.1 Ma respectively. This gives an age of the seamount in the range of 121.2 - 119.2 Ma and 69.9 - 59.4 Ma respectively. This signifies that SM-3 loaded when the lithosphere was very young which is also consistent with its low flexural rigidity of 2.3×10^{21} N m, as opposed to 2.9×10^{22} N m for SM-4. A low flexural rigidity was also determined for SM-5 ($D=1.3 \times 10^{21}$ Nm), while Bartlett and other seamounts, SM-C, SM-D, and SM-4 were loaded on comparatively older and more rigid lithosphere (Table 4.3). The age of seamounts obtained using this method are very similar to those obtained by Hoernle et al. (2011). The trend of the thickness vs age curve in Fig 4.8 is more consistent with the 600° C isotherm of Parsons and Sclater (1977), suggesting the large deformation associated with the seamounts induces a long-lived elastic response of the oceanic lithosphere (Watts, 1978). These elastic deformational events have remarkable longevity (Watts, 1978). The 600° C isotherm trend is consistent with these seamounts forming on a young oceanic plate, suggesting a hot dry rheology. As the lithosphere increases in age, it cools and becomes more rigid towards surface loads, but also becomes on average more hydrated, and the elastic lithosphere trends toward the 300° C isotherm (Watts, 1978; Bodine et al., 1981; Watts and Ribe, 1984).

Similarly, Shcherbakov, SM-5, and SM-3 were formed on very young oceanic crust in the range of 11 - 5 Ma. These values are comparable with the ages estimated earlier in Table 4.3 but as the lithosphere gets old, the uncertainties associated with it also get larger. Additionally, it is possible that these seamounts experienced multiple stages of volcanism that have not been radiometrically dated.

Table 4.3: Age of lithosphere at the time of loading for the two islands and seamounts of the Northeast Indian Ocean using the relation suggested by Bodine et al. (1981) for loads in the interior of the plate. Comparison of estimates of the age of the lithosphere at the time of loading were made by subtracting the radiometric age (Hoernle et al., 2011) from the age of sea-floor, as discussed by Watts and Ribe (1984). The Late Cretaceous age of Christmas Island has not been dated, but younger age between 44 – 4 Ma has been obtained by Hoernle et al. (2011) and Taneja et al. (2014). * represents age of the lithosphere at the time of loading using 44 – 4 Ma ages of Christmas Island, which is not representative of the Late Cretaceous loading.

Island/ Seamount	**T_e (km)**	**Age of the Seafloor (Ma) T_{sf}**	**Age (elastic) at the time of loading (Myrs) T_{al}**		**Age (elastic) of the seamount (Ma) (T_{sf-al})**	**Age (radiometric) of load (Ma) t_L (Hoernle et al., 2011)**	**Age (radiometric) at the time of loading (Myrs) $t_{sf} - t_L$**
			Dry rheology (T_{al-d})	**Wet rheology (T_{al-w})**			
Cocos (K) Is.	22.0	67.7	26.2	44.4	41.5 - 23.3	56 - 47	21 - 12
Christmas Is.	18.0	105.0	17.5	29.8	87.5 - 75.2	44 - 4	101 – 61*
SM-B	13.1	56.0	9.3	15.8	46.7 - 40.2	47	9
SM-C	16.7	83.0	15.1	25.6	67.9 - 57.4	71	12
SM-D	15.2	83.0	12.6	21.3	70.4 - 61.7	71 - 65	18 - 12
Shcherbakov	6.6	90.0	2.4	4.0	87.6 - 86.0	85	5
Bartlett	18.2	110.0	17.9	30.4	92.1 - 79.6	107 - 102	8 - 3
SM-1	11.0	56.0	6.6	11.2	49.4 - 44.8	47	9
SM-3	7.2	124.0	2.8	4.8	121.2 - 119.2	115 - 113	11 - 9
SM-4	16.7	85.0	15.1	25.6	69.9 - 59.4	71 - 64	21 - 14
SM-5	6.0	120.0	2.0	3.4	118.0 - 116.6	115	5

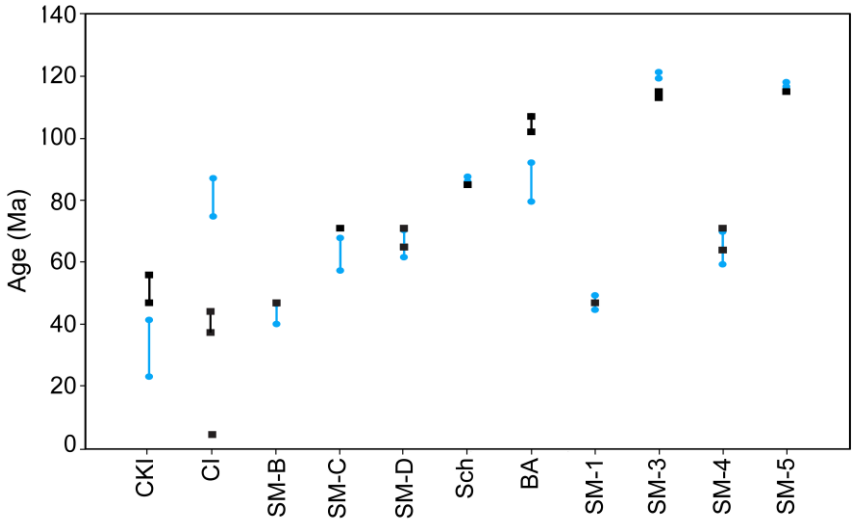

Fig 4.7: Comparison of age of the seamount calculated in Table 4.3 using plate flexural of the seamount in the interior of the plate (Bodine et al., 1981), with the ages obtained by Hoernle et al. (2011). Blue represents age calculated in this study, while black are ages from Hoernle et al. (2011). CKI is Cocos Keeling Islands, CI is Christmas Island and other seamounts names are given in Fig 4.1. Loading age of most of the seamounts are close to the radiometric ages. Christmas Island has no Late Cretaceous volcanic exposure, but this study has calculated a loading age between 88 – 75 Ma. Also plotted are the later stages of volcanism at Christmas Island as reported by Hoernle et al. (2011) and Taneja et al. (2014).

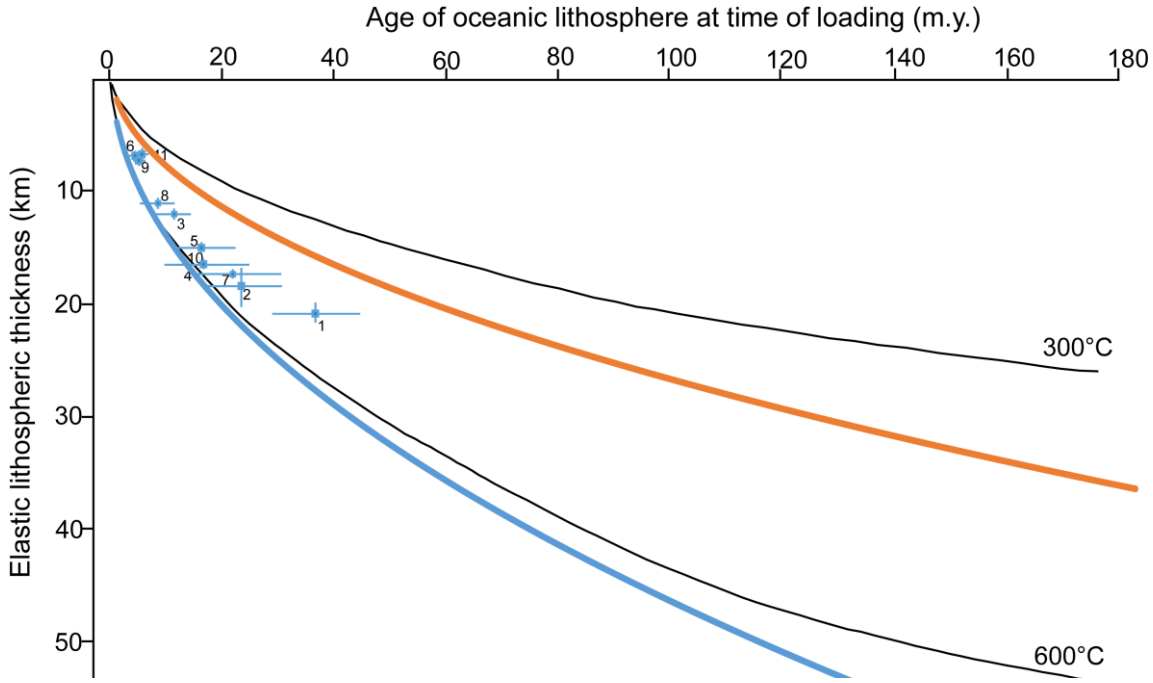

Fig 4.8: Elastic lithospheric thickness as a function of age of oceanic lithospheric at the time of loading taken from Watts et al. (1980). 1,Cocos (Keeling) Is.; 2, Christmas Island; 3, SM-B; 4, SM-C; 5, SM-D; 6, Shcherbakov; 7, Bartlett; 8, SM-1; 9, SM-3; 10, SM-4; 11. SM-5. 300° C and 600° C isotherms are based on the cooling plate model of Parsons and Sclater (1977). The seamounts are closer to the 600° C isotherm suggesting that they were formed on a young oceanic plate with a dry rheology. As the oceanic plate increases in age, it becomes more hydrated and elastic lithosphere falls closer to the 300° C isotherm. Blue (dry) and orange (wet) lines represent the relation of T_e and age of the lithosphere at the time of loading given in Equation 4.4.

4.4.3: Age Depth Relation

The ages derived through age-depth subsidence relations suggests three age groups for when these seamounts were exposed. The oldest activity occurred around Early to Late Cretaceous, 140 - 65 Ma; followed by a second in Middle Eocene, 48 - 40 Ma; and the youngest in Late Oligocene to Early Miocene, 28 - 20 Ma (see Table 4.4). Christmas Island may have recorded two of these three volcanic ages. However, the older Late Cretaceous phase is currently submerged (only exposures in inland caves) on Christmas Island, and there is no evidence of an Early Miocene age (Hoernle et al., 2011; Taneja et al., 2014).

An age progressive trend can be observed through the five flat-topped seamounts in the region (Fig 4.9). As we move eastwards towards the North West Shelf, the seamounts become older. The age of oldest exposed seamount SM 3 is ~124 Ma whereas the youngest exposed seamount in this progressive trend is SM 2 at ~32 - 21 Myr old (Table 4.4). SM 2 is an exception to this trend because, firstly, it doesn't lie within the 10° - 15°S east-west trending seamount province, but is further north, and secondly it could be affected by its close proximity to the northern end of Sunda Trench, and the fact that it has passed through the flexural bulge produced on the subducting lithosphere (Fig 4.1).

The conical or rounded peak seamounts may have signatures of being sub-aerially exposed that were not observed here. Winterer and Metzler (1984) have shown that the rounded peak seamounts are evidences of sub-aerial exposure that have undergone later stages of erosion or re-shaping of pelagic caps on top of flat topped volcanic cover. The data sets used in this approach are regional and hence small flat-top coverage will appear rounded in satellite data (due to a higher resolution of swath bathymetry data). Moreover, Lawver et al. (2012) collected bathymetry data in the Western Ross Sea region and has shown that rounded mounds in satellite low resolution data appear flat topped in their high resolution data. Due to this ambiguity, the time since exposure for conical peaked seamounts within the seamount provinces was also

calculated and has been presented in Table 4.4 and it follows the same age trend. Some seamounts might have been influenced by the uplift of the lithosphere associated with the flexural bulge. Since the magnitude of uplift is within 200 – 300 m, this value is subtracted from the depth of the seamount for Shcherbakov, and SM-G2, giving an age of 80 – 76 Ma, and 97 – 94 Ma respectively. Umbgrove seamount, however, has descended the flexure and thus the subsidence of the seamount is neutralised by the flexural rise giving it an age of 103 – 101 Ma (Table 4.4).

Table 4.4: Last exposure ages for the seamounts in the Northeast Indian Ocean calculated using the relation suggested by Tucholke and Smooth (1990). Age obtained using lithospheric subsidence provide minimum constraint on the age of the seamount that roughly equates to the time of origin of the seamount (Tucholke and Smoot, 1990), and can be used when conventional geochronology is not available in under-sampled regions. Age for Shcherbakov, Golden Bo' Sunbird, and SM-G2 is calculated by subtracting uplift of 200 – 300 m due to the flexure, while the drop of Umbgrove will be neutralised by the uplift. Age without correction for uplift is given in parenthesis. The uncertainty in seafloor ages within the CNS (120 – 83.5 Ma) is between 0.1 - 3 Ma, for older ages (120 – 110 Ma) the error is between 2 – 3 Ma, and for younger ages, (110 – 83.5) the error is between 0.1 - 1 Ma (Müller at el., 2008). * represents age not calculated due to the presence of a plume below the Cocos (Keeling) Island (Montelli et al. 2004).

Name of the Seamount	Lat. (°S)	Long. (°E)	Depth below sea-level (m)		Last exposure age (Ma)		Ages (Ma) by Hoernle et al. (2011) (locations are approximate)
			Min	Max	Min	Max	
SM-1	12.5	95.4	1537	1635	28	31	47
SM-2	4.4	99.4	1325	1700	21	32	-
SM-3	14.7	108.9	3126	3300	123	124	115 - 113
SM-4	11.2	99.3	1156	1470	44	55	71 - 64
SM-5	13.5	108.7	2182	2400	108	112	115
Golden Bo Sunbird	11.3	104.4	294	334	21 (11)	28 (13)	85 - 81
Umbgrove	10.8	109.2	2334	2444	101	103	-
Vening Meinesz	11.0	102.4	2065	2144	70	72	71 - 70
Shcherbakov	10.7	104.8	1878	1965	76 (71)	80 (73)	85
Flying Fish	10.7	102.1	3055	3099	83	83	71 - 70
Bartlett	13.6	105.7	2032	2086	93	94	107 - 102
SM-A2	12.7	112.9	1611	1690	109	111	-
SM-A1	12.6	111.9	1758	1799	108	109	-
SM-G2	11.7	107.0	1892	1957	94 (91)	97 (93)	107 - 94
SM-G1	11.7	103.6	916	1006	40	43	65 - 64
SM-D	11.9	101.8	1304	1348	48	49	71 - 64
SM-C	12.0	101.1	651	737	22	26	-
SM-B	13.2	96.3	125	145	-*	-*	51 - 47

Ages determine by Hoernle et al. (2011) in the vicinity of these seamounts are presented in Table 4.4, and a broad similarity in ages can be seen for most of the seamounts. For example, Vening Meinesz, Shcherbakov, SM-G2 have similar ages to those determined radiometrically. SM-B, however, gives a negative age with the subsidence model, and this may be due to uplift of the seamount associated with mantle flow (Montelli et al., 2004). The plume underneath Cocos (Keeling) Island has a radius of 200 – 300 km and can influence neighbouring seamounts (SM-B), but will have little affect on seamounts further to the east. Similarly, Golden Bo'Sunbird gives a much younger age, suggesting that it too may have experienced the later uplift and/or volcanic rejuvenation observed on Christmas Island. In general, the subsidence ages post-date the volcanic ages, as the final submergence of a seamount may postdate the cessation of volcanic activity by 5 – 10 Myrs (eg. Hawaii, Duncan and Clague, 1985).

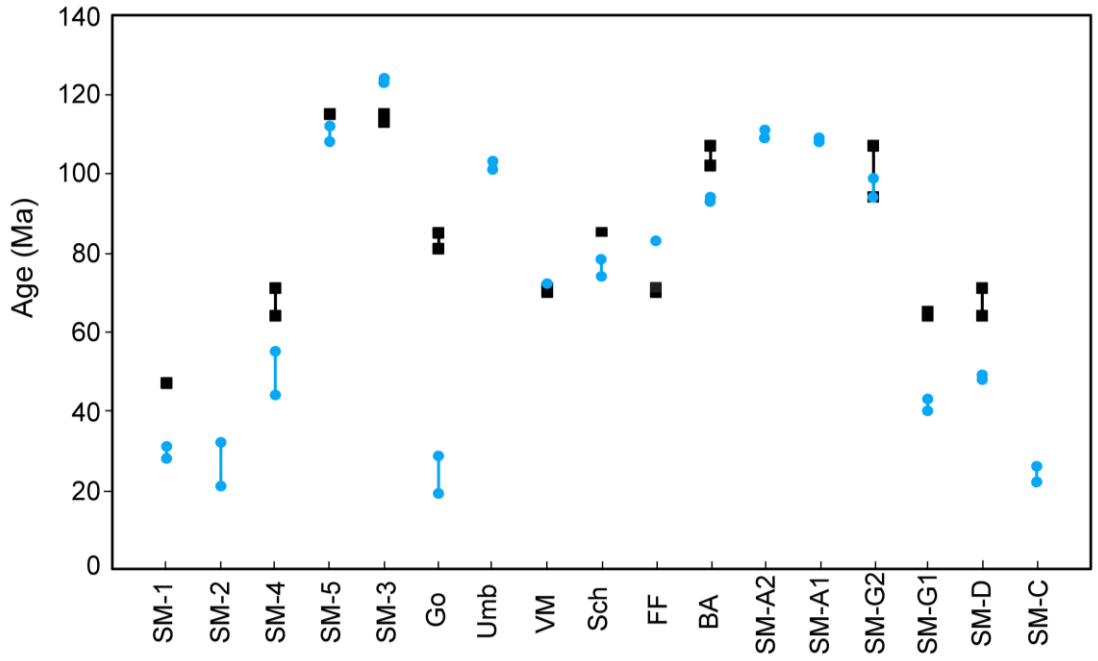

Fig 4.9: Comparison of age of the seamount using age-depth relation of Tucholke and Smoot (1980) and constrained in this study (blue circles) with ages (black squares) obtained by Hoernle et al. (2011). No geochronology age is available for seamount SM-2, SM-A1, SM-A2, and Umbgrove (Umb). For location of the seamounts see Fig 4.1.

Having developed a sub-surface crustal structure underneath Cocos (Keeling) Island and constrained the probable thickness of the limestone cap, we have calculated the time when the basalts were last exposed above sea-level using the subsidence relation described above for other seamounts. Using gravity modelling, the study constrained the thickness of limestone or the depth to basalt in the range of 900 to 2100 m as shown in Table 4.5. Assuming shallow basaltic depth of less than 1000 m, an exposure age of ~21 Ma is suggested, whereas assuming a depth of over 1800 m, the time since exposure of basalt is calculated at 47 Ma. If a depth to the basalt contact of ~2100 m is assumed, an age of 54 Ma is calculated. This is similar to an age of 56 Ma dredged near the island by Hoernle et al. (2011) and those obtained using T_e earlier.

Table 4.5: Time since basaltic exposure at Cocos (Keeling) Island constrained using age-depth subsidence of the basaltic layer obtained from gravity modelling.

Depth to basalt (m) at Cocos (Keeling) Island	Basaltic last exposure, Ma
900	17
1000	21
1100	25
1200	28
1800	47
1900	49
2000	52
2100	54
2200	56
2500	61

4.4.4: Outer rise volcanism at Christmas Island

The Indo-Australian Plate undergoing subduction at the Sunda-Java Trench experiences uplift on the seaward side of the lithosphere (Walcott, 1970b). Due to this bulge in the lithosphere, the crest of the flexure is shallower than the surrounding abyssal plain. The crest is 4000-4100 m, and Christmas Island presently sits on the bulge. Additionally, there is some overlapping of the flexural response due to the island load, and by the subducting margin (Fig 4.10).

Such lithospheric bending induces brittle fracturing and cracks within the flexed lithosphere (Hirano et al., 2001, 2006). These conduits may permit any melt present underneath the cracked lithosphere to rise to the surface (Hirano et al., 2001). The Pliocene phase of volcanism sampled at Christmas Island could have been formed by this mechanism. Back tracking the present location of the island, using a radiometric volcanic age of 4.32 Ma, and a plate motion rate 7cm/yr, a position ~300 km SW of its present location (10.5°S, 105.5°E) is calculated (Fig 4.10). This location coincides with the development of incipient bending, and flexural cracking of the lithosphere, and suggests that the Pliocene phase of volcanism at the island is associated with this mechanism.

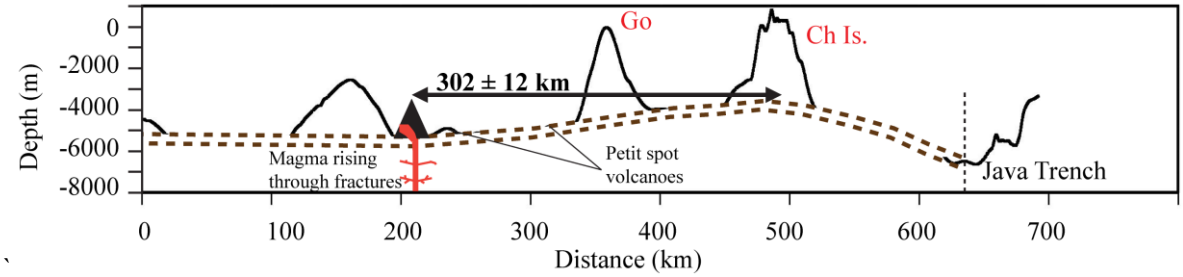

Fig 4.10: Back tracking the position of Christmas Island and the associated Pliocene volcanism at the seaward side of the outer rise of the subducting trench. Black line represents the bathymetric profile of the oceanic lithosphere in a NE-SW section perpendicular to the trench passing through Christmas Island, dashed brown line shows the bending and flexure of the lithosphere, vertical black dashed lines represents the axis of Java Trench. Cracking in the lithosphere and the associated low volume volcanic event (orange) occurs at the reconstructed position of the Island (black triangle) in the Pliocene. Go is Golden Bo'Sunbird seamount. Two small volcanoes between Golden Bo'Sunbird and the black triangle could represent former petit spot volcanoes which are younger than the recorded volcanism at Christmas Island. Modified from Taneja et al. (2014).

4.4.5: Seismic Tomography and Gplates reconstruction

During the Eocene phase of volcanism at Christmas Island, its position was within the latitudes 30° to 37°S and longitudes 91° to 95°E (Müller et al., 2008; Seton et al., 2012). All three seismic tomography models (Fig 4.11) compared in this study highlight a low velocity zone (LVZ) to the east of 90°E around latitude 30°S down to 600 km depth.

Tomography Profiles: All three tomography models shown in Fig 4.12 and Fig 4.13 show the presence of a LVZ underneath the reconstructed position of Christmas Island at ~45 Ma in the Eocene and around 5 Ma in the Pliocene. At 5 Ma the island is at ~12°S and at the edge of the slow zone in Berkeley's SAW24B16 and S20RTS model. The LVZ extends down to 700 – 800 km, though in Grand's TX2000 model Christmas Island appears to be west of the LVZ, which may extend below 1000 km. If associated with an upper mantle temperature anomaly, this slow-velocity zone could be affecting the seamounts west of Christmas Island.

In the Eocene at 50 – 45 Ma, the reconstructed position of Christmas Island is 30°S as per the reconstruction models of Seton et al. (2012). Christmas Island is seen above the LVZ in the three models. According to SAW24B16, the zone has a well-defined lens-like structure extending down ~800 km at its western limit, and down to 1500 km further eastwards. The S20RTS model has a similarly deeper low velocity feature, but the intensity is much lower compared to SAW24B16. TX2000 shows a more disseminated low velocity area in mid mantle. In the Middle Eocene (45 Ma) reconstruction, a faint LVZ is extending to deeper depths of 2500 km in S20RTS and TX2000 models.

Tomography depth slices: Seismic tomography depth slices (Fig 4.11 and Fig 4.13) by TX2000 demonstrate the presence of a characteristic low velocity zone around the reconstructed position of Christmas Island in the Eocene at 50 - 45 Ma. This zone extends down to a depth of 900 km but is visible to 1600 km, beyond which it is weak. S20RTS shows a LVZ around 30°S during the Eocene (55 - 35 Ma) in 350 and 600 km depth slices (Fig 4.13). The same zone can be further traced down to 900 km depth, however it becomes faint at 1600 km depth. Thereafter, a very narrow faint low intensity zone can be observed between 30°S to 40°S, extending to the core-mantle boundary, connecting to the above mentioned stronger anomaly. SAW24B16 documents similar anomalies at varying depths, and a feeder anomaly ~ 40°S at 2400 km depth is more clearly distinct in the model and can be traced to 30°S. The

resolution, however, is an issue and will be discussed in the next section. Montelli et al.'s (2004) P-wave velocity model shows a low velocity area from ~35°S, ~100°E that extends eastwards up to the coast of Australia visible down to 1900 km below which the resolution is poor (Fig 4.14). Additionally, two plumes, one starting from the CMB underneath South of Java, and another below Cocos (Keeling) Island have also been identified by Montelli et al. (2004).

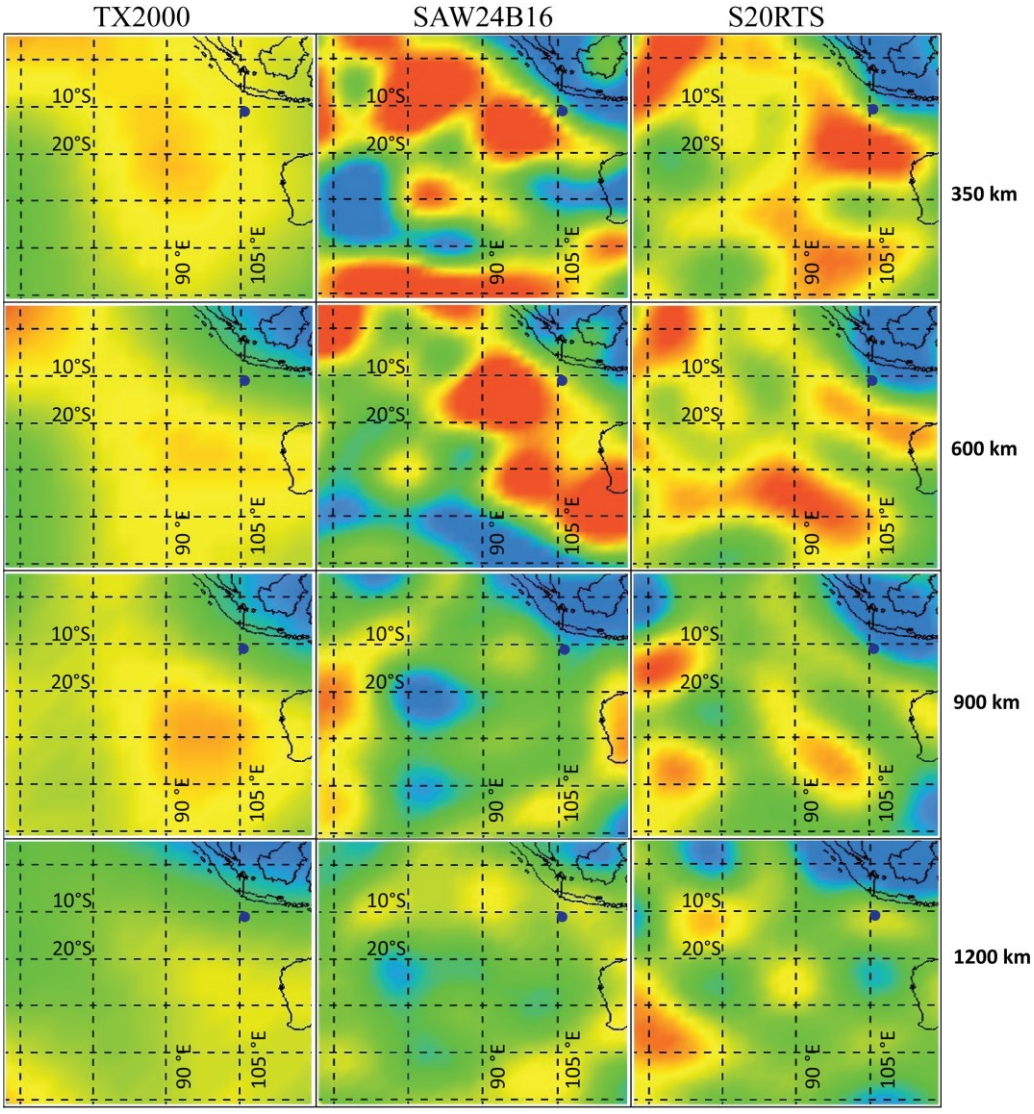

Fig 4.11: Seismic tomography depth section for the Indian Ocean. The present position of Christmas Island is 10.5°S, 105.5°E (blue dot) and the reconstructed position of the island in the Eocene is around ~30°S, ~91°E. Two low velocity zones are distinguishable, one just south of the trench and the other around 30°S, 90°E. The second LVZ is believed to have led to the formation of the seamount province. TX2000 seismic tomography model is from Grand (2002), SAW24B16 is from Mégnin and Romanowicz (2000), and S20RTS from Ritsema et al. (1999).

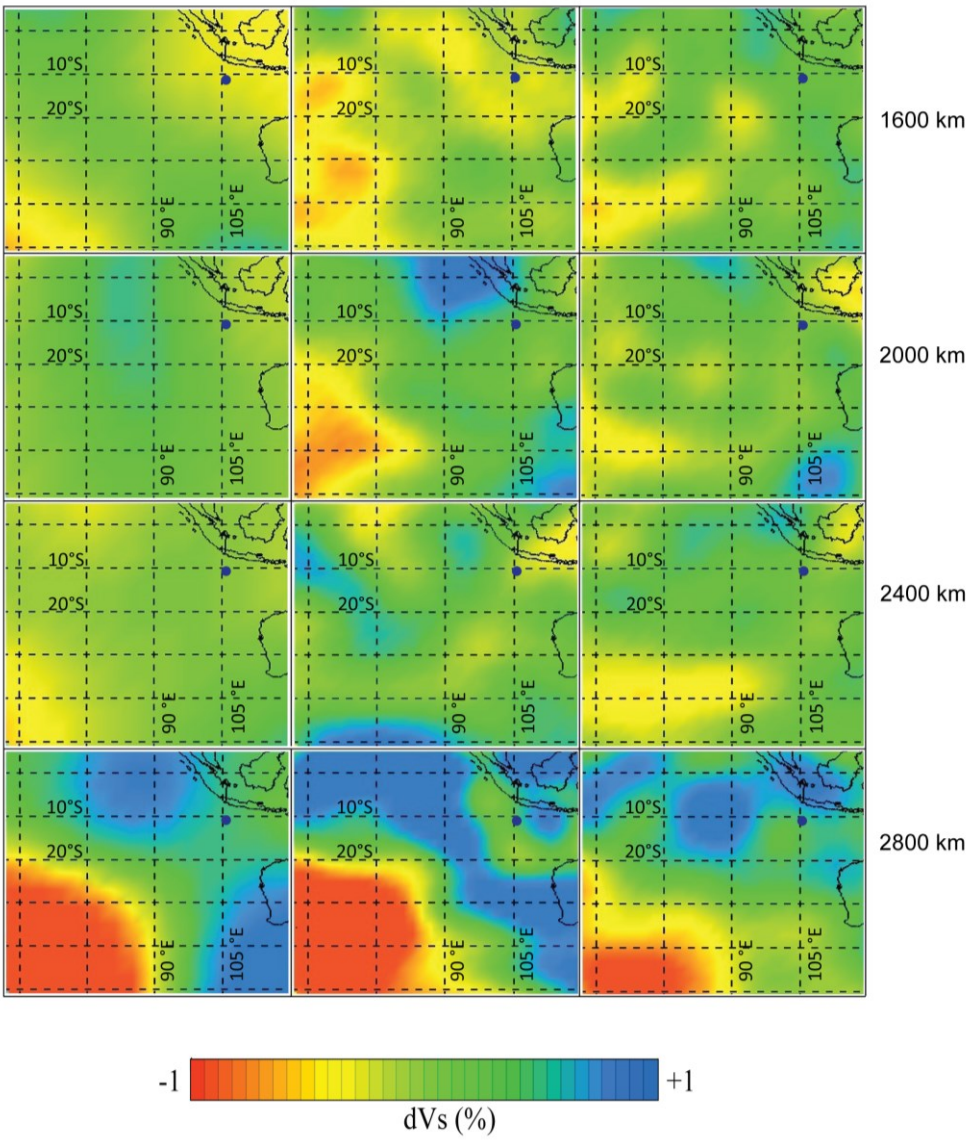

Fig 4.11 Continued

A second low velocity zone in the north is observed in the three models that lie south of the trench between 22° - 15°S in the 350 km depth slice, and narrows down to a more confined shape at 600 km but can still be traced up to 1200 km in the TX2000 and S20RTS models. It can, however, be traced down to 1600 km in the SAW24B16. This anomaly becomes very faint deeper into the mantle and is difficult to delineate.

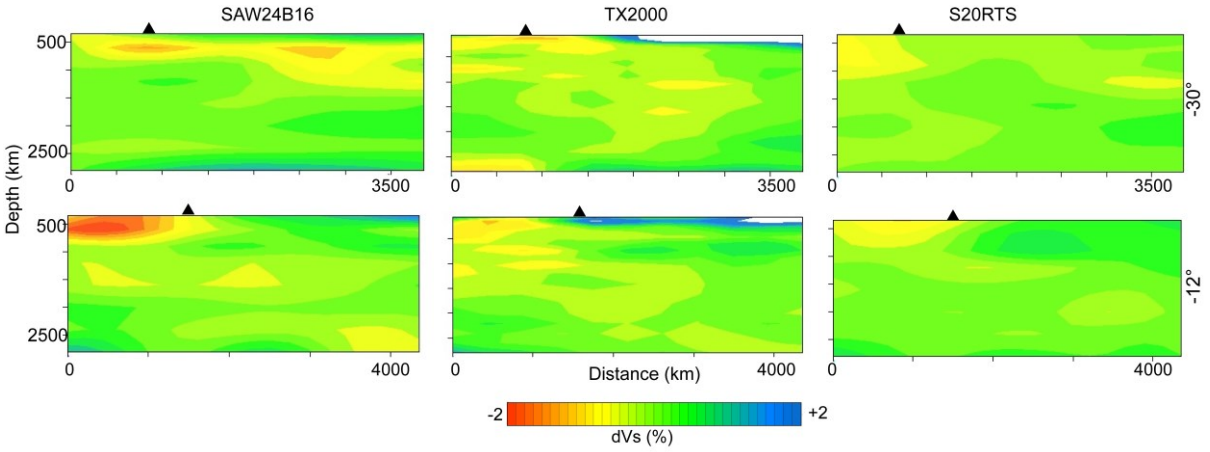

Fig 4.12: Seismic tomography profiles across 12°S and 30°S at the reconstructed position of Christmas Island. Black triangle represents the position of Christmas Island according to plate reconstruction model of Seton et al. (2012). Christmas Island was at ~30°S at ~45 Ma and ~12°S at 5 Ma. There is a potentially deep low velocity zone visible at 30°S, which might have led to volcanism in the region, while the low velocity anomaly at 12°S has not been documented as active volcanism. TX2000 seismic tomography model is from Grand (2002), SAW24B16 is from Mégnin and Romanowicz (2000), and S20RTS from Ritsema et al. (1999).

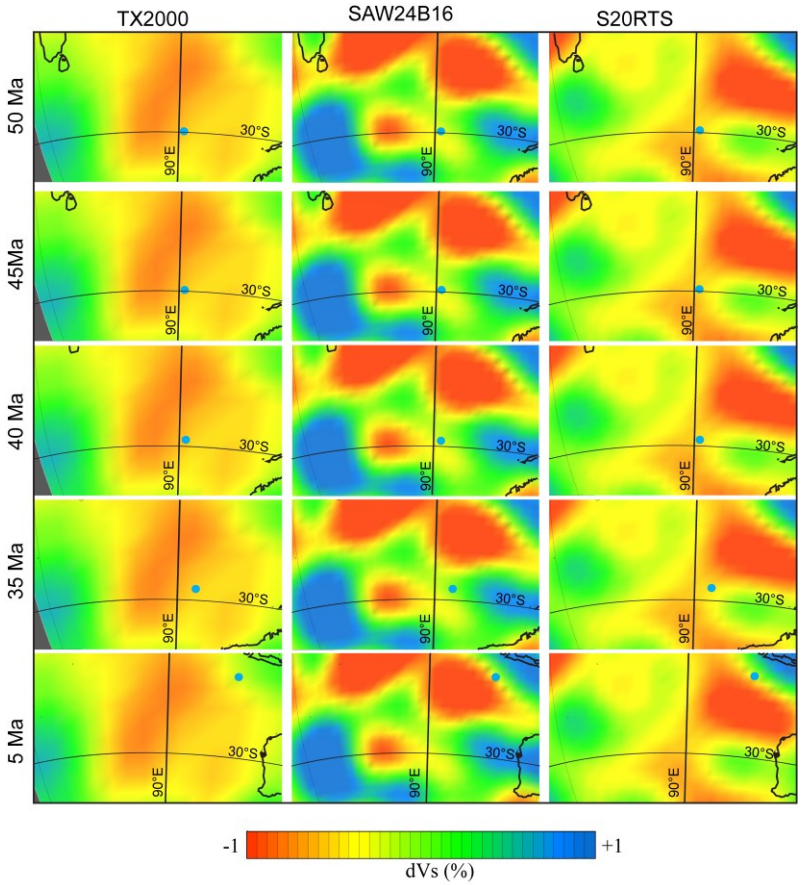

Fig 4.13: Seismic tomography depth slices (350 km) overlayed on Gplates. Blue circle represents the position of Christmas Island according to the plate reconstruction model of Seton et al. (2012). Such a large low velocity zone centred around 30°S and 90°E underneath the reconstructed position at ~ 50 Ma supports the implication that it might have led to the formation of the seamount province. TX2000 seismic tomography model is from Grand (2002), SAW24B16 is from Mégnin and Romanowicz (2000), and S20RTS from Ritsema et al. (1999).

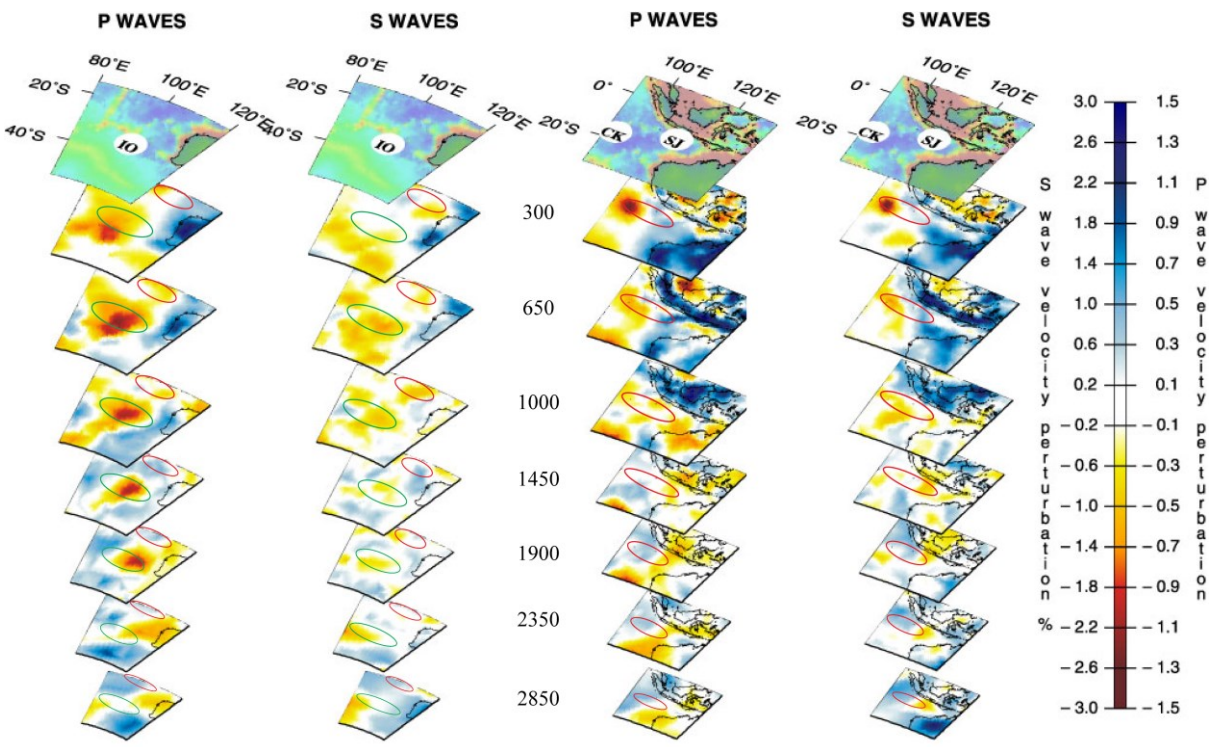

Fig 4.14: Finite frequency seismic tomography models of Montelli et al. (2004, 2006). Three mantle plumes in the East Indian Ocean can be seen down to lower mantle depths. A plume underneath Cocos (Keeling) Island is a potential deep plume that may be responsible for uplift of seamounts in the vicinity. A starting plume underneath south of Java is visible down to depths of 1450 km. Another plume further south centred around 35°S and 100°E is visible down to depths of 1900 km, below which the resolution is poor. It is suggested that this plume may have been responsible for the volcanism in the Christmas Island Seamount Province. The red oblong represents the present position of CHRISP, the green oblong represents the reconstructed position of the seamount province using Seton et al.'s (2012) reconstruction models.

4.5: Discussion

4.5.1: Geophysical attributes

The Northeast Indian Ocean seamount province presents a very rich and complex evolutionary history. Gravity modelling, modelling age-depth subsidence of oceanic lithosphere, along with plate flexural studies, can provide important constraints on the dynamic and tectonic effects of this complex volcanic history.

Gravity data from the two exposed islands has helped to constrain the crustal thickness, and depth-to-basalt in case of the Cocos (Keeling) Islands. This study has constrained the limestone thickness at the Cocos (Keeling) Islands to between 900 - 2100 m (Table 4.5), and this has

been confirmed by dredging of volcanic rock from depths of 2400 m by Hoernle et al. (2011). On the other hand, multiple episodes of volcanism have been recorded on Christmas Island (Trueman, 1965; Grimes, 2001; Hoernle et al. 2011; Taneja et al. 2014), which are primarily exposed along its shoreline. One limitation of our modelling is the lack of spatial constraints on individual layers within the volcanic sequences, as no geological/seismic profiles were available. A high gravity anomaly for Christmas Island, compared to Cocos (Keeling) Island, is due to the large volume of Late Cretaceous volcanism which forms the core of Christmas Island, and extends to shallow depths within the upper sedimentary layer. There is no volcanic exposure within the upper 1 - 2 km of limestone at Cocos (Keeling) Island (Fig 4.4).

This study identified five flat-topped seamounts in the region implying these volcanic features were exposed to erosion and weathering while sub-aerially exposed (Hess, 1946; Winterer, 1998; Winterer and Metzler, 1984). We backtracked these seamounts using age-depth relations, and found an age progressive trend, that youngs towards the west, a trend paralleled by Hoernle et al. (2011). Such an exercise constrains the time when these seamounts were last sub-aerially exposed which provides a minimum constraint on the age of the seamount (Tucholke and Smoot, 1990). While complementing traditional radioisotope geochronology, by providing an additional age constraint (of submergence, as opposed to eruption), this technique is also extremely useful in regions for which traditional geochronology is not available. The ages obtained through subsidence modelling are either similar or less than the age of the dredged samples dated through geochronological methods by Hoernle et al. (2011) (Table 4.5 and Fig 4.9). Additionally, SM-3 is a flat topped seamount at depth of ~3200 m below sea-level and has yielded a last exposure age of ~123 Ma. This suggests that the seamount was formed very close to the mid oceanic ridge at a depth of ~2500 m below sea-level, and has since subsided with the oceanic crust.

Coral reefs on the fringes of seamounts form if the mean subsidence rate of a seamount is slow enough for coral growth to keep pace (Darwin, 1843; Hess, 1946). Woodroffe et al. (1991) suggested a mean subsidence rate of 0.1 mm/yr for the Cocos (Keeling) Islands with a range between 0.08 to 0.12 mm/yr for the last 124,000 years. For this range of subsidence rate, the basalt contact would be at the surface between 26 - 17.5 Ma. We, however, calculated the last exposure age of CKI (basaltic top) at ~55 Ma. This implies, that the effective time-averaged subsidence of the Cocos (Keeling) Island was less than at present. A potentially deep plume at 17°S below the Cocos (Keeling) Island has been reported by Montelli et al. (2004, 2006), and is also evident in the seismic tomography models shown in Fig 4.11 and Fig 4.14. Isotopic ages of 56 – 47 Ma in the vicinity of Cocos (Keeling) Islands have been yielded by Hoernle et al. (2011) - suggesting little influence of the nascent plume, which would have produced much younger volcanism. However, the rise associated with a deep plume might be why the time-averaged subsidence rate is less than at present. Karner (1985) discussed possible effects of thermal resetting of oceanic lithosphere associated with hotspot traces and extinct spreading centres. Thermal resetting induces cumulative uplift of the region, and may result in flexural changes, and was suggested by Karner (1985) to be relevant to the uplift – or at least subdued subsidence - of Cocos (Keeling) Island.

McNutt and Menard (1978), and Detrick and Crough (1978) both observed that coral atolls in the Pacific Ocean were uplifted as they rode over thermal anomalies. McNutt and Menard (1978) also suggested that a coral atoll or a seamount can be uplifted in response to loading effects and flexure imposed by neighbouring seamounts, a situation which is common in the Christmas Island Seamount Province (Fig 4.1), and may have influenced the early loading history of these seamounts. Finally, the Golden Bo'Sunbird seamount has started to rise over the fore-bulge associated with the Sunda subduction zone, resulting in a recent shallowing to ~300 m below sea-level (Table 4.4 and Fig 4.10).

The seamount age distribution also shows the time since last sub-aerial exposure is younger in the west, compared to those in the east, a relationship that is paralleled in the seafloor age. This is consistent with the spreading history of the region, where the spreading started between Greater India and the western margin of Australia (Veevers et al., 1991; Müller et al., 1998; Müller et al., 2000). Older magnetic anomalies can be seen along the west coast of Australia, which young progressively westwards. The extinct Wharton Ridge, which now lies in the Wharton Basin, constitutes the youngest seafloor in the region (Liu et al., 1983; Müller et al., 2008; Jacob et al., 2014).

The elastic lithospheric thickness of oceanic lithosphere is a function of thermal age of the lithosphere at the time of loading as suggested by earlier studies (Detrick and Crough, 1978; Watts, 1978). The T_e at Cocos (Keeling) is within 21 - 23 km, whereas, at Christmas Island it is in the range of 17 - 20 km. The age of the lithosphere, when the two features loaded the oceanic lithosphere was in the range of 44 - 26 Myrs and 30 - 17 Myrs, respectively (Table 4.3). Cocos (Keeling) Island has a higher flexural rigidity (D) of 6.0–7.4 x 10^{22} N m, whereas Christmas Island has a lower D of 2.9 – 4.8 X 10^{22} N m (Table 4.2). Low T_e and D at Christmas Island is attributed to thermal weakness of the oceanic lithosphere and its complicated relationship with the underlying plate (Bodine et al., 1981; Watts, 1994) and also by fracturing on the seaward side of the lithosphere as the island rides over the bulge overprinting its flexural signature. Royer et al. (1989) stated that, the intraplate deformation in the region extends from the Central Indian Ocean up to the Northwest Shelf, causing east-west undulation within the lithosphere that has the ability to destroy or hide the tectonic fabric. Additionally, while calculating T_e, it is assumed, that loading is representative of a point load, with a short volcanic history (Watts, 1994). The low T_e calculated for Christmas Island suggest a loading age of 87.5 - 75.2 Ma – far older than the oldest radiometric age (e.g. Taneja et al., 2014). This suggests that either the oldest core of the Island is not sampled, or that something has affected the

calculated elastic lithosphere. Christmas Island, has experienced multiple stages of volcanism, after its initial eruption, presumably in the Late Cretaceous (Hoernle et al., 2011; Taneja et al., 2014). This could have the effect of thermal resetting of the lithosphere, and the duration of loading may have been protracted, as the island has experienced ongoing volcanism in the Pleistocene. This ongoing volcanism may have thermally reset the lithosphere, resulting in a much lower effective T_e during its protracted loading history (e.g. Calmant and Cazenava, 1986). A similar effect has been proposed for the low T_e observed at French Polynesia, where a hot ascending plume, imaged as a low P wave velocity anomaly (McNutt and Fischer, 1987; Calmant and Cazenava, 1986), may have thermally reset the lithosphere. As previously mentioned, upper mantle low velocity anomalies (see Fig 4.11 and 4.13) are observed beneath the reconstructed position of the province ~40 Ma, and may have induced a similar effect. The low T_e of other seamounts suggests that these were formed on very young ocean floor – consistent with the local seafloor, and their eruption ages. Grimes (2001) documented a Late Cretaceous episode of volcanism that formed the core of the island, however, $^{40}Ar/^{39}Ar$ geochronology conducted on the dredged samples by Hoernle et al., (2011), or the field samples of Taneja et al. (2014), have not yielded any older volcanism. This study, however, has provided evidence from lithospheric flexural modelling that Christmas Island was formed between 88 – 75 Ma (Table 4.3), thus, supporting the idea that the bulk of Christmas Island was formed in Late Cretaceous, and that the dredging expedition by Hoernle et al. (2011) did not sample this phase.

Plumes suggested to originate from the CMB are believed to have a lifespan of ~100 Myr (Courtillot et al., 2003). O'Neill (2005) performed hotspot reconstructions within the Indian Ocean domain, using density anomaly models and suggested that the observed density anomalies and mantle structures are long-lived features and can exceed 50 Myrs. Present day seismic tomography models have highlighted a low velocity zone underneath the reconstructed

position of Christmas Island Seamount Province that can be clearly seen in models by Mégnin and Romanowicz (2000) and Ritsema et al. (1999) (Fig 4.11). Montelli et al. (2004) have suggested an anomaly at 35°S and 100°E that is close to the reconstructed position of the seamount province and Christmas Island (Fig 4.14). Another plume identified by Montelli et al. (2004) is near the Cocos (Keeling) Island, and could be responsible for recent volcanism, but such activity is yet to be documented. The most recent ages documented by Hoernle et al. (2011) for volcanism around the Cocos (Keeling) Island are 56 – 47 Ma, and do not support ongoing volcanic activity. The starting plume south of Java ascends up to 1450 km from the CMB (Montelli et al., 2004) and is too deep to influence the present position of the seamounts in the province, while the influence of the larger seismic anomaly (e.g. Grand, 2002; Fig 4.11) near the present position is unclear as there is no documented evidence of recent volcanic activity, except at Christmas Island which is related to plate bending stresses.

A complication to the plume model for the East Indian Ocean is that compositional variations may also induce significant velocity anomalies. Hoernle et al. (2011) previously identify a continental-lithosphere-like component to be the cause of the volcanism in the region, and an important question is, could some of these broad shallow-mantle low velocity zones be a relic of sub-Gondwanan lithosphere, detached during breakup? An important test of this would be the Vp/Vs ratio for these anomalies, this to date has not been done. The resolution of seismic tomographic models is an issue within the Indian Ocean, as few seismic stations are spread across the region, leading to gaps in ray-path coverage, and a lack of resolving power. In addition the distribution of earthquakes is heavily weighted towards the northern Sunda Trench, and the resolution power of imaging intraplate anomalies is therefore limited (Nolet et al., 2007). Moreover, each tomography model uses different data, and inversion approaches, and hence do not always agree. This is a compounding factor in the dissimilarity between the models, as seen in comparison studies regarding the exact position of these seismic anomalies

(Grand, 2002; Nolet et al., 2007). Nevertheless, an association of the reconstructed volcanic province, with deep-seated low velocity mantle anomalies, is apparent, though the ultimate origin of these anomalies (compositional or thermal) is unclear.

4.5.2: Low volume intraplate volcanism

The petit spot volcanism that has been observed on the seaward side of the outer rise of the Hokkaido Rise exists on Cretaceous seafloor. Seismic studies carried out by Fujiwara et al. (2007) on the petit spots volcanoes in the northwest Pacific Ocean have shown volcanic reflectors injected within the neighbouring sedimentary layers. They conclude that the total thickness of sills can be up to 100 m, and seismic sections reveal dykes within the host sedimentary layers.

The timing of renewed volcanism on Christmas Island (~4 Ma), as it started to ascend the flexural fore-bulge, is striking, and we suggest a similar "petit-spot" volcanic mechanism in this region. Field analyses, and observation in the Murray Hill region suggest most Pliocene volcanism was in the form of dyking within fault networks, with limited flows (Winifred Beach, Taneja et al. 2014; Baxter and Weeks, 1984) – consistent with the Hokkaido Rise example.

Two small rounded peak volcanic seamounts are present south-west of Christmas Island (see Fig 4.10). One lies just before Golden Bo'Sunbird seamount, while the other is to the southwest. The southern seamount lies on the point at which lithospheric flexure becomes significant – and where the local stress regime in the lithosphere may be favourable to magma ascent, as shown in Fig 4.10. Fujiwara et al. (2007) have argued petit-spot small volcanoes are characteristically ~2 - 3 km in diameter, and ~100 m in height. These two seamounts possess similar characteristics to those observed through swath bathymetry and seismic reflection surveys by Fujiwara et al. (2007). High-resolution swath bathymetry data acquisition along the

flexed zone and dredging of the oceanic floor could further validate this model. Following volcanism in the Eocene, Christmas Island moved north-west in the Oligocene and Miocene as the spreading in SEIR initiated (Liu et al., 1983). The plume south of Java, identified by Montelli et al. (2004), does not seem to have been the source for the Pliocene event, as it is apparently a starting plume, ascending from the CMB to a shallowest depth of 1450 km.

4.6: Conclusion

Our geophysical investigations of the Christmas Island Seamount Province within the Northeast Indian Ocean provides important age constraints on the loading history of the region. These islands and seamounts have had a varied history, in terms of their exposure above sea-level. Cocos (Keeling) Island is demonstrating present-day subsidence rates far beyond its long-term average, and Christmas Island has recently been uplifted. Using gravity modelling this study has constrained the thickness of the limestone cover at Cocos (Keeling) Island to be between 900 - 2100 m. This thickness is supported by dredged volcanic samples from depths of 2400 m (Hoernle et al., 2011). This implies that the volcanic surface of the island was exposed above sea-level at ~55 Ma - an age that concurs with the geochronological age. Modelling the subsidence of submerged seamounts in the region shows a westwards younging trend, which is also observed in the oceanic crustal age. Flat topped seamounts SM-5 and SM-3 are the oldest seamounts, and were exposed above sea-level around 124 - 108 Ma. Golden Bo'Sunbird and SM-B are the shallowest seamounts in the region, which could be due to the uplift caused by the flexure of the subducting lithosphere, or due to a topographic rise produced by the presence of a seismically imaged plume near the Cocos (Keeling) Islands in the case of SM-B. Flexural modelling has been able to constrain the elastic lithospheric thickness (T_e) of Christmas Island, and we find a Late Cretaceous loading age for Christmas Island of 88 – 75 Ma, an age which is significantly older than the oldest dated volcanism (44 Ma), suggesting this phase may not have been sampled. Other flat topped seamounts, such as SM-3, SM-5 and

Shcherbakov have low T_e values, implying these seamounts were formed on very young oceanic floor and their loading ages of 121.2 – 119.2, 118.0 – 116.6, and 87.6 – 86.0 Ma, respectively, are similar to those determined through radiometric dating by Hoernle et al. (2011).

Seismic tomography models support deep origin for the seamount province and a large low velocity seismic anomaly is believed to be an important component in the formation of the Christmas Island Seamount Province. This anomaly extends to depths of at least 1600 - 2000 km beyond which the low velocity zone is less resolved. The exact nature of this seismic anomaly is not known. Pliocene intraplate volcanism observed at Christmas Island is probably a direct consequence of lithospheric plate flexure. Such flexure drastically alters the stress state of the lithosphere allowing crack-induced volcanism to rise to the surface in a similar fashion to that described for the Hokkaido Rise (Hirano et al., 2001).

Acknowledgement

We are grateful to Robert Hall and an anonymous reviewer for their constructive comments that greatly improved this manuscript. We would also like to thank CCFS/GEMOC for their support during this research. This work in in part supported by Australian Research Council (ARC) funding DP110104145, DP088801, and FT100100717. This is contribution 477 from the ARC Centre of Excellence for Core to Crust Fluid Systems (http://www.ccfs.mq.edu.au) and 947 in the GEMOC Key Centre (http://gemoc.mq.edu.au).

References

Abercrombie RE, Antolik M, Ekström G (2003) The June 2000 Mw 7.9 earthquakes south of Sumatra: Deformation in the India–Australia Plate. J Geophys Res 108 (B1):2018. doi:10.1029/2001jb000674

Aitchison JC, Ali JR, Davis AM (2007) When and where did India and Asia collide? J Geophys Res 112 (B5):B05423. doi:10.1029/2006jb004706

Andrews CW (1900) A monograph of Christmas Island (Indian Ocean): Physical Features and Geology. British Museum (Natural History), London

Baxter JL, Weeks GC (1984) Phosphatised volcanic ore from the Christmas Island, Indian Ocean. Western Australia Institute of Technology

Bodine J, Steckler M, Watts A (1981) Observations of Flexure and the Rheology of the Oceanic Lithosphere. J Geophys Res 86 (B5):3695-3707. doi:10.1029/JB086iB05p03695

Calmant S, Cazenave A (1986) The effective elastic lithosphere under the Cook-Austral and Society islands. Earth Planet Sci Let 77 (2):187-202. doi:http://dx.doi.org/10.1016/0012-821X(86)90160-3

Chapple WM, Forsyth DW (1979) Earthquakes and bending of plates at trenches. J Geophys Res 84 (B12):6729-6749. doi:10.1029/JB084iB12p06729

Cloetingh S, Wortel R (1985) Regional stress field of the Indian Plate. Geophys Res Lett. 12 (2):77-80. doi:10.1029/GL012i002p00077

Courtillot V, Davaille A, Besse J, Stock J (2003) Three distinct types of hotspots in the Earth's mantle. Earth Planet Sci Lett. 205 (3-4):295-308. doi:http://dx.doi.org/10.1016/S0012-821X(02)01048-8

Darwin C (1842) The Structure and Distribution of Coral Reefs. Being the first part of the geology of the voyage of the beagle, under the command of Capt. Fitzroy, R.N. during the years 1832 to 1836. Smith, Elder and Co., London

Davies HL, Sun Ss, Frey FA, Gautier I, McCulloch MT, Price RC, Bassias Y, Klootwijk CT, Leclaire L (1989) Basalt basement from the Kerguelen Plateau and the trail of a Dupal plume. Contributi to Mineral and Petrol 103 (4):457-469. doi:10.1007/bf01041753

Davy B, Wood R (1994) Gravity and magnetic modelling of the Hikurangi Plateau. Marine Geology 118 (1-2):139-151. doi:http://dx.doi.org/10.1016/0025-3227(94)90117-1

DePaolo DJ, Manga M (2003) Deep origin of hotspots-the mantle plume model. Science 300 (5621):920-920

Desa M., Ramana M.V, Ramprasad T, 2009. Evolution of the Late Cretaceous crust in the equatorial region of the Northern Indian Ocean and its implication in understanding the plate kinematics. Geophysical J International 177, 1265-1278.

Detrick RS, Crough ST (1978) Island subsidence, hot spots, and lithospheric thinning. J Geophys Res 83:1236-1244

Dominguez S, Lallemand S, Malavieille J, von Huene R (1998) Upper plate deformation associated with seamount subduction. Tectonophysics 293 (3):207-224. doi:http://dx.doi.org/10.1016/S0040-1951(98)00086-9

Duncan RA (1978) Geochronology of basalts from the Ninetyeast Ridge and continental dispersion in the eastern Indian Ocean. J of Volcanol and Geotherm Res 4 (3-4):283-305. doi:http://dx.doi.org/10.1016/0377-0273(78)90018-5

Duncan RA (1991) 26. Age distribution of volcanism along aseismic ridges in the eastern Indian Ocean. In: Weissel J, Peirce J, Taylor E, Alt J (eds) Proceedings of the Ocean Drilling Program, Scientific Results, 121, vol 121. College Station, TX: Ocean Drilling Program, pp 507-517

Duncan RA (2002) A Time Frame for Construction of the Kerguelen Plateau and Broken Ridge. J of Petrol 43 (7):1109-1119. doi:10.1093/petrology/43.7.1109

Duncan RA, Clague DA (1985) Pacific Plate Motion Recorded by Linear Volcanic Chains. In: Nairn AEM, Stehli F, Uyeda S (eds) The Ocean Basins and Margins. Springer US, pp 89-121. doi:10.1007/978-1-4613-2351-8_3

Eagles G, König M (2008) A model of plate kinematics in Gondwana breakup. Geophys J Int 173 (2):703-717. doi:10.1111/j.1365-246X.2008.03753.x

Frey F, Weis D (1995) Temporal evolution of the kerguelen plume: Geochemical evidence from 38 to 82 ma lavas forming the Ninetyeast ridge. Contributi to Mineral and Petrol 121 (1):12-28. doi:10.1007/s004100050087

Fujiwara T, Hirano N, Abe N, Takizawa K (2007) Subsurface structure of the “petit-spot” volcanoes on the northwestern Pacific Plate. Geophys Res Lett 34 (13):L13305. doi:10.1029/2007gl030439

Gaina C, Müller RD, Brown BJ, Ishihara T (2003) Microcontinent formation around Australia. Geol Soc Am Special Papers 372:405-416. doi:10.1130/0-8137-2372-8.405

Gaina C, Müller RD, Brown BJ, Ishihara T, Ivanov S (2007) Breakup and early seafloor spreading between India and Antarctica: Geophys J Int, 170 (1):151-169.

Gibbons AD, Barckhausen U, van den Bogaard P, Hoernle K, Werner R, Whittaker JM, Müller RD (2012) Constraining the Jurassic extent of Greater India: Tectonic evolution of the West Australian margin. G-Cubed 13 (5):Q05W13. doi:10.1029/2011gc003919

Gibbons AD, Whittaker JM, Müller RD (2013) The breakup of East Gondwana: Assimilating constraints from Cretaceous ocean basins around India into a best-fit tectonic model. J Geophys Res: Solid Earth 118 (3):808-822. doi:10.1002/jgrb.50079

Grand SP (2002) Mantle shear-wave tomography and the fate of subducted slabs. Philosophical Transactions of the Royal Society of London Series A: Mathematical, Physical and Engineering Sciences 360 (1800):2475-2491. doi:10.1098/rsta.2002.1077

Grand SP, van der Hilst RD, Widiyantoro S (1997) Global Seismic Tomography: A Snapshot of Convection in the Earth. GSA Today 7 (4):1-7

Grigg RW, Jones AT (1997) Uplift caused by lithospheric flexure in the Hawaiian Archipelago as revealed by elevated coral deposits. Mar Geol 141 (1-4):11-25. doi:http://dx.doi.org/10.1016/S0025-3227(97)00069-8

Grimes KG (2001) Karst Features of Christmas Islands. Helictite 37:41-58

Hall R (2012) Late Jurassic-Cenozoic reconstructions of the Indonesian region and the Indian Ocean. Tectonophysics 570-571:1-41. doi:http://dx.doi.org/10.1016/j.tecto.2012.04.021

Heine C, Müller RD (2005) Late Jurassic rifting along the Australian North West Shelf: margin geometry and spreading ridge configuration. Australian Journal of Earth Sciences: An International Geoscience Journal of the Geological Society of Australia 52 (1):27 - 39

Heirtzler JR, Cameron P, Cook PJ, Powell T, Roeser HA, Sukardi S, Veevers JJ (1978) The Argo Abyssal Plain. Earth Planet Sci Lett. 41 (1):21-31

Hess HH (1946) Drowned ancient islands of the Pacific Basin. Am J Science 244 (11):772-791. doi:10.2475/ajs.244.11.772

Hesse R (1973) Diagenesis of a seamount oolite from the west Pacific, Leg 20, DSDP. Initial Reports of the Deep Sea Drilling Project 20:363-387

Hirano N, Kawamura K, Hattori M, Saito K, Ogawa Y (2001) A new type of intra-plate volcanism; Young alkali-basalts discovered from the subducting Pacific Plate, Northern Japan Trench. Geophys Res Lett 28 (14):2719-2722. doi:10.1029/2000GL012426

Hirano N, Takahashi E, Yamamoto J, Abe N, Ingle SP, Kaneoka I, Hirata T, Kimura J-I, Ishii T, Ogawa Y, Machida S, Suyehiro K (2006) Volcanism in Response to Plate Flexure. Science 313 (5792):1426-1428. doi:10.1126/science.1128235

Hoernle K, Hauff F, Werner R, van den Bogaard P, Gibbons AD, Conrad S, Müller RD (2011) Origin of Indian Ocean Seamount Province by shallow recycling of continental lithosphere. Nature Geoscience 4 (12):883-887. doi:10.1038/ngeo1331

Johnson BD, Powell CM, Veevers JJ (1980) Early spreading history of the Indian Ocean between India and Australia. Earth Planet Sci Lett. 47 (1):131-143

Karig DE, Peterson MNA, Short GG (1970) Sediment-capped guyots in the Mid-Pacific mountains. Deep Sea Research and Oceanographic Abstracts 17 (2):373-378. doi:http://dx.doi.org/10.1016/0011-7471(70)90029-X

Karner GD (1985) Thermally induced residual topography within oceanic lithosphere. Nature 318:527-532

Krishna KS, Gopala Rao D, 2000. Abandoned Paleocene spreading center in the northeastern Indian Ocean: evidence from magnetic and seismic reflection data. Mar Geol 162, 215-224.

Larson RL (1975) Late Jurassic Sea-Floor Spreading in the Eastern Indian Ocean. Geology 3 (2):69-71. doi:10.1130/0091-7613(1975)3<69:ljssit>2.0.co;2

Larson RL (1977) Early Cretaceous breakup of Gondwanaland off western Australia. Geology 5 (1):57-60. doi:10.1130/0091-7613(1977)5<57:ecbogo>2.0.co;2

Lawver L, Lee J, Kim Y, Davey F, 2012. Flat-topped mounds in western Ross Sea: Carbonate mounds or subglacial volcanic features? Geosphere 8(3): 645-653.

Leech ML, Singh S, Jain AK, Klemperer SL, Manickavasagam RM (2005) The onset of India-Asia continental collision: Early, steep subduction required by the timing of UHP

metamorphism in the western Himalaya. Earth Planet Sci Lett. 234 (1-2):83-97. doi:http://dx.doi.org/10.1016/j.epsl.2005.02.038

Lei J, Zhao D (2006) A new insight into the Hawaiian plume. Earth Planet Sci Let 241 (3):438-453

Liu C-S, Curray JR, McDonald JM (1983) New constraints on the tectonic evolution of the eastern Indian Ocean. Earth Planet Sci Let 65 (2):331-342. doi:http://dx.doi.org/10.1016/0012-821X(83)90171-1

Luyendyk BP, Rennick W (1977) Tectonic history of aseismic ridges in the eastern Indian Ocean. Geol Soc Am Bulletin 88 (9):1347-1356. doi:10.1130/0016-7606(1977)88<1347:thoari>2.0.co;2

Matthews KJ, Seton M, Müller R.D, 2012. A global-scale plate reorganization event at 105−100 Ma. Earth and Planetary Science Letters, 355–356(0): 283-298.

Mattielli N, Weis D, Grégoire M, Mennessier JP, Cottin JY, Giret A (1996) Kerguelen basic and ultrabasic xenoliths: Evidence for long-lived Kerguelen hotspot activity. Lithos 37 (2-3):261-280. doi:http://dx.doi.org/10.1016/0024-4937(95)00040-2

McNutt MK, Fischer KM (1987) The South Pacific superswell. In: Keating BH, Fryer P, Batiza R, Boehlert GW (eds) Seamounts, Islands and Atolls, vol 43. Am Geophys Union, Washington DC, pp 25-34

McNutt MK, Menard HW (1978) Lithospheric flexure and uplifted atolls. J Geophys Res 83 (B3):1206-1212. doi:10.1029/JB083iB03p01206

Mégnin C, Romanowicz B (2000) The three-dimensional shear velocity structure of the mantle from the inversion of body, surface and higher-mode waveforms. Geophys J Int 143 (3):709-728. doi:10.1046/j.1365-246X.2000.00298.x

Melosh H (1978) Dynamic support of the outer rise. Geophys Res Lett 5 (5):321-324. doi:10.1029/GL005i005p00321

Mihut D, Müller RD (1998) Revised sea-floor spreading history of the Argo Abyssal Plain. In: Purcell PG, Purcell RR (eds) The Sedimentary Basins of Western Australia 2. Petroleum Exploration Society of Australia, WA Branch, Perth, WA, pp 73-80

Miles PR (1982) Gravity models of the Amirante Arc, western Indian Ocean. Earth Planet Sci Let 61 (1):127-135. doi:http://dx.doi.org/10.1016/0012-821X(82)90045-0

Montelli R, Nolet G, Dahlen F, Masters G (2006) A catalogue of deep mantle plumes: new results from finite-frequency tomography. G-Cubed 7 (11):Q11007. doi:10.1029/2006GC001248

Montelli R, Nolet G, Dahlen FA, Masters G, Engdahl ER, Hung S-H (2004) Finite-Frequency Tomography Reveals a Variety of Plumes in the Mantle. Science 303 (5656):338-343. doi:10.1126/science.1092485

Morgan WJ (1971) Convection plumes in the lower mantle. Nature 230 (5288):42-43

Müller RD, Gaina C, Clark S (2000) Seafloor spreading around Australia. In: Veevers JJ (ed) Billion-year Earth History of Australia and neighbours in Gondwanaland. GEMOC Press, Sydney, pp 18-28

Müller RD, Mihut D, Baldwin S (1998) A new kinematic model for the formation and evolution of the west and northwest Australian margin. In: Purcell PG, Purcell RR (eds) The Sedimentary Basins of Western Australia 2. Petroleum Exploration Society of Australia, WA Branch, Perth, WA, pp 55-72

Müller RD, Sdrolias M, Gaina C, Roest WR (2008) Age, spreading rates, and spreading asymmetry of the world's ocean crust. G-Cubed 9 (4):Q04006. doi:10.1029/2007gc001743

Naini BR (1973) Appendix 1. A Marine Geophysical Survey (Site 211 DSDP) in the Wharton basin, Indian Ocean. Initial Reports of the Deep Sea Drilling Project 22:835-842. doi:10.2973/dsdp.proc.22.app1.1974

Nolet G, Allen R, Zhao D (2007) Mantle plume tomography. Chemic Geol 241 (3-4):248-263. doi:http://dx.doi.org/10.1016/j.chemgeo.2007.01.022

O'Neill C, Müller D, Steinberger B (2005) On the uncertainties in hot spot reconstructions and the significance of moving hot spot reference frames. G-Cubed 6 (4):Q04003

Parsons B, Sclater JG (1977) An analysis of the variation of ocean floor bathymetry and heat flow with age. J Geophys Res 82 (5):803-827. doi:10.1029/JB082i005p00803

Paulay G, McEdward L (1990) A simulation model of island reef morphology: the effects of sea level fluctuations, growth, subsidence and erosion. Coral Reefs 9 (2):51-62. doi:10.1007/bf00368800

Ritsema J, Heijst HJv, Woodhouse JH (1999) Complex Shear Wave Velocity Structure Imaged Beneath Africa and Iceland. Science 286 (5446):1925-1928. doi:10.1126/science.286.5446.1925

Royer JY, Gordon RG (1997) The motion and boundary between the Capricorn and Australian plates. Science 277 (5330):1268-1274. doi:10.1126/science.277.5330.1268

Royer JY, Sclater J, Sandwell D (1989) A preliminary tectonic fabric chart of the Indian Ocean. Proceedings of the Indian Academy of Sciences - Earth Planet Sciences 98 (1):7-24. doi:10.1007/bf02880373

Sager WW, Fullerton LG, Buffler RT, W. HD (1992) Argo Abyssal Plain Magnetic Lineations Revisited: Implications for the Onset of Seafloor Spreading and Tectonic Evolution of the Eastern Indian Ocean. Proceedings of the Ocean Drilling Program Scientific Results 123:659 – 669

Sandwell DT, Smith WHF (2009) Global marine gravity from retracked Geosat and ERS-1 altimetry: Ridge segmentation versus spreading rate. J Geophys Res 114 (B1):B01411. doi:10.1029/2008jb006008

Seton M, Müller RD, Zahirovic S, Gaina C, Torsvik T, Shephard G, Talsma A, Gurnis M, Turner M, Maus S, Chandler M (2012) Global continental and ocean basin reconstructions since 200 Ma. Earth Science Rev 113 (3-4):212-270. doi:10.1016/j.earscirev.2012.03.002

Shurbet L, Worzel. L (1955) Gravity Anomalies Associated with Seamounts. Geol Soc Am Bull 66 (6):777-782. doi:10.1130/0016-7606(1955)66[777:gaaws]2.0.co;2

Smith WHF, Sandwell DT (1997) Global Sea Floor Topography from Satellite Altimetry and Ship Depth Soundings. Science 277 (5334):1956-1962. doi:10.1126/science.277.5334.1956

Taneja R, O'Neill C, Lackie M, Rushmer T, Schmidt P, Jourdan F (2014) $^{40}Ar/^{39}Ar$ geochronology and the palaeoposition of Christmas Island (Australia), Northeast Indian Ocean. Gondwana Res. doi:http://dx.doi.org/10.1016/j.gr.2014.04.004

Trueman NA (1965) The phosphate, volcanic and carbonate rocks of Christmas Island (Indian Ocean). J of the Geol Soc of Aust 12 (2):261 - 283

Tucholke BE, Smoot NC (1990) Evidence for Age and Evolution of Corner Seamounts and Great Meteor Seamount Chain From Multibeam Bathymetry. J Geophys Res 95 (B11):17555-17569. doi:10.1029/JB095iB11p17555

Turcotte DL, Schubert G (2002) Geodynamics. 2 edn. Cambridge University Press, Cambridge

Veevers, J.J., 1971. Phanerozoic history of Western Australia related to continental drift. J of the Geological Soc of Australia, 18(2): 87-96.

Veevers JJ, McElhinny MW (1976) The separation of Australia from other continents. Earth Science Rev 12 (2-3):139-143

Veevers JJ, Powell CM, Roots SR (1991) Review of seafloor spreading around Australia. I. synthesis of the patterns of spreading. Aust J Earth Sciences: An Int Geoscience J of Geol Soc Aust 38 (4):373 - 389. doi:10.1080/08120099108727979

Vogt P, Tucholke B (1979) The New England seamounts: testing origins. Initial Rep Deep Sea Drill Proj 43:847-856

Walcott RI (1970)a Flexure of the lithosphere at Hawaii. Tectonophysics 9 (5):435-446. doi:http://dx.doi.org/10.1016/0040-1951(70)90056-9

Walcott RI (1970)b Flexural rigidity, thickness, and viscosity of the lithosphere. J Geophys Res 75 (20):3941-3954. doi:10.1029/JB075i020p03941

Watts AB (1978) An analysis of isostasy in the world's oceans 1. Hawaiian-Emperor Seamount Chain. J Geophys Res 83 (B12):5989-6004. doi:10.1029/JB083iB12p05989

Watts AB (1994) Crustal structure, gravity anomalies and flexure of the lithosphere in the vicinity of the Canary Islands. Geophys J Int 119 (2):648-666. doi:10.1111/j.1365-246X.1994.tb00147.x

Watts AB (2001) Isostasy and Flexure of the Lithosphere. Cambridge University Press, Cambridge

Watts AB, Bodine JH, Steckler MS (1980) Observations of Flexure and the State of Stress in the Oceanic Lithosphere. J Geophys Res 85 (B11):6369-6376. doi:10.1029/JB085iB11p06369

Watts AB, Cochran JR 1974. Gravity Anomalies and Flexure of the Lithosphere along the Hawaiian-Emperor Seamount Chain. Geophys J of the Royal Astro Soc 38(1): 119-141.

Watts AB, Cochran JR, Selzer G (1975) Gravity anomalies and flexure of the lithosphere: A three-dimensional study of the Great Meteor Seamount, northeast Atlantic. J Geophys Res 80 (11):1391-1398. doi:10.1029/JB080i011p01391

Watts AB, Ribe NM (1984) On geoid heights and flexure of the lithosphere at seamounts. J Geophys Res 89 (B13):11152-11170. doi:10.1029/JB089iB13p11152

Watts AB, ten Brink US, Buhl P, Brocher TM (1985) A multichannel seismic study of lithospheric flexure across the Hawaiian-Emperor seamount chain. Nature 315 (6015):105-111

Weigel W, Grevemeyer I (1999) The Great Meteor seamount: seismic structure of a submerged intraplate volcano. J Geodyn 28 (1):27-40. doi:http://dx.doi.org/10.1016/S0264-3707(98)00030-1

Weissel JK, Anderson RN, Geller CA (1980) Deformation of the Indo-Australian plate. Nature 287 (5780):284-291

Wessel P, Smith WHF (1991) Free software helps map and display data. Eos Trans AGU 72 (41):441-446. doi:10.1029/90EO00319

Whittaker JM, Williams SE, Müller RD (2013) Revised tectonic evolution of the Eastern Indian Ocean. G-Cubed 14:1891–1909. doi:10.1002/ggge.20120

Winterer EL (1998) Cretaceous karst guyots: New evidence for inheritance of atoll morphology from subaerial erosional terrain. Geology 26 (1):59-62. doi:10.1130/0091-7613(1998)026<0059:ckgnef>2.3.co;2

Winterer EL, Metzler CV (1984) Origin and subsidence of Guyots in Mid-Pacific Mountains. J Geophys Res 89 (B12):9969-9979. doi:10.1029/JB089iB12p09969

Woodroffe C (1988) Vertical movement of isolated oceanic islands at plate margins: evidence from emergent reefs in Tonga (Pacific Ocean), Cayman Islands (Caribbean

Sea) and Christmas Island (Indian Ocean). Zeitschrift fur Geomorphologie, Supplementband 69:17-37

Woodroffe CD, Falkland AC (1997) Chapter 31 Geology and hydrogeology of the Cocos (Keeling) islands. In: Vacher HL, Terrence MQ (eds) Developments in Sedimentology, vol Volume 54. Elsevier, pp 885-908. doi:http://dx.doi.org/10.1016/S0070-4571(04)80053-0

Woodroffe CD, Veeh HH, Falkland A, McLean RF, Wallensky E (1991) Last interglacial reef and subsidence of the Cocos (Keeling) Islands, Indian Ocean. Mar Geol 96:137-143

Zhao D (2001) Seismic structure and origin of hotspots and mantle plumes. Earth Planet Sci Lett. 192 (3):251-265

Chapter 5: Geochronology and Paleomagnetism*

Gondwana Research xxx (2014) xxx–xxx

Contents lists available at ScienceDirect

Gondwana Research

journal homepage: www.elsevier.com/locate/gr

$^{40}Ar/^{39}Ar$ geochronology and the paleoposition of Christmas Island (Australia), Northeast Indian Ocean

Rajat Taneja [a,*], Craig O'Neill [a], Mark Lackie [a], Tracy Rushmer [a], Phil Schmidt [b], Fred Jourdan [c]

[a] Department of Earth and Planetary Sciences, Australian Research Council Centre of Excellence for Core to Crust Fluid Systems/GEMOC, Macquarie University, Sydney, Australia
[b] CSIRO Earth Science and Resource Engineering, North Ryde, NSW, Australia
[c] Western Australian Argon Isotope Facility, JdL Centre & Dept. of Applied Geology, Curtin University, Perth, Australia

5.1: Abstract

The Christmas Island Seamount Province is an extensive zone of volcanism in the Northeast Indian Ocean, consisting of numerous submerged seamounts and flat-topped guyots. Within this region lies two subaerial island groups, Christmas Island, and the Cocos Keeling Archipelago. Christmas Island has experienced multiple episodes of volcanism that are exposed sporadically along its coastline. Here, we dated these volcanics using $^{40}Ar/^{39}Ar$ geochronology and analysed them for paleomagnetism. The oldest exposed volcanism occurred in the Eocene between 44 and 37 Ma. This is followed by a time gap of ~33 million years, before the eruption of a younger episode of Pliocene age (4.3 ± 0.2 Ma). It has, however, been suggested by previous workers that there is a much older Late Cretaceous event beneath the limestone which is unexposed. In addition, this study conducted the first paleomagnetic analysis of samples from Christmas Island to determine its paleoposition and the paleomagnetic polarity of the sampled sites. Two normal and two reversal magnetic events have been recorded, that agree with the geomagnetic reversal timescales. Late Eocene (39 – 37 Ma) paleomagnetic data suggests a paleolatitude of $-43.5°^{+9.0°}_{-11.2°}$, which is further south than

* This is a published paper in Gondwana Research and includes comments from the thesis reviewers.

paleolatitudes (around 30°S) derived from existing plate reconstruction models for the Australian Plate. However, the Late Eocene paleomagnetic data are limited (only two sites) and secular variation may not have been averaged out. During the Pliocene (ca. 4 Ma) we estimate a paleolatitude of approximately 13°S. The presence of the Late Eocene ages at Christmas Island correlates well with the cessation of spreading of the Wharton Ridge (~43 – 36.5 Ma), the initiation of spreading along the South East Indian Ridge, and the transit of Christmas Island over a broad low velocity zone in the upper mantle. This suggests that changes in stress regimes following the tectonic reorganisation of the region (prior to ~43 Ma) may have allowed deeper-origin mantle melts to rise. Similarly, changes in the plate's stress regime at the flexural bulge of the Sunda-Java subduction zone may be implicated in renewed melting at ~4Ma, suggesting that tectonic stresses have exerted a first-order effect on the timing and emplacement of volcanism at Christmas Island.

5.2: Introduction

5.2.1: Christmas Island Seamount Province (CHRISP)

The Northeast Indian Ocean is an understudied area, but the occurrence of large intraplate and subduction-zone earthquakes in the last ten years within the intraplate and subduction region of the Indo-Australian Plate and a recent scientific expedition have led to a re-emergence of geological interest (Abercrombie et al., 2003; DeMets and Royer, 2003; Hoernle et al., 2011; Hall, 2012; Yue et al., 2012). The Northeast Indian Ocean region is dominated by numerous submerged seamounts and two ocean islands whose origin has not received much attention until recently (Hoernle et al. 2011). The distribution of volcanism does not follow a linear hotspot model (Morgan, 1971). The region is dominated by numerous north-south trending fracture zones, but again, these do not seem to be exerting a fundamental control on the distribution of seamount volcanism, which predominantly trends east-west.

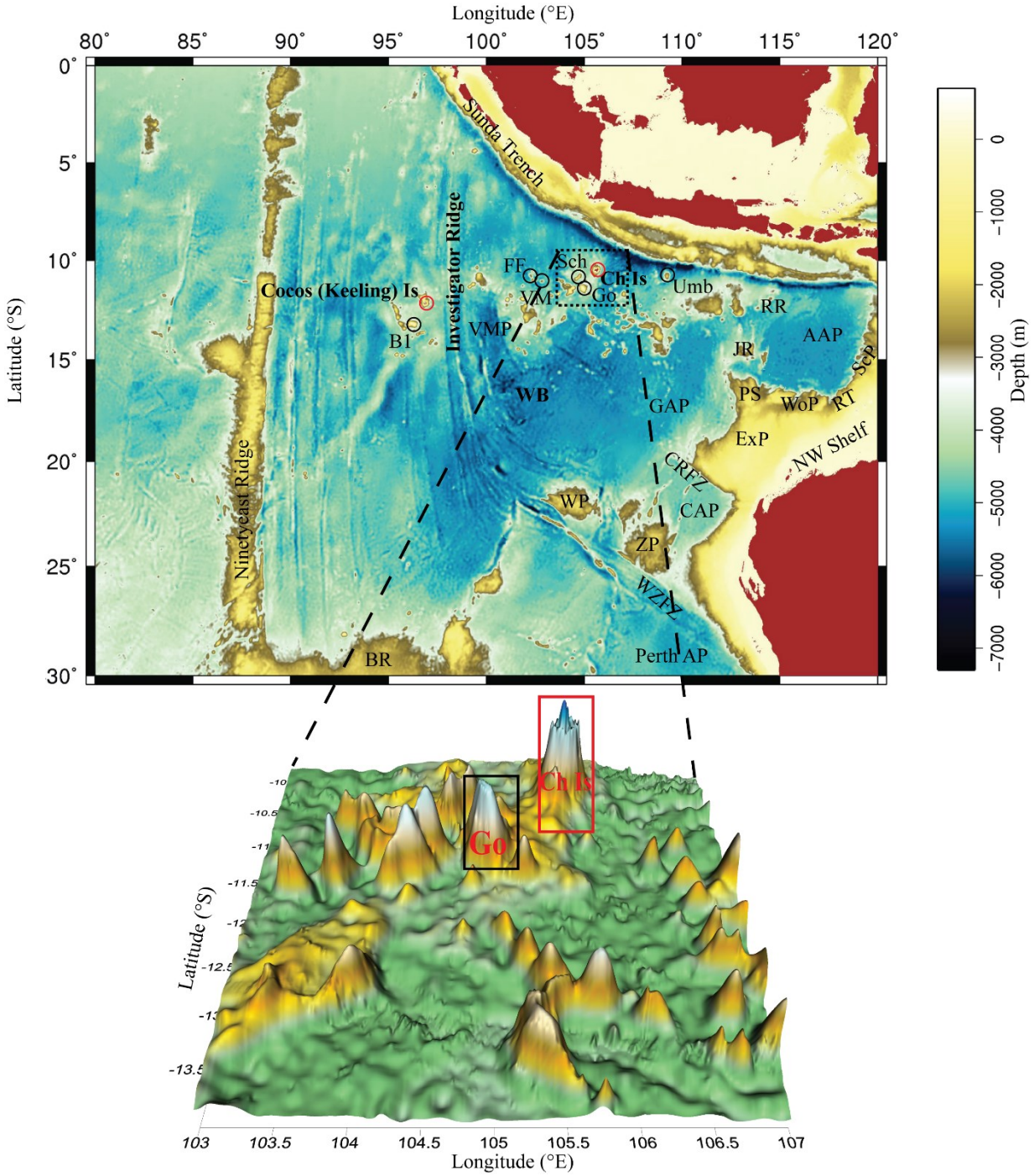

Figure 5.1: Regional bathymetry map of the Northeast Indian Ocean showing various tectonic features and the two islands (red circle) within the region. AAP, Argo Abyssal Plain; GAP, Gascoyne Abyssal Plain; CAP, Cuvier Abyssal Plain; Perth AP, Perth Abyssal Plain; RR, Roo Rise; JR, Joey Rise; ExP, Exmouth Plateau ScP, Scott Plateau; WoP, Wombat Plateau; PS, Platypus Spur; RT, Rowley Terrace; WP, Wallaby Plateau; ZP, Zenith Plateau; CRFZ, Cape Range Fracture Zone, WZFZ, Wallaby-Zenith Fracture Zone; VMP, Vening Meinesz Province; WB, Wharton Basin; BR, Broken Ridge. Ch Is, Christmas Island and Go, Golden Bo'Sunbird (85 Ma) seamount are represented in red and black rectangle. Other seamounts are FF, Flying Fish (70 Ma); VM, Vening Meinesz (72 Ma); Sch, Shcherbakov (~81 Ma); and Umb, Umbgrove (no age available).

The Northeast Indian Ocean is divided into various physiographic divisions as shown in Figure 5.1 comprising; The North West Shelf, Exmouth Plateau, Wombat Plateau, Argo Abyssal Plain, Cuvier Abyssal Plain, Gascoyne Abyssal Plain, and Platypus Spur. The North West Shelf is a continental margin extending from northern Australia to the Exmouth Plateau off the west coast that was formed due to multiple episodes of rifting and removal of continental fragments following the disintegration of Gondwana in the Late Cretaceous (Stagg et al., 1999; Heine and Müller, 2005; Gibbons et al. 2012). The Argo Abyssal Plain is located west of the North West Shelf in the easternmost corner of the Indian Ocean. It is surrounded by the Java Trench in the north, and the submerged continental crust of the Scott Plateau in the northeast, the Rowley Terrace in the east and the Wombat Plateau in the south. The Exmouth Plateau lies further south of the Wombat Plateau. The western edges of the Argo Abyssal Plain are separated by the Joey and Roo Rises north of Platypus Spur, and by the Gascoyne Abyssal Plain in the west. The Gascoyne Abyssal Plain is bounded by the Exmouth Plateau in the west, Cuvier Abyssal Plain in the south and the Java Trench in the north, with Argo Abyssal Plain in the east and Wharton Basin and Christmas Islands in the west. The Investigator Ridge, a roughly 1800 km long ridge trending north south along 98°E longitude is a distinctive feature of the Indo-Australian Plate. It can be seen prominently in bathymetric maps as a continuous linear ridge that extends from 7° - 18°S, beyond which it becomes patchy and broken before subducting underneath Sumatra as evident from Figure 5.1.

The most important characteristic features of the Northeast Indian Ocean are the numerous submerged seamounts, volcanic guyots and two sub-aerial islands. The Christmas Island Seamount Province (CHRISP) lies within the Northeast Indian Ocean, south of the Java Trench and between the Ninetyeast Ridge and the North West Shelf off the west coast of Australia (Figure 5.1). These volcanic edifices rise up to 3000 m below sea-level in a region where the abyssal plain depth ranges between 5500 and 6000 m. Most of these volcanic features occur within the latitudes 10°S and 15°S as a wide zone of seamounts rather than a linear volcanic chain. Some of the seamounts within the

region includes Golden Bo'Sunbird, Flying Fish, Bartlett, Vening Meinesz, Shcherbakov, and Umbgrove seamount.

The two sub aerially exposed island groups are the Cocos (Keeling) Archipelago, and Christmas Island. The Cocos (Keeling) Islands are a coral atoll archipelago consisting of 27 islands. There are no volcanic exposures on the islands (Woodroffe et al., 1991; Woodroffe and Falkland, 1997), nor were any encountered during the field trip to the island. Drilling and seismic surveys have, however, encountered a Pleistocene Limestone at a variable depth of 8 – 13m below the mean sea-level (Woodroffe and Falkland, 1997). Hoernle et al. (2011) dredged volcanic rocks at depths of 2400 - 3100 m that yielded Late Paleocene ages of 55.6 ± 0.2 Ma and 56.0 ± 0.2 Ma.

Christmas Island, on the other hand, is the sole island to have recorded sub-aerial intraplate volcanism, in the form of basaltic rocks that are exposed in some places on the island. Little published literature exists concerning Christmas Island's geology. There are few reports (Polak, 1976; Pettifer and Polak, 1979, Barrie, 1967) that deal with the geology, but they mostly concentrate on the phosphates of the island as it was once the main economic industry, and on the limestone and karst topography, primarily to delineate fresh water aquifers. Prominent amongst these are the works done by Andrew (1900) and Trueman (1965) on the geology of the island. There is a report of paleomagnetic analysis carried out at Christmas Island by the Bureau of Mineral Resources. This preliminary study was based on one sample per site to understand rock properties, and it suggested locations for detailed paleomagnetic investigations (Polak, 1976). We, therefore, conduct a detailed high resolution paleomagnetic analyses using a larger sample size to effectively constrain paleomagnetic evolution of Christmas Island, the only volcanically exposed representative of submarine volcanism in the region. Geology of the Island will be discussed in the following sub-section.

Hoernle et al. (2011) have put forward a mechanism describing the origin of the CHRIS Province. They proposed shallow recycling of continental lithosphere as a mechanism for volcanic generation of the CHRISP. They argue that decompressional melting of volatile rich Archean SCLM and MORB

source mantle lead to the formation of CHRISP near the MOR during the dispersal of Gondwana. In addition, Hoernle et al. (2011) suggested that the volcanic province was formed near the mid-oceanic ridge. They carried out $^{40}Ar/^{39}Ar$ age dating on dredged samples within the intraplate region, and found that they get younger towards the west. Ages between 136.2 ± 1.7 Ma in the Argo Abyssal Plain, and 46.7 ± 0.2 Ma in the west, south of Cocos (Keeling) Island have been yielded by Hoernle et al. (2011). The Eastern Wharton Basin contains ages in the range of 115.9 ± 3.8 Ma – 94.3 ± 0.3 Ma, while the Vening-Meinesz province is between 95.6 ± 1.4 - 63.5 ± 0.3 Ma.

Although there are numerous tectonic models for the evolution of the Northeast Indian Ocean and the western coast of Australia (Veevers, 1971; Heirtzler et al., 1978; Müller et al., 1998; Heine and Müller, 2005; Müller et al., 2008; Hall, 2012), none have integrated age constraints from volcanism in the area, with paleomagnetic constraints on the volcanic suite, to examine the causative mechanism of volcanism. In this paper, we present high resolution $^{40}Ar/^{39}Ar$ geochronology dating results to determine the ages and duration of volcanism on the island. In addition, this study presents a paleomagnetic analysis on the Christmas Island volcanics to determine the magnetic polarity of the lava flows, and compare these magnetic polarities with the geomagnetic timescale to constrain the reconstructed position of Christmas Island.

5.2.2: Geology of Christmas Island

Christmas Island is a roughly "T" shaped (Figure 5.2) limestone capped island that lies 400 km south of the Java Trench. Its present position is 105°E, 10.5°S and is 360 m above sea-level, rising 5700 - 5900 m from the bottom of sea floor. Christmas Island has been previously surveyed essentially for exploitation of its groundwater aquifers (Pettifer and Polak, 1979; Polak, 1976) and phosphate mining operations (Doak et al., 1965; Trueman, 1965). Large parts of the island are now a world heritage site due to its unique fauna, including the annual red crab migration (O'Dowd and Lake, 1989; O'Dowd and Lake, 1991).

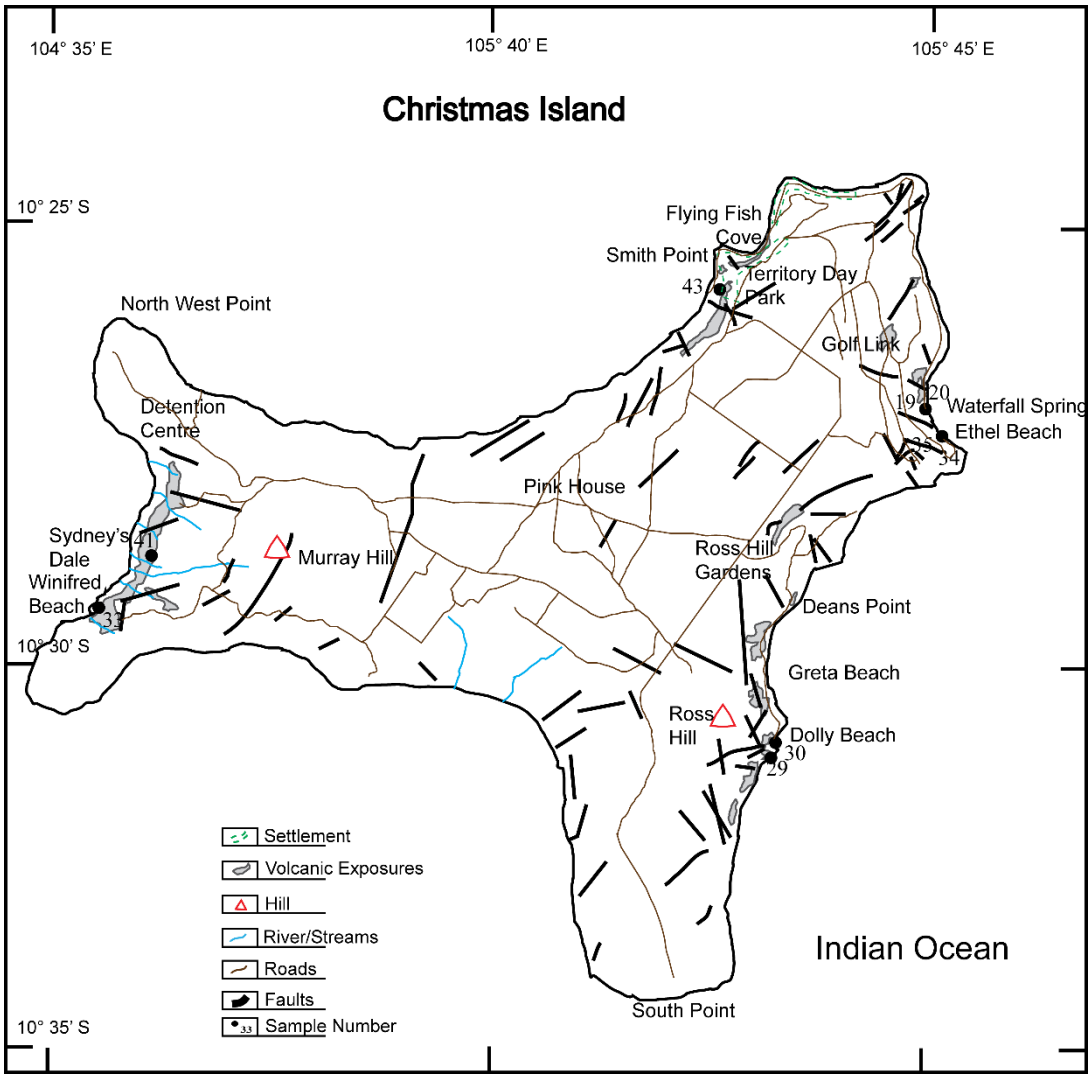

Figure 5.2: A map of Christmas Island showing the location of volcanic sites sampled for geochronology and paleomagnetism. Volcanic exposures and roads network re-drawn from maps provided by the Christmas Island National Park. Settlement area and drainage network modified from maps provided by the Christmas Island Tourism Centre. Structural details are re-drawn from Barrie (1967).

Barrie (1967) discussed the phosphates of the island with minor volcanic examination based essentially on visual and field observations. Earlier work on Christmas Island by Rivereau (1965), Polak (1976), Pettifer and Polak (1979), were primarily geomorphological and geophysical surveys carried out mainly for locating groundwater aquifers and karst topography. By visual examination of volcanic rocks and soils, Pettifer and Polak (1979) suggested in their unpublished report, that the main phase of volcanism ceased in the Early Cenozoic and the island became volcanically extinct in the Pliocene. The presence of these volcanic outcrops, therefore, makes this island significant in constraining the tectonic and volcanic evolution.

The island is believed to have been formed initially in the Late Cretaceous as an undersea volcano (Grimes, 2001). It now sits on the bulge of the Australian Plate subducting beneath the Sunda and Java Trenches which has led to its re-emergence above the sea-level (Grimes, 2001). Field studies of volcanic rocks at Sydney's Dale and Waterfall Spring suggests that the island was volcanically active in the Eocene but this had ceased by the Miocene (Barrie, 1967). Pettifer and Polak (1979) by visual examination of volcanic rocks and soils suggested, in their unpublished report, that the main phase of volcanism ceased in the Early Cenozoic and the island became volcanically extinct in the Pliocene. There is no evidence of any volcanic activity in the Oligocene on the island and it has been suggested as a period of erosion (Barrie, 1967). The rise of the island due to the island riding the flexural bulge on the subducting plate is estimated to be around 140 mm per thousand years (Woodroffe, 1988) and has been subjected to sea-level fluctuation in the recent past (Grimes, 2001).

Table 5.1: Main geological units at the Christmas Islands, Northeast Indian Ocean (Modified from Grimes, 2001).

Time Period	**Geological Description**
Quaternary	Phosphate deposits.
Pliocene (3-5 Ma)	Upper Volcanic Series, the youngest volcanism.
Late Oligocene- Mid Miocene	Upper Carbonate Series.
Eocene (35-40 Ma)	The Lower Volcanic Series, second episode of volcanism.
Eocene	Lower Carbonate Series.
Late Cretaceous-Early Cenozoic Volcanic	The core volcanic part, mostly submerged and the oldest.

Barrie (1967) has reported the occurrence of a phosphatised volcanic material near the highlands on the western part of the island, more specifically, close to the Murray Hill region. In addition, it has been suggested that the volcanic outcrops at Flying Fish Cove and Dolly Beach are a result of faulting or wave cutting and are pre Miocene to early Miocene in age (Barrie, 1967). Baxter and Weeks (1984) have reported the volcanism in Pliocene was accompanied by faulting near the Murray Hill region. Some of the sub-aerial deposits fill limestone depressions, which suggests that the island was partly emergent in Early Pliocene (Grimes, 2001). Using geophysical investigations, Polak (1976)

suggests the presence of rift zones to be responsible for a three pronged shape of the island. These rift zones partly cut deep erosion channels before the island emerged (Polak, 1976).

Works by Andrew (1900) and Trueman (1965) have documented three stages of volcanic eruptions with interbedded sequences of Tertiary limestone and phosphate rich soils. These interbeds have more specifically been exposed in the north near Flying Fish Cove and in the east close to Dolly Beach. The Late Cretaceous volcanic core of the island is buried, though earlier work has cited some exposures in the bottom of some limestone caves that are now being used for groundwater exploitation purposes, and are now inaccessible (Grimes, 2001). A Late Cretaceous phase of volcanism has been inferred from stratigraphic and faunal correlations (Grimes, 2001), and from flexural plate modelling (Taneja and O'Neill, 2014). It is overlain by basalts, basanites and trachytes of Middle to Late Eocene with limestones and dolomites (Table 5.1). The Pliocene phase of volcanism at the island occurs as minor volcanic dykes and tuffs that are overlain by phosphate rich soils.

5.3: Methodology and Analytical Techniques

5.3.1: Sample Collection

Samples were collected during the field trip to the island in November, 2010. The rock cores were obtained using a water-cooled two-stroke powered motor drill. Samples were drilled in the field and oriented using a magnetic and a sun compass as described by Butler (1992) and McElhinny and McFadden (2000). Each individual core measured 3 to 5 cm in length with a diameter of 2.5 cm. Of the sites sampled, three were on the east coast (Waterfall Spring, Ethel Beach and the Dolly Beach), two on the west coast (Winifred Beach and Sydney's Dale) and one site in the north (Flying Fish Cove) as shown in Figure 5.2 and Figure 5.3.

Figure 5.3: Outcrop photographs during sample collection at Christmas Island, A, Waterfall Spring (XM-19C and XM-20); B, Dolly Beach (XM-29 and XM-30B), the width of the volcanic exposure is 1.5 m; C, Ethel Beach (XM-34 and XM-35), the height of the volcanic exposure is 1 m; D, Sydney's Dale (XM-40).

The three east coast sites and one western site (Winifred Beach) were used for paleomagnetism. All of the above mentioned sites were drilled except the Sydney's Dale due to its protected status under the Ramsar Convention on Wetlands. These four sites and additional hand samples from Sydney's Dale and Flying Fish Cover have been dated using $^{40}Ar/^{39}Ar$ geochronology. Dolly Beach on the east coast contains a verti cally dipping basaltic dyke protruding through the shore, with a strike of ~45°, containing phenocrysts of olivine. The sub-horizontal sills at the base of the cliffs at Ethel Beach and Waterfall Spring are vesicular basalts. Winifred Beach and Sydney's Dale, the sampling sites on the west coast of the Island, outcrop inland and occur under a thick canopy of forest. Waterfall Spring and Ethel Beach are small outcrops spread across 3 - 5 m^2. Furthermore, the sampling sites on the east coast are located at the shore as compared to those on the west coast, which are at a higher elevation. All available volcanic rock exposures as discussed in literature (Trueman, 1965; Grimes, 2001) and marked on volcanic exposure GIS maps provided by the Christmas Island National Park

were visited and sampled. Only limited outcrop exposure was found in the central region of the Island near Murray Hill and it appeared to be a heavily phosphatised dyke. Since most of the island is a dense tropical forest under the management of Parks Australia and a phosphate mining hub, access to certain parts of the island was limited or not possible, affecting sampling in some areas. In addition, the onset of the famous red crab migration limited exploration in to the dense forest, and the ongoing construction activity hindered field sampling near Flying Fish Cove.

5.3.2: Geochronological Techniques

Six samples were selected from Christmas Island for $^{40}Ar/^{39}Ar$ dating and were separated into unaltered, 600 – 800 μm-size groundmass. Selected groundmass material (consisting of homogenous unoxidised pyroxene and plagioclase) was further leached in diluted HF for 1 minute and then thoroughly rinsed with distilled water in an ultrasonic cleaner. Separates of plagioclase crystals have been shown to provide more accurate results than groundmass, as it facilitates the optical selection of the freshest grains (e.g., Hofmann et al., 2000; Jourdan et al., 2007; Verati and Jourdan, 2013), but their small size in our samples prevented us from using this approach.

Samples were loaded into six large wells of 1.9 cm diameter and 0.3 cm depth aluminium disc. These wells were bracketed by small wells that included Fish Canyon sanidine (FCs) used as a neutron fluence monitor for which an age of 28.305 ± 0.036 Ma (1σ) was adopted (Renne et al., 2010). The discs were Cd-shielded (to minimize undesirable nuclear interference reactions) and irradiated for 2 hours in the Hamilton McMaster University nuclear reactor (Canada) in position 5C. The mean J-values computed from standard grains within the small pits range from 0.00068800 ± 0.00000220 to 0.00071000 ± 0.00000099 determined as the average and standard deviation of J-values of the small wells for each irradiation disc. The range of J factor for each of the samples are, 0.00069100 ± 0.00000200, Waterfall Beach; 0.00069100 ± 0.00000200, Dolly Beach; 0.00069100 ± 0.00000200 Winifred Beach; 0.00069100 ± 0.00000200, Ethel Beach; 0.00069100 ± 0.00000200 Flying Fish Cove, and 0.00071000 ± 0.00000099 Sydney's Dale. Mass discrimination was monitored using an

automated air pipette and is 1.004492 ± 0.29 (%1σ) per dalton (atomic mass unit), Sydneys Dale; 1.006116 ± 0.37 (%1σ), Dolly Beach, Flying Fish Cove, and Winifred Beach; 1.006078 ± 0.37 (%1σ), Ethel Beach and; 1.006127 ± 0.38 (%1σ), Waterfall Beach relative to an air ratio of 298.56 ± 0.31 (Lee et al., 2006). The correction factors for interfering isotopes were $(^{39}Ar/^{37}Ar)_{Ca} = 7.30x10^{-4}$ (± 11%), $(^{36}Ar/^{37}Ar)_{Ca} = 2.82x10^{-4}$ (± 1%) and $(^{40}Ar/^{39}Ar)_{K} = 6.76x10^{-4}$ (± 32%) (e.g., Jourdan and Renne, 2007). The samples were analysed 6 – 8 months after irradiation.

The $^{40}Ar/^{39}Ar$ analyses were performed at the Western Australian Argon Isotope Facility at Curtin University. The samples were wrapped in degassed niobium foil packages and step-heated using a 110 W Spectron Laser Systems, with a continuous Nd-YAG (IR; 1064 nm) laser rastered over the sample for 1 minute to ensure a homogenously distributed temperature. The gas was purified in a stainless steel extraction line using two SAES AP10 and one GP50 getter and a liquid nitrogen condensation trap. Argon isotopes were measured in static mode using a MAP 215-50 mass spectrometer (resolution of ~450; sensitivity of $4x10^{-14}$ mol/V) with a Balzers SEV 217 electron multiplier mostly using nine to ten cycles of peak-hopping. The data acquisition was performed with the Argus programme written by M.O. McWilliams and ran under a LabView environment. The raw data was processed using the ArArCALC software (Koppers, 2002) and the ages have been calculated using the decay constants recommended by Renne et al. (2010). Blanks were monitored every three to four steps and typical ^{40}Ar blanks range from 1×10^{-16} to 2×10^{-16} mol. Ar isotopic data corrected for blank, mass discrimination and radioactive decay are given in Appendix 1, Table 1. Individual errors (in Appendix 1, Table 1) are given at the 1σ and 2σ levels, while age and K/Ca (Figure 5.5) are given at 2σ level. Our criteria for the determination of plateau are as follows: plateaus must include at least 70% of ^{39}Ar. The plateau should be distributed over a minimum of three consecutive steps agreeing at 95% confidence level and satisfying a probability of fit (P) of at least 0.05. Plateau ages (Figure 5.5) are given at the 2σ level and are calculated using the mean of all the plateau steps, each weighted by the inverse variance of their individual analytical error. Mini-plateaus are defined similarly except that they include between 50% and 70% of ^{39}Ar. Inverse isochrons

include the maximum number of steps with a probability of fit ≥ 0.05. All sources of uncertainties are included in the calculation.

5.3.3: Paleomagnetic Laboratory Techniques

The drilled cores were cut into 2.2 cm individual core samples and used for paleomagnetic analysis. A select set of samples were demagnetised using an alternating-field progressive demagnetiser (Model 2G600) and another separate set of samples were thermally demagnetised using MMTD80 programmable thermal demagnetiser at CSIRO, North Ryde. The oven within the demagnetiser is surrounded by four layers of mu-metal shielding with a residual field of less than 10 nT. It is capable of heating up to 80 one inch samples automatically. Remanent intensities were measured using 2G Enterprise three-axis cryogenic magnetometer (Model 755). Alternating field demagnetisation was carried out in 14 demagnetisation steps mostly with increments of 5 - 10 mT up to maximum of 70 mT. Selected samples underwent thermal demagnetisation from 200°C in increments of 50° C up to 500° C, thereafter in increments of 5 - 20° C up to 570° C. Magnetic susceptibilities were measured using a Sapphire Instruments SI2B susceptibility instrument.

The demagnetisation steps with their inclinations and declinations were plotted on orthogonal vector diagrams. Magnetic remanence locked within the sample consists of a primary magnetic component, and often associated with it is later secondary magnetisation. This auxiliary magnetic character is acquired, in geological time, due to secondary processes like viscous acquisition or effects of stray fields from lightning. Metamorphism of the rock body, or alteration due to chemical reactions, can either leave secondary or later stage magnetic imprints. Interpretation of demagnetisation was done by preparing visually identifiable univectorial decay vectors on orthogonal vector plots, called orthogonal diagrams (Zijderveld, 1967), to determine the polarity and progressive demagnetisation. This helps in identifying the primary magnetic component, also called Characteristic Remanent Magnetisation (ChRM), and differentiating it from secondary components. Principal component analysis (PCA) was used in calculating mean directions and mean intensity of ChRM (Kirschvink,

1980). Fisherian analysis is used for calculation of mean inclination (I_m) and declination (D_m) for each site as shown in Table 5.4 and Table 5.5, using the software Paleomagnetic Tools (PMAGTOOL) V 4.2a, and an in-house software developed by Phil Schmidt, CSIRO. Mean inclination, of a sample can be used to calculate the paleolatitude by a simple relation,

$$\tan I_m = 2tan\lambda \quad 5.1$$

Where, λ, is the latitude of the paleosite.

5.4: Results

5.4.1: Petrology

Only fresh samples from Christmas Island were selected for geochronology, and in-situ sites were drilled for paleomagnetic analysis. The Dolly Beach site on the east cost of the island consists of a vertical basaltic dyke emerging from the coast. Petrographically (Figure 5.4), it contains a fine-grained groundmass (~70 vol.%) consisting of microliths of plagioclase (50 μm to 200 μm), glass, and opaque minerals. Phenocrysts of olivine (25 vol.%) and clinopyroxene (5 vol.%) form the remaining 30 vol.% of the sample. Phenocrysts of olivine vary from <50μm to several cm and are euhedral to subhedral. Magnetite inclusions (~10μm) occur in pyroxenes within the groundmass, and occasionally surrounding grain boundaries of olivine. Waterfall Spring and Ethel Beach are very similar petrographically, with a fine-grained groundmass (plagioclase, groundmass and opaque oxides) that comprises ~80 vol.%. of the sample. Plagioclase occurs as elongate euhedral to subhedral needles that are randomly oriented and range from 50 μm to over 100 μm. Phenocrysts of olivine (15 vol.%) are fractured (affected by serpentinisation), and are euhedral to subhedral (100 μm to 400 μm), while the remaining 5 vol.% comprises clinopyroxenes (50 μm - 200μm). Needle shaped magnetite (50 μm) are present within chromite.

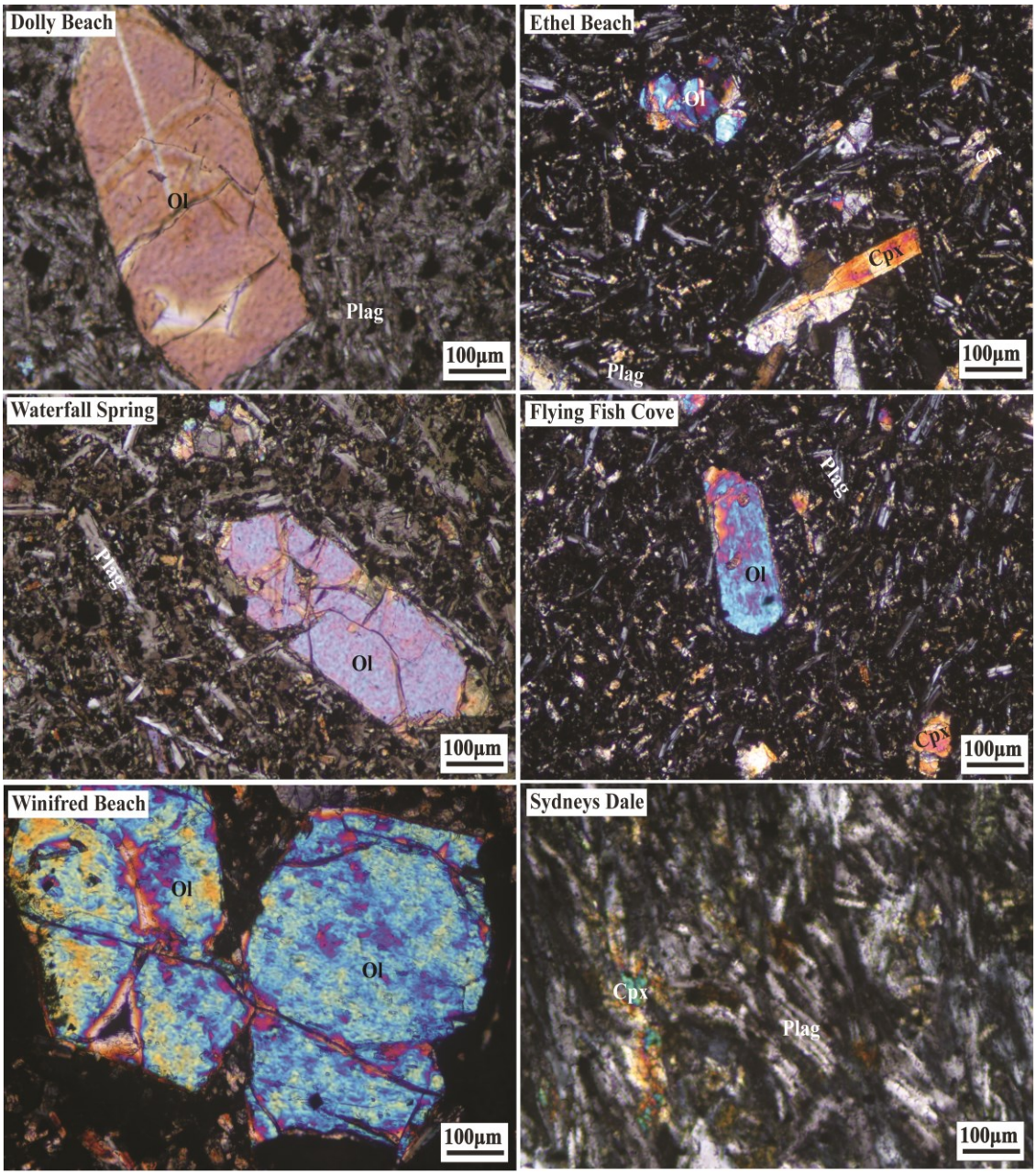

Figure 5.4: Petrological examination of volcanic rocks from Christmas Island. Primary mineralogy consists of phenocrysts of olivine and clinopyroxene, in a fine grained matrix comprising of plagioclase, glass, and opaque oxides. Modal abundance of groundmass in volcanic rocks from Christmas Island varies between 70% and 80%. Phenocrysts of olivine are euhedral to subhedral (~50 µm to several mm), while plagioclase occurs as needle like ranging from 50 µm to 300 µm. All photos taken in crossed polars.

Flying Fish Cove, on the north side of the island, consists of phenocrysts of olivine (150 µm to several cm), and minor clinopyroxene comprising total 30 vol.% of the sample, while the remaining part is fine-grained groundmass. Plagioclase averages 100 µm in size, and forms 80 vol.% of the groundmass volume, while 20 vol.% of the groundmass is glass and opaques, both occurring in equal proportions. Some sections of the sample have evidence of alteration that appears to have affected

grain boundaries of olivine. Winifred Beach samples exhibit a fine-grained groundmass of clinopyroxene (25 vol.%, 25 μm to 200 μm) that are euhedral to subhedral in shape. Plagioclase laths (60 vol.%, 25 μm to 150 μm) form the majority of the groundmass, together with minor opaques and glass (15%). Olivine is the primary phenocryst observed (~70 vol.% of the total phenocrysts), with minor clinopyroxene (~30 vol.%). Randomly oriented needle-like magnetite appear within the chromite. Sydney's Dale exhibits a characteristic trachyte texture of flow-oriented mineral grains. The samples are very fine grained, making it difficult to identify minerals, but the sample predominantly consists of oriented plagioclase (50 μm to 200 μm), with opaque and glass and rare clinopyroxene. Plagioclase appears to have undergone sericitic alteration, and glass and earlier mafic phases have altered to chlorite.

5.4.2: $^{40}Ar/^{39}Ar$ Geochronology

The step wise laser heating experiment for sample from Dolly Beach (XM-30B) gave a plateau age of 43.6 ± 0.4 Ma (MSWD = 1.4; P =0.14; Figure 5.5 A) including 99% of ^{39}Ar released. The K/Ca (Figure 5.5 A) (derived from $^{39}Ar_K$ and $^{37}Ar_{Ca}$) spectra shows a slight variation typically observed for basalt samples (McDougal & Harrison, 1999). The inverse isochron (Figure 5.5 A) gives an age of 43.5 ± 0.7 Ma (MSWD = 1.4; P = 0.14) and with a $^{40}Ar/^{36}Ar$ intercept of 300.8 ± 2.5, indistinguishable from the atmospheric ratio of 298.6 ± 0.3 (Lee et al., 2006) adopted in this study. This indicates that no excess argon is present in this sample, and hence we take the plateau age as indicating the time since the eruption of the magma.

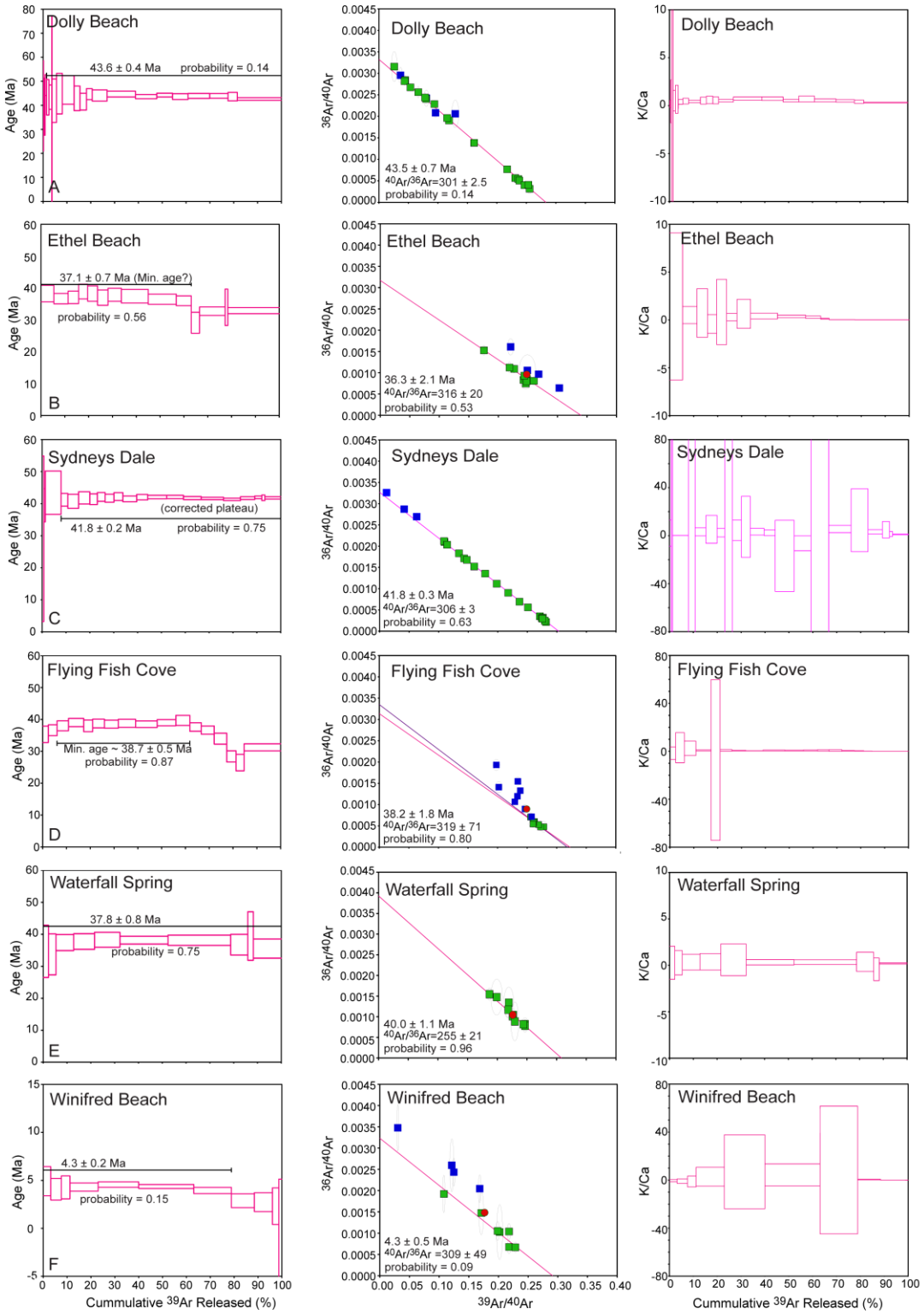

Figure 5.5: Age plateau (left), inverse isochron (center), and K/Ca (right) plot for the six sampling sites at Christmas Island. Uncorrected sample from Sydney's Dale did not produce an age plateau, but an age was obtained from Inverse Isochron (highlighted in bold), and a corrected sample yielded an age which is shown above. Squares in green are those used for age calculations. Ages in bold are the ages adopted in this study. Ages in italics are minimum ages.

Ethel Beach (XM-34) shows a two-level age spectrum suggesting that alteration perturbed this sample to some extent. A mini-plateau (minimum) age of ≥ 37.1 ± 0.7 Ma (MSWD = 0.86; P = 0.56) including 63% of the ^{39}Ar released, suggests that the effects of alteration were not extensive (Figure 5.5 B). The shape of the K/Ca spectrum match the shape of the age spectrum and shows a decrease of the K/Ca ratio toward high temperature steps (Figure 5.5 B). The inverse isochron yielded an age of 36.3 ± 2.1 Ma (MSWD = 0.9; P = 0.53) and a ^{40}Ar/^{36}Ar trapped ratio of 316 ± 20, indistinguishable from the atmospheric ratio. We conservatively interpret the plateau age as being a minimum age, albeit probably close to the eruption age of this sample.

Sample XM-41 at Sydney's Dale on the west coast did not yield a plateau age as the age spectrum shows a barely visible, but nevertheless individual, step age variation. However, it did yield a well-behaved inverse isochron age of 41.8 ± 0.3 Ma (MSWD = 0.85; P = 0.63) including 92% of cumulative ^{39}Ar and an intercept ^{40}Ar/^{36}Ar trapped value of 306.1 ± 3.4 (Figure 5.5 C). The ^{40}Ar/^{36}Ar value suggests that some excess ^{40}Ar* is present in the sample, but is fully accounted for in the inverse isochron age calculation (e.g. Sharp and Renne, 2005; Jourdan et al., 2012). As an exercise, we calculated a plateau age of 41.8 ± 0.2 Ma (MSWD = 0.75; P =0.75) using a ^{40}Ar/^{36}Ar value of 306.1 instead of 298.6 (Figure 5.5 C) but we retain the inverse isochron age for the discussion.

Table 5.2: ^{40}Ar/^{39}Ar analysis for six samples from Christmas Island; p, probability of fit (P) of at least 0.05; MSWD, mean square weighted deviation; * calculated using the measured ^{40}Ar/^{36}Ar intercept ratio. Age in bold are the age adopted in this study. Ages underlined and accompanied with the sign ≥ are minimum ages.

Sample No.	Location	Plateau Age				^{39}Ar(k) released (%)	Inverse Isochron			^{40}Ar/^{36}Ar	
		Age	2σ	MSWD	p		Age	2σ	MSWD	Intercept	2σ
XM-30B	Dolly Beach	**43.6**	**0.4**	1.37	0.14	99	43.5	0.7	1.38	301	2.5
XM-34	Ethel Beach	≥37.1	0.7	0.86	0.56	63	36.3	2.1	0.88	316	20
XM-41	Sydney's Dale	41.8	0.2*	2.01	0.75	92	**41.8**	**0.3**	0.85	306	4
XM-43	Flying Fish Cove	≥38.6	0.5	0.48	0.87	56	38.2	1.8	0.54	319	71
XM-19C	Waterfall Spring	**37.8**	**0.8**	0.65	0.75	100	39.9	1.1	0.3	255	21
XM-33D	Winifred Beach	**4.3**	**0.2**	1.56	0.15	79	4.3	0.5	1.85	309	49

The results for the sample from Flying Fish Cove (XM-43) near the north shore of the island, however, shows a more disturbed age spectrum (Figure 5.5 D). Such a spectrum with decreasing apparent ages at high temperature is characteristic of an alteration overprint (Koppers et al. 2000), where the effects of alteration (usually neo-crystalized K-rich phases) on apparent step ages are more apparent on K-poor domains compare to K-rich domains. A contribution from alteration cannot be excluded from the low temperature steps and probably lowers the age of the mini-plateau. It only provides qualitative constraints for the age of this sample, with a minimum age of ≥ 38.6 ± 0.5 Ma (MSWD = 0.48; P = 0.87) as given by a mini-plateau including 56 % of the ^{39}Ar released. The K/Ca spectrum show little compositional zoning in the sample (Figure 5.5 D). The inverse isochron shows only little spread, but the trapped ratio (319 ± 71), although imprecise, seems to suggest that no excess ^{40}Ar* is present.

Waterfall Spring (XM-19) yielded a plateau over 100% of the ^{39}Ar released and gave an age of 37.8 ± 0.8 Ma (MSWD = 0.65; P = 0.75, Table 5.2). The K/Ca spectrum suggests little zoning in this sample (Figure 5.5 E). The inverse isochron has a small spreading factor preventing an estimate of the proper age and intercept value (Figure 5.5 E).

Winifred Beach (sample XM-33) on the other hand is the youngest sample, and gave a plateau age of 4.3 ± 0.2 Ma (MSWD = 1.56; P = 0.15) including 79% of cumulative ^{39}Ar (Figure 5.5 F). The age spectrum shows that the step ages get slightly younger over the last 21% of the age spectrum, possibly due to minor alteration. The breadth of the plateau suggest that it is not affected by any secondary process, and we interpret the ^{40}Ar/^{39}Ar plateau age as indicating the eruption age of this sample. The inverse isochron yielded an imprecise intercept ^{40}Ar/^{36}Ar ratio of 309 ± 49, indistinguishable of atmospheric composition. The K/Ca ratio suggests that very little Ca was present in this sample and there is more glass and groundmass. Even though there are large error in K/Ca for the steps used for age calculation, the last three steps (with low error values) are influenced by alteration (see Section 5.4.1). They thus cannot be used for age calculation. In addition, the last three steps do not fit the ^{40}Ar/^{39}Ar intercept and hence give little reliable information for age calculation.

5.4.3: Paleomagnetic analysis

The Koenigsberger ratio (Q) is the ratio of the remanent magnetization to the induced magnetization (product of susceptibility and the Earth's magnetic field strength). It is an effective parameter to provide an indication of the significance of remanence magnetism. A large Q implies that the magnetic material will tend to retain significant remanent magnetization and hence is a strong magnetic recorder. Nakanishi and Gee (1995) calculated the Q values for north-western Pacific guyots and concluded that these are reliable enough for paleolatitude determination. The Koenigsberger ratio (Q ratio) mathematically, is defined as:

$$Q = \frac{NRM}{k*H} \qquad 5.2$$

Where, NRM, is the remanent magnetism measured before AF demagnetisation; k is the susceptibility; H is the total magnetic field at Christmas Island. Both remanent and field intensities are measured in units of A/m.

Relatively high Q values for most of the samples as shown in Table 5.3 make them suitable for paleomagnetic analyses. The orthogonal projections displaying magnetic vector components are the most common tool to determine and analyse paleomagnetism properties by selecting vector end points that decay univectorially towards the origin as shown in Figure 5.6 and Figure 5.7. The Ethel Beach (XM-35) and Waterfall Spring (XM-20) sampling sites are located on the east coast, and are ~300 m apart. The assumed primary ChRM for both the sites is resolvable after 10-15 mT demagnetisation steps. Both sites have a mean declination that is northwards with a steep inclination of -57.2° and -65.5° (directed upwards) respectively. The two sites being in close proximity of each other and their similar geochronology age imply that both of the sites have recorded the same event of magnetism and magma solidification.

Dolly Beach (XM-29) on the east coast has a steeper inclination of 77.6° that points down, opposite to Waterfall Spring and Ethel Beach. Stereographic projection (Figure 5.6) shows a declination centred near the south. Winifred (XM-33), on the west coast is the youngest at ~4.3 Ma and has a

primary magnetism pointing east-southeast in the down direction. The inclination points in the same direction as the oldest site (XM-29); it is, however, opposite to Waterfall Spring and Ethel Beach (Figure 5.6). Samples from Winifred Beach were demagnetised thermally in addition to AF-demagnetisation (Figure 5.7). This proved to be more effective in resolving the characteristic component of up to 500°C. Beyond this temperature erratic behaviour was observed for thermally demagnetised specimens indicating that the samples had been demagnetised.

Table 5.3: Koenigsberger ratio (Q) for paleomagnetic samples from Christmas Island. The total magnetic field at Christmas Island is 46800 nT. The high intensity for Winifred Beach represents minimum value measured and could be stronger, thus their Q values could be higher, while the Q values for other sites are well within the ranges measured by 2G and are precise.

Location	Sample	Susceptibility, SI	NRM (mA/m)	Q
Winifred Beach	XM-33A2	0.011453	17796.32	42.43
	XM-33B2	0.010422	18807.59	49.27
	XM-33B3	0.010578	17928.37	46.28
	XM-33C2	0.011421	16877.63	40.35
	XM-33E2	0.011066	17647.42	43.54
	XM-33A1	0.011736	17794.71	41.40
	XM-33B1	0.010502	16859.29	43.83
	XM-33C1	0.011474	17079.56	40.64
	XM-33D1	0.010575	18867.6	48.72
	XM-33E1	0.011084	18222.28	44.89
Waterfall Spring	XM-20C2	0.001298	1071.77	22.55
	XM-20A1	0.001312	1343.00	27.95
	XM-20C1	0.001188	1097.00	25.22
	XM-20D1	0.002269	2926.16	35.22
Dolly Beach	XM-29B2	0.005275	8278.63	42.85
	XM-29C2	0.005293	4281.45	22.09
	XM-29B1	0.005786	7052.01	33.28
	XM-29C1	0.005687	8206.05	39.40
	XM-29D1	0.012293	9698.66	21.54
Ethel Beach	XM-35A1	0.003156	8210.56	71.04
	XM-35B1	0.002556	4146.05	44.30

Furthermore, two sites (Dolly Beach and Winifred) have positive inclinations. Assuming a southern hemisphere origin of these volcanics, this denotes that the Earth's magnetic polarity reversed while magnetism was locked within these sites.

These are very large errors associated with some of the site VGP's in the paleomagnetic analysis and hence appear doubtful if these can be used effectively to find paleoposition (e.g. Ethel Beach and

Dolly Beach have dp and dm of 25.0 and 34.4, and 23.0 and 24.5, Table 5.4). Antretter et al. (2002) conducted paleomagnetic investigations for the central and northern Kerguelen Plateau, and obtained α_{95} in the range of 1.9° – 7.8°, giving dp and dm of 2.2 and 2.9, and 7.4 and 10.8 respectively, much lower than those obtained in this study. Therefore, a combined position was obtained for the Eocene volcanism at Christmas Island (Table 5.5) by combining all the Eocene dates. In addition, the Fisher mean of the individual fisher means (means of the three Eocene VGP sites) was calculated to constrain the errors (Table 5.5).

Table 5.4: Summary of paleomagnetic results of four sites from Christmas Island. D_m°, I_m° represents mean declination and mean inclination respectively; α_{95}°, semi-angle of cone of 95% confidence about mean direction; k, Fishers precision parameter, n, number of specimen in a site; λ° represents the paleolatitude; dp and dm, are the errors associated with the pole.

Site	Age (Ma)	D_m°	I_m°	α_{95}°	k	n	Paleo latitude (λ°S)	Paleolat. error		VGP Pole		Error	
								+	-	Lat °	Long °	dp	dm
Waterfall	37.8 ± 0.8	8.8	-65.5	5.8	255.7	4	47.6	7.1	-8.3	52.1	275.8	7.6	9.4
Ethel	37.1 ± 0.7	354.7	-57.2	23.5	28.5	3	37.8	19.4	-34.1	62.2	294.5	25.0	34.3
Dolly	43.5 ± 0.4	162.2	77.6	13.1	35.0	5	66.2	22.3	-19.9	-32.9	113.9	23.0	24.5
Winifred	4.3 ± 0.2	137.3	24.7	19.2	23.6	4	12.9	12.8	-10.2	-48.1	187.7	11.0	20.6

Table 5.5: Summary of paleomagnetic results by combining the Eocene sites from Christmas Island to determine a single pole position. Abbreviations are same as Table 5.4.

Site	D_m°	I_m°	α_{95}°	k	n	Paleo latitude (λ°)	Paleolat. error		Pole Lat°	Pole Long °	dp	dm
							+	-				
Waterfall+ Ethel Beach	1.7	-62.2	8.3	54.5	7	-43.5	9.0	-11.2	56.9	283.2	10.0	12.9
Eocene Phase	11.4	-78.2	12.9	12.2	12	-67.3	20.0	-20.3	-32.6	280.3	22.9	24.4
Mean of 3 VGP's (W+E+D)	357.4	-67.0	17.1	52.9	3	-49.7	19.0	-28.7	-50.7	288.1	23.4	28.3

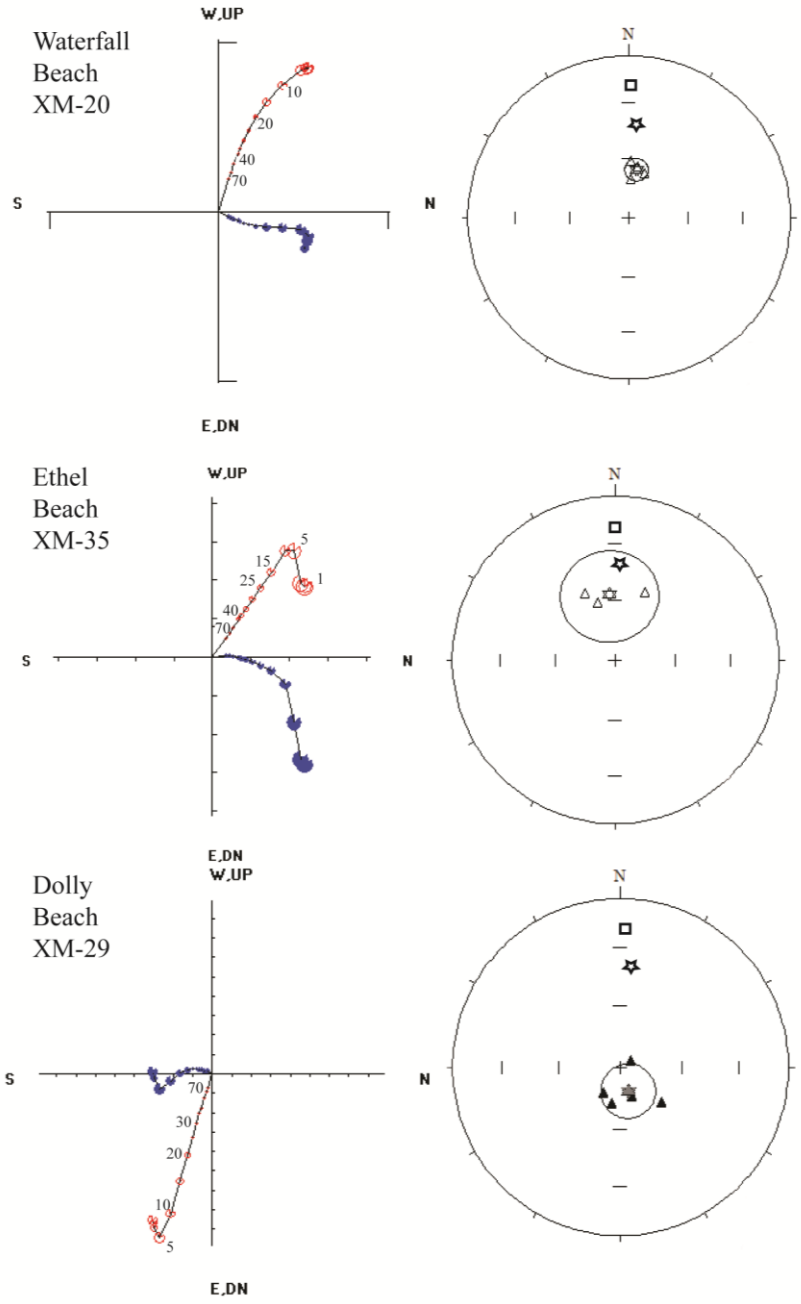

Figure 5.6: Representative orthogonal vector plots (left) and site stereonet plots (right) illustrating demagnetisation. Blue (solid) data points are projected onto the horizontal plane, red (open) data points are projected onto vertical plane. First tick point on orthogonal vector plot represents 1000 mA/m. Black star (within stereonet) is the present magnetic field, D=1.5°, I=-39° and the Black square is the dipole field at Christmas Island. Curved demagnetisation at Waterfall Beach is due to overlapping of secondary and primary magnetisation, while there is no overlapping between the two magnetic events at Ethel Beach resulting in a sharp bend. Secondary magnetisation can be isolated by applying low intensity demagnetisation.

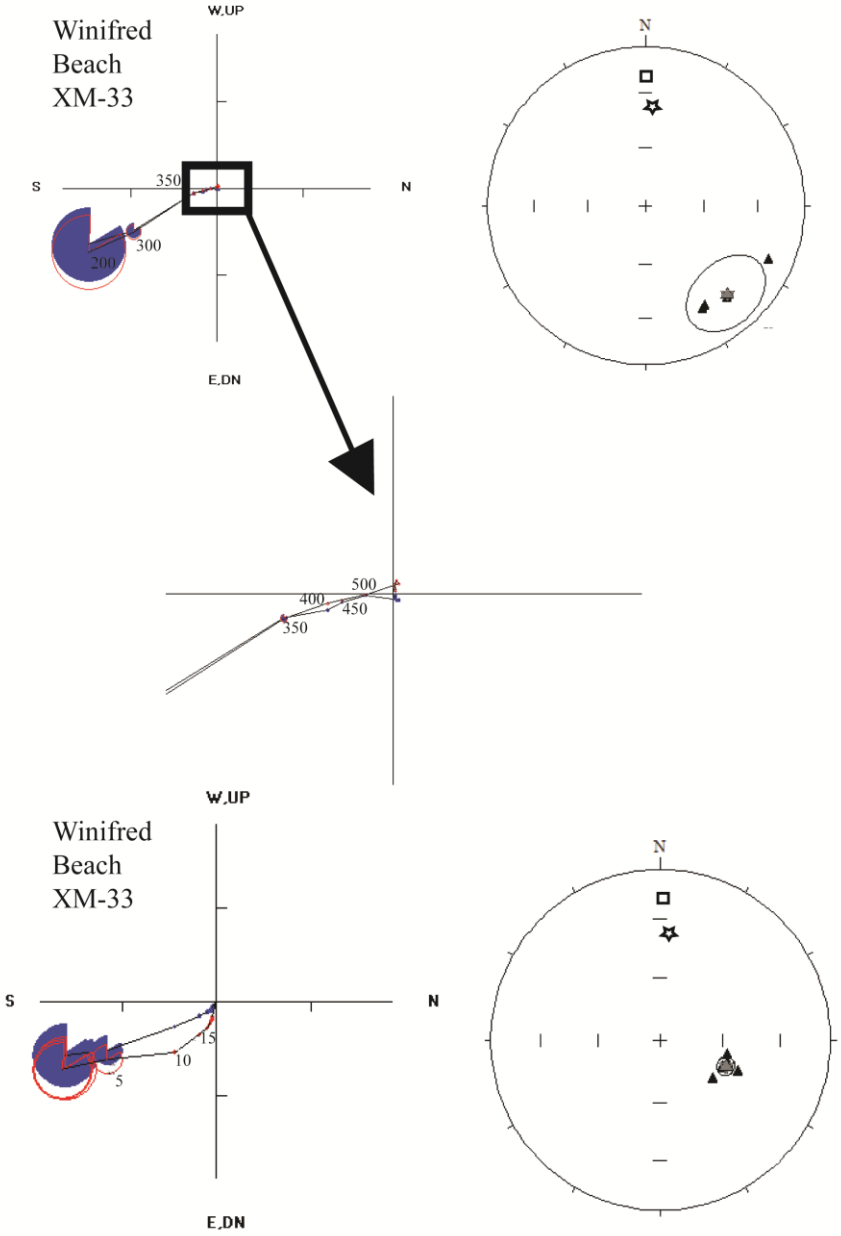

Figure 5.7: Representative orthogonal vector plot (top left) and site stereonet plot (top right) and a close up of orthogonal vector diagram (middle) illustrating thermal demagnetisation level up to 570°C for Winifred Beach. Representative orthogonal vector plot (bottom left) and site stereonet plot (bottom right) for Winifred Beach obtained using AF-demagnetisation. First tick on orthogonal vector plot represents 1000 mA/m. Blue (solid) data points are projected onto the horizontal plane, red (open) data points are projected onto vertical plane. Black star (within stereonet) is the present magnetic field, D=1.5°, I=-39° and the Black square is the dipole field at Christmas Island.

5.5: Discussion

5.5.1: Duration of volcanism

$^{40}Ar/^{39}Ar$ geochronology shows multiple stages of volcanism at Christmas Island. Two suites of volcanism at the island have been dated and identified, an older Lower Volcanic Suite (LVS), and a younger Upper Volcanic Suite (UVS) (Figure 5.8). The oldest ages within the LVS are found at Dolly Beach on the east coast and Sydney's Dale on the west coast. We believe that this volcanism initiated in the Middle Eocene between 42 and 44 Ma. Further on, Late Eocene (~38 - 39 Ma) volcanism is evident at Waterfall Spring and Ethel Beach on the east coast, and Flying Fish Cove in the north. Hoernle et al. (2011) conducted $^{40}Ar/^{39}Ar$ geochronology analyses that yielded a lowest age of 37.0 ± 0.6 Ma, and an oldest age of 43.6 ± 0.4 Ma. Hoernle et al. (2011) also obtained intermediate ages of 39.6 ± 0.4 Ma, 40.2 ± 0.2 Ma, 41.1 ± 0.1 Ma and 42.6 ± 0.4 Ma. Combining ages from this study and those obtained by Hoernle et al. (2011), it appears that volcanism on the island was continuous from 44 Ma to 37 Ma.

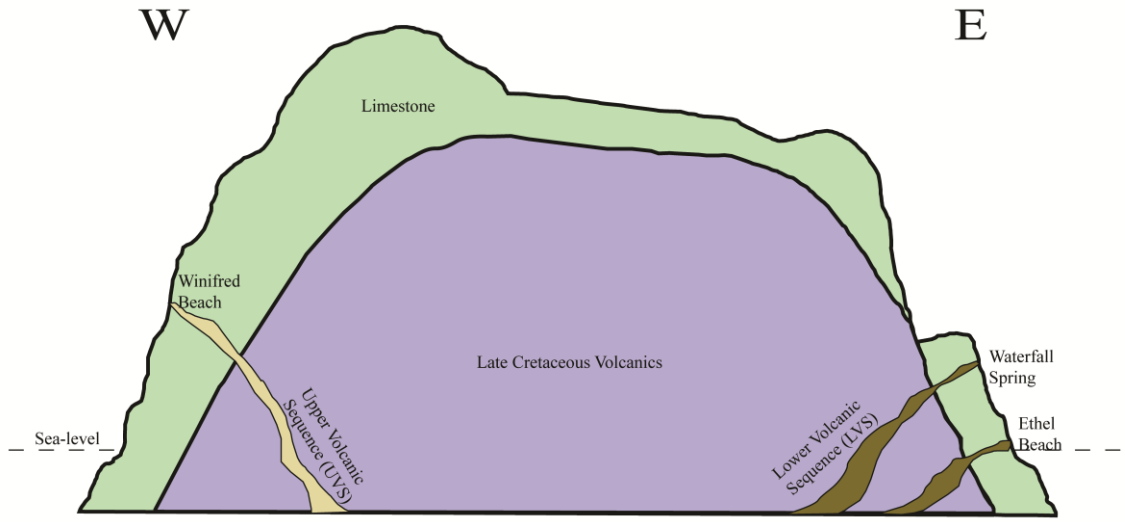

Figure 5.8: A proposed diagrammatic vertically exaggerated (x10) west to east cross section of Christmas Island showing the main submerged Late Cretaceous volcanic and LVS and UVS. There is a lower volcanic sequence outcropping on the west coast at Sydney's Dale but has not been shown in this section, modified from Grimes, 2001.

The last and final episode of volcanism at the island started after a time gap of ~33 Myr in the Early Pliocene at 4.3 ± 0.2 Ma. Hoernle et al. (2011) yielded similar young ages in the range of 4.5 ± 0.2 – 4.3 ± 0.1 Ma. New high resolution geochronology dating of the basaltic rocks obtained from this study and those dated by Hoernle et al. (2011) confirms two dated episodes of volcanism at the island, and it strongly contradicts a middle phase in the Miocene as argued by Barrie (1967). A Late Cretaceous volcanic core of the island is, however, not exposed hence no dates are available for it. However, stratigraphic studies on interbedded limestones on the Island (Grimes, 2001), and recent plate flexural modelling (Taneja and O'Neill, 2014) have suggested a Late Cretaceous volcanic episode, which led to elastic loading of the young oceanic lithosphere around 88 –75 Ma.

5.5.2: Petit spot low volume volcanism

Low volume "petit spot" volcanism formed away from the mid oceanic ridge and subduction zones has been recently described off the north-western Pacific Plate (Hirano et al., 2001, 2006). Hirano et al. (2008) calculated the volume of these petit spot monogenetic volcanoes and suggested that these are usually <1 km^3. These are further differentiated on the basis of acoustic reflectivities with the petit spot features having a higher reflectance than those compared to the older and much larger submarine volcanoes (Fujiwara et al., 2007).

Oceanic lithosphere behaves as an elastic sheet when loaded, for stresses below its intrinsic yield stress (Bodine et al., 1981; Watts, 2001). Hirano et al. (2001, 2006) while discussing the petit spot intraplate volcanism at Hokkaido Rise, in the northwest Pacific Ocean suggested that these were formed due to fracturing within the flexed outer rise of the lithospheric bulge. The flexure induced by bending of the plate as it approaches a subduction zone causes redistribution of internal stresses leading to fracturing of the lithosphere that may cause decompression melting in subjacent asthenospheric mantle, potentially allowing the ascent of small volumes of melt in nascent cracks (Hirano et al., 2001). Konter and Jackson (2011) suggested decompressional melting and cracking of the plate to have led to rejuvenation of volcanism in the Samoan Islands that are in a similar

tectonic setting at Hokkaido Rise and the northern plate boundary of the East Indian Ocean. The Indo-Australian Plate in the region below the Java and Sunda Trench is undergoing subduction and demonstrates flexure on the outer rise of the subducting plate (Levitt and Sandwell, 1995; Smith and Sandwell, 1997). A cross section of such a flexure produced along a line perpendicular to the trench passing through the island is shown in Figure 5.9. The flexure produced by the load of Christmas Island is overprinted on the crest of the flexed lithosphere as it subducts at the trench. A similar local flexure is produced by Golden Bo'Sunbird, a seamount, south west of Christmas Island as shown in Figure 5.9.

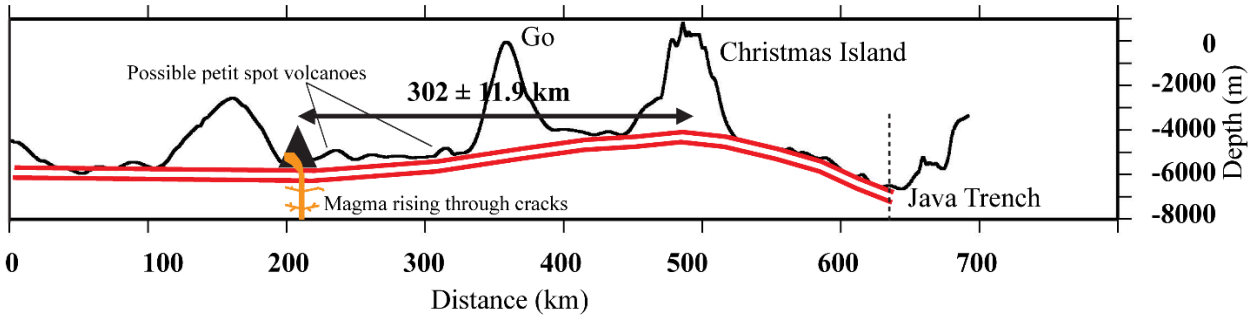

Figure 5.9: Back tracking the position of Christmas Island and associated Pliocene volcanism at the seaward side of the outer rise of the subducting trench. Black line represents the profile of the oceanic lithosphere in a NE-SW section perpendicular to the trench, red line showing the bending and flexing of the lithosphere. Golden Bo'Sunbird and two small seamounts (SW of Christmas Island) represent petit spot features produced due to flexure.

Magma flow rising through these cracks reaches the surface in the form of petit spot volcanism. The younger episode of volcanism on Christmas Island may share some characteristics with these low-volume eruptions. Even though there are no constraints on the volume of volcanism at Christmas Island, as it is covered by thick sequences of limestone, the exposure of the Pliocene phase of volcanism at Winifred Beach on the west coast of the island, emplaced through the older volcanic core and limestone cliffs and terraces, bears similarity to this petit spot model. Field mapping carried out at the island (near Murray Hill), and studies conducted by Baxter and Weeks (1984) suggest that volcanism around the Murray Hill was accompanied by faulting which led to volcanic vents, fractures, and dykes. Hoernle et al. (2011) sampled Pliocene volcanism at the island and this study

has sampled one location on the Island. The limited occurrences of the younger phase of volcanism, far less than the older dated samples, and its association with faulting and emplacement as dykes suggest that this is a small phase.

Additionally, if the Pliocene phase of volcanism is indeed produced due to flexure, then the onset of volcanism should correlate with the onset of flexure, which can be determined from present observations of the forebulge morphology, using plate reconstructions and past plate velocities. To determine the paleoposition of the erupted younger volcanics, we backtracked the island from its present position at 10.5°S using a plate motion rate of 7 cm/yr (Tregoning et al., 1994). Tracing the island back to its position at 4.32 ± 0.17 Ma, we calculate its reconstructed position 302 ± 11.9 km (12.70° – 12.85°S) southwest of its present day location as shown in Figure 5.9. Two additional small volcanic features are present between the point of lithospheric cracking, and Golden Bo'Sunbird seamount. These two features might represent petit spot volcanic features documented by Hirano et al. (2001) for which additional dredging expeditions should be carried out. This, however, is beyond the scope of the current study.

Hirano et al. (2006) report petit spot volcanism could represent a new intraplate type volcanic setting. They, along with Buchs et al. (2013), are of the opinion that petit spot volcanism has been inadequately sampled, compared to other known volcanic islands in the Pacific and elsewhere, and that this volcanic setting could be more common than previously thought, and it also presents a tremendous scope for further geophysical, geochemical and geodynamic investigations.

5.5.3: Magnetic polarity and paleoposition

The Eocene epoch has been marked by magnetic reversals and paleomagnetism analysis can uncover changes in magnetic polarity locked within a rock. This study matched magnetic polarity and geochronological ages with Cande and Kent's (1995) and Wei's (1995) Geomagnetic Polarity Time Scale (GPTS) in a comparison with Earth's paleomagnetic field record. Dolly Beach with an age of 43.6 ± 0.4 Ma has positive inclination (Table 5.4) implying a reverse paleomagnetic field. Dolly

Beach falls within polarity chron C20n - C20r as summarised in Table 5.6. Waterfall Spring and Ethel Beach with an age of 37.8 ± 0.8 and 37.1 ± 0.7 Ma respectively have normal polarity (present day). Winifred Beach with an age of 4.3 ± 0.2 Ma has a reverse polarity as evident from positive inclination in stereographic projection in Figure 5.7 and Table 5.4 and Table 5.6.

Table 5.6: Magnetic polarity of the four sampling sites from Christmas Island and their comparison with the Geomagnetic Polarity Time Scale (Cande and Kent, 1995).

Location	**Sample No.**	**Age (Ma)**	**Polarity**	**Magnetic Chron (Cande and Kent, 1995)**	**Magnetic Chron (Wei, 1995)**
Dolly	XM-29	43.6 ± 0.4	Reverse	C20n - C20r	C20n - C20r
Waterfall	XM-20	37.8 ± 0.8	Normal	C17n.1n - C17n.2n – C18n.1n	C17n.1n - C17n.2n – C18n.1n
Ethel	XM-35	37.1 ± 0.7 (min age)	Normal	C16n.2r - C17n.1n – C17n.2n	C16n.2n - C17n.1n – C17n.2n
Winifred	XM-33	4.3 ± 0.2	Reverse	C2An.3r-C3n.2n (Gilbert)	C2An.3r-C3n.2n (Gilbert)

Paleomagnetic investigations for Dolly Beach and Waterfall Spring have very steep inclinations, and this indicates a high paleolatitude for these sites. Polak (1976) found similar high inclinations for two of the three sites where measurements were taken. An inclination of -65.5° has been reported for Waterfall Beach and 67.9° for Dolly Beach - similar and comparable to our analysis. The third site on the west coast near Winifred Beach has a low inclination of 16.1°. The magnetic polarity of both the data is similar. Polak (1976) has, however, not given details regarding the paleomagnetic analysis of these samples. The results are based on just one sample per site and it is not clear if drilled, or in-situ samples were used for these calculations - lumps and chips have been mentioned while describing some rock properties.

Paleomagnetic analyses of the Ethel Beach, Waterfall Spring and Dolly Beach have given a VGP latitudes of $-37.8°^{+19.4°}_{-34.1°}$, $-47.6°^{+7.1°}_{-8.3°}$, and $-66.2°^{+19.9°}_{-22.3°}$ respectively. There are large error associated

with individual site VGP's, hence the average of the Eocene volcanism was calculated as shown in Table 5.5. By doing this, multiple flows of lava are generally included within the combined data and are more effective in averaging any secular variation experienced while the basaltic body cooled. The pole calculated from combining the results can only be considered to be a virtual geomagnetic pole (VGP). The paleolatitude is therefore not tightly constrained and can only be taken as indicative. While we tried to maximise the sampling of volcanic flows a lack of suitable outcrops limits the statistical averaging of the VGPs. The same can be said for Winifred Beach where the single flow sampled may record a transient field during a reversal. The combination of Fisher means of the 3 VGP sites (Table 5.5) gives a combined paleolatitude of $-49.7°^{+19.0°}_{-28.7°}$ (with a full range of paleolatitude between -30.47° and -78.4°) This position is further south than the reconstructed position of the Island, using reconstruction models of Seton et al. (2012) based on the moving hotspot model (O'Neill et al., 2005), which positions the island at ~30°S at 45 Ma, and ~28°S at 37 Ma. The position of the Island during most recent phase of volcanism during the Pliocene, at ~5 Ma, would be around 11.5 - 12°S.

The drilling operations were carried out using a portable hand drill and it is probable that an insufficient number of flows were sampled within the sites to reduce the errors. Similar issues were encountered by Nakanishi and Gee (1995) in their magnetic studies in the Northwestern Pacific Ocean Guyots, where they suffered from secular variations and subsequent differences in paleolatitudes. Dupont-Nivet et al. (2010), while calculating paleolatitude and the age of Indo-Asia collision suggested $k>50$ and $n\geq5$ as a sufficient dataset to represent time averaged geomagnetic variations. Montes-Lauar et al. (1995) adopted a methodology of using two samples per site to determine the mean, they admit poor statistical quality in the data but consider worth including these due to consistent directions. Tauxe (2005) recommends that a higher sample set is needed to average out secular variations, which this study probably has not been able to, therefore resulting in large dp and dm (Table 5.4 and 5.5).

Hence, instead of using the three Eocene sites, the study combines the two Late Eocene (Waterfall Beach and Ethel Beach) sites, to get a slightly shallower paleolatitude of $-43.5°^{+9.0°}_{-11.2°}$ (with a full range of paleolatitude between -34.4° and -54.7°). This is still quite different from the reconstructed position, but the errors induced are significantly smaller. It seems quite reasonable to combine the two sites because, firstly, they have similar ages (Table 5.2) and secondly, they are separated by 300 m and therefore, represent different lava flows of the same sequence, whereas Dolly Beach is 7 - 9 km south of the two sites. By combining these two events, we hope to have sampled at least two flows of the same event. And with an increased number of samples we hope to have constrained secular variations slightly better as compared to individual sites. Given the relationship between the two sites, it is possible that the recalculated paleolatitude might be a spot reading of the geomagnetic field, and should be considered indicative. Moreover, the reconstructed position is now closer to the position ascribed by reconstruction model of O'Neill et al. (2005) of ~30°S, when the error range is considered.

Seismic tomography models of Grand (2002) and Montelli et al. (2004) document the presence of low velocity zone beneath the Eocene position of Christmas Island as shown in Figure 5.10. Grand's (2002) seismic tomography model has very clearly documented a seismic low velocity zone underneath the reconstructed position of Christmas Island in the Eocene down to at least 900 km, and potentially deeper down to 1600 km, beyond which the resolution is poor. Montelli et al. (2004) documented a plume in the East Indian Ocean using both P and S waves centred around 35°S and 100°E down to a depth of 1900 km below which they argue the resolution is poor. They also discussed a deep plume underneath the Cocos (Keeling) Island and a starting plume South of Java. Therefore the association of deep seated low velocity seismic anomalies around the reconstructed position of Christmas Island is striking (Montelli et al., 2004), and may be implicated in the re-emergence of volcanism at Christmas Island.

Oceanic islands are susceptible to tilting as they begin to ride the bulge produced due to subduction at the trench. Tilt associated with Christmas Island is between 0.23° and 1.27° and the Island presently sits right at the crest of the bulge (Figure 5.9). The effect of tilt is more clearly seen at the Golden Bo'Sunbird seamount, which is riding the bulge, south-west of Christmas Island. After correcting the inclinations for the observed tilt, paleolatitude of the Pliocene phase of volcanism is between 12.03°S and 12.88°S, and Waterfall and Ethel Beach combined is in the range of 41° – 43°S which is still significantly larger than existing reconstruction models.

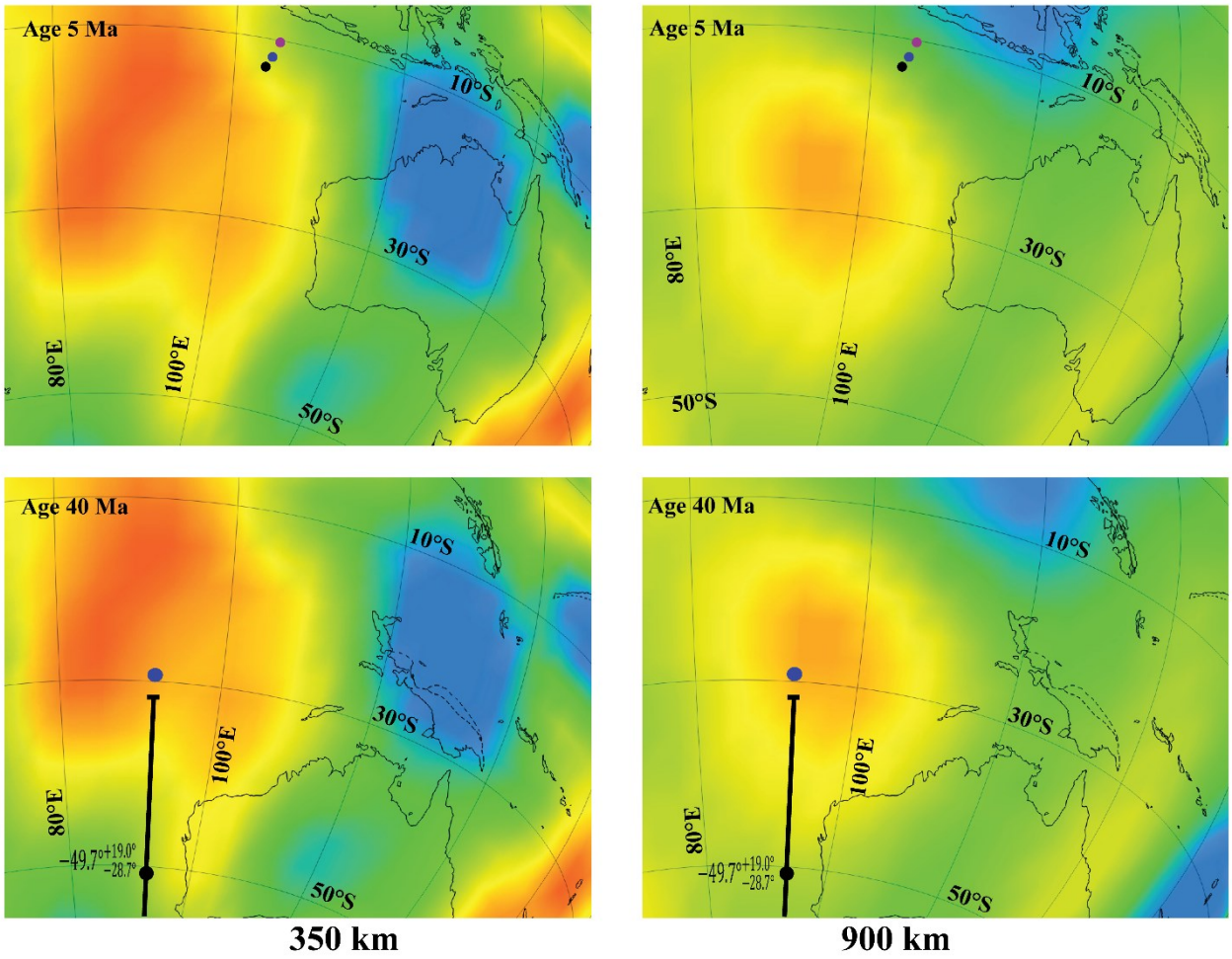

Figure 5.10: Paleoposition of Christmas Island overlayed on Grand's (2002) seismic tomography model at 350 and 900 km depth slices. Blue circle represents an approximate position of Christmas Island as per reconstruction model, black represents reconstructed paleoposition according to this study and purple circle represents present position of the island. The paleoposition of the Eocene age is shown by vertical bar at 40 Ma where the circle represents the paleolatitude. This position is further south of that suggested by the moving hotspot model of O'Neill et al. (2005).

It is possible that the volcanic sites sampled were influenced by structural and tectonic forces that were not possible to determine in the field and might be responsible for such high inclination. Barrie (1967) and Polak (1976) have documented that the island has been affected by a networks of faults. Trueman (1965) mentions faulting has played a major role in shaping the coastline of the island with normal faults of high angle and tens of metres of displacement being observed at many locations. Faults around the Murray Hill region have already been mentioned earlier (Polak, 1976; Baxter and Weeks, 1984). Rivereau (1965) mentions that the geomorphology of the island is influenced by terraces, faults and scarps. It is further discussed that the coastlines are affected by faulting, especially, the south-west and east-south-east, whereas the north coast is little affected by it. Two major network of fault-lines have been reported east-west and north-north-west (Rivereau, 1965). It is conceivable that these volcanic sampling sites were influenced by faulting and associated block movements (Figure 5.2), but our field observations (like, continuity of sediments, and lack of marker beds to demonstrate faulting) at our sample sites suggest minimal interference that would have rotated or tilted the sampling site.

The Indian Plate and the Australian Plate has undergone major transformation in terms of plate motion since its breakup from Gondwana and its subsequent northward journey. Following the cessation of spreading in the Wharton Basin around ~43 Ma as reported by Liu et al., 1983 (or between 38.0 – 36.5 Ma as recently reported by Jacob et al., (2014)), and the initiation of spreading along the South East Indian Ridge (Müller et al., 2000), the once separate Indian and Australian plates became one rigid plate. The northern boundary of the plate changes from a continental collision in the west, to a subduction zone in the east. This change in tectonic setting along the northern margin, and the relative motion of India and Australia, is causing torsional stresses within the centre of the plate (Cloetingh and Wortel, 1986). Deplus et al. (1998) discussed the distinct deformation on either side of the Ninetyeast Ridge. Towards the west, folds and east-west oriented reverse faults are common, whereas, on the east of the ridge, left lateral strike slip faulting is prevalent along a north-

south trending fracture zone (Deplus et al., 1998). The deformation zone has been called as the Capricorn Plate (Royer and Gordon, 1997). Such a distinct deformation pattern within the diffuse plate boundary could have altered the tectonic fabric of the seamount province, which might influence the reconstructed paleoposition of Christmas Island. The discrepancies in the paleolatitude of the Eocene phase of Christmas Island with those from global reconstructions models (O'Neill et al., 2005; Seton et al., 2012) could possibly be related to this deformation, and provide a further scope to constrain the paleomagnetic history of this intraplate region.

Additionally, dynamic tomography produced due to mantle flow variations and density changes can induce elevation or subsidence in continental and oceanic areas (Nyblade and Robinson, 1994; Lithgow-Bertelloni and Silver, 1998; Moucha et al., 2008). Dynamic subsidence of the order of 300 m has been reported in the Southeast Asia by Wheeler and White (2002). Variations of these natures have been observed in Southern and Eastern Africa, producing regions of elevation of the order of 1 km, that are underlain by large scale low velocity zones (Lithgow-Bertelloni and Silver, 1998). The East Indian Ocean contains three significant low velocity zones, described by Montelli et al. (2004), and suggested to be deep mantle plumes, which can cause local uplift (Hager et al., 1985; Braun, 2010). Global dynamic tomography models have been presented by Heine et al. (2008) and Steinberger et al. (2001). Heine et al. (2008) constrained present day dynamic topographic in the CHRISP between -500 to 500 m, and -100 to 500 m around the reconstructed position of Christmas Island at 70 Ma. Moucha et al. (2008) prepared global ocean dynamic topography, and constrained it within -500 to 0 m. Thus, the Northeast Indian Ocean and CHRISP have been affected by the variation in sea-floor depths in response to dynamic tomography, and this could disturb the preserved tilts within the sampled units, during the progressive cooling of magmatic material, though the magnitude of this effect is likely to be similar, or less, than that ascribed to tilting due to subduction flexure.

The re-emergence of volcanism at Christmas Island in the Late Eocene is synchronous with tectonic reorganisation in the East Indian Ocean around 43 Ma (Liu et al., 1983). Plate reorganisation within the Pacific Plate is exemplified by the change in the Hawaii Emperor Bend (HEB). Dalrymple and Clague (1976) first suggested an age of 43 Ma, but Sharp and Clague (2006), using new $^{40}Ar/^{39}Ar$ geochronology data from other islands revised it to 50 Ma. Tarduno (2007), however, is critical of such a value, and rather argues for an age of 47 Ma. Whittaker et al. (2007) suggested major reorganisations events correlated with HEB, such as subduction of Izanagi - Pacific spreading ridge, and initiation of Marianas and Tonga-Kermadec subduction. Such events also caused plate motion changes in the Australian Plate. Slab-pull north of Australia, due to westerly subducting Wharton Ridge, led to a change in Australian Plate motion, from northwest, to north, around 50 Ma (Whittaker et al., 2007). Shortly after, spreading in the Wharton Ridge ceased at 43 Ma (Liu et al., 1983, Müller et al., 2000; Singh et al., 2011). Jacob et al. (2014) reported that Wharton spreading centre ceased around 38.0 – 36.5 Ma. Spreading rates in the SEIR changed from 140 mm/yr to 60 mm/yr at 51.9 Ma to 45.3 Ma, respectively, when plate reorganisation took place in the Australian Plate (Cande et al., 2010). Deplus et al. (1998) suggested that there are differential stress patterns on either side of the Ninetyeast Ridge, with reverse faults in the west, and left-lateral north-south strike slip faults in the east. Thus, the combined change in plate reorganisation at 50 Ma and slowing down of SEIR between 51 and 45 Ma resulted in changed stress regime of now intact Indo-Australian Plate. Even though new evidence has emerged that pushes the closure of Wharton spreading centre to around 38.0 – 36.5 Ma (Jacob et al., 2014), the change in stress regime at the junction of SEIR and Wharton spreading centre and increased slab pull north of Australia, (Whittaker et al., 2007) could have led to re-activation of volcanism at Christmas Island. It is possible that local re-activation of volcanism occurred elsewhere, but has not yet been documented.

To summarise, our study shows that the position of Christmas Island can be calculated using paleomagnetic data. Our study has attempted to constrain such a position of the island with

reasonable errors and found it to be further south than that predicted by the existing reconstructions model of O'Neill et al. (2005) and Seton et al. (2012). The paleoposition for the Pliocene phase of the island appears to constrain the island effectively, and is consistent with global reconstructions (Seton et al., 2012). Paleomagnetic analysis and plate reconstructions all position the island around 12 – 13°S at 4.3 Ma.

5.6: Conclusion

Volcanism in the Northeast Indian Ocean is represented in the form of submerged flat topped and rounded peak seamounts and two sub-aerially exposed islands, Christmas Island and Cocos (Keeling) Archipelago. Of these, Christmas Island is the only island within the region to have recorded this intraplate volcanism in the form of basaltic rocks that are presently exposed above sea-level. $^{40}Ar/^{39}Ar$ dating of the island has revealed ongoing Cenozoic volcanism, from 44 Ma to 37 Ma. This was followed by a more recent Pliocene volcanic phase at 4.5 ± 0.2 - 4.3 ± 0.2 Ma. The younger volcanic event is probably related to the onset of lithospheric plate flexure, and associated asthenospheric decompression, on the seaward side of the outer rise. An older event, in the Late Cretaceous, probably formed the core of island and is presently not exposed on the surface. We carried out a paleomagnetic investigation by drilling basalts at Christmas Island and have attempted to constrain island's position. The high paleolatitude of the island in the Eocene ($-43.5°^{+9.0°}_{-11.2°}$) is suggestive of a more southerly position than that predicted by plate reconstruction models. This could either be due to inadequately averaged secular variation, due limited outcrop, or because of intraplate deformation within the Capricorn Plate, altering the tectonic fabric. The youngest phase, at 4.3 Ma, resolved through thermal demagnetisation, yielded a paleoposition of ~13°S which agrees well with the edge of the lithospheric bulge at that time, and with existing plate reconstruction models. It was argued by Hirano et al. (2008) that low volume intraplate volcanism could be observed at similar tectonic settings to the Japan and Tonga trench, and we put forward the Indo-Australian Plate

subduction setting as a likely candidate for this phase of intraoceanic volcanism. The Late Eocene event, however, is coincident with the cessation of spreading at Wharton Ridge at 43 Ma and the subsequent opening of the South East Indian Ridge. Tectonic reorganisation changed the stress regime of the once separate Indian and Australian Plates, allowing deeper fertile mantle, imaged in seismic tomography, to melt, and ascend through the plate, which may have resulted in the re-activation of volcanic activity at Christmas Island between 44 and 37 Ma.

Acknowledgement:

We are grateful to Trond Torsvik, and an anonymous reviewer for their constructive comments that greatly improved this manuscript. The authors are thankful to the staff at Western Australian Argon Isotope Facility at Curtin University and at CSIRO, North Ryde, for helping with the analytical techniques. We also thank Christmas Island National Park staff for their time and discussions on sharing the locations of volcanic exposures at Christmas Island. This work was in part supported by ARC funding DP110104145, DP0880801, and FT100100717. This is contribution 444 from the ARC Centre of Excellence for Core to Crust Fluid Systems and 936 in the GEMOC Key Centre.

References

Abercrombie, R.E., Antolik, M., Ekström, G., 2003. The June 2000 Mw 7.9 earthquakes south of Sumatra: Deformation in the India–Australia Plate. Journal of Geophysical Research 108, 2018.

Andrews, C.W., 1900. A monograph of Christmas Island (Indian Ocean): Physical Features and Geology. British Museum (Natural History), London.

Antretter, M., Steinberger, B., Heider, F., Soffel, H., 2002. Paleolatitudes of the Kerguelen hotspot: new paleomagnetic results and dynamic modeling. Earth and Planetary Science Letters 203, 635-650.

Barrie, J., 1967. The Geology of Christmas Island. Bureau of Mineral Resources, Australia, 104. (Unpublished report)

Baxter, J.L., Weeks, G.C., 1984. Phosphatised volcanic ore from the Christmas Island, Indian Ocean. Western Australia Institute of Technology, 20. (Unpublished report)

Bodine, J., Steckler, M., Watts, A., 1981. Observations of Flexure and the Rheology of the Oceanic Lithosphere. Journal of Geophysical Research 86, 3695-3707.

Braun, J., 2010. The many surface expressions of mantle dynamics. Nature Geoscience 3, 825-833.

Buchs, D.M., Pilet, S., Cosca, M., Flores, K.E., Bandini, A.N., Baumgartner, P.O., 2013. Low-volume intraplate volcanism in the Early/Middle Jurassic Pacific basin documented by accreted sequences in Costa Rica. Geochemistry, Geophysics, Geosystems 14, 1552-1568.

Butler, R.F., 1992. Paleomagnetism: Magnetic domains to geologic terranes. Blackwell Scientific Publications, Boston.

Cande, S.C., Kent, D.V., 1995. Revised calibration of the geomagnetic polarity timescale for the Late Cretaceous and Cenozoic. Journal of Geophysical Research 100, 6093-6095.

Cande, S.C., Patriat, P., Dyment, J., 2010. Motion between the Indian, Antarctic and African plates in the early Cenozoic. Geophysical Journal International 183, 127-149.

Cloetingh, S., Wortel, R., 1986. Stress in the Indo-Australian plate. Tectonophysics 132, 49-67.

Dalrymple, G.B., Clague, D.A., 1976. Age of the Hawaiian-Emperor bend. Earth and Planetary Science Letters 31, 313-329.

DeMets, C., Royer, J., 2003. A new high-resolution model for India-Capricorn motion since 20 Ma: Implications for the chronology and magnitude of distributed crustal deformation in the Central Indian Basin. Current Science 85, 339-345.

Deplus, C., Diament, M., Hébert, H., Bertrand, G., Dominguez, S., Dubois, J., Malod, J., Patriat, P., Pontoise, B., Sibilla, J.-J., 1998. Direct evidence of active deformation in the eastern Indian oceanic plate. Geology 26, 131-134.

Doak, B., Gallagher, P., Evans, L., Muller, F., 1965. Low-temperature calcination of “C”-grade phosphate from Christmas Island. New Zealand Journal of Agricultural Research 8, 15-29.

Dupont-Nivet, G., van Hinsbergen, D.J.J., Torsvik, T.H., 2010. Persistently low Asian paleolatitudes: Implications for the India-Asia collision history. Tectonics 29, TC5016.

Fujiwara, T., Hirano, N., Abe, N., Takizawa, K., 2007. Subsurface structure of the "petit-spot" volcanoes on the northwestern Pacific Plate. Geophysical Research Letters 34, L13305.

Gibbons, A.D., Barckhausen, U., van den Bogaard, P., Hoernle, K., Werner, R., Whittaker, J.M., Müller, R.D., 2012. Constraining the Jurassic extent of Greater India: Tectonic evolution of the West Australian margin. Geochemistry, Geophysics, Geosystems 13, Q05W13.

Grimes, K.G., 2001. Karst Features of Christmas Islands. Helictite 37, 41-58.

Grand, S.P., 2002. Mantle shear-wave tomography and the fate of subducted slabs. Philosophical Transactions of the Royal Society of London. Series A: Mathematical, Physical and Engineering Sciences 360, 2475-2491.

Hager, B.H., Clayton, R.W., Richards, M.A., Comer, R.P., Dziewonski, A.M., 1985. Lower mantle heterogeneity, dynamic topography and the geoid. Nature 313, 541-545.

Hall, R., 2012. Late Jurassic-Cenozoic reconstructions of the Indonesian region and the Indian Ocean. Tectonophysics 570-571, 1-41.

Heine, C., Müller, R.D., 2005. Late Jurassic rifting along the Australian North West Shelf: margin geometry and spreading ridge configuration. Australian Journal of Earth Sciences: An International Geoscience Journal of the Geological Society of Australia 52, 27 - 39.

Heine, C., Müller, R.D., Steinberger, B., Torsvik, T.H., 2008. Subsidence in intracontinental basins due to dynamic topography. Physics of the Earth and Planetary Interiors 171, 252-264.

Heirtzler, J.R., Cameron, P., Cook, P.J., Powell, T., Roeser, H.A., Sukardi, S., Veevers, J.J., 1978Abyssal Plain. Earth and Planetary Science Letters 41, 21-31.

Hirano, N., Kawamura, K., Hattori, M., Saito, K., Ogawa, Y., 2001. A new type of intra-plate volcanism; Young alkali-basalts discovered from the subducting Pacific Plate, Northern Japan Trench. Geophysical Research Letters 28, 2719-2722.

Hirano, N., Koppers, A.A.P., Takahashi, A., Fujiwara, T., Nakanishi, M., 2008. Seamounts, knolls and petit-spot monogenetic volcanoes on the subducting Pacific Plate. Basin Research 20, 543-553.

Hirano, N., Takahashi, E., Yamamoto, J., Abe, N., Ingle, S.P., Kaneoka, I., Hirata, T., Kimura, J.I., Ishii, T., Ogawa, Y., 2006. Volcanism in response to plate flexure. Science 313, 1426-1428.

Hoernle, K., Hauff, F., Werner, R., van den Bogaard, P., Gibbons, A.D., Conrad, S., Müller, R.D., 2011. Origin of Indian Ocean Seamount Province by shallow recycling of continental lithosphere. Nature Geoscience 4, 883-887.

Hofmann, C., Féraud, G., Courtillot, V., 2000. $^{40}Ar/^{39}Ar$ dating of mineral separates and whole rocks from the Western Ghats lava pile: further constraints on duration and age of the Deccan traps. Earth and Planetary Science Letters 180, 13-27.

Jourdan, F., Renne, P.R., 2007. Age calibration of the Fish Canyon sanidine $^{40}Ar/^{39}Ar$ dating standard using primary K-Ar standards. Geochimica et Cosmochimica Acta 71, 387-402.

Jourdan, F., Féraud, G., Bertrand, H., Watkeys, M.K., Renne, P.R., 2007. Distinct brief major events in the Karoo large igneous province clarified by new $^{40}Ar/^{39}Ar$ ages on the Lesotho basalts. Lithos 98, 195-209.

Jourdan, F., Reimold, W.U., Deutsch, A., 2012. Dating Terrestrial Impact Structures. Elements 8, 49-53.

Kirschvink, J., 1980. The least-squares line and plane and the analysis of paleomagnetic data. Geophysical Journal of the Royal Astronomical Society 62, 699-718.

Koppers, A.A.P., 2002. ArArCALC-software for $^{40}Ar/^{39}Ar$ age calculations. Computers & Geosciences 28, 605-619.

Koppers, A.A.P., Staudigel, H., Wijbrans, J.R., 2000. Dating crystalline groundmass separates of altered Cretaceous seamount basalts by the $^{40}Ar/^{39}Ar$ incremental heating technique. Chemical Geology 166, 139-158.

Lee, J.Y., Marti, K., Severinghaus, J.P., Kawamura, K., Yoo, H.S., Lee, J.B., Kim, J.S., 2006. A redetermination of the isotopic abundances of atmospheric Ar. Geochimica et Cosmochimica Acta 70, 4507-4512.

Levitt, D.A., Sandwell, D.T., 1995. Lithospheric bending at subduction zones based on depth soundings and satellite gravity. Journal of Geophysical Research 100, 379-400.

Lithgow-Bertelloni, C., Silver, P.G., 1998. Dynamic topography, plate driving forces and the African superswell. Nature 395, 269-272.

Liu, C.-S., Curray, J.R., McDonald, J.M., 1983. New constraints on the tectonic evolution of the eastern Indian Ocean. Earth and Planetary Science Letters 65, 331-342.

McDougall, I., Harrison, T.M., 1999. Geochronology and Thermochronology by the $^{40}Ar/^{39}Ar$ Method. Oxford University Press.

McElhinny, M.W., McFadden, P.L., 2000. Paleomagnetism: continents and oceans. Academic Press, San Diego.

Montelli, R., Nolet, G., Dahlen, F.A., Masters, G., Engdahl, E.R., Hung, S.-H., 2004. Finite-Frequency Tomography Reveals a Variety of Plumes in the Mantle. Science 303, 338-343.

Montes-Lauar, C.R., Pacca, I.G., Melfi, A.J., Kawashita, K., 1995. Late Cretaceous alkaline complexes, southeastern Brazil: Paleomagnetism and geochronology. Earth and Planetary Science Letters 134, 425-440.

Morgan, W.J., 1971. Convection plumes in the lower mantle. Nature 230, 42-43.

Moucha, R., Forte, A.M., Mitrovica, J.X., Rowley, D.B., Quéré, S., Simmons, N.A., Grand, S.P., 2008. Dynamic topography and long-term sea-level variations: There is no such thing as a stable continental platform. Earth and Planetary Science Letters 271, 101-108.

Müller, R.D., Mihut, D., Baldwin, S., 1998. A new kinematic model for the formation and evolution of the west and northwest Australian margin, In: Purcell, P.G., Purcell, R.R. (Eds.), The Sedimentary Basins of Western Australia 2. Petroleum Exploration Society of Australia, WA Branch, Perth, WA, 55-72.

Müller, R.D., Gaina, C., Tikku, A., Mihut, D., Cande, S.C., Stock, J.M., 2000. Mesozoic/Cenozoic tectonic events around Australia, In: Richards, M.A., Gordon, R.G., van der Hilst, R.D. (Eds.), The History and Dynamics of Global Plate Motions. AGU, Washington, DC, pp. 161-188.

Müller, R.D., Sdrolias, M., Gaina, C., Roest, W.R., 2008. Age, spreading rates, and spreading asymmetry of the world's ocean crust. Geochemistry, Geophysics, Geosystems 9, Q04006.

Nakanishi, M., Gee, J.S., 1995. 34: Paleomagnetic investigations of volcanic rocks: paleolatitudes of the northwestern Pacific guyots, In: Haggerty, J.A., Premoli Silva, I., Rack, F., McNutt, M.K. (Eds.), Proceedings of the Ocean Drilling Program. Scientific results. Ocean Drilling Program, 585-604.

Nyblade, A.A., Robinson, S.W., 1994. The African Superswell. Geophysical Research Letters 21, 765-768.

O'Dowd, D.J., Lake, P.S., 1989. Red crabs in rain forest, Christmas Island: removal and relocation of leaf-fall. Journal of Tropical Ecology 5, 337-348.

O'Dowd, D.J., Lake, P.S., 1991. Red crabs in rain forest, Christmas Island: removal and fate of fruits and seeds. Journal of Tropical Ecology 7, 113-122.

O'Neill, C., Müller, D., Steinberger, B., 2005. On the uncertainties in hot spot reconstructions and the significance of moving hot spot reference frames. Geochemistry Geophysics Geosystems 6, Q04003.

Pettifer, G.R., Polak, E.J., 1979. Christmas Island (Indian Ocean) geophysical survey for groundwater, 1976. Bureau of Mineral Resources, Australia, 75. (Unpublished report)

Polak, E.J., 1976. Christmas Island (Indian Ocean) geophysical survey for groundwater, 1973. Bureau of Mineral Resources, Australia, 66. (Unpublished report)

Renne, P.R., Mundil, R., Balco, G., Min, K., Ludwig, K.R., 2010. Joint determination of 40K decay constants and $^{40}Ar^*/^{40}K$ for the Fish Canyon sanidine standard, and improved accuracy for $^{40}Ar/^{39}Ar$ geochronology. Geochimica et Cosmochimica Acta 74, 5349.

Rivereau, J.C., 1965. Notes on a Geomorphological Study of Christmas Island, Indian Ocean, Bureau of Mineral Resources, Geology and Geophysics, Canberra, 5. (Unpublished report)

Royer, J.Y., Gordon, R.G., 1997. The motion and boundary between the Capricorn and Australian plates. Science 277, 1268-1274.

Seton, M., R. D. Müller, S. Zahirovic, C. Gaina, T. Torsvik, G. Shephard, A. Talsma, M. Gurnis, M. Turner, S. Maus, and M. Chandler (2012), Global continental and ocean basin reconstructions since 200 Ma, Earth-Science Reviews, 113, 212-270.

Sharp, W.D., Clague, D.A., 2006. 50-Ma Initiation of Hawaiian-Emperor Bend Records Major Change in Pacific Plate Motion. Science 313, 1281-1284.

Sharp, W.D., Renne, P.R., 2005. The $^{40}Ar/^{39}Ar$ dating of core recovered by the Hawaii Scientific Drilling Project (phase 2), Hilo, Hawaii. Geochemistry, Geophysics, Geosystems 6, Q04G17.

Singh, S.C., Carton, H., Chauhan, A.S., Androvandi, S., Davaille, A., Dyment, J., Cannat, M., Hananto, N.D., 2011. Extremely thin crust in the Indian Ocean possibly resulting from Plume–Ridge Interaction. Geophysical Journal International 184, 29-42.

Smith, W.H.F., Sandwell, D.T., 1997. Global Sea Floor Topography from Satellite Altimetry and Ship Depth Soundings. Science 277, 1956-1962.

Stagg, H.M.J., Wilcox, J.B., Symonds, P.A., O'Brein, G.W., Colwell, J.B., A., H.P.J., C-S., L., G., M.A.M., Struckmeyer, I.M., 1999. Architecture and evolution of the Australian continental margin. AGSO Journal of Australian Geology & Geophysics 17, 17 - 33.

Steinberger, B., Schmeling, H., Marquart, G., 2001. Large-scale lithospheric stress field and topography induced by global mantle circulation. Earth and Planetary Science Letters 186, 75-91.

Taneja, R., O'Neill, C., 2014. Constraining the age and origin of the seamount province in the Northeast Indian Ocean using geophysical techniques. Marine Geophysical Research, 1-23.

Tarduno, J.A., 2007. On the motion of Hawaii and other mantle plumes. Chemical Geology 241, 234-247.

Tregoning, P., Brunner, F.K., Bock, Y., Puntodewo, S.S.O., McCaffrey, R., Genrich, J.F., Calais, E., Rais, J., Subarya, C., 1994. First geodetic measurement of convergence across the Java Trench. Geophysical Research Letters 21, 2135-2138.

Trueman, N.A., 1965. The phosphate, volcanic and carbonate rocks of Christmas Island (Indian Ocean). Journal of the Geological Society of Australia 12, 261 - 283.

Veevers, J.J., 1971. Phanerozoic history of Western Australia related to continental drift. Journal of the Geological Society of Australia 18, 87-96.

Verati, C.l., Jourdan, F., 2013. Modelling effect of sericitization of plagioclase on the $^{40}K/^{40}Ar$ and $^{40}Ar/^{39}Ar$ chronometers: implication for dating basaltic rocks and mineral deposits. Geological Society, London, Special Publications 378.

Watts, A.B., 2001. Isostasy and Flexure of the Lithosphere. Cambridge University Press, Cambridge.

Wei, W., 1995. Revised age calibration points for the geomagnetic polarity time scale. Geophysical Research Letters 22, 957-960.

Wheeler, P., White, N., 2002. Measuring dynamic topography: An analysis of Southeast Asia. Tectonics 21, 1040.

Woodroffe, C., 1988. Vertical movement of isolated oceanic islands at plate margins: evidence from emergent reefs in Tonga (Pacific Ocean), Cayman Islands (Caribbean Sea) and Christmas Island (Indian Ocean). Zeitschrift fur Geomorphologie, Supplementband 69, 17-37.

Woodroffe, C.D., Falkland, A.C., 1997. Chapter 31 Geology and hydrogeology of the Cocos (Keeling) islands, In: Vacher, H.L., Terrence, M.Q. (Eds.), Developments in Sedimentology. Elsevier, 885-908.

Woodroffe, C.D., Veeh, H.H., Falkland, A., McLean, R.F., Wallensky, E., 1991. Last interglacial reef and subsidence of the Cocos (Keeling) Islands, Indian Ocean. Marine Geology 96, 137-143.

Whittaker, J.M., Müller, R.D., Leitchenkov, G., Stagg, H., Sdrolias, M., Gaina, C., Goncharov, A., 2007. Major Australian-Antarctic Plate Reorganization at Hawaiian-Emperor Bend Time. Science 318, 83-86.

Yue, H., Lay, T., Koper, K.D., 2012. En echelon and orthogonal fault ruptures of the 11 April 2012 great intraplate earthquakes. Nature 490, 245-249.

Zijderveld, J., 1967. AC demagnetization of rocks: analysis of results, In: Collinson, D.W., Creer, K.M., Runcorn, S.K. (Eds.), Methods in paleomagnetism. Elsevier, Amsterdam, 254-268.

Chapter 6: Geochemistry

Mantle heterogeneities beneath the Northeast Indian Ocean as sampled by intraplate volcanism at Christmas Island

Rajat Taneja[1*], Tracy Rushmer[1], Simon Turner[1], Craig O'Neill[1], Janne Blichert-Toft[2]
[1]Centre for Core to Crust Fluid Systems, Macquarie University, Sydney, Australia
[2]Ecole Normale Supérieure de Lyon, 46 Allée d'Italie, 69364 Lyon, Cedex 07, France

6.1: Abstract

The intraplate region of the Northeast Indian Ocean lying between the Ninetyeast Ridge and the North West Shelf of Australia contains numerous submerged seamounts and two sub-aerially exposed volcanic island groups, the Cocos (Keeling) Archipelago and Christmas Island. While the Cocos (Keeling) Archipelago is a coral atoll and does not have any volcanic exposures, Christmas Island is the only sub-aerially exposed volcanic island in the seamount province and thus a prime accessible example of the submarine volcanism in this region. Though the evolution of the western margin of Australia and the seismicity in the intraplate region has received considerable attention, the origin of the seamount province in the Northeast Indian Ocean is still a matter of debate. Christmas Island can provide some key inputs into the geochemical history of the region.

This work aims to constrain the origin of Christmas Island and the associated volcanism in the Christmas Island Seamount Province (CHRISP). The trace element pattern of the lavas are similar to ocean island basalts, however high $^{208}Pb/^{204}Pb$ and $^{207}Pb/^{204}Pb$ for given $^{206}Pb/^{204}Pb$

values suggest an affiliation with the DUPAL anomaly of the Indian Ocean. The reconstructed position of Christmas Island during the Eocene (44 – 37 Ma) places the island in close proximity to the (present day) upper mantle low seismic velocity anomalies. Moreover, an enriched mantle (EM-2) type component in addition to the DUPAL anomaly is observed in the Eocene volcanic phase. The younger Pliocene (~4 Ma) sequences at Christmas Island are inferred to be a product of partial melting of existing material induced by lithospheric flexure.

6.2: Introduction

Morgan (1971) suggested that many instances of intraplate, aseismic, ocean island basalt (OIB) hotspot volcanism are caused by upwelling mantle plumes originating from the lower mantle. An implication of this model is that volcanism should form an age-progressive linear volcanic chain. The Hawaiian Island chain in the Pacific Ocean, and the Ninetyeast Ridge, associated with the Kerguelen hotspot in the Indian Ocean, are good examples, and this model has been successful in explaining the linear age-distance relationship relative to plate motion for many other volcanic chains (Mahoney et al., 1983; Duncan, 1984; McDougall and Duncan, 1988; Duncan, 1990; Duncan, 1991; Koppers et al., 1998; Frey et al., 2000; O'Neill et al., 2003; Geldmacher et al., 2005). However, there are examples of volcanic chains that differ from this relationship, including the Marshall, Cook-Austral and Wake seamounts, which have a complex age-distance pattern (Sandwell et al., 1995; Davis et al., 2002; Koppers et al., 2003; Ballmer et al., 2009).

Since Morgan's (1971) work, different mechanisms for intraplate volcanism have been put forward. For example, Morgan's (1971) original hotspot model was refined into primary, secondary, and tertiary plumes by Courtillot et al. (2003). These were earlier classified as Hawaiian and Marquesian respectively, on the basis of their geochemistry (Duncan et al., 1986; Haase, 1996). The primary (Hawaiian) type consists of strong plumes that rise from the core-mantle boundary and are usually active over long periods of geologic time (Courtillot et al.,

2003). In contrast, the secondary type is usually broad, and perhaps formed within the upper mantle, additionally they may spread out to produce small weak hotspots (Courtillot et al., 2003). Tertiary hotspots may be linked to the asthenosphere, and form due to stress response in the lithosphere and decompression melting (Courtillot et al., 2003). Alternate models have also been proposed to explain intraplate OIB volcanism. Examples include lithospheric cracking through tensional stresses (Sandwell et al., 1995) or thermal contraction of young lithosphere (Gans et al., 2003), which may result in leaking faults producing seamounts that do not follow a linear age distribution. In addition, volcanism along hotlines in the upper mantle as a source of volcanism was proposed by Bonatti and Harrison (1976). The hotspot induced linear age progression model has received the most recognition and is due to the model's ability to explain a wide set of geological intraplate tectonic settings (e.g. Duncan, 1984, 1990; O'Neill et al., 2003). This is in contrast to alternative models, which are often more region-specific and hence not as widely applicable to varied local tectonic settings (Koppers et al., 2003).

Ocean island basalts are thought to be the result of decompression melting and most record significant compositional heterogeneities within the mantle (Hofmann, 1997). Heterogeneities within the upper mantle are the prime explanation for the wide variety of composition observed in volcanics within intraplate oceanic and continental areas (Hofmann, 1997; Kellogg et al., 1999). Originally, four end-members were defined (Zindler and Hart, 1986; Hofmann, 1997) largely on the basis of radiogenic isotopic compositions: HIMU (high- U/Pb mantle component), EM-1 (enriched mantle -1), EM-2 (enriched mantle -2), and DMM (depleted MORB mantle). HIMU, as exemplified by St Helena and the Azores, has the most radiogenic Pb isotope ratios and the lowest $^{87}Sr/^{86}Sr$, both of which are suggested to have evolved over time in an ancient subducted oceanic crust (Hoffman, 1997). DMM is characterised by the highest $^{143}Nd/^{144}$ Nd and lowest $^{87}Sr/^{86}Sr$ and $^{206}Pb/^{204}Pb$, $^{207}Pb/^{204}Pb$ and $^{208}Pb/^{204}Pb$ (Hofmann, 1997) and represents the most depleted, presumably shallow, reservoir sampled by

mid-ocean ridge basalts (MORB). EM-1 (as exemplified by Pitcairn and Tristan da Cunha hotspots) is characterised by low $^{87}Sr/^{86}Sr$ and $^{143}Nd/^{144}Nd$ whereas EM-2 (as exemplified by Societies and Samoa hotspots) is characterised by high $^{87}Sr/^{86}Sr$ and low $^{143}Nd/^{144}Nd$ (Hofmann, 1997).

Various materials and processes have been proposed for the origin of the two enriched mantle components ranging from subduction of continental crust, sediments, or oceanic crust, to delamination of subcontinental lithosphere (Zindler and Hart, 1986). The EM-2 signature of the OIB in the southern hemisphere is linked to the DUPAL anomaly observed in the South-Atlantic Indian Ocean. Dupré and Allègre (1983) recognised high $^{207}Pb/^{204}Pb$ and $^{208}Pb/^{204}Pb$ ratios for given $^{206}Pb/^{204}Pb$ in the ocean island basalts from the South Atlantic Ocean and Indian Ocean. Hart (1984) showed that this "DUPAL" anomaly extends into the southern Central Pacific Ocean and has potentially existed for billions of years even though the magnitude of this anomaly is lower. Castillo (1988) suggested the signature of the DUPAL anomaly was closely related to large-scale regions of very low seismic velocities in the lower mantle. Goldstein et al. (2008) documented DUPAL anomaly under the western Gakkel Ridge in the Arctic upper mantle and suggested delaminated subcontinental lithospheric mantle as the source of this anomaly. Prior to this, Escrig et al. (2004) suggested that the source was from the contamination of lower continental crust and not subcontinental lithospheric mantle or recycled sediments. Davies et al. (1989) suggested, on the basis of geochemical and isotopic data, that the anomaly has existed for a minimum of 270 Ma, and has been observed in many locations across the region such as the Tadhak alkaline complex of Mali, the Karoo Basalts in South Africa, the Parana Basalts in Brazil, the Walvis Ridge in the Atlantic Ocean, the Ninetyeast Ridge, and the Kerguelen and Heard Islands in the Indian Ocean.

In a paper by Hirano et al. (2001), a new type of intraplate volcanism has been reported that is suggested to have no relation with magma generated at conventional tectonic settings

(convergent, divergent boundaries, and hotspots). These volcanic features are usually less than 1 km^3 and have been termed as "petit spot" intra plate volcanism. These were first found near oceanic-continental collision zones off the north-western coast of the Pacific Ocean along the Hokkaido Rise (Hirano et al., 2001, 2006; Fujiwara et al., 2007; Valentine and Hirano, 2010). More recently, ancient petit spot volcanism has been reported off the coast of Costa Rica (Buchs et al., 2013). These minuscule volcanic features formed away from the mid-oceanic ridges and have alkalic compositions indicative of low degrees of partial melting. Costa Rica's ancient petit spot volcanic features are similar in trace elemental composition to the Hokkaido Rise, and are distinct from typical OIB and MORB (Buchs et al., 2013). Hirano et al. (2001) proposed an origin whereby cracks were formed within the lithosphere due to plate flexure at the lithospheric bulge adjacent to the trench on the seaward side, and that these cracks permit extraction of small degree melts that they propose are ubiquitously present within the upper mantle.

6.3: Christmas Island Seamount Province (CHRISP)

The study area within the Northeast Indian Ocean contains the Christmas Island Seamount Province (CHRISP), comprising of two sub-aerially exposed islands, and numerous submerged seamounts, that lies south of the Sunda Java Trench, and is bounded by the Ninetyeast Ridge to the west, and the Australian North West Shelf to the east (Figure 6.1). The region has not been an area of intense scientific research in the past although considerable work has been done on the Ninetyeast Ridge (Sclater and Fisher, 1974; Duncan, 1978; Souriau, 1981; Mahoney et al., 1983; Weis et al., 1991; Klootwijk et al., 1992), the Sunda Java Trench (Masson et al., 1990; Widiyantoro and van der Hilst, 1996; Lay et al., 2005; Whittaker et al., 2007; Hall et al., 2012), and the North West Shelf (e.g. Müller et al., 1998; Heine and Müller, 2005).

Recently Hoernle et al. (2011) conducted a dredging expedition in the CHRISP to both date the volcanism, and propose a model for its formation. They analysed geochemistry and geochronology for 38 seamounts and obtained ages in the range of 136.2 ± 1.7 – 46.7 ± 0.2 Ma with older ages in the east (Argo Abyssal Plain) and younger ages in the west (south of the Cocos (Keeling) Islands). The Eastern Wharton Basin contains ages in the range of 115.9 ± 3.8 Ma – 94.3 ± 0.3 Ma, while the Vening-Meinesz province is between 95.6 ± 1.4 - 63.5 ± 0.3 Ma (Figure 6.1). They proposed that the seamount province was formed near the mid-oceanic ridge through recycling of delaminated continental lithosphere. This study adds geochemical analyses of land samples from this study to the dataset (that includes both dredged and land samples) of Hoernle et al. (2011) and tests the model for the origin of Christmas Island.

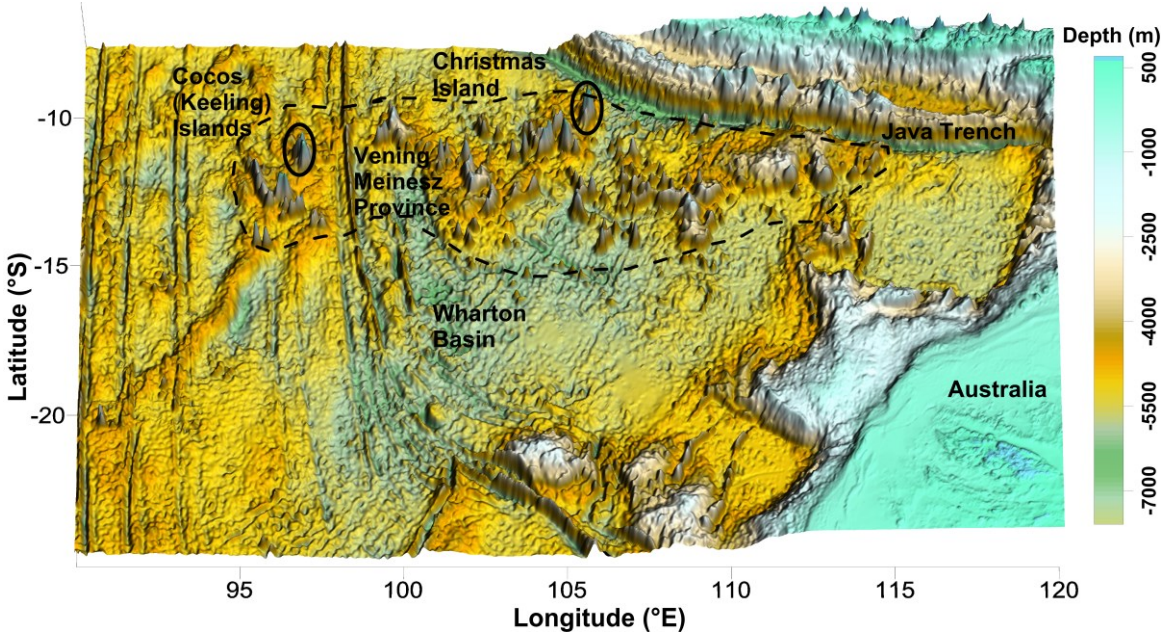

Figure 6.1: 3D Surface bathymetry map of the Northeast Indian Ocean showing the Australian landmass in the east, and the Java Trench in the north. CHRISP is highlighted in black dashed line between 10° – 15°S. Cocos (Keeling) Island (CKI), and Christmas Island (CI) are the two exposed islands of this seamount province. While the former is a coral atoll, the latter is a limestone capped volcanic island.

The numerous submerged seamounts, and volcanic guyots of CHRISP often extend 2000 m above the abyssal plain, which has typical depths of around 5900 m (Smith and Sandwell, 1997). The southern island group of the Cocos (Keeling) Archipelago is a coral atoll with a maximum elevation of 11 m (Woodroffe and Falkland, 1997). The islands are composed of poorly consolidated Holocene sand and coral limestone, underlain by Pleistocene limestone

(Woodroffe et al., 1991). The islands are completely void of any volcanic exposures at the surface (Searle, 1994), though Hoernle et al. (2011) have dredged volcanic rocks from the atoll at depths of ~2400 m below sea-level and yielded ages of 55.6 ± 0.2 – 56.0 ± 0.2 Ma. Gravity modelling by Taneja and O'Neill (2014) have documented that the basaltic core of the island probably lies beneath 2100 m of limestone. In contrast, volcanic outcrops on Christmas Island have recorded the magmatic evolution of the region. A distinct characteristic of the CHRISP is its non-linearity which contrasts markedly with the adjacent Ninetyeast Ridge (e.g. Duncan, 1978; Klootwijk et al., 1992; O'Neill et al., 2003). This province instead occurs as a widespread zone of distributed volcanism that is 1500 km long and 600 km wide. The conventional hotspot model of Morgan (1971), where a plate moves over a fixed mantle plume, does not address the volcanic distribution. Fracture induced volcanic activity (Sandwell et al. 1995; Gans et al. 2003; Natland and Winterer, 2005) is unlikely as these fractures zones trend north-south, while the distributed seamount province trends roughly east-west.

To understand the evolution of the Northeast Indian Ocean it is essential to study the processes that led to the formation of the sub-aerial islands and submerged seamounts. In this paper we combine the data from this study and that obtained by Hoernle et al. (2011) to focus on the geochemistry of Christmas Island in order to develop a multi-disciplinary understanding of the processes involved in the formation of this island.

6.3.1: Geology of Christmas Island

Christmas Island is a roughly "T" shaped (Figure 6.2), heavily-forested tropical island. Previous studies on the geology and geomorphology of the island have been carried out by Andrew (1900), Barrie (1967), and Trueman (1965). Three stages (Table 6.1) of volcanic evolution have been documented by previous workers: the oldest event occurred in the Late Cretaceous (Taneja and O'Neill, 2014), the second in the Eocene, and the youngest around the Pliocene (Hoernle et al., 2011; Taneja et al., 2014). These are overlain by sequences of Tertiary

limestone and capped by phosphate rich soils. The oldest episode of volcanism is documented within the limestone caves that are now utilised by the Island's water authority, but these are now inaccessible (Grimes, 2001). The most recent minor volcanics are found in the Pliocene in the form of dykes and tuffs that is accompanied by faulting and fracturing (Grimes, 2001). Geochronological dating of the basaltic rocks from the island have shown two episodes of volcanism: an old Eocene event, also called the Lower Volcanic Sequences (LVS) from 44 - 37 Ma, and a Pliocene event, called the Upper Volcanic Sequences (UVS) ~4 Ma (Hoernle et al. 2011; Taneja et al., 2014). Hoernle et al. (2011) obtained two clusters of ages for the volcanism at the island, an older event between 37.0 ± 0.6 Ma and 43.6 ± 0.4 Ma, and a younger volcanic phase between 4.31 ± 0.14 Ma and 4.52 ± 0.18 Ma.

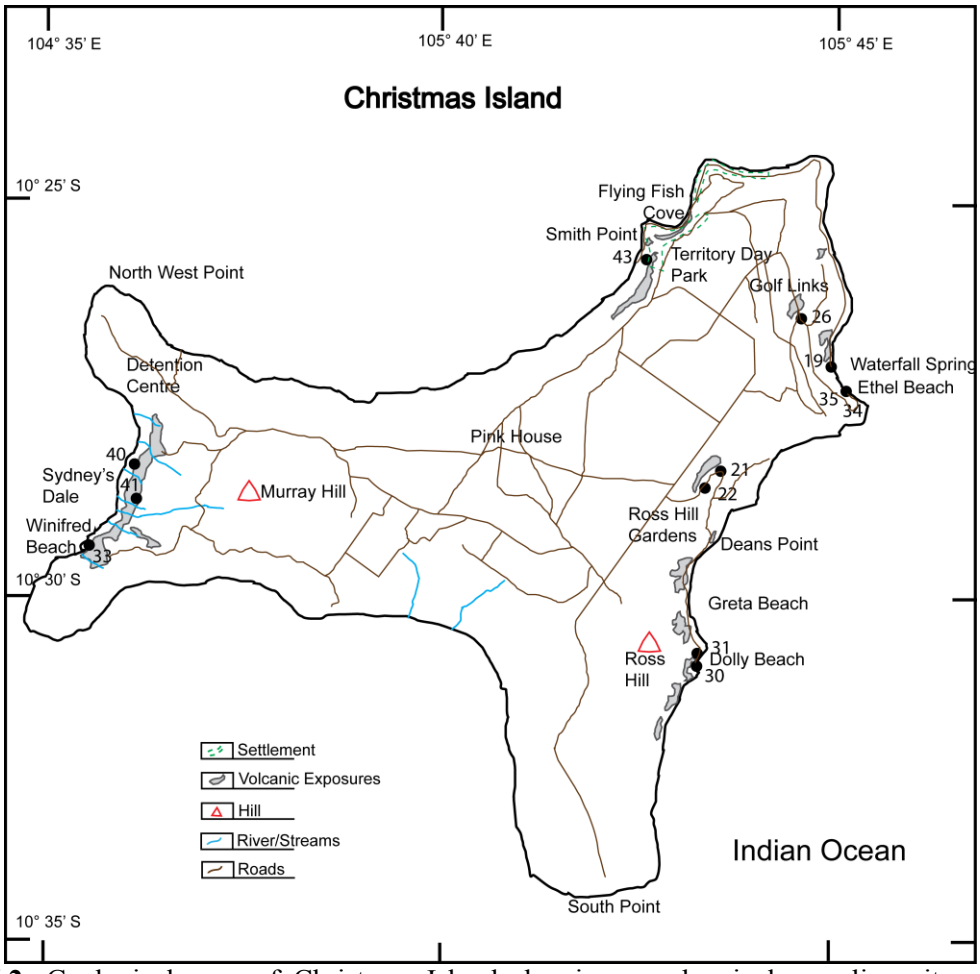

Figure 6.2: Geological map of Christmas Island showing geochemical sampling sites. Volcanic exposures and road network drawn from maps provided by the Christmas Island National Park. Settlement area and drainage network re-drawn from maps provided by the Christmas Island Tourist Centre. Numbers represent volcanic sampling sites. A heavily phosphatised dyke was found near the Murray Hill area but was not sampled. Samples from Ross Hill Gardens and Golf Link appear weathered as compared to other volcanic outcrops.

Table 6.1: Main geological units at Christmas Island, Northeast Indian Ocean (modified from Grimes, 2001). The Late Cretaceous episode of the island has not been dated, but flexural modelling by Taneja at el. (2014) has provided evidence that the island loaded the lithosphere ~88 – 75 Ma.

Time Period	**Geological Description**
Quaternary	Phosphate deposits.
Pliocene (3-5 Ma)	Upper Volcanic Series, the youngest volcanism.
Late Oligocene- Mid Miocene	Upper Carbonate Series.
Eocene (40- 35 Ma)	The Lower Volcanic Series, second episode of volcanism.
Eocene	Lower Carbonate Series.
Late Cretaceous-Early Cenozoic Volcanic	Purported volcanic core.

6.4: Methodology and Analytical Techniques

6.4.1: Sample Collection

Samples were collected during field work on the island in November, 2010. Careful planning and extensive studies were made prior to sample collection from different locations spread across the island. Volcanic samples were selected from different locations spread across the island, and visual examination ensured only freshest available and least weathered samples were collected. While heavily weathered samples were not included in sample collection, it is possible that samples collected from the field might have undergone minor alteration and weathering. Of the locations sampled, five sites were located on the east coast. Outcropping on the coast, from north to south, were Waterfall Spring, Ethel Beach, and Dolly Beach outcrops, while Ross Hill Gardens and Golf Link outcrop inland. On the west coast were Sydney's Dale, and Winifred Beach, while the northern part of the island incorporates the Territory Day Park, near Flying Fish Cove (Figure 6.2). Volcanic outcrops on Waterfall Beach and Ethel Beach were separated by approximately 300 m, and occurred within the limestone units. The former site is comprised of a ~3m x 5m wide mafic vesicular basalt, with exposures on the adjacent cliff. The Ethel Beach locale is at the base of a cliff, and only accessible at low tide. The Ethel Beach outcrop appears to be an extension of the volcanic exposure at Waterfall

Beach. Dolly Beach, on the south central part of the east coast, lies 8 km south of Waterfall Beach and contains a basaltic dyke that rises roughly 2-3 m through the beach surface (Figure 6.3).

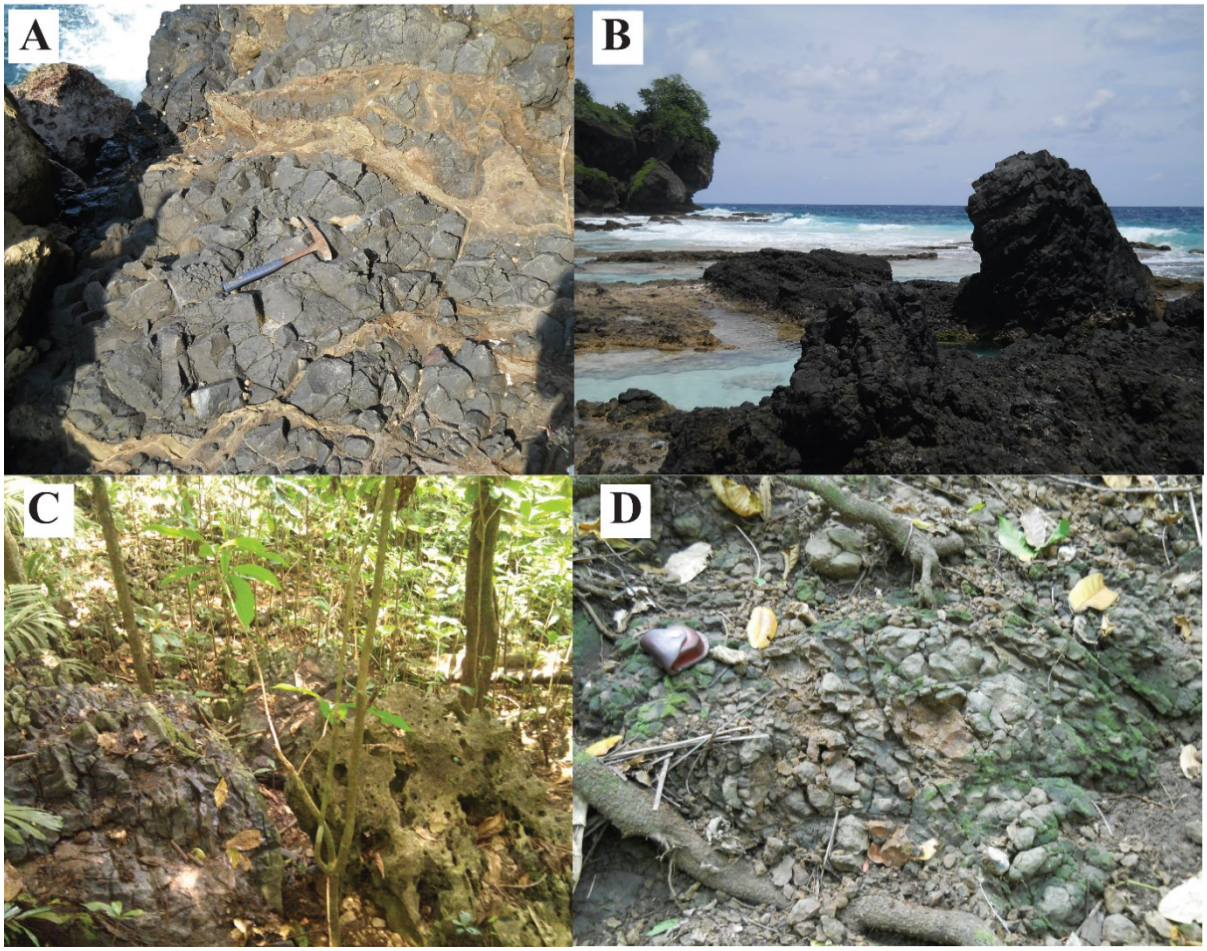

Figure 6.3: Outcrop photos of four selected sites from Christmas Island. A, Waterfall Spring; B, Dolly Beach; C, Golf Road; D, Ross Hill Gardens. Scale: B, the width of the sub-vertical volcanic exposure on the right is 1.5 m; C, width of the outcrop exposure on left is 1 m.

Of the two sites on the west coast, Winifred Beach is an in-situ volcanic outcrop, whereas the location at Sydney's Dale occurs inland. The Flying Fish Cove locale, within the Territory Day National Park, consisted of exposed outcrops within a detritus and soil-dominated creek. During sample collection it was ensured that only the least weathered materials were chosen. All the sampling localities are part of LVS, while Winifred Beach is the only sample from the UVS.

Since Christmas Island is covered by dense tropical forest, and some regions restricted due to phosphate mining, access to certain parts of the island was limited or not possible, resulting in some areas remaining unsampled. In addition, construction activity in the northern part around Flying Fish Cove limited sampling in the region. As mentioned previously, the oldest documented episode is now no longer exposed, therefore our results span only the Eocene and Pliocene phases.

6.4.2: Analytical Techniques

6.4.2.1: Major and Trace Elements

Only the freshest samples possible (determined through examination of general site conditions, hand specimen, and a hand lens) were selected for major and trace element analysis at Macquarie University, and any weathered components were removed using a diamond saw, though in some samples minor weathering was still present. A hydraulic press with tungsten carbide plates was used to mechanically crush selected pieces of fresh rock into small pieces. The press was cleaned thoroughly with 100% ethanol between samples to prevent cross contamination. Approximately 50 g of crushed sample was then reduced to a fine powder in a tungsten carbide mill. The mill was cleaned with ethanol and Milli-Q (18 Mohm) water between each sample to prevent cross-contamination. Loss on ignition was measured by comparing the weights of the powders before and after heating to 1050° C for 1.5 hours. Glass disks for major element analysis were prepared using 0.4 g of powdered sample, 2.5 g of lithium tetraborate/metaborate flux and an ammonium iodide wetting agent. This mixture was heated to 1000°C in a furnace for ~15 minutes, and press-quenched into 30 mm glass disks. Major element analysis was undertaken on a SPECTRO XEPOS energy dispersive XRF spectrometer machine in the Department of Geosciences, University of Wollongong. Pressed powder pellets were prepared for trace element analysis by X-ray fluorescence (XRF).

Approximately 6-6.5 g of rock powder and 10-12 drops of elvanol solution were mixed together and then pressed to 80 kN in an aluminium cup. The pellets were dried in an oven at 120 °C for 2 hours. Samples were analysed on a Spectro XLAB2000 energy dispersive XRF spectrometer at the Macquarie University. Lower limits of detection are presented in Appendix 2 Table 1.

Whole-rock trace-element compositions were determined by solution ICP-MS. Analyses were conducted on an Agilent 7500cs ICP-MS housed at the Geochemical Analysis Unit (GAU), at the Australian Research Council (ARC) National Key Centre for Core to Crust Fluid Systems, (CCFS), in the Department of Earth and Planetary Sciences at Macquarie University, Australia. Powdered samples were weighed to approximately 0.1g and placed in Teflon beakers and then digested with concentrated HNO_3 (16 N) and HF (27 N) for 24 hours. Precisely measured spikes of an internal standard (containing ^{6}Li, ^{75}As, ^{103}Rh, ^{115}In, ^{209}Bi) were added to the samples. Method blank measurement was subtracted from the samples to provide background counts. A series of external calibration standards (BCR-2a) and reference samples (BIR-1 and BHVO-2) were run at the start and end of all runs. ICP-MS data was not used for W, and As. Results from BCR-2a, BIR-1 and BHVO-2 are presented in Appendix 2 Table 2.

6.4.2.2: Hf, Nd, Pb Isotopes

Samples were sent to the Ecole Normale Supérieure de Lyon (ENSL) for analysis of Nd, Hf and Pb isotope compositions. Samples were leached and digested in Savillex beakers and Hf, Nd, and Pb separated using ion-exchange chromatography and their isotope compositions measured using the Nu Plasma HR MC-ICP-MS at ENSL according to the chemistry and mass spectrometry protocols of Blichert-Toft and Albarède (2009) and references therein. The external 2σ error on the Pb isotopes are of the order of ± 50-100 ppm (Janne Blichert-Toft, personal communication).

6.5: Results

6.5.1: Petrology of volcanic rocks

Volcanic rocks from Christmas Island were examined under a microscope. Samples from Ross Hill Garden and Golf Link are highly weathered, and altered (occurring inland and in-situ), while, those from Waterfall Spring, Ethel Beach, and Dolly Beach are fresh and from in-situ locations along the coast., whereas outcrops at Flying Fish Cove, and Sydney's Dale occur inland.

The sample from Ross Hill Garden (CX-22A and CX-21A) consists of very fine-grained aphanitic groundmass predominantly consisting of plagioclase laths (~60 vol.%, 150 μm to 250 μm), and glass with some opaques (~10 vol.%). Grain boundaries of olivine are intact, but have been heavily altered. Phenocrysts of olivine (30 vol.%) are mostly subhedral with rounded grains possibly as result of alteration though some fractures can still be observed. These phenocrysts range in size from 50 μm to 400 μm (Figure 6.4 A, and B).

Dolly Beach (CX-30B) consists mainly of phenocrysts of olivine and clinopyroxene. Grain sizes vary from <5 μm up to several cm, and are euhedral to subhedral. Groundmass appears fresh and consists mostly of plagioclase, clinopyroxene (20 vol.%), opaque and glass (10 vol.%). Plagioclase forms ~70 vol.% of the groundmass and appears as elongate microliths (50 μm to 200 μm). Magnetite inclusions (~10 μm) can be observed in pyroxenes within the groundmass and occasionally surrounding the grain boundaries of olivine (Figure 6.4 C).

Samples from other locales, such as Ethel Beach (CX-34), Waterfall Spring (CX-19A), Flying Fish Cove (CX-43), and Winifred Beach (CX-33) appear fresh with only minor alteration of olivine. Mineral assemblages typically comprise of olivine (~20 vol.%), clinopyroxene (~5 vol.%), and groundmass (70 – 80 vol.%, consisting of plagioclase, clinopyroxene, altered glass, and opaques). Phenocrysts of olivine are randomly distributed throughout the sample and

appear as euhedral to subhedral with grain sizes ranging from 50 - 200 µm. Olivine is affected by serpentinisation preferentially along the fractures and grain boundaries. Plagioclase appears as randomly oriented microcrysts, ranging from 50 µm to over 100 µm in length, while opaques are disseminated within the groundmass and can occasionally be seen around the edge of olivine.

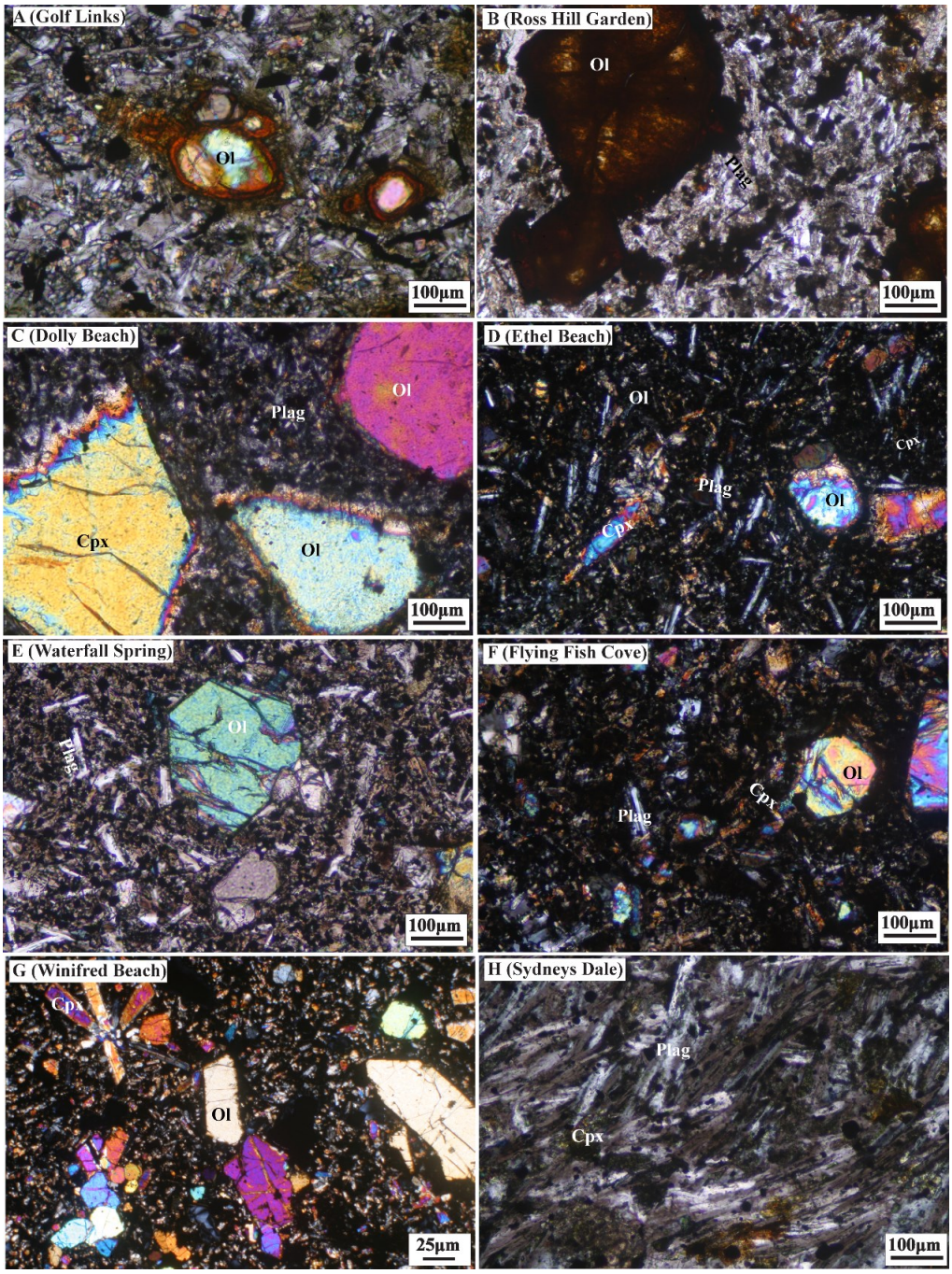

Figure 6.4: Petrographic images of volcanic rocks from Christmas Island. The samples from Golf Links and Ross Hill Gardens are heavily weathered with a Loss on Ignition (LOI) of >4%, while the remaining samples appear fresh with a LOI of 3-4% or less. The trachyte from Sydney's Dale has a trachytic texture and plagioclase are oriented in the flow direction. All images taken under crossed polars.

The Sydney's Dale (CX-40) sample exhibits a characteristic trachyte texture of flow-oriented mineral grains (Figure 6.4 H). The sample is very fine grained, where the groundmass consists predominantly of clinopyroxenes (20 vol.%, 100μm) and oriented plagioclase (70 vol.%, 50 μm to 200 μm), with opaques and glass (~10 vol.%). Plagioclase appears to have undergone sericitic alteration, and glass and earlier mafic phases have altered to chlorite.

6.5.2: Major Elements

Major and trace element data from the island are presented in Table 6.2. Of all the volcanic locations sampled at Christmas Island, outcrops at Ross Hill Garden and Golf Link are heavily weathered. This is evident through their heavily altered petrology and large values of Loss on Ignition (LOI), which is around 9 - 12 % and 4 % respectively. However, samples from Waterfall Beach (CX-19), Ethel Beach (CX-34), and Flying Fish Cove (CX-43) have LOI of ~3.5%, while the two samples from Sydney's Dale have LOI of 1.91 and 2.28 % (Table 6.2). The Total Alkali Silica (TAS) diagram shows that the Christmas Island volcanic rocks can be divided into two distinct geochemical units (Figure 6.5). The majority of these fall in the tephrite basanite-basalt domain, except those from Sydney's Dale, which are classified as trachytes. Geographically, the north and east coast sites are basaltic in composition with 4 - 5 wt.% Na_2O+K_2O and 45 - 50 wt.% SiO_2. The trachytes of Sydney's Dale have a higher Na_2O+K_2O and SiO_2 content at ~11 wt% and 60~ wt.% respectively (Figure 6.5).

The concentration of MgO is between 0.4 - 0.7 wt.% for the Sydney's Dale samples, whereas it is between 9 - 14 wt.% for the remaining samples (Figure 6.5). A similar observation is made for TiO_2, Fe_2O_3 and CaO, where the east coast samples have a higher concentration than the Sydney's Dale samples. The trend, however, is opposite for Al_2O_3 with the Sydney's Dale samples having a higher concentration than the others. The major element composition of the LVS and UVS are indistinguishable, as they all fall within the same compositional space,

except for Sydney's Dale (Figure 6.5). Two sampling locales, Ross Hill Garden and Golf Link, have very high CaO concentration indicating excessive carbonate alteration. The two locations also have low MgO, indication excessive alteration. Such values of CaO and MgO and high LOI values (Table 6.2) are indicative of secondary alteration.

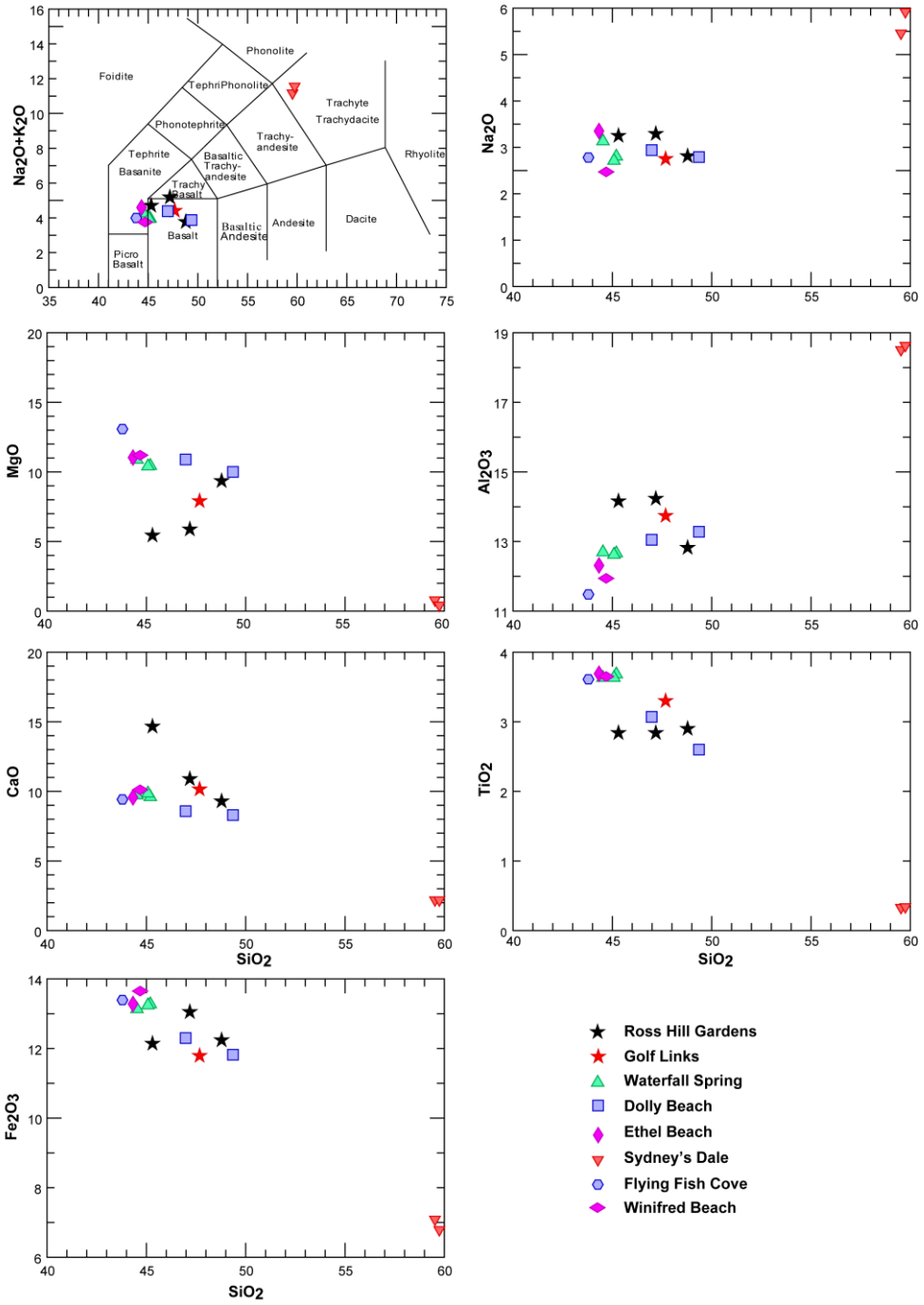

Figure 6.5: Total Alkali Silica (TAS) and major element composition diagrams for volcanic rocks from Christmas Island. Two samples from Sydney's Dale have a high SiO_2 content and similar trend can be seen in Al_2O_3, Na_2O, while they possess a negative correlation in CaO, TiO_2, and MgO. Geochemically LVS and UVS are similar in major element composition with the sample from Winifred Beach (UVS) falling close to samples from the Waterfall Spring, Ethel Beach, and Flying Fish Cove sites.

6.5.3: Trace Elements

Trace elemental concentrations for the Eocene volcanics are presented in Figure 6.6 and Table 6.2. The two volcanic suits (LVS & UVS) have similar trace element geochemistry except for the Sydney's Dale trachytes from the west coast.

All samples have Hf concentration of 4.6 – 8.6 ppm except the two Sydney's Dale trachytes, which have higher concentrations of 17.1 and 18.7 ppm. The Sydney's Dale trachytes have one-third of the amount of Ba compared to the rocks of the east coast and their Sr concentration is 30 and 40 ppm, compared to 460 – 1000 ppm from those on the east coast. The concentration of Th, U, and Nb is much higher for Sydney's Dale compared to other sampling sites within the LVS. In addition, the Ce concentration for Sydney's Dale is almost double those of Waterfall Spring, Ethel Beach, Dolly Beach, and Flying Fish Cove, and the same is true for most of the other incompatible elements. The trace element pattern of Christmas Island volcanic rocks has been compared (Figure 6.6 A and B) with those of Hoernle et al. (2011), along with that of OIB (Sun and McDonough, 1989). In general the trace element diagram for Christmas Island volcanic rocks is typical of OIB. Sydney's Dale trachytes have a distinct spidergram plot, whereas the others sampling sites follow a smoother trend. Trace element composition of the two trachytes from Sydney's Dale (Figure 6.6 D) shows heavy depletion in Ba, Sr, Ti, and V. The Sydney's Dale trachytes are enriched in Rb, Th, U, Nb, Ta, Zr, Hf and REE as compared to those from the Winifred Beach, and the LVS outcropping on the east coast. The primitive mantle normalised trend is enriched and parallel, with respect to HREE such as Tb, Dy, Ho, Y etc, as shown in Figure 6.6 D. REE for Christmas Island samples shows a smoother trend except for depletion in Eu and will be discussed in Section 6.6.5.

Table 6.2: Major and trace element composition for Christmas Island sampling sites. Major elements are given in wt.%, and trace elements are presented in ppm. Sample from Winifred Beach was analysed using XRF and not ICP-MS. Gaps represents no value was obtained for that element. * denotes that concentration in italics represents heavily weathered samples with a LOI of more than 4%. ' – ' signifies missing value.

	CX-21A	CX-21C	CX-22A	CX-26	CX-19A	CX-19B	CX-19C	CX-30B	CX-31	CX-34	CX-40	CX-41	CX-43	CX-33
	Ross Hill Gardens			Golf Link	Waterfall Spring			Dolly Beach		Ethel Beach	Sydney's Dale		Flying Fish Cove	Winifred Beach
Age (Taneja et al., 2014)	Lower Volcanic Sequence (LVS)													Upper Volcanic Sequence (UVS)
SiO_2	43.11	39.88	47.35	45.99	44.79	44.39	44.27	47.96	49.28	43.86	59.88	60.24	43.39	43.77
TiO_2	2.59	2.50	2.82	3.19	3.64	3.62	3.57	3.14	2.60	3.66	0.33	0.34	3.57	3.57
Al_2O_3	13.00	12.46	12.44	13.25	12.54	12.65	12.39	13.32	13.26	12.18	18.62	18.78	11.37	11.69
Fe_2O_3	11.92	10.69	11.88	11.37	13.15	13.09	13.00	12.56	11.80	13.14	7.13	6.85	13.26	13.37
MnO	0.08	0.08	0.13	0.17	0.15	0.15	0.15	0.15	0.14	0.15	0.21	0.18	0.15	0.16
MgO	5.38	4.79	9.07	7.63	10.33	10.84	10.21	11.12	9.98	10.91	0.79	0.42	12.96	10.97
CaO	9.95	12.90	9.01	9.79	9.50	9.68	9.67	8.76	8.29	9.47	2.22	2.20	9.33	9.90
Na_2O	3.00	2.86	2.73	2.65	2.77	3.12	2.66	3.01	2.79	3.32	5.50	5.97	2.75	2.42
K_2O	1.73	1.27	0.93	1.61	1.14	1.12	1.21	1.47	1.08	1.23	5.75	5.68	1.20	1.26
P_2O_5	0.60	0.59	0.68	0.82	1.08	1.04	1.07	0.59	0.63	1.04	0.17	0.17	1.07	0.82
SO3	< 0.01	< 0.01	0.02	0.15	0.06	0.06	0.05	0.09	0.02	0.63	0.54	0.57	0.48	0.06
S=O	-	-	-	-0.03	-0.01	-0.01	-0.01	-0.02	-	-0.13	-0.11	-0.11	-0.10	-
LOI	*9.61**	*12.58**	3.82	*4.16**	3.61	3.76	3.38	1.46	3.52	3.20	2.28	1.91	3.09	1.74
Total	100.96	100.60	100.89	100.75	102.74	103.49	101.61	103.60	103.37	102.65	103.30	103.20	102.53	99.72
Li	19.1	17.1	5.1	8.1	12.2	10.3	10.4	6.6	7.1	12.9	11.2	7.7	9.2	10.2
Be	1.5	1.5	1.6	1.5	2.1	2.0	1.9	1.9	2.7	2.1	6.6	6.1	1.9	2.0
Sc	21.1	19.8	21	21	21	20	19.0	26.6	26	20	19.2	18.0	19	27
Ti	16897	16155	17660	16406	23109	21651	20895	20829	21604	23649	2306	2121	21227	17359
V	155	146	177	169	207	195	188	229	225	210	1.2	1.3	184	236
Cr	285	288	320	327	295	270	269	313	329	339	4.5	4.3	367	297
Mn	701	727	1142	1191	1334	1235	1180	1387	1612	1323	1873	1520	1238	1269
Co	50.2	44.6	74.1	54.8	70.1	63.1	61.0	85.2	67.0	58	14.7	32.1	72.3	106
Ni	272	232	237	256	204	189	184	304	260	246	1.0	1.2	292	176

Cu	57.5	51.5	59.0	51.8	58.8	55.5	49.1	93.7	78.2	61	3.8	3.6	55.0	53
Zn	121	114.9	119	116	135	128	121	124.0	129	137	162	152	126	114
Ga	20.1	19.1	19.5	20	21.6	20.6	19.2	20.9	21.7	21	34.3	31.5	18.8	18.2
Rb	28.1	26.3	10.3	18	21.3	23.0	19.4	31.2	31.5	23	143.6	138.6	26.2	33.4
Sr	476	461	573	465	1028	981	913	592	978	1022	40	30	936	1058
Y	27.6	26.3	28	28	31.7	30.3	28.5	31	32	31	59	56	29	26.9
Zr	206	198	220	207	283	269	252	304	403	280	950	869	253	256
Nb	41.1	39.6	46.0	40.0	71.7	68.3	64.6	63.3	76.8	72.2	195	181	68.9	59.3
Mo	0.9	1.0	1.8	1.2	3.0	2.6	2.3	1.5	2.0	3.0	4.3	4.8	2.7	3.9
Cd	0.1	0.1	0.1	0.1	0.1	0.1	0.1	0.1	0.1	0.1	0.0	0.0	0.1	0.1
Cs	0.14	0.14	0.72	0.09	0.29	0.31	0.26	0.54	0.36	0.30	1.03	0.59	0.37	0.54
Ba	371	345	422	365	605	567	530	427	670	565	238	223	580	787
La	29.4	28.3	32.0	28.9	56.8	53.6	49.6	46.6	63.6	55.2	122.7	116.6	51.0	50.8
Ce	59.2	57.7	65.2	58.7	115	110	103	94.0	127	114	240	229	106	103
Pr	7.5	7.2	8.2	7.3	14.1	13.3	12.4	11.1	14.9	13.7	26.3	24.9	12.8	13.05
Nd	31.2	30.6	35.5	30.5	58.2	56.0	50.8	44.2	58.9	56.7	96.9	92.3	53.7	50.7
Sm	7.2	6.9	7.55	7.05	11.19	10.56	9.9	8.6	10.19	10.9	16.5	15.7	10.29	9.8
Eu	2.4	2.4	2.53	2.37	3.57	3.37	3.2	2.7	3.25	3.5	3.2	3.0	3.28	3.06
Tb	1.05	1.01	1.08	1.04	1.39	1.32	1.23	1.15	1.28	1.34	2.07	1.97	1.27	1.12
Gd	7.15	6.93	7.42	7.10	10.10	9.60	8.88	7.96	8.97	9.69	13.70	13.01	9.28	8.24
Dy	5.44	5.25	5.50	5.39	6.58	6.27	5.85	5.93	6.28	6.35	10.58	10.07	6.03	5.28
Ho	0.98	0.95	0.98	0.97	1.14	1.09	1.00	1.09	1.15	1.10	1.97	1.89	1.03	0.90
Er	2.37	2.29	2.35	2.36	2.63	2.51	2.31	2.68	2.83	2.52	5.12	4.89	2.35	2.11
Yb	1.70	1.64	1.65	1.70	1.77	1.69	1.57	1.97	2.13	1.68	4.18	3.98	1.58	1.47
Lu	0.23	0.22	0.22	0.23	0.24	0.23	0.21	0.27	0.30	0.22	0.59	0.57	0.21	0.18
Hf	4.77	4.60	4.93	4.65	6.29	5.94	5.48	6.60	8.58	5.96	18.68	17.13	5.46	5.42
Ta	2.31	2.20	2.67	2.21	4.18	3.95	3.70	3.80	4.41	3.81	10.31	9.76	3.86	4.24
Pb	3.10	2.98	3.33	2.98	4.26	4.02	3.72	4.38	6.30	3.99	9.55	9.65	3.53	6.11
Th	3.26	3.12	3.50	3.15	5.18	4.95	4.51	5.26	7.90	4.76	16.84	15.58	4.59	5.50
U	0.79	0.77	0.84	0.39	1.30	1.21	1.08	1.13	1.70	1.20	3.07	3.40	1.13	1.23

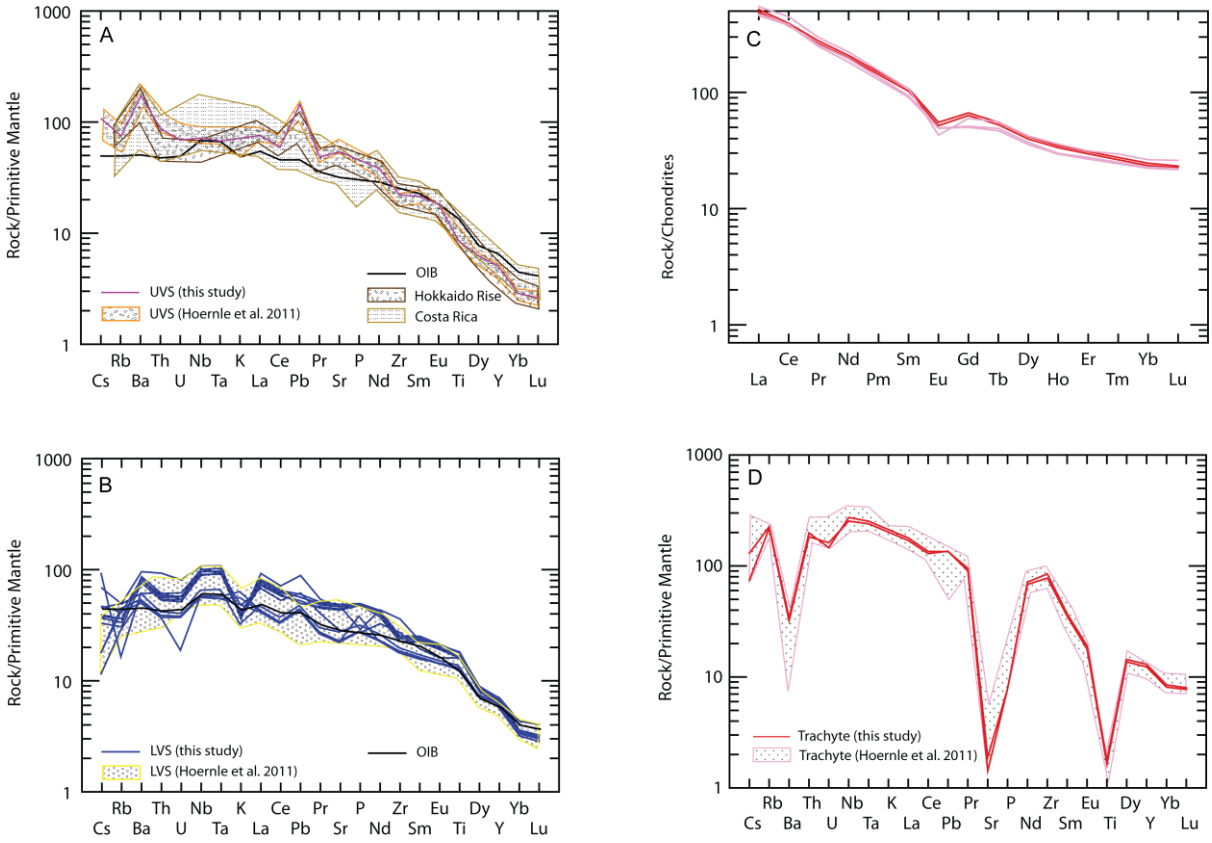

Figure 6.6: Trace element spider diagram plot for sampling sites from Christmas Island. A, UVS data from this study and results from Hoernle et al. (2011). Petit spot volcanism of Hirano et al. (2001), and Santa Rosa sills and lava flows from Costa Rica (Buchs et al., 2013) have been added for comparison with the UVS from Christmas Island. The trace element pattern of UVS correlates well with the Petit spot volcanoes of the NW Pacific Ocean and the Santa Rosa sills and lava flows from Costa Rica. B, LVS data from Christmas Island sampled in this study and dredged and land samples from Hoernle et al. (2011). C, REE normalised to Chondrites (Sun and McDonough, 1989) for the trachytes from Christmas Island. D, Trachytes at the Sydney's Dale locale and land samples from Hoernle et al. (2011). For discussion on trachytes see text (Section 6.6.5). All data is normalised to primitive mantle, and the OIB data is from Sun and McDonough (1989).

6.5.4: Hf, Nd, Pb Isotopes

The Christmas Island basalts from Dolly Beach fall on the lower side of the spectrum for $^{176}Hf/^{177}Hf$ (0.282810 - 0.282826) and $^{143}Nd/^{144}Nd$ (0.512684 - 0.512711). This locale also has the lowest ratios of $^{206}Pb/^{204}Pb$ (18.7874 & 18.8056), and one sample from Ross Hill Gardens (CX-22A) falls within the $^{206}Pb/^{204}Pb$ range of Dolly Beach. The two silica rich trachytes from Sydney's Dale have $^{176}Hf/^{177}Hf$ ratios of 0.2828339 and 0.2828347, and $^{143}Nd/^{144}Nd$ ratios of 0.5127155 and 0.5127123. On a $^{206}Pb/^{204}Pb$ versus $^{143}Nd/^{144}Nd$ diagram (Figure 6.7), Sydney's Dale trachytes and Dolly Beach basalts have the lowest $^{143}Nd/^{144}Nd$ ratios, and Dolly Beach has the lowest $^{206}Pb/^{204}Pb$ values. Dolly Beach and Sydney's Dale plot as a distinct unit separate from other sampling sites. On the $^{207}Pb/^{204}Pb$ vs $^{206}Pb/^{204}Pb$ variation diagram, all the sites sampled plot as a unit, but with the Sydney's Dale having a higher ratio, and Dolly Beach with the most extreme values of $^{207}Pb/^{204}Pb$. A single UVS sample from Winifred Beach (west coast) is similar in isotopic composition to the LVS. A repeat analysis conducted for Pb isotopes on this sample gave similar results confirming its isotopic similarity with the LVS (Table 6.3). Even though the samples from Ross Hill Gardens, and Golf Link are heavily weathered, they fall within the same isotope space of the LVS, and there is no clear distinction between weathered and fresh samples. This implies that weathering has not significantly altered their isotopic signatures (Table 6.3 and Figure 6.7).

Table 6.3: Hf, Nd, Pb isotope concentration for Christmas Island sampling sites. The sample from Winifred Beach (UVS) was re-analysed for Pb isotopes and duplicate results were obtained, but no duplicate Hf and Nd analyses were carried out for the second sample. All samples are from LVS, except the Winifred Beach sample. The external 2σ error on the Pb isotopes are of the order of ± 50 - 100 ppm. Pb isotopes ratios are measured values.

Location	Sample number	$^{176}Hf/^{177}Hf$	2 σ	eHf	$^{143}Nd/^{144}Nd$	2 σ	eNd	$^{206}Pb/^{204}Pb$	$^{207}Pb/^{204}Pb$	$^{208}Pb/^{204}Pb$
Ross Hill Gardens	CX-21A	0.282912	0.000003	4.94	0.512784	0.000004	2.84	18.8195	15.6123	38.8604
	CX-22A	0.282916	0.000004	5.09	0.512786	0.000005	2.89	18.7917	15.6053	38.8529
Golf Link	CX-26	0.282915	0.000003	5.05	0.512785	0.000004	2.87	18.8173	15.6099	38.9904
Waterfall Spring	CX-19A	0.282914	0.000004	5.03	0.512788	0.000004	2.92	18.8349	15.6113	38.9069
	CX-19B	0.282912	0.000004	4.96	0.512785	0.000004	2.87	18.8742	15.6304	38.9764
Dolly Beach	CX-30B	0.282826	0.000004	1.92	0.512711	0.000004	1.43	18.8056	15.5585	39.0013
	CX-31	0.282810	0.000004	1.34	0.512684	0.000006	0.89	18.7874	15.6417	39.0089
Ethel Beach	CX-34	0.282913	0.000004	4.99	0.512794	0.000006	3.05	18.8716	15.6051	38.9853
Sydney's Dale	CX-40	0.282835	0.000004	2.22	0.512712	0.000003	1.45	18.8347	15.6265	38.9819
	CX-41	0.282834	0.000004	2.19	0.512716	0.000005	1.51	18.9725	15.6402	39.1234
Flying Fish Cove	CX-43	0.282905	0.000003	4.71	0.512798	0.000006	3.12	18.8359	15.6136	38.9404
Winifred Beach (UVS)	CX-33	0.282917	0.000004	5.12	0.512792	0.000006	3.00	18.8776	15.6225	38.9552
	CX-33 (Dup)	-	-	-	-	-	-	18.8688	15.6187	38.9489

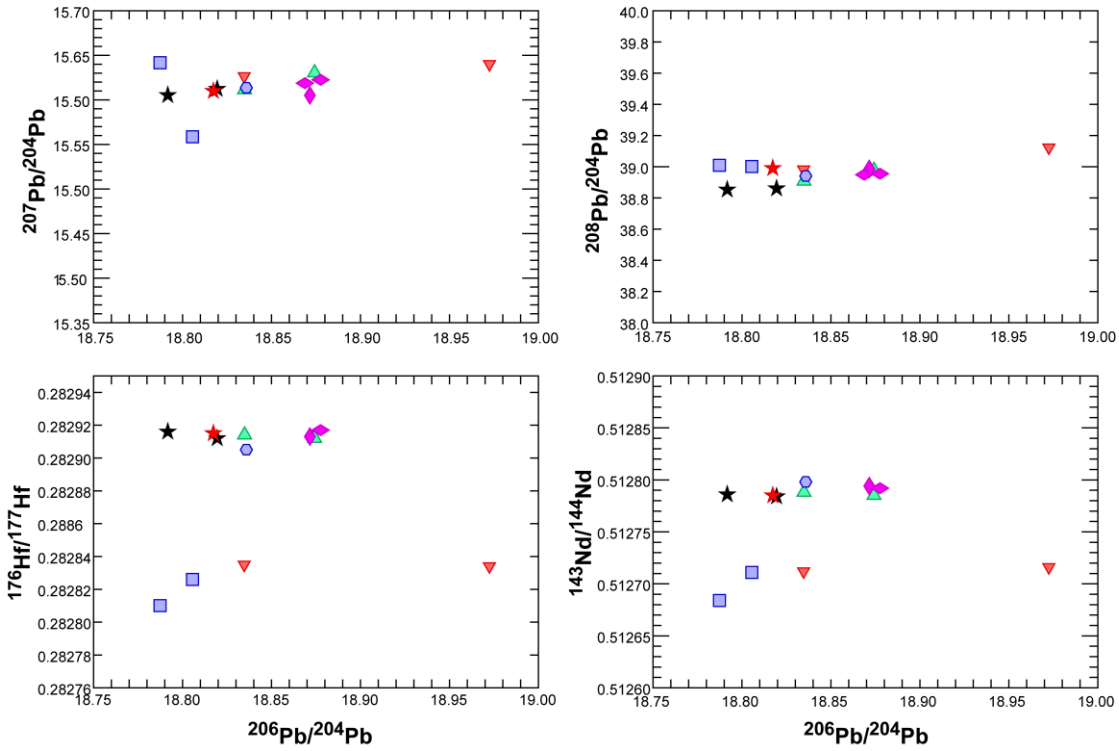

Figure 6.7: $^{206}Pb/^{204}Pb$ versus $^{143}Nd/^{144}Nd$, vs $^{176}Hf/^{177}Hf$, vs $^{207}Pb/^{204}Pb$ and $^{208}Pb/^{204}Pb$ isotopic correlation diagram for sampling sites from Christmas Island. The UVS sample was re-analysed for Pb isotopes, and a similar ratio was obtained as represented by pink horizontal diamond in the two plots on top. The duplicate sample was not re-analysed for Hf and Nd isotopes. Symbols are same as depicted in Figure 6.5.

6.6: Discussion

The aim of this geochemical investigation is to determine the relationship of Christmas Island basalts to the larger seamount province in the Northeast Indian Ocean. Hoernle et al. (2011) presented a detailed geochemical analysis, including major and trace element analyses (ICP-MS), and Sr-Nd-Hf-Pb isotope data (TIMS) for the submerged seamount province by dredging 38 submerged seamounts, and analysing land samples from Christmas Island. This study combines the data collected in this project with that collected by Hoernle et al. (2011).

OIB samples are susceptible to alteration by sea-water (Kelley et al., 2003; Hoernle et al., 2011). Halliday et al. (1995) compared OIB and MORB samples to analyse them for source enrichment and alteration patterns. The Chemical Index of Alteration (CIA) is a good indicator of weathering in volcanic rocks. The index value for basalts is between 30 and 45, with higher

values indicating stronger chemical weathering. The volcanic rocks from Christmas Island fall within 30 – 40. A large range in Ce/Pb and a positive correlation with U/Pb but not with Pb also indicates lack of any significant alteration. Halliday et al. (1995) analysed trace elements ratios of MORB and OIB samples and published canonical ratios that are indicator of alteration. Unaltered OIB's generally have Ce/Pb ratios of 35±11, Ce/U of 88±26, and Ba/Ce of 4.5±1.3. The samples from Christmas Island have a Ce/Pb, Ce/U and Ba/Ce values of 19 - 29 (except for Ross Hill Garden and Golf Links), 74 – 95 (except, 149 for one sample from Ross Hill Garden), and 4.5 – 6.4 (higher values for Ross Hill Garden and Golf Links), suggesting that these two sites have been be affected by alteration, as is apparent from visual inspection. The trachytes from Sydney's Dale fall within these ranges of Ce/Pb and Ce/U, except for Ba/Ce which is due to fractionation of plagioclase (see Section 6.6.5).

The samples from Christmas Island fall within the compositional range exhibited by the seamount province and those dredged from the flank around Christmas Island (Hoernle et al., 2011) as shown in Figure 6.9. The Lower Volcanic Sequence (LVS) and the Upper Volcanic Sequence (UVS) both sampled by Hoernle et al. (2011) are distinct in terms of their $^{206}Pb/^{204}Pb$ isotope ratios as shown in Figure 6.9. However, a single UVS (Winifred Beach) sample from this study falls within the domain of LVS. To ensure there was no error in analysis of this sample, it was re-analysed and the earlier result was reproduced confirming its occurrence within the LVS (Figure 6.7 and Table 6.3).

Christmas Island samples fall within the "Society-type" oceanic island basalts overlapping with a MORB signature as shown in $^{206}Pb/^{204}Pb$ vs. $^{207}Pb/^{204}Pb$ compositional space (White, 1985). The Society-type basalt group have high $^{207}Pb/^{204}Pb$ and $^{208}Pb/^{204}Pb$ ratios for a given $^{206}Pb/^{204}Pb$. These include the Society and Marquesas island chains of French Polynesia and Sao Miguel Island in the Azores (White, 1985). Various authors have also defined this high $^{207}Pb/^{204}Pb$ and $^{208}Pb/^{204}Pb$ for a given $^{206}Pb/^{204}Pb$ ratios as representing the DUPAL anomaly

in the southern hemisphere (Davies et al., 1989; Weis et al., 1989; Weis et al., 1991; Wen, 2006).

The vertical derivation of Pb isotopic anomaly that is representative of the DUPAL anomaly is calculated with reference to the Northern Hemisphere Reference Line (NHRL) as defined by Hart (1984), and is given below:

$$\left(\frac{^{207}\mathrm{Pb}}{^{204}\mathrm{Pb}}\right)\mathrm{NHRL} = 0.1084\left(\frac{^{206}\mathrm{Pb}}{^{204}\mathrm{Pb}}\right) + 13.491 \quad 6.1$$

$$\left(\frac{^{208}\mathrm{Pb}}{^{204}\mathrm{Pb}}\right)\mathrm{NHRL} = 1.2090\left(\frac{^{208}\mathrm{Pb}}{^{204}\mathrm{Pb}}\right) + 15.627 \quad 6.2$$

Hence, the magnitude of the isotopic anomaly defined as per the vertical derivation of individual $^{207}Pb/^{204}Pb$ and $^{208}Pb/^{204}Pb$ over that of $^{206}Pb/^{204}Pb$ is then defined as follows and presented in Appendix 2 Table 3.

$$\frac{\Delta 7}{4} = \left[\left(\frac{^{207}Pb}{^{204}Pb}\right) - \left(\frac{^{207}Pb}{^{204}Pb}\right)NHRL\right] * 100 \quad 6.3$$

$$\frac{\Delta 8}{4} = \left[\left(\frac{^{208}\mathrm{Pb}}{^{204}\mathrm{Pb}}\right) - \left(\frac{^{208}\mathrm{Pb}}{^{208}\mathrm{Pb}}\right)\mathrm{NHRL}\right] * 100 \quad 6.4$$

This study suggests that the two volcanic sequences (LVS and UVS) have a different mechanism for their origin. The Eocene phase of volcanism (44 – 37 Ma) is characterised by an EM 2 type component within the upper mantle, and also carries the DUPAL anomaly signatures of the Indian Ocean originating from the core mantle boundary. The Upper Volcanic Sequences (4.32 ± 0.17 Ma), on the other hand, represents magmatism that may be associated with decompressional melting in the flexed lithosphere as the Indo-Australian Plate subducts into the Java Trench. The mechanism for both the events is discussed in the following sections.

6.6.1: EM 2 & DUPAL anomaly signature in the LVS

One of the most common models for ocean island basalts is that they are sourced from enriched lower mantle that is distinct and isolated from the upper depleted mantle (Cohen and O'Nions, 1982; Morgan, 1971) from which MORB's are derived. Christmas Island OIB differs from those erupted on Hawaii in terms of their Pb isotopic compositions, with Hawaii IOB's having a composition of $^{208}Pb/^{204}Pb$ ~37.6; $^{206}Pb/^{204}Pb$ ~15.43; $^{206}Pb/^{204}Pb$ ~ 17.7 (White, 1985).

Hofmann (1997) notes that Indian Ocean MORB has higher ratio of $^{208}Pb/^{204}Pb$ and $^{87}Sr/^{86}Sr$ suggesting a source region different from that of Pacific and Atlantic MORB, and one that may have been contaminated either by ancient sediment or subcontinental lithosphere. Recycling of continental material within the upper mantle could account for the difference between the isotopic signature of Indian and Pacific-Atlantic MORB. Hofmann (1997) further notes that OIB's in the southern hemisphere are more enriched in EM-1 and EM-2 components. The Christmas Island basalts plot very close to the enriched mantle (EM-2) field showing intermediate radiogenic Pb isotope ratios (Figure 6.9). Hoernle et al. (2006) interprets such a close proximity to the EM field to reflect the influence of subduction-modified lithospheric mantle that is present in the shallow mantle.

Weaver (1991) discussed various OIB heterogeneity using trace elements where EM-2 type composition shows higher ratios of Rb/Nb, Th/Nb, La/Nb, Ba/Nb and Ba/La than HIMU, whereas, Rb/Nb, Ba/Nb, Ba/La are lower in EM-2 than EM-1 which is indicative of contamination by sediments. Samples from Christmas Island plot well within the EM-2 field, and different from HIMU and EM-1 range (Figure 6.8). The LVS and UVS sampled in this study and LVS by Hoernle et al. (2011) show an EM-2 signature, the UVS sampled by Hoernle et al. (2011) are closer to the EM-1 end member composition. Tatsumoto and Nakamura (1991) noted that such Nd and Pb composition shows an affinity with EM-2 type composition that are contaminated with subcontinental material.

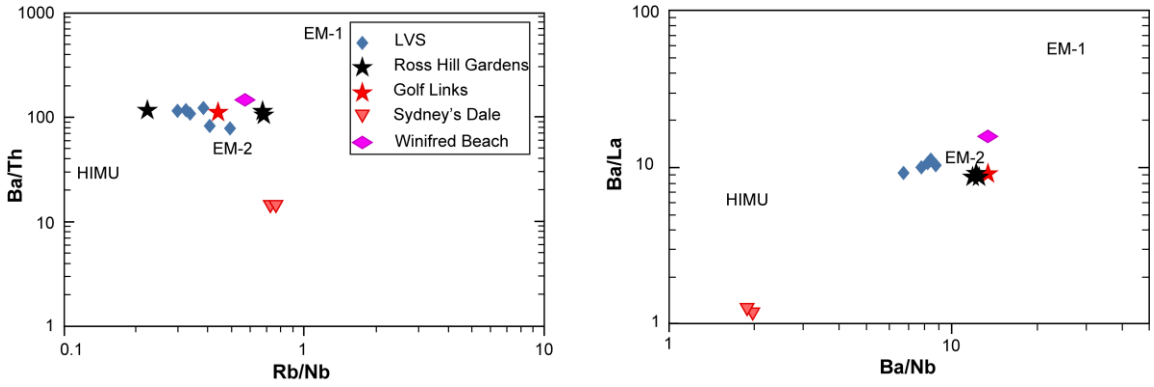

Figure 6.8: Selected trace element ratios showing the affinity of Christmas Island land samples to EM-2. All the samples including the weathered ones (Ross Hill Gardens and Golf Links) plot closer to the least weathered samples. A single UVS sample from this study is plotted within the LVS suggesting it sourced a similar chemical composition as that of LVS (also see Figure 6.9).

The Christmas Island Seamount Province is suggested to have been formed at a spreading ridge between India and Australia (Hoernle et al., 2011; Hall, 2012). The geochemical analyses by Hoernle et al (2011) display enriched EM-1 and EM-2 type compositions. The LVS from Christmas Island and the Cocos (Keeling) province sampled by Hoernle et al. (2011) have an EM-2 type compositions, while the UVS sampled by Hoernle et al. (2011) has an EM-1 type composition that is formed from small-scale heterogeneities of the recycled material in the upper mantle. They further suggested the source regions of the seamount province formed from mixing of Pacific/Atlantic MORB type mantle with Archaean continental lithosphere. Xu and Castillo (2004) derived similar observations that the OIB isotopic signature of Indian Ocean may be derived from contamination of upper mantle by delamination of sub-Asian lithosphere or the flow of Pacific and Atlantic MORB into the Indian Ocean suboceanic mantle in response to asthenospheric flow caused due to tectonic reorganisations from the opening and closure of ocean basins in the Gondwanan times. Hanan et al. (2004) further discussed that the Indian MORB signature is saturated with contamination from ancient recycled altered crust or with detachment and delamination of continental lithosphere into the lithosphere during rifting events during breakup of Gondwana.

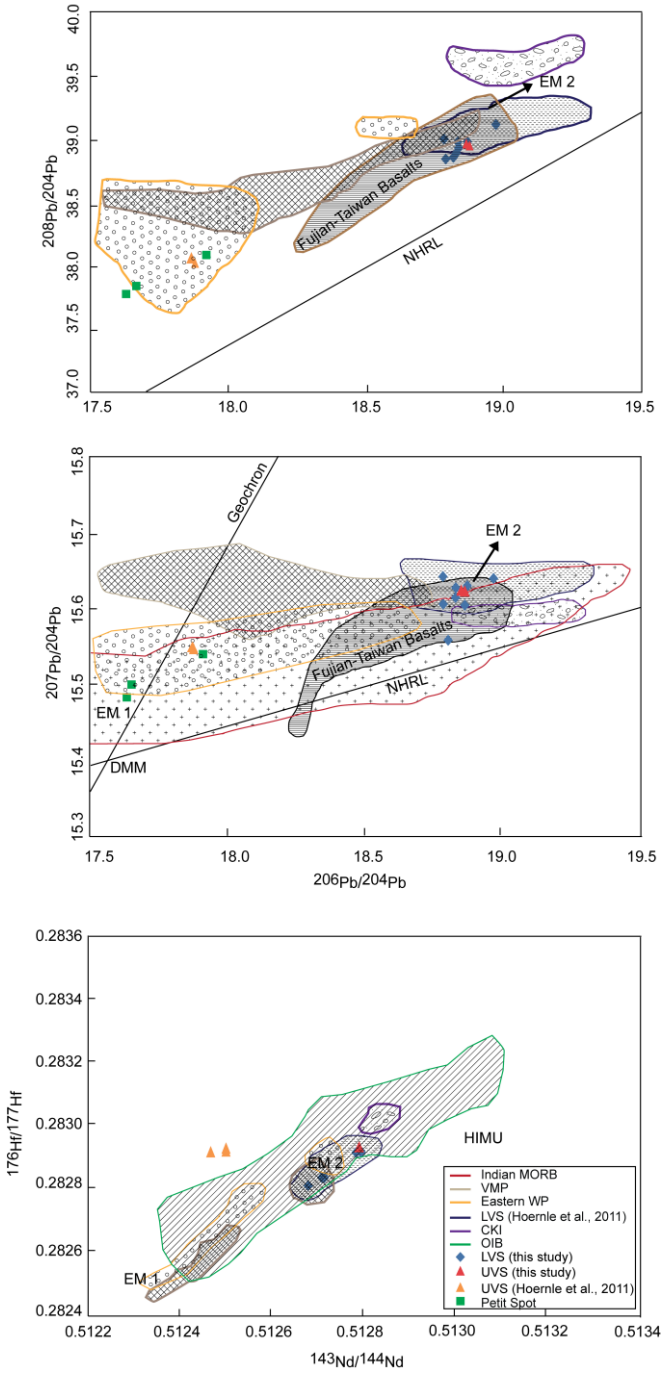

Figure 6.9: $^{206}Pb/^{204}Pb$ vs $^{207}Pb/^{204}Pb$ and $^{208}Pb/^{204}Pb$ and $^{143}Nd/^{144}Nd$ vs $^{176}Hf/^{177}Hf$ isotope diagram showing variation within LVS and UVS sequences from Christmas Island. A single UVS sampled in this study has an isotopic composition of LVS, which is distinct from those sampled by Hoernle et al. (2011). The similarity of UVS with the LVS of this study is also shown in Nd-Hf isotope diagram. LVS of Christmas Island (both this study and Hoernle et al, 2011), UVS (this study) and CKI lie closer to the EM-2 composition, whereas UVS of Hoernle et al. (2011) are closer to the EM-1 composition. UVS was re-analysed only for Pb isotopes (and not for Hf and Nd isotopes) and duplicate result was obtained. Also shown are Fujian-Taiwan Basalt, NHRL from Chung et al. (1995); Enriched mantle (EM 1, EM 2), and Depleted MORB Mantle (DMM) from Castillo (1996), Indian MORB, and Petit Spot field from Machida et al. (2009). WP is Wharton Province, VMP is Vening Meinesz Province (Hoernle et al., 2011). Also plotted are Wharton Province and Vening Meinesz Province that display a broad EM-2 to EM-1 composition.

The Pb isotopic ratios for Christmas Island LVS basalts have an EM-2 type character and, lie above the Northern Hemisphere Regression Line (Chung et al., 1995; Hart, 1984; Zindler and Hart, 1986) as shown in Figure 6.9. This is similar to that of the South China Sea, and Fujian-Taiwan basalts (Chung et al., 1994; Tu et al., 1992). Chung et al. (1994) suggested that a rifted continental mantle fragment from Gondwanaland could have been mixed into the convecting asthenosphere to provide the source for the Fujian-Taiwan basalts. Hoernle et al. (2011) suggested a similar model for the Christmas Island Seamount Province where the separation of the West Burma block from Greater India and Australia led to shallow recycling of lithospheric mantle under a mid-oceanic ridge.

A steep trajectory in $^{208}Pb/^{204}Pb$, and $^{207}Pb/^{204}Pb$ vs $^{206}Pb/^{204}Pb$ space is often taken as an indication of contamination by silicic crust or sediments in a subduction zone (Tu et al., 1991). However, Christmas Island basalts form an array parallel to the NHRL implying a strong relationship with the DUPAL anomaly (Figure 6.9). Weis et al. (1991) have suggested that the DUPAL anomaly has an ancient source and this could have important implications for the Indian Ocean region as the sub continental lithosphere could have been delaminated during the dispersal of Gondwana along the western margin of Australia. They further suggested, on the basis of the Ninetyeast Ridge, and Heard Island samples, that the DUPAL anomaly is deep seated. It is quite possible that the EM -2 type component pre-existed within the upper mantle, and following the dispersal of Gondwana mixed with the DUPAL source. The source for the DUPAL anomaly is, however, controversial. Some of the earlier works (e.g. Rekhamper and Hoffman, 1997) argue that the source of DUPAL is large-scale mantle contamination by ancient recycled sediments or delaminated continental lithosphere. Goldstein et al. (2008) proposed that the anomaly in the Arctic upper mantle is a result of subcontinental lithospheric mantle. Other recent studies proposed that the isotopic signature of the Indian Ocean DUPAL

is due to large amounts of recycled lower continental crust (Escrig et al., 2004; Hanan et al., 2004; Nishio et al., 2007).

Hart (1988) suggested that the DUPAL anomaly is associated with ocean island basalts and also contains EM-1 and EM-2 signatures. Such a signature is observed in volcanic rocks from South China Sea (Tu et al., 1991) and also from the neighbouring Philippine Island arc (Castillo, 1996). Cross contamination due to heterogeneous mixing both of DUPAL-type compositional signatures, with an EM-2 type composition, might have produced the source material for the province.

6.6.2: Seismically determined DUPAL anomaly in the region

The DUPAL anomaly is geographically extensive, extending from the South Atlantic well into the Indian Ocean, as well as being observed in the Pacific Ocean (Hart, 1984; Klein et al., 1988; Castillo, 1988). Few studies have investigated the seismic properties of the deep mantle DUPAL anomaly. Wen (2001) discussed a seismic velocity anomaly 200 km from the core mantle boundary beneath the Indian Ocean, associated with compositional variations within the Ultra-Low Velocity Zone (ULVZ) that may have formed early during Earth's history. Seismic models by Wen (2001, 2006) further show these velocity anomalies have steep dipping edges. The relationship between the DUPAL anomaly, the reconstructed Ninetyeast Ridge, and several other volcanic islands near the seismic anomaly have been discussed by Weis et al. (1989) and Wen (2001). Wen (2001) concludes that the compositional variation of this reduced seismic velocity layer could have a relationship with the DUPAL signature at the surface. Moreover, Wen (2006) suggests that three hotspots (Tristan, Marion, and Kerguelen) coincide with the DUPAL anomaly and that the Ninetyeast Ridge is a surface expression of this anomaly. Using seismic techniques, Wen (2001) suggested a boundary for the anomaly at the

core-mantle boundary that extends to ~98°E and past 40°S, covering the Kerguelen Plateau, Broken Ridge, and parts of the Ninetyeast Ridge.

The Eocene reconstructed position of Christmas Island lies at the edge of the seismically determined compositionally distinct layer that Wen (2001) associates with the DUPAL anomaly. Anomalously high $^{207}Pb/^{204}Pb$ and $^{208}Pb/^{204}Pb$ ratios, for given $^{206}Pb/^{204}Pb$ ratios have been noted for basalts from the Indian Ocean and the mantle entity associated with the anomaly may have existed for billions of years (Hart, 1984; Castillo, 1988; Wen, 2000). There are other hotspots (Reunion, Comoros) that fall outside of the seismically determined DUPAL boundary but are in the vicinity of this very low velocity anomaly (Wen, 2006). Wen (2006) suggests horizontal stress experienced in this low velocity province interacts with the surrounding mantle that causes thickening of the basal thermal boundary layer leading to the development of the thermal plumes. This idea is supported by the existence of small-scale heterogeneity at the lower mantle boundary underneath the Comoros hotspot (Wen, 2000). The CHRISP may have been influenced by similar dynamics, as the reconstructed position of the volcanic province is near an early rift between the western margin of Australia and Greater India ca. 150 Ma that also falls within the boundary zone of the very low velocity province.

6.6.3: Likelihood of "double flood basalt" mechanism producing a time gap?

A model of double flood basalts was proposed by Bercovici and Mahoney (1994), where non-linear ascent may lead to a second plume "head" on the trailing conduit, resulting in two major volcanic events for a given plume. These flood basalts may be separated by 20 to 40 million years (Bercovici and Mahoney, 1994). The head separates due to viscosity changes from the lower mantle to the upper mantle, and the decapitated conduit emerges later. This, however, conflicts with the continuous volcanic activity observed in the seamount province, which is without any major time lag, from 136 Ma up to 37 Ma (Hoernle et al., 2011). It can, however, be argued that Christmas Island did experience its oldest activity in the Late Cretaceous, prior

to a second major event in the Eocene (44 – 37 Ma, Taneja et al. (2014)). Though there may be a time gap, there is no age or geochemical data to analyse the oldest event and its mechanism. Similarly there is a gap of more than 30 million years between the Eocene event and the Pliocene event but the double flood basalt mechanism of Bercovici and Mahoney (1994) doesn't seem plausible here as the youngest event is readily explained as a product of lithospheric cracking-induced partial melting (see below). Moreover, if it is assumed that the Pliocene event is a trailer plume of the Eocene event, the volcanic expression should lie further south, near the reconstructed position of the intermediate event, and not in the north around ~13°S (Taneja et al., 2014).

6.6.4: Lithospheric flexure induced UVS

The major and trace element compositions of the UVS is similar to the LVS (Figure 6.5 and Figure 6.6). Both dredged and land samples analysed by Hoernle et al. (2011) have a similar geochemistry to their counterparts from this study. Isotopically, on Pb variation diagrams, the younger volcanic sequences sampled by Hoernle et al. (2011) are distinct from the Eocene phase and are closer to the EM-1 component field, though one of the samples (Winifred Beach, from this study) within the UVS has an Eocene EM-2 signature (Figure 6.9). Therefore, the single UVS sample from Winifred Beach may have intermittently tapped the composition of the LVS (Eocene-source) material. This has important implications for CHRISP as it demonstrates that the older Eocene (Hoernle at el., 2011, Taneja et al., 2014) composition was present at 5 Ma. The composition of this phase (LVS, and UVS of this study) is similar to that of the Indian MORB and possesses DUPAL signatures much like their older counterparts (Figure 6.9).

The upper volcanic suite of rocks on Christmas Island have a high K_2O content and Na_2O+K_2O ratios similar to the petit spot volcanoes of Hokkaido Rise (Hirano et al., 2001), and the Santa Rosa sills and lava flows in Costa Rica (Buchs et al., 2013). The trace element pattern of the

UVS sequence follows the pattern of the Hokkaido Rise and Santa Rosa petit spot volcanoes (Figure 6.6). Hirano et al. (2001) suggested that petit spot volcanoes are formed due to decompressional melting in the flexed lithosphere undergoing subduction. Bending of the lithosphere in this case causes fracturing through which melt rises upward to appear at the surface in form of petit spot volcanoes (Hirano et al. 2001). Such a tectonic setting is prevalent in the Northeast Indian Ocean as the Indo-Australian Plate subducts underneath the Sunda-Java Trench (Levitt and Sandwell, 1995).

Due to similarities in the geochemistry of the UVS with the petit spot volcanoes of Hirano et al. (2011) (Figure 6.6), and the lithospheric flexure due to subducting slabs in both tectonic settings (Taneja et al., 2014), we will ascertain if a similar mechanism could produce the younger volcanic sequences on Christmas Island. As the Indo-Australian Plate is subducting underneath the Java Trench, the downgoing slab is flexed upwards prior to subduction (Watts, 2001). Since this type of volcanic exposure is formed on the outer side of the bulge (Hirano et al., 2006), Christmas Island's position was back-tracked to determine if its palaeoposition coincided with the flexed part of the lithosphere. The island presently sits on the bulge of the convex lithosphere, and flexure due to subduction is overprinted by the loading of Christmas Island, and Golden Bo' Sunbird seamount southwest of it (Taneja and O'Neill, 2014).

Using plate motion rates of 7 cm/yr, a reconstructed position 302 ± 11.9 km southwest of the present position has been calculated for the Pliocene phase occuring at 4.32 Ma **(**Taneja et al. (2014). This position lies at the nascent bulge, and where the oceanic lithosphere undergoes significant stress changes, which may permit extraction of magma to the ocean floor. Younger volcanism reported from the Murray Hill regions is suggested to have resulted in faulting and emplacement of dykes and sills (Grimes, 2001). The exposure of this low volume phase of volcanism along Christmas Island's western edge at Winifred Beach, emplaced through the older volcanic core, bears similarity to Hirano et al.'s (2006) model of petit spot volcanoes.

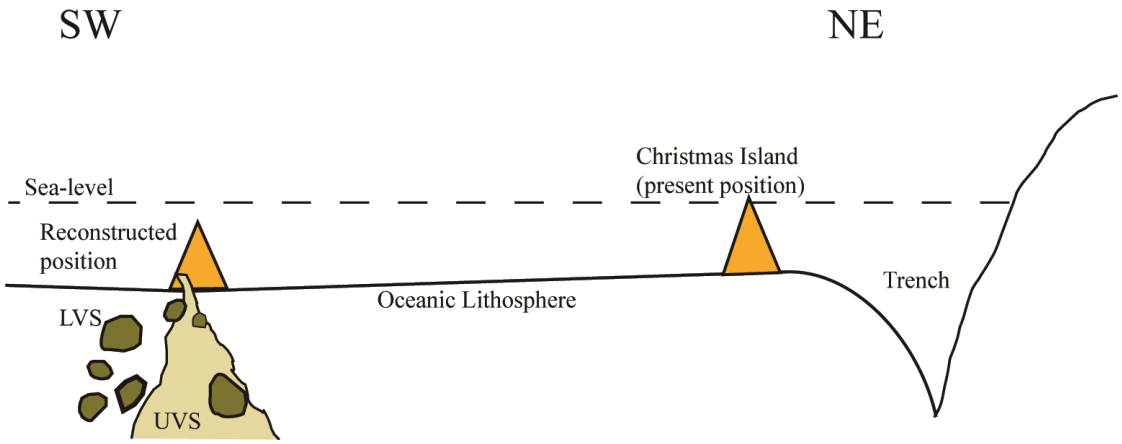

Figure 6.10: A proposed diagrammatic representation of the Upper Volcanic Sequence in the Pliocene and the lower volcanic event at Christmas Island and the reconstructed position of the island before the bulge. The cracks in the oceanic lithosphere act as conduits through which molten material rises up (Hirano et al, 2001). The exact depth of the source material and the number of cracks within the lithosphere is unknown. One of the Upper Volcanic samples (Winifred Beach) has LVS type composition that has been sourced from a pre-existing LVS material shown by dark green blobs.

The reconstructed position of the Island in the Pliocene is at the edge of a low velocity zone that stretches up to 25°S and can be traced further below 30°S. Although this is a very large low velocity zone (Mégnin and Romanowicz, 2000; Ritsema et al., 1999), it is highly doubtful there is any contribution from it. The Pliocene phase is a low volume event (Grimes, 2001), and any contribution from a mantle plume would be expected to be several orders of magnitude larger (Hirano et al., 2006).

Although geochemical similarity of Christmas Island basalts with the petit spot volcanoes of Hirano et al. (2001) does not uniquely define them to the tectonic setting, it does support the model based on back-tracking the island's position using plate motion rates, plate reconstruction, and lithospheric flexure. Cracking associated with the lithospheric bulge suggests its formation through magma infiltration in a tensional lower lithospheric regime at the nascent fore-bulge (Hirano et al. 2001). An enriched incompatible composition and high alkali nature indicates these type of basalts are formed due to low degree of partial melting (Buchs et al., 2013). The two different geochemical reservoirs sampled as part of the UVS suggests the older LVS component is present within the lithosphere/asthenosphere (Figure

6.10). This suggests that older geochemical source compositions can survive within the upper mantle for millions of years and be re-trapped by renewed volcanism.

6.6.5: Occurrence of trachytes at Christmas Island

One of the compositionally interesting samples from Christmas Island obtained in this study and sampled by Hoernle et al. (2011) exhibits a trachytic texture. Magma that formed the trachytes of Sydney's Dale probably stalled long enough to differentiate, and hence have a signature totally distinct from the rest of the group. Various models have been put forward to explain the presence of trachytes; including fractional crystallisation (West et al., 1988; Weis et al., 1993; Cousens et al., 2003), partial melting (Lightfoot et al., 1987) or assimilation of crustal components (Chen et al., 2012; Angelo et al., 2013). Vervoort and Green (1997) suggests that trachytes are highly fractionated assemblages that have evolved from mafic compositions. The evolved nature of the trachyte, having low CaO, TiO_2, Fe_2O_3, and MgO, and high Al_2O3 and Na_2O, suggest fractionation from their mafic counterparts. This is supported by highly fractionated trace element composition compared to the LVS (Figure 6.6), enriched (Figure 6.11) Zr/Hf and Rb/Sr ratios, and lower Sr/Nd, Ba/Th, and Ba/Nb ratios (Weis et al., 1993). Trachytes of Sydney's Dale also have very low Sr (Table 6.2), and very low Sr/Nd ratio of ~0.35 (compared to ~16 for LVS) and negative Eu anomaly which are strong indicators of fractional crystallisation. Such low Sr/Nd ratios are strong indicators of feldspar fractionation (Weis et al., 1993). Very low Sr concentration relative to Ce and Nd is evident in the trace element spider diagram (Figure 6.6 D) is due to plagioclase fractionation (Weaver et al., 1987) which forms the dominant composition of trachytes (Figure 6.4).

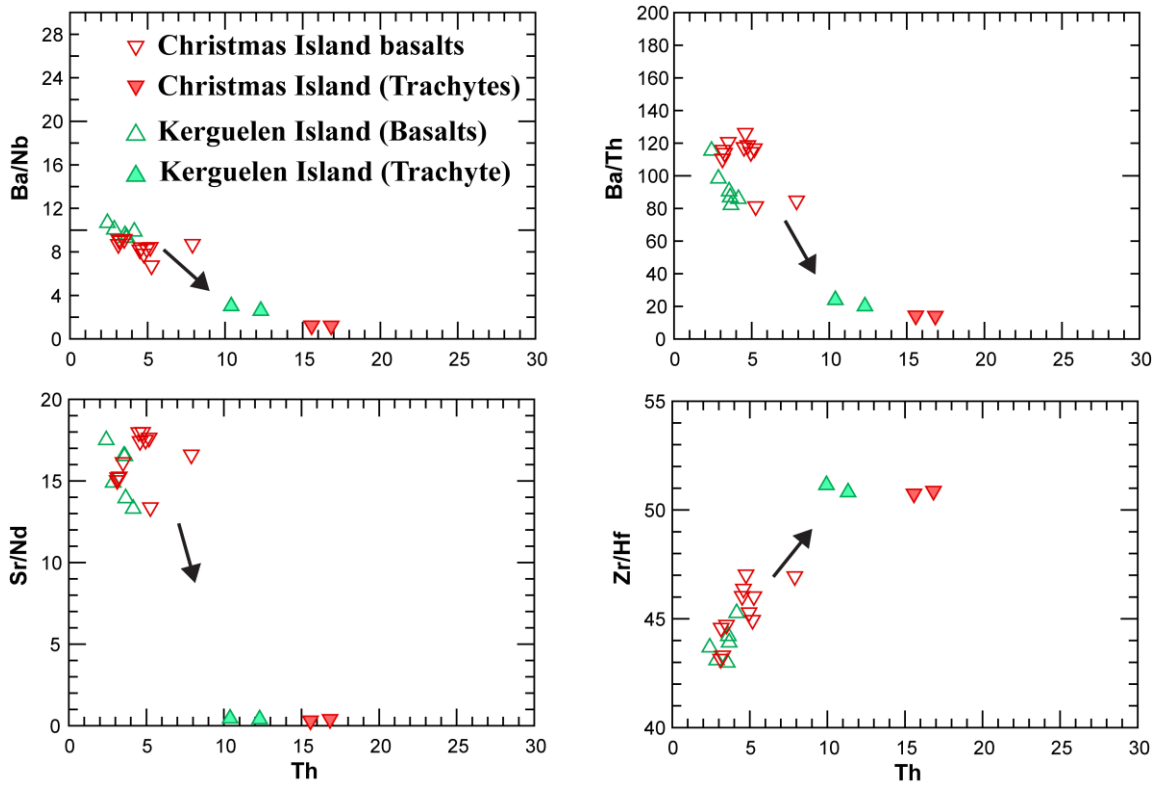

Figure 6.11: Selected trace element ratios vs. Th abundance for the trachyte from Sydney's Dale. Trachytes and basalts for the Kerguelen Archipelago are from Weis et al. (1993). Trachytes from Christmas Island have a similar trend as those from Southern Province of the Kerguelen Archipelago that have undergone extreme fractionalisation from their parental magma composition.

Weis et al. (1993) documented low TiO_2 and V contents of the trachytes from the Kerguelen Archipelago that appear to be related to segregation of Fe-Ti oxides from their parental basalts. Angelo et al. (2013) also observed negative anomalies of Ba, Sr, and Ti that point towards fractionation of alkali feldspar, plagioclase and Fe-Ti oxides in the trachytic rocks of Ponza Island (Italy) of the Pontine Archipelago. Trachytes from Christmas Island exhibit such negative anomalies (Figure 6.6 C and D). Chen et al. (2012) documented high Zr/Nb ratios in Miocene trachytes from Lhasa block of the Tibetan Plateau, and suggested fractional crystallisation of these trachytes from their parental alkali lavas. Since the LVS falls within the same isotopic space, the major and trace element abundances of the trachytes may reflect extreme fractionation of comparable basalts, in a similar fashion to that documented by Weis et al. (1993) for trachytes from the Southeast Province of the Kerguelen Archipelago (Figure 6.11).

If crustal contamination is invoked as a possible mechanism for the occurrences of trachyte then they should not have negative Sr and Eu anomalies (Chen et al., 2012) which is not the case for trachytes of Christmas Island (Figure 6.6 C and D). Though there is a shift in the Pb isotopes for one trachyte sample, a fractional crystallisation model is favoured due to pronounced negative Ba, Sr, Ti and Eu anomalies. An overlap in isotopic composition between parental basalts and trachyte (Figure 6.7) strongly point towards fractional crystallisation from a parental basaltic magma (Cousens et al., 2003). A more quantitative model for the trachyte formation require detailed information on the mineralogical, and chemical makeup of the samples, and a larger sample base than that available to this study.

6.7: Conclusion

The basaltic rocks at Christmas Island are the sole sub-aerially exposed representative of intraplate volcanism that formed the Christmas Island Seamount Province. The geochemical analyses of these rocks have documented mantle heterogeneities within the upper mantle, particularly near the Eocene reconstructed position of Christmas Island. The Lower Volcanic Sequence exhibits an enriched mantle (EM-2) type end member composition showing intermediate radiogenic Pb and Nd ratios. Such a composition can be produced from either the injection of sediments within the upper mantle, or through contamination by continental lithosphere following the dispersal of Gondwana. The Eocene phase also contains a DUPAL anomaly signature, a long-lived mantle heterogeneity that has been argued to have a deep origin (Wen, 2001). Seismic models by Wen (2001, 2006) have characterised this as a compositionally distinct layer near the core mantle boundary.

The UVS, however, is most likely a product of plate flexure produced on the outer rise of the flexed oceanic lithosphere as it subducts under the Java Trench. A torsional stress regime at the inflection of this flexure can facilitate melt infiltration, causing magma to rise up to in the

form of low volume "petit spot" volcanism (Hirano et al., 2001, 2006) with an EM-1 type component (Machida et al., 2009). One of the UVS specimens falling within the domain of LVS has sampled the pre-existing EM-2 source material suggesting that the older EM-2 composition is present underneath the seamount province. Outcropping of trachytes at Sydney's Dale in an oceanic island are unsual and appear to have been derived from extreme fractional crystallisation of basaltic parental magma.

References

Andrews, C.W., 1900. A monograph of Christmas Island (Indian Ocean): Physical Features and Geology. British Museum (Natural History), London

Angelo, P., 2013. Petrogenesis of trachyte and rhyolite magmas on Ponza Island (Italy) and its relationship to the Campanian magmatism. Journal of Volcanology and Geothermal Research, 267(0): 15-29.

Ballmer, M.D., van Hunen, J., Ito, G., Bianco, T.A. and Tackley, P.J., 2009. Intraplate volcanism with complex age-distance patterns: A case for small-scale sublithospheric convection. Geochemistry, Geophysics, Geosystems, 10(6): Q06015.

Barrie, J., 1967. The Geology of Christmas Island. Bureau of Mineral Resources, Australia, Canberra, 104.

Bercovici, D. and Mahoney, J., 1994. Double Flood Basalts and Plume Head Separation at the 660-Kilometer Discontinuity. Science, 266(5189): 1367-1369.

Blichert-Toft, J. and Albarède, F., 2009. Mixing of isotopic heterogeneities in the Mauna Kea plume conduit. Earth and Planetary Science Letters, 282(1-4): 190-200.

Bonatti, E. and Harrison, C., 1976. Hot lines in the Earth's mantle. Nature, 263(5576): 402-404.

Buchs, D.M., Pilet, S., Cosca, M., Flores, K.E., Bandini, A.N. and Baumgartner, P.O., 2013. Low-volume intraplate volcanism in the Early/Middle Jurassic Pacific basin documented by accreted sequences in Costa Rica. Geochemistry, Geophysics, Geosystems, 14(5): 1552-1568.

Castillo, P., 1988. The Dupal anomaly as a trace of the upwelling lower mantle. Nature, 336(6200): 667-670.

Castillo, P.R., 1996. Origin and geodynamic implication of the Dupal isotopic anomaly in volcanic rocks from the Philippine island arcs. Geology, 24(3): 271-274.

Chen, J.-L., Zhao, W.-X., Xu, J.-F., Wang, B.-D. and Kang, Z.-Q., 2012. Geochemistry of Miocene trachytes in Bugasi, Lhasa block, Tibetan Plateau: Mixing products between mantle- and crust-derived melts? Gondwana Research, 21(1): 112-122.

Chung, S.-L., Jahn, B.-M., Chen, S.-J., Lee, T. and Chen, C.-H., 1995. Miocene basalts in northwestern Taiwan: Evidence for EM-type mantle sources in the continental lithosphere. Geochimica et Cosmochimica Acta, 59(3): 549-555.

Chung, S.-L., Sun, S.-s., Tu, K., Chen, C.-H. and Lee, C.-y., 1994. Late Cenozoic basaltic volcanism around the Taiwan Strait, SE China: product of lithosphere-asthenosphere interaction during continental extension. Chemical Geology, 112(1): 1-20.

Cohen, R.S. and O'Nions, R.K., 1982. The Lead, Neodymium and Strontium Isotopic Structure of Ocean Ridge Basalts. Journal of Petrology, 23(3): 299-324.

Courtillot, V., Davaille, A., Besse, J. and Stock, J., 2003. Three distinct types of hotspots in the Earth's mantle. Earth and Planetary Science Letters, 205(3-4): 295-308.

Cousens, B.L., Clague, D.A. and Sharp, W.D., 2003. Chronology, chemistry, and origin of trachytes from Hualalai Volcano, Hawaii. Geochemistry, Geophysics, Geosystems, 4(9): 1078.

Davies, H.L., Sun, S.s., Frey, F.A., Gautier, I., McCulloch, M.T., Price, R.C., Bassias, Y., Klootwijk, C.T. and Leclaire, L., 1989. Basalt basement from the Kerguelen Plateau and the trail of a Dupal plume. Contributions to Mineralogy and Petrology, 103(4): 457-469.

Davis, A.S., Gray, L.B., Clague, D.A. and Hein, J.R., 2002. The Line Islands revisited: New $^{40}Ar/^{39}Ar$ geochronologic evidence for episodes of volcanism due to lithospheric extension. Geochemistry, Geophysics, Geosystems, 3(3): 1-28.

Duncan, R.A., 1978. Geochronology of basalts from the ninetyeast ridge and continental dispersion in the eastern Indian Ocean. Journal of Volcanology and Geothermal Research, 4(3-4): 283-305.

Duncan, R.A., 1984. Age progressive volcanism in the New England Seamounts and the opening of the central Atlantic Ocean. Journal of Geophysical Research: Solid Earth, 89(B12): 9980-9990.

Duncan, R.A., 1990. The volcanic record of the Reunion hotspot. In: R. Duncan, J. Backman and L. Peterson (Editors), Proceedings of Ocean Drilling Program Scientific Results, College Station, TX (Ocean Drilling Program), pp. 3-10.

Duncan, R.A., 1991. 26. Age distribution of volcanism along aseismic ridges in the eastern Indian Ocean. In: J. Weissel, J. Peirce, E. Taylor and J. Alt (Editors), Proceedings of the Ocean Drilling Program, Scientific Results, 121, College Station, TX: Ocean Drilling Program, pp. 507-517.

Duncan, R.A., McCulloch, M., Barsczus, H.G. and Nelson, D., 1986. Plume versus lithospheric sources for melts at Ua Pou, Marquesas Islands. Nature, 322: 534-538

Dupré, B. and Allègre, C.J., 1983. Pb-Sr isotope variation in Indian Ocean basalts and mixing phenomena. Nature, 303(5913): 142-146.

Escrig, S., Capmas, F., Dupré, B. and Allègre, C., 2004. Osmium isotopic constraints on the nature of the DUPAL anomaly from Indian mid-ocean-ridge basalts. Nature, 431(7004): 59-63.

Frey, F.A., Coffin, M.F., Wallace, P.J., Weis, D., Zhao, X., Wise Jr, S.W., Wähnert, V., Teagle, D.A.H., Saccocia, P.J., Reusch, D.N., Pringle, M.S., Nicolaysen, K.E., Neal, C.R., Müller, R.D., Moore, C.L., Mahoney, J.J., Keszthelyi, L., Inokuchi, H., Duncan, R.A., Delius, H., Damuth, J.E., Damasceno, D., Coxall, H.K., Borre, M.K., Boehm, F., Barling, J., Arndt, N.T. and Antretter, M., 2000. Origin and evolution of a submarine large igneous province: the Kerguelen Plateau and Broken Ridge, southern Indian Ocean. Earth and Planetary Science Letters, 176(1): 73-89.

Fujiwara, T., Hirano, N., Abe, N. and Takizawa, K., 2007. Subsurface structure of the “petit-spot” volcanoes on the northwestern Pacific Plate. Geophysical Research Letters, 34(13): L13305.

Gans, K.D., Wilson, D.S. and Macdonald, K.C., 2003. Pacific Plate gravity lineaments: Diffuse extension or thermal contraction? Geochemistry, Geophysics, Geosystems, 4(9): 1074.

Geldmacher, J., Hoernle, K., Bogaard, P.v.d., Duggen, S. and Werner, R., 2005. New $^{40}Ar/^{39}Ar$ age and geochemical data from seamounts in the Canary and Madeira volcanic provinces: Support for the mantle plume hypothesis. Earth and Planetary Science Letters, 237(1-2): 85-101.

Goldstein, S.L., Soffer, G., Langmuir, C.H., Lehnert, K.A., Graham, D.W. and Michael, P.J., 2008. Origin of a 'Southern Hemisphere' geochemical signature in the Arctic upper mantle. Nature, 453(7191): 89-93.

Grimes, K.G., 2001. Karst Features of Christmas Islands. Helictite, 37: 41-58.

Haase, K.M., 1996. The relationship between the age of the lithosphere and the composition of oceanic magmas: Constraints on partial melting, mantle sources and the thermal structure of the plates. Earth and Planetary Science Letters, 144(1-2): 75-92.

Hall, R., 2012. Late Jurassic-Cenozoic reconstructions of the Indonesian region and the Indian Ocean. Tectonophysics, 570-571: 1-41.

Halliday, A.N., Lee, D.-C., Tommasini, S., Davies, G.R., Paslick, C.R., Godfrey Fitton, J. and James, D.E., 1995. Incompatible trace elements in OIB and MORB and source enrichment in the sub-oceanic mantle. Earth and Planetary Science Letters, 133(3-4): 379-395.

Hanan, B.B., Blichert-Toft, J., Pyle, D.G. and Christie, D.M., 2004. Contrasting origins of the upper mantle revealed by hafnium and lead isotopes from the Southeast Indian Ridge. Nature, 432(7013): 91-94.

Hart, S.R., 1984. A large-scale isotope anomaly in the Southern Hemisphere mantle. Nature, 309: 753-757.

Hart, S.R., 1988. Heterogeneous mantle domains: signatures, genesis and mixing chronologies. Earth and Planetary Science Letters, 90(3): 273-296.

Heine, C. and Müller, R.D., 2005. Late Jurassic rifting along the Australian North West Shelf: margin geometry and spreading ridge configuration. Australian Journal of Earth

Sciences: An International Geoscience Journal of the Geological Society of Australia, 52(1): 27 - 39.

Hirano, N., Kawamura, K., Hattori, M., Saito, K. and Ogawa, Y., 2001. A new type of intra-plate volcanism; Young alkali-basalts discovered from the subducting Pacific Plate, Northern Japan Trench. Geophysical Research Letters, 28(14): 2719-2722.

Hirano, N., Takahashi, E., Yamamoto, J., Abe, N., Ingle, S.P., Kaneoka, I., Hirata, T., Kimura, J.-I., Ishii, T., Ogawa, Y., Machida, S. and Suyehiro, K., 2006. Volcanism in Response to Plate Flexure. Science, 313(5792): 1426-1428.

Hoernle, K., Hauff, F., Werner, R., van den Bogaard, P., Gibbons, A.D., Conrad, S. and Muller, R.D., 2011. Origin of Indian Ocean Seamount Province by shallow recycling of continental lithosphere. Nature Geoscience, 4(12): 883-887.

Hoernle, K., White, J.D.L., van den Bogaard, P., Hauff, F., Coombs, D.S., Werner, R., Timm, C., Garbe-Schönberg, D., Reay, A. and Cooper, A.F., 2006. Cenozoic intraplate volcanism on New Zealand: Upwelling induced by lithospheric removal. Earth and Planetary Science Letters, 248(1-2): 350-367.

Hofmann, A., 1997. Mantle geochemistry: the message from oceanic volcanism. Nature, 385(6613): 219-229.

Kelley, K.A., Plank, T., Ludden, J. and Staudigel, H., 2003. Composition of altered oceanic crust at ODP Sites 801 and 1149. Geochemistry, Geophysics, Geosystems, 4(6).

Kellogg, L.H., Hager, B.H. and van der Hilst, R.D., 1999. Compositional Stratification in the Deep Mantle. Science, 283(5409): 1881-1884.

Klein, E., Langmuir, C., Zindler, A., Staudigel, H. and Hamelin, B., 1988. Isotope evidence of a mantle convection boundary at the Australian-Antarctic Discordance. Nature, 333(6174): 623-629.

Klootwijk, C.T., Gee, J.S., Peirce, J.W. and Smith, G.M., 1992. The origin of Ninetyeast Ridge: palaeomagnetic constraints from ODP Leg 121. Journal of Southeast Asian Earth Sciences, 7(4): 247-252.

Koppers, A.A.P., Staudigel, H., Pringle, M.S. and Wijbrans, J.R., 2003. Short-lived and discontinuous intraplate volcanism in the South Pacific: Hot spots or extensional volcanism? Geochemistry, Geophysics, Geosystems, 4(10): 1089.

Koppers, A.A.P., Staudigel, H., Wijbrans, J.R. and Pringle, M.S., 1998. The Magellan seamount trail: implications for Cretaceous hotspot volcanism and absolute Pacific plate motion. Earth and Planetary Science Letters, 163(1-4): 53-68.

Lay, T., Kanamori, H., Ammon, C.J., Nettles, M., Ward, S.N., Aster, R.C., Beck, S.L., Bilek, S.L., Brudzinski, M.R., Butler, R., DeShon, H.R., Ekström, G., Satake, K. and Sipkin, S., 2005. The Great Sumatra-Andaman Earthquake of 26 December 2004. Science, 308(5725): 1127-1133.

Levitt, D.A., Sandwell, D.T., 1995. Lithospheric bending at subduction zones based on depth soundings and satellite gravity. Journal of Geophysical Research 100, 379-400.

Lightfoot, P.C., Hawkesworth, C.J. and Sethna, S.F., 1987. Petrogenesis of rhyolites and trachytes from the Deccan Trap: Sr, Nd and Pb isotope and trace element evidence. Contributions to Mineralogy and Petrology, 95(1): 44-54.

Machida, S., Hirano, N. and Kimura, J.-I., 2009. Evidence for recycled plate material in Pacific upper mantle unrelated to plumes. Geochimica et Cosmochimica Acta, 73(10): 3028-3037.

Mahoney, J.J., Macdougall, J.D., Lugmair, G.W. and Gopalan, K., 1983. Kerguelen hotspot source for Rajmahal Traps and Ninetyeast Ridge? Nature, 303: 385-389.

Masson, D.G., Parson, L.M., Milsom, J., Nichols, G., Sikumbang, N., Dwiyanto, B. and Kallagher, H., 1990. Subduction of seamounts at the Java Trench: a view with long-range sidescan sonar. Tectonophysics, 185(1-2): 51-65.

McDougall, I. and Duncan, R.A., 1988. Age progressive volcanism in the Tasmantid Seamounts. Earth and Planetary Science Letters, 89(2): 207-220.

Mégnin, C. and Romanowicz, B., 2000. The three-dimensional shear velocity structure of the mantle from the inversion of body, surface and higher-mode waveforms. Geophysical Journal International, 143(3): 709-728.

Morgan, W.J., 1971. Convection plumes in the lower mantle. Nature, 230(5288): 42-43.

Müller, R.D., Mihut, D. and Baldwin, S., 1998. A new kinematic model for the formation and evolution of the west and northwest Australian margin. In: P.G. Purcell and R.R. Purcell (Editors), The Sedimentary Basins of Western Australia 2. Petroleum Exploration Society of Australia, WA Branch, Perth, WA, pp. 55-72.

Nishio, Y., Nakai, S.i., Ishii, T. and Sano, Y., 2007. Isotope systematics of Li, Sr, Nd, and volatiles in Indian Ocean MORBs of the Rodrigues Triple Junction: Constraints on the origin of the DUPAL anomaly. Geochimica et Cosmochimica Acta, 71(3): 745-759.

Natland, J.H. and Winterer, E.L., 2005. Fissure control on volcanic action in the Pacific. Geological Society of America Special Papers, 388: 687-710.

O'Neill, C., Müller, D. and Steinberger, B., 2003. Geodynamic implications of moving Indian Ocean hotspots. Earth and Planetary Science Letters, 215(1-2): 151-168.

Rehkamper, M. and Hofmann, A.W., 1997. Recycled ocean crust and sediment in Indian Ocean MORB. Earth and Planetary Science Letters, 147(1–4): 93-106.

Ritsema, J., Heijst, H.J.v. and Woodhouse, J.H., 1999. Complex Shear Wave Velocity Structure Imaged Beneath Africa and Iceland. Science, 286(5446): 1925-1928.

Sandwell, D.T., Winterer, E.L., Mammerickx, J., Duncan, R.A., Lynch, M.A., Levitt, D.A. and Johnson, C.L., 1995. Evidence for diffuse extension of the Pacific Plate from Pukapuka ridges and cross-grain gravity lineations. Journal of Geophysical Research, 100(B8): 15087-15099.

Sclater, J.G. and Fisher, R.L., 1974. Evolution of the East: Central Indian Ocean, with Emphasis on the Tectonic Setting of the Ninetyeast Ridge. Geological Society of America Bulletin, 85(5): 683-702.

Searle, D.E., 1994. Late Quaternary morphology of the Cocos (Keeling) Islands. Atoll Research Bulletin, 401: 1-13.

Smith, W.H.F. and Sandwell, D.T., 1997. Global Sea Floor Topography from Satellite Altimetry and Ship Depth Soundings. Science, 277(5334): 1956-1962.

Souriau, A., 1981. The upper mantle beneath Ninetyeast Ridge and Broken Ridge, Indian Ocean, from surface waves. Geophysical Journal of the Royal Astronomical Society, 67(2): 359-374.

Sun, S.-s. and McDonough, W.F., 1989. Chemical and isotopic systematics of oceanic basalts: implications for mantle composition and processes. Geological Society, London, Special Publications, 42(1): 313-345.

Taneja, R., O'Neill, C., Lackie, M., Rushmer, T., Schmidt, P. and Jourdan, F., 2014. Geochronology and the palaeoposition of Christmas Island (Australia), Northeast Indian Ocean.

Taneja, R. and O'Neill, C., 2014. Constraining the age and origin of the semaount province in the Northeast Indian Ocean. Marine Geophysical Research.

Tatsumoto, M. and Nakamura, Y., 1991. DUPAL anomaly in the Sea of Japan: Pb, Nd, and Sr isotopic variations at the eastern Eurasian continental margin. Geochimica et Cosmochimica Acta, 55(12): 3697-3708.

Trueman, N.A., 1965. The phosphate, volcanic and carbonate rocks of Christmas Island (Indian Ocean). Journal of the Geological Society of Australia, 12(2): 261 - 283.

Tu, K., Flower, M.F., Carlson, R.W., Xie, G., Chen, C.-Y. and Zhang, M., 1992. Magmatism in the South China Basin: 1. Isotopic and trace-element evidence for an endogenous Dupal mantle component. Chemicaeology, 97(1): 47-63.

Tu, K., Flower, M.F., Carlson, R.W., Zhang, M. and Xie, G., 1991. Sr, Nd, and Pb isotopic compositions of Hainan basalts (south China): implications for a subcontinental lithosphere Dupal source. Geology, 19(6): 567-569.

Valentine, G.A. and Hirano, N., 2010. Mechanisms of low-flux intraplate volcanic fields - Basin and Range (North America) and northwest Pacific Ocean. Geology, 38(1): 55-58.

Vervoort, J.D. and Green, J.C., 1997. Origin of evolved magmas in the Midcontinent rift system, northeast Minnesota: Nd-isotope evidence for melting of Archean crust. Canadian Journal of Earth Sciences, 34(4): 521-535.

Watts, A.B., 2001. Isostasy and Flexure of the Lithosphere. Cambridge University Press, Cambridge.

Weaver, B.L., 1991. Trace element evidence for the origin of ocean-island basalts. Geology, 19(2): 123-126.

Weaver, B.L., Wood, D.A., Tarney, J. and Joron, J.L., 1987. Geochemistry of ocean island basalts from the South Atlantic: Ascension, Bouvet, St. Helena, Gough and Tristan da Cunha. In: J.G. Fitton and B.G.J. Upton (Editors), Alkaline igneous rocks. Geological Society, Special Publications, London, pp. 253-267.

Weis, D., Bassias, Y., Gautier, I. and Mennessier, J.-P., 1989. Dupal anomaly in existence 115 Ma ago: Evidence from isotopic study of the Kerguelen Plateau (South Indian Ocean). Geochimica et Cosmochimica Acta, 53(8): 2125-2131.

Weis, D., Frey, F.A., Saunders, A. and Gibson, I., 1991. Ninetyeast Ridge (Indian Ocean): A 5000 km record of a Dupal mantle plume. Geology, 19(2): 99-102.

Weis, D., Frey, F.A., Leyrit, H. and Gautier, I., 1993. Kerguelen Archipelago revisited: geochemical and isotopic study of the Southeast Province lavas. Earth and Planetary Science Letters, 118(1-4): 101-119.

Wen, L., 2000. Intense seismic scattering near the Earth's core-mantle boundary beneath the Comoros hotspot. Geophysical Research Letters, 27(22): 3627-3630.

Wen, L., 2001. Seismic evidence for a rapidly varying compositional anomaly at the base of the Earth's mantle beneath the Indian Ocean. Earth and Planetary Science Letters, 194(1-2): 83-95.

Wen, L., 2006. A compositional anomaly at the Earth's core-mantle boundary as an anchor to the relatively slowly moving surface hotspots and as source to the DUPAL anomaly. Earth and Planetary Science Letters, 246(1-2): 138-148.

Wen, L., Silver, P., James, D. and Kuehnel, R., 2001. Seismic evidence for a thermo-chemical boundary at the base of the Earth's mantle. Earth and Planetary Science Letters, 189(3-4): 141-153.

West, H.B., Garcia, M.O., Frey, F.A. and Kennedy, A., 1988. Nature and cause of compositional variation among the alkalic cap lavas of Mauna Kea Volcano, Hawaii. Contributions to Mineralogy and Petrology, 100(3): 383-397.

White, W.M., 1985. Sources of oceanic basalts: Radiogenic isotopic evidence. Geology, 13(2): 115-118.

Whittaker, J.M., Müller, R.D., Sdrolias, M. and Heine, C., 2007. Sunda-Java trench kinematics, slab window formation and overriding plate deformation since the Cretaceous. Earth and Planetary Science Letters, 255(3-4): 445-457.

Widiyantoro, S. and van der Hilst, R., 1996. Structure and Evolution of Lithospheric Slab Beneath the Sunda Arc, Indonesia. Science, 271(5255): 1566-1570.

Woodroffe, C.D. and Falkland, A.C., 1997. Chapter 31 Geology and hydrogeology of the Cocos (Keeling) islands. In: H.L. Vacher and M.Q. Terrence (Editors), Developments in Sedimentology. Elsevier, pp. 885-908.

Woodroffe, C.D., Veeh, H.H., Falkland, A., McLean, R.F. and Wallensky, E., 1991. Last interglacial reef and subsidence of the Cocos (Keeling) Islands, Indian Ocean. Marine Geology, 96: 137- 143.

Xu, J.-F. and Castillo, P.R., 2004. Geochemical and Nd–Pb isotopic characteristics of the Tethyan asthenosphere: implications for the origin of the Indian Ocean mantle domain. Tectonophysics, 393(1–4): 9-27.

Zindler, A. and Hart, S., 1986. Chemical Geodynamics. Annual review of earth and planetary sciences, 14(1): 493-571.

Chapter 7: Discussion

The previous chapters looked at the available geophysical and geochemical constraints on the evolution of the Christmas Island Seamount Province. Global seismic tomography models support an association of the volcanism with deep mantle velocity anomalies, while paleomagnetism suggested a paleoposition for Christmas Island significantly further south than previous models (Seton et al., 2012). Geochemical analyses of the basaltic rocks from Christmas Island document mantle heterogeneities in the form of an enriched mantle component (EM-1 and EM-2) alongside a DUPAL signature. Using geochronology a long volcanic history of Christmas Island was discovered with intermittent volcanic episodes occurring since the island's formation in Late Cretaceous. The island, therefore, has been at the forefront of this research in constraining the evolution of CHRISP since its formation, following the dispersal of Gondwana.

This chapter will discuss formation mechanisms for CHRISP. It will put forward a number of models suggested by previous workers (e.g. Bonatti and Harrison, 1976; Sandwell et al., 1995; Gans et al., 2003) and determine if these could lead to the formation of such a broad and extensive volcanic zone. This chapter will revisit some mechanisms proposed in Chapter 1, and will present arguments to justify why some of those mechanisms for intraplate volcanism cannot lead to the formation of CHRISP.

The widely ascribed simple mantle plume model put forward by Morgan (1971) cannot explain the disseminated nature of CHRISP due to the non-linear nature of the province. In addition, a

number of complicating factors like post Gondwana break-up volcanism, and geodynamic factors need to be addressed to understand the evolution of CHRISP. This chapter attempts to do so in the following sections.

7.1: Plume or no plume debate-A brief

There is an ongoing debate regarding hotspot volcanism on whether it is from the base of the lower mantle (Morgan, 1971; DePaolo and Manga, 2003; Montelli et al., 2004) or if it is a consequence of plate tectonics (Foulger and Natland, 2003; Natland and Winterer, 2005). The pro-mantle plume group has presented varied arguments in the form of seismic tomography (Courtillot et al., 2003, Montelli et al., 2004; Lei and Zhao, 2006), high temperatures around the plume heads (Ribe and Christensen, 1999), high $^{3}He/^{4}He$ ratios (Kurz et al., 1982; Breddam et al., 2000; Stuart et al., 2003) and numerical simulations (Ribe and Christensen, 1999), to argue for a deep core-mantle boundary origin for these hotspots. On the other hand, the anti-mantle plume group contests the above mentioned observations and inferences (e.g. Foulger and Natland, 2003), and instead suggests widespread melting of oceanic crust at shallow depths to account for primitive lavas, for instance at Hawaii (Foulger and Natland, 2003). This study, through the geophysical and geochemical investigation undertaken in the previous chapters believes that the combination of the two investigation techniques, can help in explaining the history of many complex tectonic settings, including the Christmas Island Seamount Province of the Northeast Indian Ocean.

7.2: Multiple mechanisms for intraplate volcanism

While the mantle plume model put forward by Morgan (1971) has been the most widely accepted, and most applicable to oceanic island basalts, a number of other mechanisms have

been proposed and this chapter will assess their applicability to the tectonic setting of the CHRISP.

7.2.1: Hotlines within the Upper Mantle

Volcanism alongside lineaments can lead to simultaneous volcanic activity that is associated with "hotlines" in the mantle as discussed by Bonatti and Harrison (1976). Proposing it as a mechanism for Easter Island, Bonatti and Harrison (1976) mentioned that the volcanism is restricted along the length of the lineament, and not far on either side of it. The source for such an event is located within the upper mantle, and is a result of mantle convection rolls aligned parallel to the plate motion. The CHRISP seamounts are aligned east-west, and these were formed when an ancient spreading ridge (Wharton Ridge) trended northeast-southwest, while the plate moved almost east-west (Seton et al., 2012). The seamount province is believed to have originated from a much deeper source than those sampled by the hotlines mechanism as discussed in Chapter 4. Moreover, the seamount province is 600 km wide - too large for a single convective roll to be able to produce intermittent volcanism (e.g. The Easter Island chain is around 150 km wide). Even if it is assumed there was more than one "hotline" producing the seamounts in the region, the seamounts produced by each "hotline" should be aligned linearly and parallel to each other. This is something which is not apparent in the region.

Age progressive linear trails attributed to deep mantle plumes have been used as a reflection of absolute plate motion. Changes in linearity, or bends in their linear evolution, may be used to determine changes in plate motion, spreading, and subduction at the plate's periphery. Notable examples of such a change are the bend in the Hawaiian-Emperor seamount chain (Steinberger et al., 2004; Sharp and Clague, 2006; Tarduno et al., 2007), and the Gilbert Ridge and the Tokelau Seamount Trail (Koppers et al., 2007). The reconstruction model of Gibbons et al. (2012) shows that the seamount province formed near the Wharton Ridge and it continued to

form while spreading was still active. The major re-organisation of the tectonic plate at ~99 Ma, the dual orientations of fracture zones (Northwest-southeast in Perth Abyssal Plain, and north-south in Wharton Basin), and the cessation of spreading at the Wharton Ridge at 43 Ma (Liu et al., 1983) have already been discussed in Chapter 2, and Chapter 5 (Taneja et al., 2014). If the "hotline" model of Bonatti and Harrison (1976) is the cause of such a long and broad voluminous phase, it would involve convective rolls that are responsible for such hotlines, to be rotated with the change in spreading direction. Lithospheric plates float above the viscous asthenosphere, and are susceptible to change in motion (Watts, 2001), but for the convection rolls to change, there has to be major changes within the upper mantle convection models. Rotation of these linear hotlines within the upper mantle does not seem to be a plausible mechanism on dynamical grounds, and moreover, flow models of Steinberger (2000) do not show any changes in the convection models between 80 Ma, to the present day.

7.2.2: Lithospheric cracking producing linear volcanic ridges

Multiple mechanisms were put forward on gravity lineaments and their relationship with volcanism by Sandwell et al. (1995), Gans et al. (2003), and Sandwell and Fialko (2004). Thermal stress, due to uneven top to bottom cooling of the lithosphere, produces cracks within regularly spaced, convex upward flexure of the lithosphere (Gans et al., 2003). Gans et al. (2003) proposed that such cracks may be associated with long volcanic chains within the gravity lows. Linear cracks of this nature are putatively associated with gravity lows due to extension and thinning of the lithosphere, and lead to the creation of boudinage structures (Sandwell and Fialko, 2004). The cracks within these troughs can act as conduits for magmatism associated with volcanic ridges (Sandwell and Fialko, 2004). These are not associated with any plume activity or convective rolls, but are produced due to lithospheric cooling and thermal contraction, and have been proposed as a mechanism for Pukapuka Ridge in the Pacific Ocean (Sandwell and Fialko, 2004).

An extensional mechanism producing volcanic ridges within the gravity troughs can create large guyots, like the Wahoo Guyot in the Pukapuka chain (Sandwell et al., 1995). The mechanism, however, does not seem to be a plausible mechanism for the formation of the CHRISP, as the model can satisfactorily predict a linear volcanic chain or gravity lineaments, but not isolated seamounts as observed for the CHRISP, and it does not account for volcanism on either side of the Wharton Ridge. This mechanism, however, might account for some volcanic ridges in the region as these are perpendicular to the plate motion. A detailed dredging expedition targeted towards these fracture zones could confirm the possibility of this mechanism for the presence of volcanic ridge, something which is beyond the scope of this study.

7.2.3: Superplume and rising plumelets

Courtillot et al. (2003) suggested a superplume model for weak Marquesian-type hotspots where small plumelets rise from the top of super plumes at the 670 km boundary. Two such superplumes, under Africa and the central Pacific (French Polynesia), have been suggested to have risen from the lower mantle in response to cold, dense material subducting into the mantle. These super plumes may contain compositional heterogeneities (Courtillot et al., 2003; McNamara and Zhong, 2005). Such a superplume could potentially sample mantle heterogeneities in the form of HIMU, EM-1, and EM-2; these compositional signatures may then be inherited by smaller upper-mantle plumelets rising from the main anomaly (Koppers et al., 2003), and lead to the formation of volcanic islands that are composed of one or more of these end member components, or exhibit mixing of two or more components as the plate moves over the superplume. The plumelets often undergo partial melting, which can lead to volcanism as they arrive at the base of the lithosphere, or they may be entrapped and mixed within the asthenosphere (Koppers et al., 2003). The superplume model seems unlikely as a

mechanism for the CHRISP due to the fact that seismic tomographic images have not imaged a large plume at mid-lower mantle depths, as in the case of other superplumes (Koppers et al., 2011; Courtillot et al., 2003). Moreover, multiple plumelets would simultaneously lead to volcanism in the region and an age progressive trend should not be observed. The plumelets in such a case would rise independently to the lithosphere from the 670 km discontinuity, producing volcanoes on the surface with no geometrical pattern (Koppers et al., 2011).

Upwelling plumelets can contribute to lithospheric thinning following intraplate extension (Koppers et al., 2003). The continental extension associated with the dispersal of Gondwanaland is very well documented in the reconstruction models of Müller et al. (1998). Furthermore, the Eastern Wharton Basin Province (EWP) and the Vening Meinesz Volcanic Province (VMZ), have a wide ranging EM-1 to an EM-2 type end member composition (Hoernle et al., 2011). A rising plumelet and superplume model could produce this wide-ranging geochemical trend that was selectively sampled by the rising plumelets, and account for a wide chemical composition. The presence of an EM-2 component for the 44 – 37 Ma event, and an EM-1 and EM-2 type for the Pliocene phase for Christmas Island is consistent with this style of heterogeneous model. The difficulty with this model is the province's rough age progression with the westward younging trend, and the absence of a seismically large superplume structure. In addition, there is no clear north-south age progression observed within these sub-provinces, as might be expected from small plumelets.

7.2.4: Small-scale edge driven convection

Intraplate volcanism has also been ascribed to shallow small-scale convection, separate from whole mantle flow or deep plumes (King and Anderson, 1995), operating locally, and producing non-hotspot based seamounts (King and Ritsema, 2000; Ballmer et al., 2007; Ballmer et al., 2009). These are powered by temperature gradients within the upper mantle,

and/or lithosphere with no input from the deep mantle. The convective rolls produce edge driven convection at the corners of cold lithosphere in cratonic areas, and in oceanic lithosphere adjacent to large continental lithospheric thickness contrasts (King and Anderson, 1998). While this has been purported to be a plausible mechanism for several hotspots in the Atlantic Ocean, it is problematic for the CHRISP due to the velocity of the Indo-Australian Plate, and the distance of the volcanism from any lithospheric discontinuity. King and Ritsema (2000) have pointed out difficulties in understanding edge driven convection in fast moving tectonic settings, as opposed to stable Africa. King and Anderson (1998) pointed out that these are formed at the edge of oceanic-continental areas. Although the proximity of such a boundary (NW Shelf) existed when CHRISP was formed, it is unclear how the geometry of spreading in the Wharton Basin would affect this model. Shallow small-scale convection features would have to traverse an active spreading centre (the Wharton Ridge) to contribute to volcanism in the western portions of the province – a feat that seems dynamically unlikely. In addition, the model does not address how stationary these upwellings and downwellings are so as to produce large surface impressions.

This dynamical limitation is especially critical in the case of the Northeast Indian Ocean, where the tectonic plate east of the Wharton Ridge was moving at relatively higher speed, while the African Plate has been relatively fixed. As volcanism occurs close to the ocean-continent boundary, and with an eastward moving Australian Plate, the volcanism should also progress eastwards. CHRISP, on the other hand, experienced active volcanism towards the west, rather than east as Australia moved east, with a westward younging volcanic trend.

7.3: The origin of the seamount province

7.3.1: Seismic imaging and mantle heterogeneities

Seismic tomography models discussed in Chapter 4 have highlighted a low velocity zone underneath the seamount province, and plate reconstruction tools aid in understanding the evolutionary history of the region. Reconstructions at ~140 Ma, show Argo Land near the Eocene reconstructed position of Christmas Island (Gibbons et al., 2012) – which is proximal to a large upper mantle low velocity zone. Hoernle et al. (2011) argues that the seamount province formed near the position of the West Burma block at the mid-oceanic ridge.

The eastern-most seamounts in the Argo Abyssal Plain have an age of 136 Ma (Hoernle et al. 2011), and the time since their last sub-aerial exposure was ~120 Ma (Chapter 4). If the position of the seamounts are reconstructed, they begin to form when the Argo Abyssal Plain opened as Greater India and Australia separated (Hoernle et al., 2011; Gibbons et al., 2012). The seamounts in the east moved with the plate away from the ridge, and younger seamount volcanism continued to the west (Figure 7.1). This continued to 47 Ma when the last episode of volcanism was recorded south of Cocos (Keeling) Island (Hoernle et al. 2011). Around the Eocene (44 – 37 Ma) Christmas Island recorded another episode of volcanism, south of ~30°S latitude, based on our paleomagnetic analysis of Christmas Islands basalts (Taneja et al., 2014).

The resolution of seismic tomography models is generally inadequate to image plume conduits (Courtillot et al., 2003), except in a few cases (Montelli et al., 2004). The problem is compounded in the Northeast Indian Ocean, which lacks earthquakes and receiver station coverage. Montelli et al. (2004) discussed present day seismic tomography models that image deep low velocity anomalies in this region with high confidence. Montelli et al.'s (2004, 2006) analyses have raised similar concerns, but their resolution tests classified their identified features as robust, and point towards sufficient evidences that these low velocity anomalies extend well into the lower mantle.

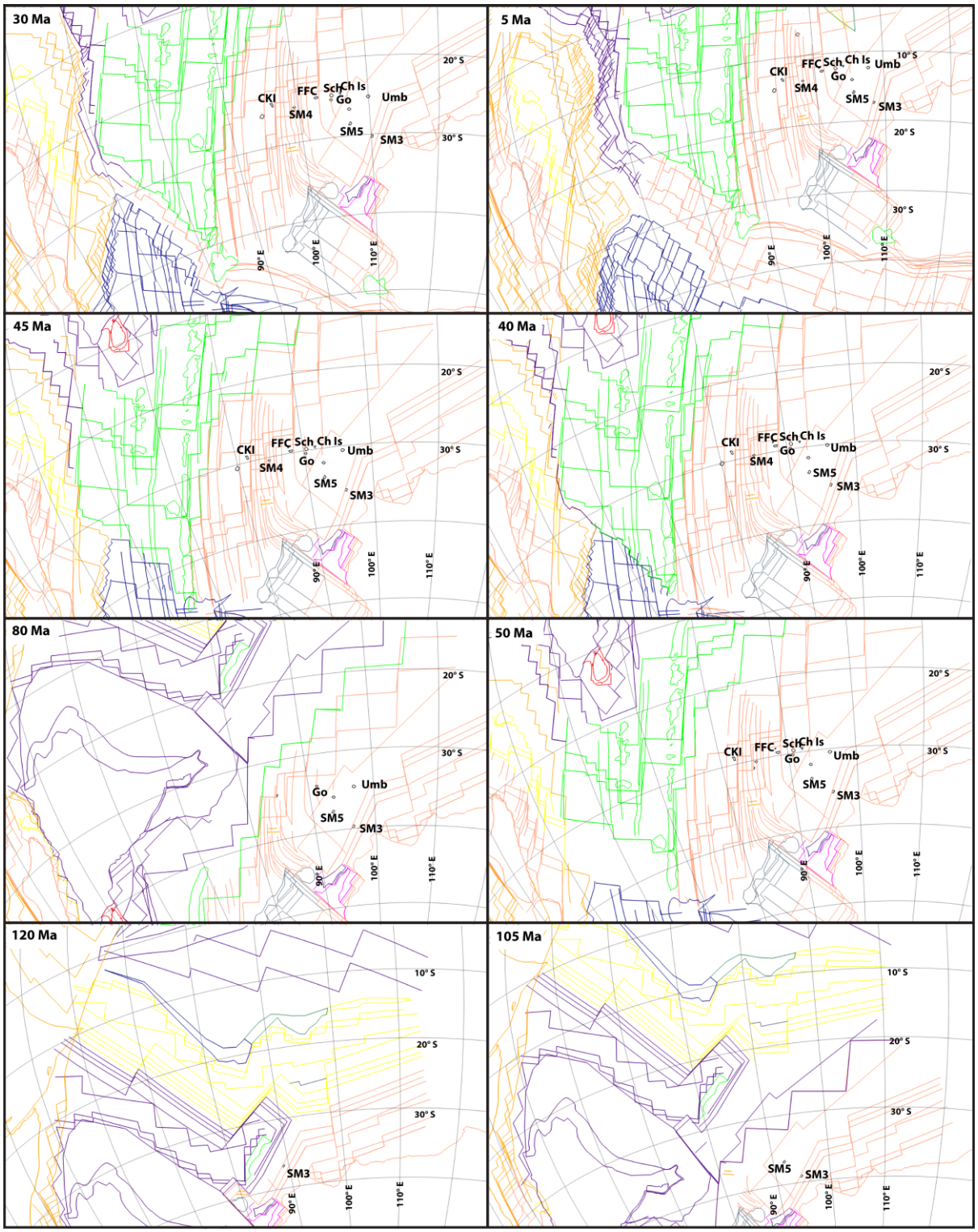

Figure 7.1: Evolution of the seamount province in the Northeast Indian Ocean as per reconstruction models of Seton et al. (2012). No age is available for the Umbgrove (Umb) seamount, but this study suggests an age of last appearance above sea-level at 103 - 101 Ma (Chapter 4). Though, there is no Late Cretaceous date available for Christmas Island plate flexural modelling has confirmed it was formed around 88 - 75 Ma.

These low velocity anomalies may also be particularly long-lived features. O'Neill et al. (2005) used dynamic modelling to show that the lifetime of a mantle plume in the Indo-Atlantic convection domain can be over ~100 Myr. Using Su et al.'s (1994) density anomaly model, O'Neill et al. (2005) reconstructed these mantle anomalies back to 120 Ma, and documented long lived low-density anomalies under Africa and East Indian Ocean that have undergone little variation in the last 50 Myr. So while tomography constrains the present mantle structure, in the Indo-Atlantic domain this structure may be long-lived, allowing us to correlate present structure and past volcanism.

The presence of a deep low velocity zone, and the Wharton spreading centre in the west, favoured upwelling of hot material in the region, which may be associated with the seamount province (Steinberger, 2000; Montelli et al. 2004). The low velocity zone may be associated with the DUPAL signature sourced by the CHRISP volcanics. Hoernle et al. (2011) proposed that shallow recycling of continental lithosphere played a major role in the formation of this volcanic province and that the enriched geochemical signature came from SCLM related to the rifting of West Burma from Australia and Greater India. Geochemical isotopic analyses (Chapter 6) have suggested an EM-2 type enriched mantle component with a DUPAL anomaly signature that is characteristic of the Indian-South Atlantic Ocean. These signatures can be seen across the Indian Ocean islands and volcanic chains, particularly the Ninetyeast Ridge, and in other islands that are proximal to the DUPAL boundary (Davies et al., 1989; Weis et al., 1991; Wen, 2006). Wen (2001, 2006) suggested the chemical signature of the DUPAL anomaly comes from the core mantle boundary, and through seismic modelling, mapped its boundaries. Therefore, it is suggested that CHRISP formed from an interplay of deep rooted DUPAL anomaly of the Indian Ocean, and an EM-2 type component (Figure 7.2) present beneath the reconstructed position of Gondwana.

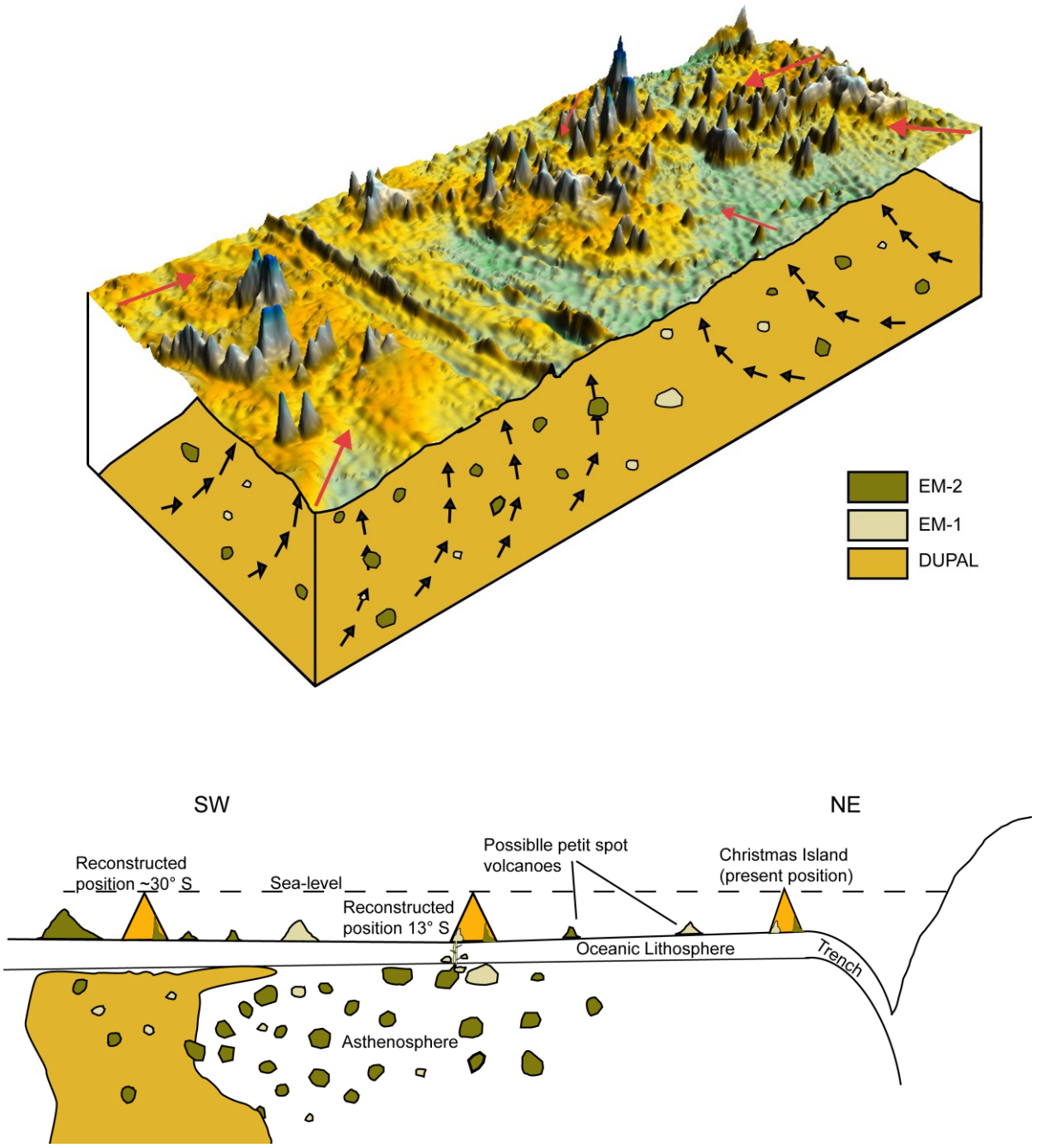

Figure 7.2: A schematic illustration depicting the mechanism for volcanism observed at Christmas Island Seamount Province. A low velocity zone observed in the seismic tomography models is suggestive of a deep mantle origin. The DUPAL anomaly (Hart, 1984) of the Indian Ocean and its signature have been observed in oceanic islands in the region (top and bottom). (Top) The model shows a combination of the DUPAL anomaly with an enriched mantle component leading to volcanism. Bottom, lithospheric cracking on the seaward side of the outer rise causes low degree partial melting. The melt rises through the cracks to the surface as UVS at Christmas Island as documented by Hirano et al. (2001) for the Hokkaido Rise. This event also picked up some pre-existing EM-2 type component now sampled at Winifred Beach. Also shown are possibly other petit spot volcanoes between the present position and the reconstructed position of Christmas Island at 13°S. Red arrows show the mantle flow directions on the horizontal plane at 670 km (O'Neill et al., 2003), and black arrows show approximate mantle flow directions from Steinberger (2000).

The shallow recycling model of Hoernle et al. (2011) does not conform with the mantle flow models of O'Neill et al. (2003) that show flow field convergence towards the seamount province at 670 km depth. Steinberger's (2000) model of mantle flow shows upwelling in the Northeast Indian Ocean, and particularly around the reconstructed position of CHRISP. Steinberger (2000) calculated that the upwelling within the region was much higher at 80 Ma, when most of CHRISP formed, than at 40 Ma when the volcanism in the province ceased. It is the deep seated DUPAL anomaly, the ULVZ (Wen, 2001; 2006), and the mantle flow lines that document the upwelling in the mantle around the reconstructed position of CHRISP (Figure 7.2) that implicate a deeper mantle component in the formation of the CHRISP, a scenario not discussed by Hoernle et al. (2011).

7.3.2 Source of mantle heterogeneities

The enriched mantle composition observed in Christmas Island basalts, and in the two sub-provinces of the region, could be due to two separate mechanisms. It could either be a pre-existing phase, or introduced during the rifting events associated with the breakup of Gondwana. The pre-existing enriched component rose to the shallow mantle along with the DUPAL component, a mechanism also suggested for the South China Sea (Chung et al., 1995; Tu et al., 1991), and in the Philippines Island arcs (Castillo, 1996). Convective instabilities and upwelling within the upper mantle following the rifting along the western margin of Australia could lead to volcanism. Steinberger (2000) has documented upwelling within the region and more specifically near the reconstructed position of the province that has existed for 80 Ma. Morris and Hart (1983) discussed such a scenario where recycled oceanic crust, and heterogeneous reservoir blobs floating in the upper mantle become stirred with the MORB matrix to erupt to the surface at MOR, or at off-ridge seamounts.

A second mechanism for such a hybrid signature in Christmas Island basalts, and the broader

seamount province, could be attributed to the assimilation of sediments or from the recycling of continental crust (Dupré and Allègre, 1983; Willbold and Stracke, 2010). Subduction of tectonic plates introduces sediments into the mantle, and Willbold and Stracke (2010) proposed that the isotopic composition of EM type oceanic island basalts is a result of recycling of marine sediments injected into the mantle through the subduction of oceanic lithosphere.

Lithospheric thinning and rifting may result in delamination, recycling or entrainment of continental lithospheric mantle (Thybo and Nielson, 2009; Willbold and Stracke, 2010), or differentially extend the crust and continental lithosphere, leaving portions of continental lithosphere trapped within oceanic regions (O'Reilly et al., 2009). Ocean island volcanism in the Cape Verde Islands (Coltorti et al., 2010) has documented continental lithospheric contamination on the islands near the African continent, and uncontaminated islands closer to the Mid-Atlantic Ridge. O'Reilly et al. (2009) and Coltorti et al. (2010) demonstrated a shallow, upper mantle fast seismic anomaly associated with this geochemical distinction, and attributed this anomaly to stretched African continental lithosphere extending far out into the Atlantic Oceanic basin. Similar "orphaned" continental lithosphere may persist beneath the CHRISP, which has seen numerous rifting events, microcontinent formation, and ridge jumps (Müller et al., 1998, 2000a; Gaina et al., 2003; Heine and Müller, 2005; Gibbons et al., 2012).

Delamination of the continental lithosphere and its subsequent sinking within the upper mantle has also been proposed as a mechanism for an EM type signature after rifting of large continental regions (Saunders et al., 1992). In addition, convective instability within the upper mantle can cause deep cold continental lithosphere to delaminate and descend into the asthenosphere (Ruppel, 1995). These materials may be entrained in rising mantle blobs or plumelets to produce EM-2 type signatures. The low velocity zone at 30° S could plausibly be implicated in similar dynamics, and has the potential to interact with the enriched composition that exists within the upper mantle. Furthermore, underplating of magma and extensional buoyancy leading to rupturing of the continental lithosphere has been discussed

by Hawkesworth et al. (1999), and could lead to thermal erosion of the lithospheric mantle.

It is not unreasonable to postulate that the EM signature observed in the seamount province reflects continental contamination, and is a derivative of the large scale rifting associated with the Gondwana breakup. As spreading initiated between the margins of Western Australia and Greater India (Gibbons et al., 2012) blobs of enriched composition may have been entrapped in the upper mantle convective circulation system or newly formed oceanic lithosphere which formed in response to the active spreading ridge.

7.4: Seismicity in the intraplate region

The intraplate region of the Indian Ocean is one of the most seismically active intraplate tectonic regions of the world (Bergman and Solomon, 1985). The intense deformation within the rigid Indo-Australian Plate is a consequence of a change in stress regime in the collision boundary as it changes from a continental collision in the west, to a subduction zone environment in the east (Weissel et al., 1980; Cloetingh and Wortel, 1985). The June 2000 M_w 7.9 left lateral strike slip earthquake, with a focal depth of 10 km, which occurred along the NNE-SSW fracture zone in the Wharton Basin, was one of the largest strike-slip earthquakes recorded (Abercrombie et al., 2003).

Subducting seafloor is subjected to extreme plate flexure as it approaches an oceanic trench (Walcott, 1970). The bending forces on the plate are so high, that they can lead to fracturing resulting in the development of scarps and fault lines (Mofjeld et al., 2004; Masson, 1991; Kobayashi et al., 1998). These bending-induced faults occur as horst and graben pairs that develop as the abyssal hill strikes more than 30° against the trench axis. Where new fault scarps are formed on the outer rise they are usually 40 - 60 km from the trench axis (Mofjeld et al., 2004) and occur parallel to the trench axis as shown by Masson (1991) and Masson et al. (1990). Such horst and graben structure in the subducting plate have the potential to produce earthquakes in the subduction zone (Mofjeld et al., 2004). Two seismic clusters were found in

the intraplate region that appear to be related to the tectonic fabric of Capricorn Plate rather than due to any active volcanism.

7.4.1: Earthquakes NE of Christmas Island

The seismic cluster mapped 250 km northeast off Christmas Island is on the outer rise side of the subducting Indo-Australian Plate (Figure 7.3). Subducting margins develop fault scarps as well as horst and graben structure that can be seismically active due to bending-induced torsional stresses (Chapple and Forsyth, 1979). As the abyssal hill strikes more than 30° to the trench axis, older faults rejuvenate and horst and graben faulting pairs develop along the subducting Indo-Australian Plate at the Java Trench northeast of Christmas Island as shown in Figure 7.4.

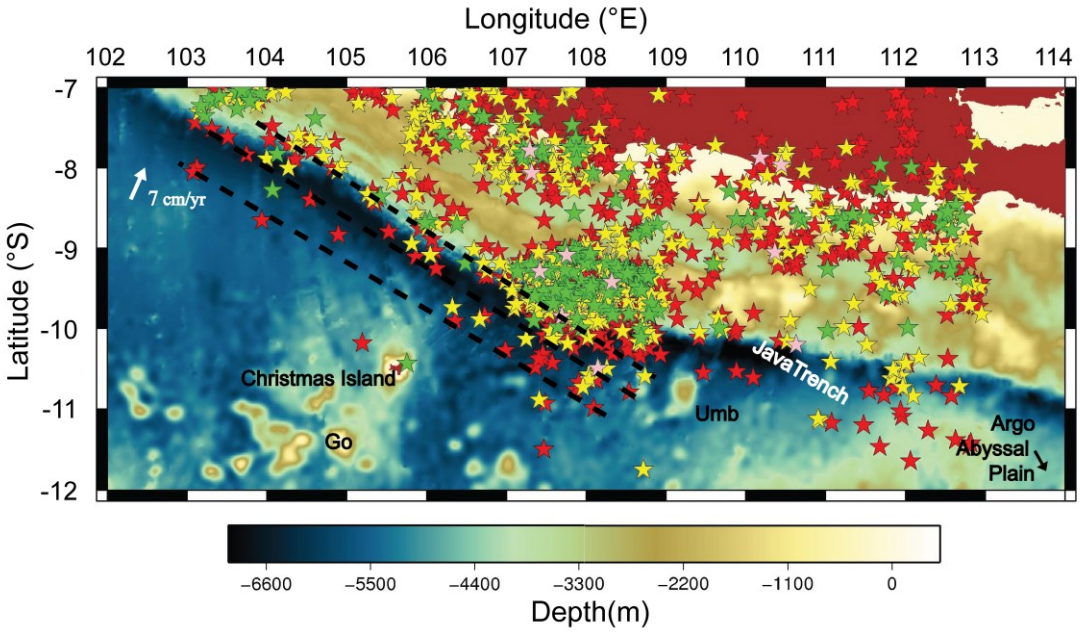

Figure 7.3: Seismicity map of the region around Christmas Island. A seismic cluster is observed 250 km northeast of Christmas Island. The seismicity data was sourced from USGS. The dataset comprises of earthquakes >M_w 4 since Jan 2000, up to Oct 2012; Red 4.0<M_w>4.5; Yellow 4.6<M_w>4.9; Green 5.0<M_w>5.9; Pink 6.0<M_w>9.9. Plate subducting underneath a trench develops horst and graben faulting pattern (shown in black dashed lines) parallel to the trench axis (Mofjeld et al., 2004). It is suggested that the seismicity NE of Christmas Island is related to such faulting pattern activated as the plate subducts. These faulting pattern can be seen in cross section in Figure 7.4. Golden Bo'Sunbird (Go) and Umbgrove seamounts (Umb) are also shown in the figure.

Moreover, earthquakes of M_w 4 - 5 occur parallel to the trench on the scarps approaching the trench axis and within 60 – 70 km from the trench axis (Figure 7.4). Therefore, the seismic cluster, NE of Christmas Island, appears to be directly related to the faulting pattern on the subducting lithosphere, and is not related to any active volcanism, nor does magma propagation leading to petit spot volcanoes appear to be causing any seismic activity. But why the seismic cluster is evident only towards the NE of Christmas Island is still unanswered, and thorough mapping of the region with high resolution swath bathymetry could help resolve this question, but this is beyond the scope of this investigation.

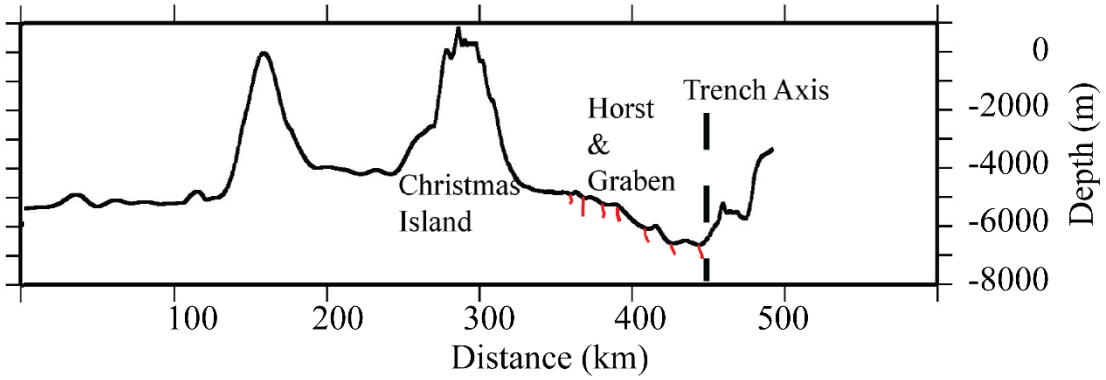

Figure 7.4: Interpreted Horst and Graben structure on the outer rise slope of the Java trench. Fault lines are marked using the interpretation methods by Mofjeld et al. (2004) on the Peru-Chile Trench and Masson (1991) on Pacific trenches. Such faulting pattern are points of seismicity northeast of Christmas Island as shown in Figure 7.3. A high resolution bathymetry survey could provide more constraints on these structures.

7.4.2: Wharton Basin intraplate earthquakes

In June 2000, a M_w 7.9 left lateral strike slip earthquake with a focal depth of 10 km occurred along the NNE-SSW fracture zone in the Wharton Basin (Figure 7.5). Aftershocks associated with large earthquakes and re-allocation analyses of these aftershocks by Abercrombie et al. (2003) show a NNW-SSE trend. Though there is argument on the epicentre of this earthquake (Robinson et al., 2001; Abercrombie et al., 2003), the left lateral strike slip nature of the earthquake correlates well with the NW-SE oriented compressive stress acting eastwards of the

Ninetyeast Ridge inherited from the collision of the two plates in the north (Cloetingh and Wortel, 1986).

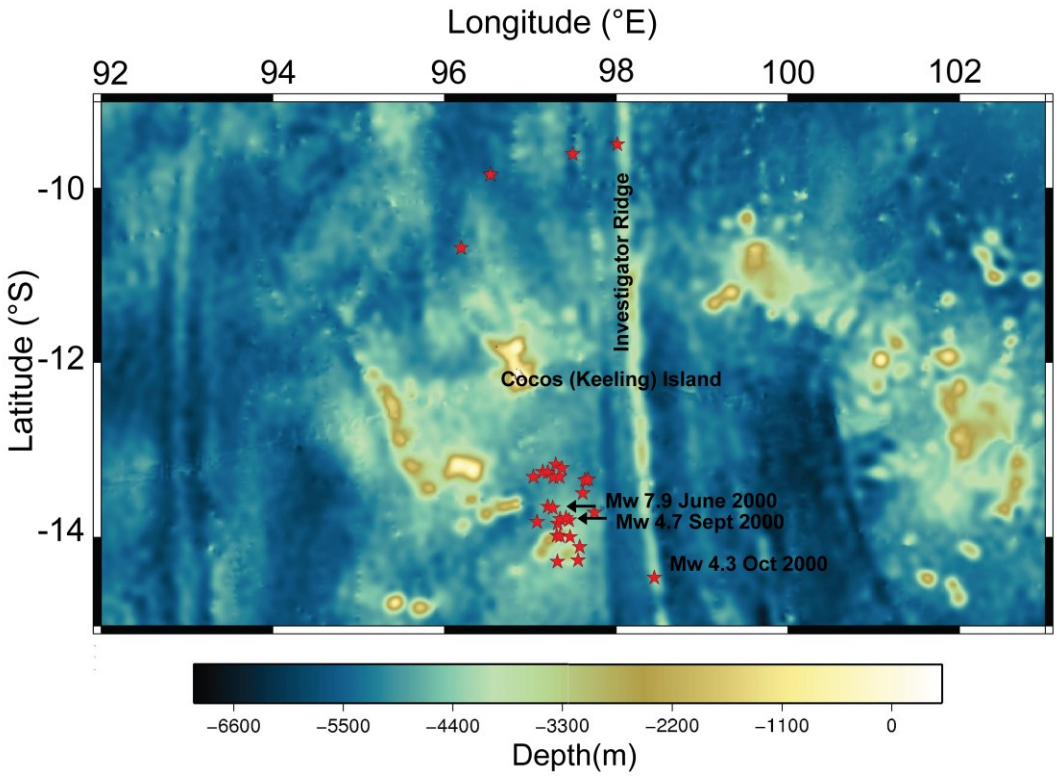

Figure 7.5: Seismicity (>M_w 4) in the proximity of the Cocos (Keeling) Islands. The largest of these earthquakes is M_w 7.9 occurred in June 2000 and was followed by aftershock of 4<M_w>5. Shallow focus and strike slip nature of these earthquakes suggests these earthquakes are controlled by the tectonism of the region and does not seem to be related to any volcanic activity, even though there is a plume underneath the Island (Montelli et al., 2004).

Deplus et al. (1998) suggested significant stresses acting throughout the intraplate region leading to high seismic activity along the NS fracture zones. The presence of a potentially deep plume beneath the Cocos (Keeling) Island could be a factor for some seismicity, provided it is still active, though Hoernle et al. (2011) did not dredge any young or recent volcanic rocks from region around Cocos (Keeling) Island). However, the shallow depth (10 km), and strike slip nature of the earthquake suggests the dominant factor is the tectonics of the incipient plate boundary and is not related to any volcanism in the region.

7.5 Summary

Christmas Island Seamount Province does not represent either a conventional linear hotpot model (Morgan, 1971), a hotline in the upper mantle (Bonatti and Harrison, 1976), nor edge driven convection model of intraplate volcanism (King and Anderson, 1995; King and Ritsema, 2000). Christmas Island basalts exhibit an enriched mantle EM-2 type signature that was produced from injection of sediments within the upper mantle, or through contamination by continental lithosphere following the dispersal of Gondwana. Christmas Island basalts also carry a DUPAL anomaly signature that is suggested to originate from the ultra-low velocity zone at the CMB (Wen, 2001), and seismic tomography models have imaged these compositional variations within the mantle. Upwelling lower mantle flow models by Steinberger (2000), and horizontal flow directions at 670 km by O'Neill et al. (2003) converge around the reconstructed position of the CHRISP – implicating deep mantle low velocity source zones, and suggesting transport through the mantle via imaged (though perhaps disseminated) upwellings (Montelli et al., 2004). The timing and evolution of volcanism was ultimately associated with spreading at the Wharton Ridge, and tectonic reorganizations within the region. The presence of shallow compositional variations, together with the DUPAL anomaly signature, and calculated mantle flow characteristics, suggests that the ultimate source of volcanism was from the deeper mantle, with subsequent entrainment of an EM-2 type signature that this study sampled at Christmas Island.

Chapter 8: Conclusion

The Christmas Island Seamount Province (CHRISP) is one of the most important physiographic features of the East Indian Ocean, covering an area of 1,000,000 km^2, between latitudes 10° to 15° S. In addition to numerous submerged volcanic seamounts and guyots, it contains two sub-aerially exposed groups of islands: Cocos (Keeling) Islands, and Christmas Island. Both island group are volcanic islands, capped by limestone units. While Cocos (Keeling) Archipelago does not have any exposed volcanic outcrops, Christmas Island exhibits volcanic outcrops along its coastline, and parts of the interior. This study undertook a geophysical, geochronological, and geochemical investigation of the seamount province to constrain a mechanism for its formation. The key finding are presented below:

- Gravity modelling of the two sub-aerially exposed islands, Cocos (Keeling) Islands and Christmas Island, constrained the crustal structure of these islands, and depth to the basalt-limestone contact for Cocos (Keeling) Island. Modelling reveals that the basaltic/gabbroic core extends to a deeper depth in the centre of the island, and is shallower towards the flanks as it grades into the abyssal plain. The integrated crustal layer may extend up to 18 - 20 km depth under the seamount to isostatically balance the excess mass of the island. The depth to basalt (or the thickness of the limestone unit) for Cocos (Keeling) Island was constrained to be between 900 to 2100 m below sea-level.

- Subsidence modelling of the oceanic lithosphere constrained the time of last sub-aerial exposure of flat and rounded-topped seamounts. Flat top seamounts indicate exposure above sea-level, and constrain the cessation of island-building by volcanic contribution. Flat topped seamounts SM-5 and SM-3 are the oldest seamounts, and were exposed above sea-level around 124 – 108 Ma. SM-2, north of the province, is the youngest seamount with an age of 32 – 21 Ma, and an undated seamount, Umbgrove, was last sub-aerially exposed between 103 – 101 Ma. The time since the last sub-aerial exposure of the basalt on Cocos (Keeling) Island was constrained on the basis of limestone deposition rates to be in the range of 55 - 49 Ma. This is in good agreement with the age of volcanic sample (56 Ma) yielded by Hoernle et al. (2011).
- The Late Cretaceous age of Christmas Island has not been confirmed with geochronology due to restrictions on site access. However, flexural modelling suggests that the oceanic lithosphere was elastically loaded by Christmas Island volcanism around 88 –75 Ma.
- $^{40}Ar/^{39}Ar$ geochronology has yielded two episodes of volcanic activity at Christmas Island. An Eocene event (44 – 37 Ma) formed the Lower Volcanic Sequences (LVS), and a much younger Pliocene phase at 4.3 ± 0.2 Ma, called the Upper Volcanic Sequence (UVS), and has been sampled at one site along the west coast. The results from this study agree with the $^{40}Ar/^{39}Ar$ ages yielded by Hoernle et al. (2011) for Christmas Island.
- Paleomagnetic analysis of Christmas Island basalts have revealed a much more southerly position of $-43.5°^{+9.0°}_{-11.2°}$ for Christmas Island in the Late Eocene (39 - 37 Ma), contrasting with existing plate reconstruction models. The error associated with this position is large (as the secular variations might not have been averaged out), but these are the first recorded paleomagnetic analysis from Christmas Island and additional data collection is recommended. The Pliocene paleoposition constrained using thermal

demagnetisation has given a position around 13°S. This is similar to the position determined by backtracking the UVS, and by using plate reconstruction models. Magnetic reversals have been recorded within the two volcanic phases and these conform to the Geomagnetic Polarity Time Scale (GPTS).

- Seismic tomography models support a deep origin for the seamount province, and a large, seismically low velocity zone is present under the reconstructed position of CHRISP at ~55 Ma. Though three plumes have been identified within the greater region, reconstructions suggest that the East Indian Ocean plume (35° S, 100° E) may be implicated in seamount volcanism in the province, and this plume can be imaged down to depths of ~1900 km, below which it is less resolved. This is also supported from upwelling lower mantle flow models that converge around the reconstructed position of the seamount province.
- The timing of the Eocene phase of volcanism at Christmas Island is possibly related to changes in the stress regime of the Indo-Australian Plate, due to continuous spreading along the South East Indian Ridge and tectonic reorganisation in the East Indian Ocean following the cessation of spreading at the Wharton Ridge at 43 Ma (Liu et al., 1983) or 38 Ma (Jacob et al., 2014), and increased slab pull north of Australia (Whittaker et al., 2007). The Pliocene (~4.3 Ma) volcanism at Christmas Island, however, has a separate mechanism and is a result of lithospheric cracking due to plate flexure as the island began to ride the fore-bulge on the seaward side of the subducting plate. Changes in the stress regime in the lower lithosphere can allow melt propagation through cracks, producing low volume “petit spot” volcanism (Hirano et al., 2001). This petit spot model may also explain volcanism at the Golden Bo’Sunbird seamount.
- The geochemical signature of the two volcanic episodes correlates with a general OIB trend. The older volcanic sequences have an enriched mantle (EM-2) type composition mixed with a characteristic Indian Ocean “DUPAL” anomaly signature. A single UVS

sample from Winifred Beach has an EM-2 signature of the LVS, different from the EM-1 signature of UVS dredged by Hoernle et al. (2011). This suggests that the older EM-2 signature is still present within the asthenosphere.

- Two separate mechanisms have been suggested for the EM-2 type component. Either the heterogeneity was pre-existing below Gondwana or was introduced in to the upper mantle while the western margin of Australia rifted from Greater India. Such a component can be produced by recycling of sediments, or continental lithosphere, either by rifting events, or by upwellings that may have scraped off sub-continental lithosphere.
- The intraplate seismicity observed in the region is related to the tectonic fabric and change in stress regime as it passes from a continental collision to subduction margin along its northern end, and is not related to any volcanism within the region. The seismic cluster northeast of Christmas Island is due to rejuvenation of older faults, and new flexure-induced faults that developed as part of horst and graben structure on the subducting lithosphere, and are thus not related to any petit spot related active volcanism.

References

Abercrombie, R.E., Antolik, M. and Ekström, G., 2003. The June 2000 Mw 7.9 earthquakes south of Sumatra: Deformation in the India–Australia Plate. Journal of Geophysical Research, 108(B1): 2018.

Anderson, D.L., 2000. The thermal state of the upper mantle; No role for mantle plumes. Geophysical Research Letters, 27(22): 3623-3626.

Andrews, C.W., 1900. A monograph of Christmas Island (Indian Ocean): Physical Features and Geology. British Museum (Natural History), London, 337 pp.

Antretter, M., Steinberger, B., Heider, F. and Soffel, H., 2002. Paleolatitudes of the Kerguelen hotspot: new paleomagnetic results and dynamic modeling. Earth and Planetary Science Letters, 203(2): 635-650.

AusGeoNews, 2009. Geoscience Australia: AusGeo News, March 2009, Issue 93. In: S. Ross (Editor). Commonwealth of Australia, Canberra, Australia. Accessed 21 5 2014

Ballmer, M.D., Conrad, C.P., Smith, E.I. and Harmon, N., 2013. Non-hotspot volcano chains produced by migration of shear-driven upwelling toward the East Pacific Rise. Geology, 41(4): 479-482.

Ballmer, M.D., van Hunen, J., Ito, G., Bianco, T.A. and Tackley, P.J., 2009. Intraplate volcanism with complex age-distance patterns: A case for small-scale sublithospheric convection. Geochemistry, Geophysics, Geosystems, 10(6): Q06015.

Ballmer, M.D., van Hunen, J., Ito, G., Tackley, P.J. and Bianco, T.A., 2007. Non-hotspot volcano chains originating from small-scale sublithospheric convection. Geophysical Research Letters, 34(23): L23310.

Barrie, J., 1967. The Geology of Christmas Island. Bureau of Mineral Resources, Australia, Canberra, pp. 104.

Baxter, J.L. and Weeks, G.C., 1984. Phosphatised volcanic ore from the Christmas Island, Indian Ocean. Western Australia Institute of Technology, pp. 20.

Bergman, E.A. and Solomon, S.C., 1985. Earthquake source mechanisms from body-waveform inversion and intraplate tectonics in the northern Indian Ocean. Physics of the Earth and Planetary Interiors, 40(1): 1-23.

Blichert-Toft, J. and Albarède, F., 2009. Mixing of isotopic heterogeneities in the Mauna Kea plume conduit. Earth and Planetary Science Letters, 282(1-4): 190-200.

Bodine, J., Steckler, M. and Watts, A., 1981. Observations of Flexure and the Rheology of the Oceanic Lithosphere. Journal of Geophysical Research, 86(B5): 3695-3707.

Bonatti, E. and Harrison, C., 1976. Hot lines in the Earth's mantle. Nature, 263(5576): 402-404.

Boyden, J.A., Müller, R.D., Gurnis, M., Torsvik, T., Clark, J.A., Turner, M., Ivey-Law, H., Watson, R.J. and Cannon, J., 2011. Next-generation plate-tectonic reconstructions using GPlates. In: G.R. Keller and C. Baru (Editors), Geoinformatics: Cyberinfrastructure for the Solid Earth Sciences. Cambridge University Press, Cambridge, pp. 95-114.

Breddam, K., Kurz, M.D. and Storey, M., 2000. Mapping out the conduit of the Iceland mantle plume with helium isotopes. Earth and Planetary Science Letters, 176(1): 45-55.

Butcher, R. and Hale, J., 2010. Ecological Character Description for The Dales Ramsar Site., Report to the Department of Sustainability, Environment, Water, Population and Communities, Canberra.

Butler, R.F., 1992. Paleomagnetism: Magnetic domains to geologic terranes, 601. Blackwell Scientific Publications, Boston.

Cande, S.C. and Mutter, J.C., 1982. A revised identification of the oldest sea-floor spreading anomalies between Australia and Antarctica. Earth and Planetary Science Letters, 58(2): 151-160.

Cande, S.C. and Kent, D.V., 1995. Revised calibration of the geomagnetic polarity timescale for the Late Cretaceous and Cenozoic. Journal of Geophysical Research, 100(B4): 6093-6095.

Carpenter, G. and Ewing, J., 1973. Crustal deformation in the Wharton Basin. Journal of Geophysical Research, 78(5): 846-850.

Castillo, P.R., 1996. Origin and geodynamic implication of the Dupal isotopic anomaly in volcanic rocks from the Philippine island arcs. Geology, 24(3): 271-274.

Chapple, W.M. and Forsyth, D.W., 1979. Earthquakes and bending of plates at trenches. Journal of Geophysical Research, 84(B12): 6729-6749.

Chung, S.-L., Jahn, B.-M., Chen, S.-J., Lee, T. and Chen, C.-H., 1995. Miocene basalts in northwestern Taiwan: Evidence for EM-type mantle sources in the continental lithosphere. Geochimica et Cosmochimica Acta, 59(3): 549-555.

Clague, D.A. and Jarrard, R.D., 1973. Tertiary Pacific Plate Motion Deduced from the Hawaiian-Emperor Chain. Geological Society of America Bulletin, 84(4): 1135-1154.

Cloetingh, S. and Wortel, R., 1985. Regional stress field of the Indian Plate. Geophysical Research Letters, 12(2): 77-80.

Cloetingh, S. and Wortel, R., 1986. Stress in the Indo-Australian plate. Tectonophysics, 132(1-3): 49-67.

Coffin, M.F. and Eldholm, O., 1994. Large igneous provinces: Crustal structure, dimensions, and external consequences. Reviews of Geophysics, 32(1): 1-36.

Coltorti, M., Bonadiman, C., O'Reilly, S.Y., Griffin, W.L. and Pearson, N.J., 2010. Buoyant ancient continental mantle embedded in oceanic lithosphere (Sal Island, Cape Verde Archipelago). Lithos, 120(1-2): 223-233.

Conrad, C.P. and Gurnis, M., 2003. Seismic tomography, surface uplift, and the breakup of Gondwanaland: Integrating mantle convection backwards in time. Geochemistry, Geophysics, Geosystems, 4(3): 1031.

Courtillot, V., Davaille, A., Besse, J. and Stock, J., 2003. Three distinct types of hotspots in the Earth's mantle. Earth and Planetary Science Letters, 205(3-4): 295-308.

Crough, S.T., 1975. Thermal model of oceanic lithosphere. Nature, 256(5516): 388-390.

Darwin, C., 1842. The Structure and Distribution of Coral Reefs. Being the first part of the geology of the voyage of the beagle, under the command of Capt. Fitzroy, R.N. during the years 1832 to 1836. Smith, Elder and Co., London.

Davies, H.L., Sun, S.s., Frey, F.A., Gautier, I., McCulloch, M.T., Price, R.C., Bassias, Y., Klootwijk, C.T. and Leclaire, L., 1989. Basalt basement from the Kerguelen Plateau and the trail of a Dupal plume. Contributions to Mineralogy and Petrology, 103(4): 457-469.

Davy, B. and Wood, R., 1994. Gravity and magnetic modelling of the Hikurangi Plateau. Marine Geology, 118(1-2): 139-151.

DeMets, C. and Royer, J., 2003. A new high-resolution model for India-Capricorn motion since 20 Ma: Implications for the chronology and magnitude of distributed crustal deformation in the Central Indian Basin. Current Science, 85(3): 339-345.

Dennis, S., 2008. Christmas Island: An Anthropological Study. Cambria Press, New York.

DePaolo, D.J. and Manga, M., 2003. Deep origin of hotspots-the mantle plume model. Science, 300(5621): 920-920.

Deplus, C., Diament, M., Hébert, H., Bertrand, G., Dominguez, S., Dubois, J., Malod, J., Patriat, P., Pontoise, B. and Sibilla, J.-J., 1998. Direct evidence of active deformation in the eastern Indian oceanic plate. Geology, 26(2): 131-134.

Desa, M., Ramana, M.V. and Ramprasad, T., 2009. Evolution of the Late Cretaceous crust in the equatorial region of the Northern Indian Ocean and its implication in understanding the plate kinematics. Geophysical Journal International, 177(3): 1265-1278.

Dickin, A.P., 2005. Radiogenic isotope geology. Cambridge University Press, Cambridge.

Dominguez, S., Lallemand, S., Malavieille, J. and von Huene, R., 1998. Upper plate deformation associated with seamount subduction. Tectonophysics, 293(3): 207-224.

Dominguez, S., Malavieille, J. and Lallemand, S.E., 2000. Deformation of accretionary wedges in response to seamount subduction: Insights from sandbox experiments. Tectonics, 19(1): 182-196.

Dubois, J., Launay, J. and Recy, J., 1975. Some new evidence on lithospheric bulges close to island arcs. Tectonophysics, 26(3): 189-196.

Duncan, R.A., 1978. Geochronology of basalts from the ninetyeast ridge and continental dispersion in the eastern Indian Ocean. Journal of Volcanology and Geothermal Research, 4(3-4): 283-305.

Duncan, R.A., 1984. Age progressive volcanism in the New England Seamounts and the opening of the central Atlantic Ocean. Journal of Geophysical Research: Solid Earth, 89(B12): 9980-9990

Duncan, R.A., 1991. 26. Age distribution of volcanism along aseismic ridges in the eastern Indian Ocean. In: J. Weissel, J. Peirce, E. Taylor and J. Alt (Editors), Proceedings of the Ocean Drilling Program, Scientific Results, 121, College Station, TX: Ocean Drilling Program, pp. 507-517.

Duncan, R.A., 2002. A Time Frame for Construction of the Kerguelen Plateau and Broken Ridge. Journal of Petrology, 43(7): 1109-1119.

Duncan, R.A. and Clague, D.A., 1985. Pacific Plate Motion Recorded by Linear Volcanic Chains. In: A.E.M. Nairn, F. Stehli and S. Uyeda (Editors), The Ocean Basins and Margins. Springer US, pp. 89-121.

Duncan, R.A., Backman, J., Peterson, L. and The Shipboard Scientific, P., 1989. Reunion hotspot activitity through tertiary time: Initial results from the ocean drilling program, leg 115. Journal of Volcanology and Geothermal Research, 36(1-3): 193-198.

Dupré, B. and Allègre, C.J., 1983. Pb-Sr isotope variation in Indian Ocean basalts and mixing phenomena. Nature, 303(5913): 142-146.

Dyment, J., 1998. Evolution of the Carlsberg Ridge between 60 and 45 Ma: Ridge propagation, spreading asymmetry, and the Deccan-Reunion hotspot. Journal of Geophysical Research, 103(B10): 24067-24084.

Eagles, G. and König, M., 2008. A model of plate kinematics in Gondwana breakup. Geophysical Journal International, 173(2): 703-717.

Fisk, M.R., Duncan, R.A., Baxter, A.N., Greenough, J.D., Hargraves, R.B. and Tatsumi, Y., 1989. Reunion hotspot magma chemistry over the past 65 m.y.: Results from Leg 115 of the Ocean Drilling Program. Geology, 17(10): 934-937.

Forsyth, D.W., Harmon, N., Scheirer, D.S. and Duncan, R.A., 2006. Distribution of recent volcanism and the morphology of seamounts and ridges in the GLIMPSE study area: Implications for the lithospheric cracking hypothesis for the origin of intraplate, non–hot spot volcanic chains. Journal of Geophysical Research, 111(B11): B11407.

Foulger, G.R. and Natland, J.H., 2003. Is "Hotspot" Volcanism a Consequence of Plate Tectonics? Science, 300(5621): 921-922.

Frey, F.A., Coffin, M.F., Wallace, P.J., Weis, D., Zhao, X., Wise Jr, S.W., Wähnert, V., Teagle, D.A.H., Saccocia, P.J., Reusch, D.N., Pringle, M.S., Nicolaysen, K.E., Neal, C.R., Müller, R.D., Moore, C.L., Mahoney, J.J., Keszthelyi, L., Inokuchi, H., Duncan, R.A., Delius, H., Damuth, J.E., Damasceno, D., Coxall, H.K., Borre, M.K., Boehm, F., Barling, J., Arndt, N.T. and Antretter, M., 2000. Origin and evolution of a submarine large igneous province: the Kerguelen Plateau and Broken Ridge, southern Indian Ocean. Earth and Planetary Science Letters, 176(1): 73-89.

Fullerton, L.G., Sager, W.W. and Handschumacher, D.W., 1989. Late Jurassic-Early Cretaceous evolution of the eastern Indian Ocean adjacent to northwest Australia. Journal of Geophysical Research, 94(B3): 2937-2953.

Fujiwara, T., Hirano, N., Abe, N. and Takizawa, K., 2007. Subsurface structure of the "petit-spot" volcanoes on the northwestern Pacific Plate. Geophysical Research Letters, 34(13): L13305.

Gaina, C., Müller, D.R., Royer, J.-Y., Stock, J., Hardebeck, J. and Symonds, P., 1998a. The tectonic history of the Tasman Sea: A puzzle with 13 pieces. Journal of Geophysical Research: Solid Earth, 103(B6): 12413-12433.

Gaina, C., Müller, R.D., Brown, B., Ishihara, T. and Ivanov, S., 2007. Breakup and early seafloor spreading between India and Antarctica. Geophysical Journal International, 170(1): 151-169.

Gaina, C., Müller, R.D., Brown, B.J. and Ishihara, T., 2003. Microcontinent formation around Australia. Geological Society of America Special Papers, 372: 405-416.

Gaina, C., Müller, R.D., Roest, W.R. and Symonds, P., 1998b. The Opening of the Tasman Sea: A Gravity Anomaly Animation. Earth Interactions, 2(4): 1-23.

Gaina, C., Müller, R.D., Royer, J.-Y. and Symonds, P., 1999. Evolution of the Louisiade triple junction. Journal of Geophysical Research: Solid Earth, 104(B6): 12927-12939.

Gans, K.D., Wilson, D.S. and Macdonald, K.C., 2003. Pacific Plate gravity lineaments: Diffuse extension or thermal contraction? Geochemistry, Geophysics, Geosystems, 4(9): 1074.

Gautier, I., Weis, D., Mennessier, J.-P., Vidal, P., Giret, A. and Loubet, M., 1990. Petrology and geochemistry of the Kerguelen Archipelago basalts (South Indian Ocean):

evolution of the mantle sources from ridge to intraplate position. Earth and Planetary Science Letters, 100(1-3): 59-76.

Georgen, J.E., Lin, J. and Dick, H.J.B., 2001. Evidence from gravity anomalies for interactions of the Marion and Bouvet hotspots with the Southwest Indian Ridge: effects of transform offsets. Earth and Planetary Science Letters, 187(3â€“4): 283-300.

Ghobarah, A., Saatcioglu, M. and Nistor, I., 2006. The impact of the 26 December 2004 earthquake and tsunami on structures and infrastructure. Engineering Structures, 28(2): 312-326.

Gibbons, A.D., Barckhausen, U., van den Bogaard, P., Hoernle, K., Werner, R., Whittaker, J.M. and Müller, R.D., 2012. Constraining the Jurassic extent of Greater India: Tectonic evolution of the West Australian margin. Geochemistry, Geophysics, Geosystems, 13(5): Q05W13.

Gibbons, A.D., Whittaker, J.M. and Müller, R.D., 2013. The breakup of East Gondwana: Assimilating constraints from Cretaceous ocean basins around India into a best-fit tectonic model. Journal of Geophysical Research: Solid Earth, 118(3): 808-822.

Gordon, R.G., 2009. Lithospheric Deformation in the equatorial Indian Ocean: Timing and Tibet. Geology, 37(3): 287-288.

Gordon, R.G., Argus, D.F. and Royer, J.-Y., 2008. Space geodetic test of kinematic models for the Indo-Australian composite plate. Geology, 36(10): 827-830.

Gradstein, F. and Ludden, J., 1992. Radiometric age determinations for basement from Sites 765 and 766, Argo Abyssal Plain and northwestern Australian margin, Proceedings of the ocean drilling program, Scientific Results, pp. 557-559.

Grand, S.P., 2002. Mantle shear-wave tomography and the fate of subducted slabs. Philosophical Transactions of the Royal Society of London. Series A: Mathematical, Physical and Engineering Sciences, 360(1800): 2475-2491.

Griffiths, R.W. and Campbell, I.H., 1990. Stirring and structure in mantle starting plumes. Earth and Planetary Science Letters, 99(1–2): 66-78.

Grigg, R.W. and Jones, A.T., 1997. Uplift caused by lithospheric flexure in the Hawaiian Archipelago as revealed by elevated coral deposits. Marine Geology, 141(1-4): 11-25.

Grimes, K.G., 2001. Karst Features of Christmas Islands. Helictite, 37: 41-58.

Hafkenscheid, E., Wortel, M. and Spakman, W., 2006. Subduction history of the Tethyan region derived from seismic tomography and tectonic reconstructions. Journal of Geophysical Research, 111(B8): B08401.

Hall, R., 2009. The Eurasian SE Asian margin as a modern example of an accretionary orogen. Geological Society, London, Special Publications, 318(1): 351-372.

Hall, R., 2012. Late Jurassic-Cenozoic reconstructions of the Indonesian region and the Indian Ocean. Tectonophysics, 570-571: 1-41.

Hart, S.R., 1984. A large-scale isotope anomaly in the Southern Hemisphere mantle. Nature, 309: 753-757.

Hawkesworth, C., Kelley, S., Turner, S., Le Roex, A. and Storey, B., 1999. Mantle processes during Gondwana break-up and dispersal. Journal of African Earth Sciences, 28(1): 239-261.

Heestand, R.L. and Crough, S.T., 1981. The effect of hot spots on the oceanic age-depth relation. Journal of Geophysical Research, 86(B7): 6107-6114.

Heezen, B.C. and Tharp, M., 1966. Physiography of the Indian Ocean. Philosophical Transactions of the Royal Society of London. Series A, Mathematical and Physical Sciences, 259(1099): 137-149.

Heine, C. and Müller, R.D., 2005. Late Jurassic rifting along the Australian North West Shelf: margin geometry and spreading ridge configuration. Australian Journal of Earth Sciences: An International Geoscience Journal of the Geological Society of Australia, 52(1): 27 - 39.

Heirtzler, J.R., Cameron, P., Cook, P.J., Powell, T., Roeser, H.A., Sukardi, S. and Veevers, J.J., 1978. The Argo Abyssal Plain. Earth and Planetary Science Letters, 41(1): 21-31.

Hess, H.H., 1946. Drowned ancient islands of the Pacific Basin. American Journal of Science, 244(11): 772-791.

Hillier, J.K. and Watts, A.B., 2005. Relationship between depth and age in the North Pacific Ocean. Journal of Geophysical Research, 110(B2): B02405.

Hirano, N., Kawamura, K., Hattori, M., Saito, K. and Ogawa, Y., 2001. A new type of intra-plate volcanism; Young alkali-basalts discovered from the subducting Pacific Plate, Northern Japan Trench. Geophysical Research Letters, 28(14): 2719-2722.

Hirano, N., Takahashi, E., Yamamoto, J., Abe, N., Ingle, S.P., Kaneoka, I., Hirata, T., Kimura, J.-I., Ishii, T., Ogawa, Y., Machida, S. and Suyehiro, K., 2006. Volcanism in Response to Plate Flexure. Science, 313(5792): 1426-1428.

Hoernle, K., Hauff, F., Werner, R., van den Bogaard, P., Gibbons, A.D., Conrad, S. and Muller, R.D., 2011. Origin of Indian Ocean Seamount Province by shallow recycling of continental lithosphere. Nature Geoscience, 4(12): 883-887.

Houtz, R.E., Hayes, D.E. and Markl, R.G., 1977. Kerguelen Plateau bathymetry, sediment distribution and crustal structure. Marine Geology, 25(1-3): 95-98, 101-130.

Kárason, H. and van der Hilst, R.D., 2000. Constraints on Mantle Convection From Seismic Tomography. In: M.A. Richards, R.G. Gordon and R.D. van der Hilst (Editors), The History and Dynamics of Global Plate Motions. Geophysical Monograph Series. AGU, Washington, DC, pp. 277-288.

Kelley, S., 2002. K-Ar and Ar-Ar Dating. Reviews in Mineralogy and Geochemistry, 47(1): 785-818.

King, S.D., 2007. Hotspots and edge-driven convection. Geology, 35(3): 223-226.

King, S.D. and Anderson, D.L., 1995. An alternative mechanism of flood basalt formation. Earth and Planetary Science Letters, 136(3-4): 269-279.

King, S.D. and Anderson, D.L., 1998. Edge-driven convection. Earth and Planetary Science Letters, 160(3-4): 289-296.

King, S.D. and Ritsema, J., 2000. African Hot Spot Volcanism: Small-Scale Convection in the Upper Mantle Beneath Cratons. Science, 290(5494): 1137-1140.

Kirschvink, J., 1980. The least-squares line and plane and the analysis of palaeomagnetic data. Geophysical Journal of the Royal Astronomical Society, 62(3): 699-718.

Klootwijk, C.T., Gee, J.S., Peirce, J.W. and Smith, G.M., 1992. The origin of Ninetyeast Ridge: palaeomagnetic constraints from ODP Leg 121. Journal of Southeast Asian Earth Sciences, 7(4): 247-252.

Kobayashi, K., Nakanishi, M., Tamaki, K. and Ogawa, Y., 1998. Outer slope faulting associated with the western Kuril and Japan trenches. Geophysical Journal International, 134(2): 356-372.

Kono, Y. and Yoshii, T., 1975. Numerical experiments on the thickening plate model. Journal of Physics of the Earth, 23(1): 63-75.

Koppers, A.A., 2011. Mantle plumes persevere. Nature Geoscience, 4(12): 816-817.

Koppers, A.A.P., 2002. ArArCALC-software for $^{40}Ar/^{39}Ar$ age calculations. Computers & Geosciences, 28(5): 605-619.

Koppers, A.A.P., Staudigel, H., Phipps Morgan, J. and Duncan, R.A., 2007. Nonlinear $^{40}Ar/^{39}Ar$ age systematics along the Gilbert Ridge and Tokelau Seamount Trail and the timing of the Hawaii-Emperor Bend. Geochemistry, Geophysics, Geosystems, 8(6): Q06L13.

Koppers, A.A.P., Staudigel, H., Pringle, M.S. and Wijbrans, J.R., 2003. Short-lived and discontinuous intraplate volcanism in the South Pacific: Hot spots or extensional volcanism? Geochemistry, Geophysics, Geosystems, 4(10): 1089.

Krishna, K.S. and Gopala Rao, D., 2000. Abandoned Paleocene spreading center in the northeastern Indian Ocean: evidence from magnetic and seismic reflection data. Marine Geology, 162(2–4): 215-224.

Kurz, M., Jenkins, W. and Hart, S., 1982. Helium isotopic systematics of oceanic islands and mantle heterogeneity. Nature, 297: 43-47.

Larson, R.L., 1975. Late Jurassic Sea-Floor Spreading in the Eastern Indian Ocean. Geology, 3(2): 69-71.

Larson, R.L., Carpenter, G.B. and Diebold, J.B., 1978. A geophysical study of the Wharton Basin near the Investigator Fracture Zone. Journal of Geophysical Research, 83(B2): 773-782.

Lay, T., Kanamori, H., Ammon, C.J., Nettles, M., Ward, S.N., Aster, R.C., Beck, S.L., Bilek, S.L., Brudzinski, M.R., Butler, R., DeShon, H.R., Ekström, G., Satake, K. and Sipkin, S., 2005. The Great Sumatra-Andaman Earthquake of 26 December 2004. Science, 308(5725): 1127-1133.

Lee, J.Y., Marti, K., Severinghaus, J.P., Kawamura, K., Yoo, H.S., Lee, J.B. and Kim, J.S., 2006. A redetermination of the isotopic abundances of atmospheric Ar. Geochimica et Cosmochimica Acta, 70(17): 4507-4512.

Lei, J. and Zhao, D., 2006. A new insight into the Hawaiian plume. Earth and Planetary Science Letters, 241(3): 438-453.

Lénat, J.-F., Merle, O. and Lespagnol, L., 2009. La réunion: An example of channeled hot spot plume. Journal of Volcanology and Geothermal Research, 184(1-2): 1-13.

Liu, C.-S., Curray, J.R. and McDonald, J.M., 1983. New constraints on the tectonic evolution of the eastern Indian Ocean. Earth and Planetary Science Letters, 65(2): 331-342.

Mahoney, J. and Coffin, F., 1997. Large Igneous Provinces: Continental, Oceanic, and Planetary Flood Volcanism. Geophysical Monograph Series. AGU, Washington, DC, 438 pp.

Mahoney, J.J., Duncan, R.A., Khan, W., Gnos, E. and McCormick, G.R., 2002. Cretaceous volcanic rocks of the South Tethyan suture zone, Pakistan: implications for the Réunion hotspot and Deccan Traps. Earth and Planetary Science Letters, 203(1): 295-310.

Mahoney, J.J., Macdougall, J.D., Lugmair, G.W. and Gopalan, K., 1983. Kerguelen hotspot source for Rajmahal Traps and Ninetyeast Ridge? Nature, 303: 385-389.

Mahoney, J.J., White, W.M., Upton, B.G.J., Neal, C.R. and Scrutton, R.A., 1996. Beyond EM-1: Lavas from Afanasy Nikitin Rise and the Crozet Archipelago, Indian Ocean. Geology, 24: 615-618.

Masson, D.G., 1991. Fault patterns at outer trench walls. Marine Geophysical Researches, 13(3): 209-225.

Masson, D.G., Parson, L.M., Milsom, J., Nichols, G., Sikumbang, N., Dwiyanto, B. and Kallagher, H., 1990. Subduction of seamounts at the Java Trench: a view with long-range sidescan sonar. Tectonophysics, 185(1-2): 51-65.

Mattielli, N., Weis, D., Grégoire, M., Mennessier, J.P., Cottin, J.Y. and Giret, A., 1996. Kerguelen basic and ultrabasic xenoliths: Evidence for long-lived Kerguelen hotspot activity. Lithos, 37(2-3): 261-280.

Matthews, K.J., Seton, M. and Müller, R.D., 2012. A global-scale plate reorganization event at 105−100 Ma. Earth and Planetary Science Letters, 355–356(0): 283-298.

McAdoo, D.C., Caldwell, J.G. and Turcotte, D.L., 1978. On the elastic-perfectly plastic bending of the lithosphere under generalized loading with application to the Kuril Trench. Geophysical Journal International, 54(1): 11-26.

McDougall, I., 1974. 12. Potassium-argon ages on basaltic rocks recovered from DSDP leg 22, Indian Ocean. Initial Reports of the Deep Sea Drilling Project 22, 22: 377-379.

McDougall, I. and Duncan, R.A., 1980. Linear volcanic chains - recording plate motions? Tectonophysics, 63(1-4): 275-295.

McElhinny, M.W. and McFadden, P.L., 2000. Paleomagnetism: continents and oceans. International Geophysical Series, 73. Academic Press, San Diego.

McNamara, A.K. and Zhong, S., 2005. Thermochemical structures beneath Africa and the Pacific Ocean. Nature, 437(7062): 1136-1139.

Mégnin, C. and Romanowicz, B., 2000. The three-dimensional shear velocity structure of the mantle from the inversion of body, surface and higher-mode waveforms. Geophysical Journal International, 143(3): 709-728.

Metcalfe, I., 1996. Pre-Cretaceous evolution of SE Asian terranes. Geological Society, London, Special Publications, 106(1): 97-122.

Metcalfe, I., 2002. Permian tectonic framework and palaeogeography of SE Asia. Journal of Asian Earth Sciences, 20(6): 551-566.

Metcalfe, I., 2011. Tectonic framework and Phanerozoic evolution of Sundaland. Gondwana Research, 19(1): 3-21.

Metcalfe, I., 2013. Gondwana dispersion and Asian accretion: Tectonic and palaeogeographic evolution of eastern Tethys. Journal of Asian Earth Sciences, 66(0): 1-33.

Mihut, D. and Müller, R.D., 1998. Revised sea-floor spreading history of the Argo Abyssal Plain. In: P.G. Purcell and R.R. Purcell (Editors), The Sedimentary Basins of Western Australia 2. Petroleum Exploration Society of Australia, WA Branch, Perth, WA, pp. 73-80.

Miles, P.R., 1982. Gravity models of the Amirante Arc, western Indian Ocean. Earth and Planetary Science Letters, 61(1): 127-135.

Mofjeld, H.O., Symons, C.M., Lonsdale, P., González, F.I. and Titov, V.V., 2004. Tsunami scattering and earthquake faults in the deep Pacific Ocean. Oceanography, 17(1): 38-46.

Molnar, P. and Atwater, T., 1973. Relative Motion of Hot Spots in the Mantle. Nature, 246: 288-291.

Molnar, P. and Tapponnier, P., 1977. The Collision between India and Eurasia. Scientific American, 236: 30-41.

Montelli, R., Nolet, G., Dahlen, F. and Masters, G., 2006. A catalogue of deep mantle plumes: new results from finite-frequency tomography. Geochemistry, Geophysics, Geosystems, 7(11): Q11007.

Montelli, R., Nolet, G., Dahlen, F.A., Masters, G., Engdahl, E.R. and Hung, S.-H., 2004. Finite-Frequency Tomography Reveals a Variety of Plumes in the Mantle. Science, 303(5656): 338-343.

Morgan, W.J., 1971. Convection plumes in the lower mantle. Nature, 230(5288): 42-43.

Morris, J.D. and Hart, S.R., 1983. Isotopic and incompatible element constraints on the genesis of island arc volcanics from Cold Bay and Amak Island, Aleutians, and implications for mantle structure. Geochimica et Cosmochimica Acta, 47(11): 2015-2030.

Müller, R.D., Gaina, C. and Clark, S., 2000a. Seafloor spreading around Australia. In: J.J. Veevers (Editor), Billion-year Earth History of Australia and neighbours in Gondwanaland. GEMOC Press, Sydney, pp. 18-28.

Müller, R.D., Gaina, C., Roest, W.R. and Hansen, D.L., 2001. A recipe for microcontinent formation. Geology, 29(3): 203-206.

Müller, R.D., Gaina, C., Tikku, A., Mihut, D., Cande, S.C. and Stock, J.M., 2000b. Mesozoic/Cenozoic tectonic events around Australia. In: M.A. Richards, R.G. Gordon and R.D. van der Hilst (Editors), The History and Dynamics of Global Plate Motions. Geophysical Monograph Series. AGU, Washington, DC, pp. 161-188.

Müller, R.D., Mihut, D. and Baldwin, S., 1998. A new kinematic model for the formation and evolution of the west and northwest Australian margin. In: P.G. Purcell and R.R. Purcell (Editors), The Sedimentary Basins of Western Australia 2. Petroleum Exploration Society of Australia, WA Branch, Perth, WA, pp. 55-72.

Müller, R.D., Royer, J.-Y. and Lawver, L.A., 1993. Revised plate motions relative to the hotspots from combined Atlantic and Indian Ocean hotspot tracks. Geology, 21(3): 275-278.

Müller, R.D., Sdrolias, M., Gaina, C. and Roest, W.R., 2008. Age, spreading rates, and spreading asymmetry of the world's ocean crust. Geochemistry, Geophysics, Geosystems, 9(4): Q04006.

Mutter, J.C. and Cande, S.C., 1983. The early opening between Broken Ridge and Kerguelen Plateau. Earth and Planetary Science Letters, 65(2): 369-376.

Naini, B.R., 1973. Appendix 1. A Marine Geophysical Survey (Site 211 DSDP) in the Wharton basin, Indian Ocean. Initial Reports of the Deep Sea Drilling Project, 22: 835-842.

Natland, J.H. and Winterer, E.L., 2005. Fissure control on volcanic action in the Pacific. Geological Society of America Special Papers, 388: 687-710.

Neprochnov, Y.P., Levchenko, O.V., Merklin, L.R. and Sedov, V.V., 1988. The structure and tectonics of the intraplate deformation area in the Indian Ocean. Tectonophysics, 156(1-2): 89-106.

Nier, A.O., 1950. A redetermination of the relative abundances of the isotopes of carbon, nitrogen, oxygen, argon, and potassium. Physical Review, 77(6): 789-793.

Nolet, G., Allen, R. and Zhao, D., 2007. Mantle plume tomography. Chemical Geology, 241(3-4): 248-263.

Nolet, G., Karato, S.-I. and Montelli, R., 2006. Plume fluxes from seismic tomography. Earth and Planetary Science Letters, 248(3): 685-699.

Norton, I. and Sclater, J., 1979. A model for the evolution of the Indian Ocean and the breakup of Gondwanaland. Journal of Geophysical Research: Solid Earth (1978â€“2012), 84(B12): 6803-6830.

O'Dowd, D.J. and Lake, P.S., 1989. Red crabs in rain forest, Christmas Island: removal and relocation of leaf-fall. Journal of Tropical Ecology, 5(3): 337-348.

O'Dowd, D.J. and Lake, P.S., 1991. Red crabs in rain forest, Christmas Island: removal and fate of fruits and seeds. Journal of Tropical Ecology, 7(01): 113-122.

O'Neill, C., Müller, D. and Steinberger, B., 2003. Geodynamic implications of moving Indian Ocean hotspots. Earth and Planetary Science Letters, 215(1-2): 151-168.

O'Neill, C., D. Müller, and B. Steinberger (2005), On the uncertainties in hot spot reconstructions and the significance of moving hot spot reference frames, Geochemistry Geophysics Geosystems, 6, Q04003.

O'Reilly, S.Y., Zhang, M., Griffin, W.L., Begg, G. and Hronsky, J., 2009. Ultradeep continental roots and their oceanic remnants: A solution to the geochemical "mantle reservoir" problem? Lithos, 112, Supplement 2: 1043-1054.

Parker, R. and Oldenburg, D., 1973. Thermal model of ocean ridges. Nature, 242(122): 137-139.

Parsons, B. and Sclater, J.G., 1977. An analysis of the variation of ocean floor bathymetry and heat flow with age. Journal of Geophysical Research, 82(5): 803-827.

Paulay, G. and McEdward, L., 1990. A simulation model of island reef morphology: the effects of sea level fluctuations, growth, subsidence and erosion. Coral Reefs, 9(2): 51-62.

Peng, Z.X. and Mahoney, J.J., 1995. Drillhole lavas from the northwestern Deccan Traps, and the evolution of Réunion hotspot mantle. Earth and Planetary Science Letters, 134(1-2): 169-185.

Pettifer, G.R. and Polak, E.J., 1979. Christmas Island (Indian Ocean) geophysical survey for groundwater, 1976. Bureau of Mineral Resources, Australia, Canberra, pp. 75.

Polak, E.J., 1976. Christmas Island (Indian Ocean) geophysical survey for groundwater, 1973. Bureau of Mineral Resources, Australia, Canberra, pp. 66.

Powell, C.M., Roots, S.R. and Veevers, J.J., 1988. Pre-breakup continental extension in East Gondwanaland and the early opening of the eastern Indian Ocean. Tectonophysics, 155(1-4): 261-283.

Powell, T.S. and Luyendyk, B.P., 1982. The sea-floor spreading history of the eastern Indian Ocean. Marine Geophysical Research, 5: 225 –247.

Ramana, M.V., Ramprasad, T. and Desa, M., 2001. Seafloor spreading magnetic anomalies in the Enderby Basin, East Antarctica. Earth and Planetary Science Letters, 191(3–4): 241-255.

Renne, P., 2000. K-Ar and $^{40}Ar/^{39}Ar$ Dating. In: J.S. Noller, J.M. Sowers and W.R. Lettis (Editors), Quaternary Geochronology: Methods and Applications, AGU Reference Shelf 4. AGU, Washington, DC, pp. 77-100.

Renne, P., 2006. Progress and Challenges in K-Ar and $^{40}Ar/^{39}Ar$ Geochronology. In: T.D. Olszewski and W.D. Huff (Editors), Geochronology: Emerging Opportunities. Paleontological Society, Philadelphia, pp. 47-66.

Renne, P.R., Mundil, R., Balco, G., Min, K. and Ludwig, K.R., 2010. Joint determination of ^{40}K decay constants and $^{40}Ar^*/^{40}K$ for the Fish Canyon sanidine standard, and improved accuracy for $^{40}Ar/^{39}Ar$ geochronology. Geochimica et Cosmochimica Acta, 74(18): 5349.

Ribe, N.M. and Christensen, U.R., 1999. The dynamical origin of Hawaiian volcanism. Earth and Planetary Science Letters, 171(4): 517-531.

Ritsema, J., Heijst, H.J.v. and Woodhouse, J.H., 1999. Complex Shear Wave Velocity Structure Imaged Beneath Africa and Iceland. Science, 286(5446): 1925-1928.

Rivereau, J.C., 1965. Notes on a Geomorphological Study of Christmas Island, Indian Ocean. Bureau of Mineral Resources, Australia, Canberra, pp. 5.

Robinson, D.P., Henry, C., Das, S. and Woodhouse, J.H., 2001. Simultaneous Rupture Along Two Conjugate Planes of the Wharton Basin Earthquake. Science, 292(5519): 1145-1148.

Royer, J.-Y. and Gordon, R.G., 1997. The motion and boundary between the Capricorn and Australian plates. Science, 277(5330): 1268-1274.

Royer, J.-Y. and Rollet, N., 1997. Plate-tectonic setting of the Tasmanian region. Australian Journal of Earth Sciences, 44(5): 543-560.

Royer, J.-Y. and Sandwell, D.T., 1989. Evolution of the Eastern Indian Ocean since the Late Cretaceous: Contsraints from Geosat altimetry. Journal of Geophysical Research, 94: 755-782.

Royer, J.-Y., Sclater, J. and Sandwell, D., 1989. A preliminary tectonic fabric chart of the Indian Ocean. Proceedings of the Indian Academy of Sciences - Earth and Planetary Sciences, 98(1): 7-24.

Rundle, C.C., Brook, M., Reynolds, P.H. and Barr, S.M., 1974. 17 Radiometric age determinations. Initial Reports of the Deep Sea Drilling Project 26 26: 513-516.

Ruppel, C., 1995. Extensional processes in continental lithosphere. Journal of Geophysical Research, 100(B12): 24187-24215.

Sager, W.W., Fullerton, L.G., Buffler, R.T. and W., H.D., 1992. Argo Abyssal Plain Magnetic Lineations Revisited: Implications for the Onset of Seafloor Spreading and Tectonic Evolution of the Eastern Indian Ocean. Proceedings of the Ocean Drilling Program Scientific Results, 123: 659 – 669.

Sandwell, D. and Fialko, Y., 2004. Warping and cracking of the Pacific plate by thermal contraction. Journal of Geophysical Research, 109(B10): B10411.

Sandwell, D.T. and Smith, W.H.F., 2009. Global marine gravity from retracked Geosat and ERS-1 altimetry: Ridge segmentation versus spreading rate. Journal of Geophysical Research, 114(B1): B01411.

Sandwell, D.T., Winterer, E.L., Mammerickx, J., Duncan, R.A., Lynch, M.A., Levitt, D.A. and Johnson, C.L., 1995. Evidence for diffuse extension of the Pacific Plate from Pukapuka ridges and cross-grain gravity lineations. Journal of Geophysical Research, 100(B8): 15087-15099.

Saunders, A.D., Storey, M., Kent, R.W. and Norry, M.J., 1992. Consequences of plume-lithosphere interactions. In: B.C. Storey, T. Alabaster and R.J. Pankhurst (Editors), Magmatism and the causes of continental break-up. Geological Society, Special Publications, London, pp. 41-60.

Sclater, J.G., Anderson, R.N. and Bell, M.L., 1971. Elevation of ridges and evolution of the central eastern Pacific. Journal of Geophysical Research, 76(32): 7888-7915.

Sclater, J.G. and Fisher, R.L., 1974. Evolution of the East: Central Indian Ocean, with Emphasis on the Tectonic Setting of the Ninetyeast Ridge. Geological Society of America Bulletin, 85(5): 683-702.

Sclater, J.G., Lawver, L.A. and Parsons, B., 1975. Comparison of long-wavelength residual elevation and free air gravity anomalies in the North Atlantic and possible implications for the thickness of the lithospheric plate. Journal of Geophysical Research, 80(8): 1031-1052.

Searle, D.E., 1994. Late Quaternary morphology of the Cocos (Keeling) Islands. Atoll Research Bulletin, 401: 1-13.

Seton, M., Müller, R.D., Zahirovic, S., Gaina, C., Torsvik, T., Shephard, G., Talsma, A., Gurnis, M., Turner, M., Maus, S. and Chandler, M., 2012. Global continental and ocean basin reconstructions since 200 Ma. Earth-Science Reviews, 113(3-4): 212-270.

Sharp, W.D. and Clague, D.A., 2006. 50-Ma Initiation of Hawaiian-Emperor Bend Records Major Change in Pacific Plate Motion. Science, 313(5791): 1281-1284.

Shurbet, L. and Worzel., L., 1955. Gravity Anomalies Associated with Seamounts. Geological Society of America Bulletin, 66(6): 777-782.

Singh, S.C., Carton, H., Chauhan, A.S., Androvandi, S., Davaille, A., Dyment, J., Cannat, M. and Hananto, N.D., 2011. Extremely thin crust in the Indian Ocean possibly resulting from Plume–Ridge Interaction. Geophysical Journal International, 184(1): 29-42.

Smith, W.H.F. and Sandwell, D.T., 1997. Global Sea Floor Topography from Satellite Altimetry and Ship Depth Soundings. Science, 277(5334): 1956-1962.

Stagg, H.M.J., Wilcox, J.B., Symonds, P.A., O'Brein, G.W., Colwell, J.B., A., H.P.J., C-S., L., G., M.A.M. and Struckmeyer, I.M., 1999. Architecture and evolution of the Australian continental margin. AGSO Journal of Australian Geology & Geophysics, 17: 17 - 33.

Stein, S. and Okal, E.A., 2007. Ultralong Period Seismic Study of the December 2004 Indian Ocean Earthquake and Implications for Regional Tectonics and the Subduction Process. Bulletin of the Seismological Society of America, 97(1A): S279-S295.

Steinberger, B., 2000. Slabs in the lower mantle - results of dynamic modelling compared with tomographic images and the geoid. Physics of the Earth and Planetary Interiors, 118(3-4): 241-257.

Steinberger, B. and O'Connell, R.J., 1998. Advection of plumes in mantle flow: implications for hotspot motion, mantle viscosity and plume distribution. Geophysical Journal International, 132(2): 412-434.

Steinberger, B., Sutherland, R. and O'connell, R.J., 2004. Prediction of Emperor-Hawaii seamount locations from a revised model of global plate motion and mantle flow. Nature, 430(6996): 167-173.

Storey, M., Mahoney, J.J., Saunders, A.D., Duncan, R.A., Kelley, S.P. and Coffin, M.F., 1995. Timing of Hot Spot--Related Volcanism and the Breakup of Madagascar and India. Science, 267(5199): 852-855.

Stuart, F.M., Lass-Evans, S., Fitton, J.G. and Ellam, R.M., 2003. High $^{3}He/^{4}He$ ratios in picritic basalts from Baffin Island and the role of a mixed reservoir in mantle plumes. Nature, 424(6944): 57-59.

Su, W.-j., R. L. Woodward, and A. M. Dziewonski (1994), Degree 12 model of shear velocity heterogeneity in the mantle, Journal of Geophysical Research: Solid Earth, 99, 6945-6980. 10.1029/93jb03408

Taneja, R., O'Neill, C., Lackie, M., Rushmer, T., Schmidt, P. and Jourdan, F., 2014. $^{40}Ar/^{39}Ar$ geochronology and the palaeoposition of Christmas Island (Australia), Northeast Indian Ocean. Gondwana Research.

Tarduno, J.A., 2007. On the motion of Hawaii and other mantle plumes. Chemical Geology, 241(3-4): 234-247.

Thybo, H. and Nielsen, C.A., 2009. Magma-compensated crustal thinning in continental rift zones. Nature, 457(7231): 873-876.

Todal, A. and Edholm, O., 1998. Continental margin off Western India and Deccan Large Igneous Province. Marine Geophysical Researches, 20(4): 273-291.

Tregoning, P., Brunner, F.K., Bock, Y., Puntodewo, S.S.O., McCaffrey, R., Genrich, J.F., Calais, E., Rais, J. and Subarya, C., 1994. First geodetic measurement of convergence across the Java Trench. Geophysical Research Letters, 21(19): 2135-2138.

Trueman, N.A., 1965. The phosphate, volcanic and carbonate rocks of Christmas Island (Indian Ocean). Journal of the Geological Society of Australia, 12(2): 261 - 283.

Tu, K., Flower, M.F., Carlson, R.W., Zhang, M. and Xie, G., 1991. Sr, Nd, and Pb isotopic compositions of Hainan basalts (south China): implications for a subcontinental lithosphere Dupal source. Geology, 19(6): 567-569.

Tucholke, B. and Vogt, P., 1979. Western North Atlantic: Sedimentary evolution and aspects of tectonic history. Initial Rep. Deep Sea Drill. Proj, 43: 791-825.

Tucholke, B.E. and Smoot, N.C., 1990. Evidence for Age and Evolution of Corner Seamounts and Great Meteor Seamount Chain From Multibeam Bathymetry. Journal of Geophysical Research, 95(B11): 17555-17569.

Turcotte, D.L. and Oxburgh, E.R., 1967. Finite amplitude convective cells and continental drift. Journal of Fluid Mechanics, 28(01): 29-42.

Turcotte, D.L. and Oxburgh, E.R., 1978. Intra-Plate Volcanism [and Discussion]. Philosophical Transactions of the Royal Society of London. Series A, Mathematical and Physical Sciences, 288(1355): 561-579.

Turcotte, D.L. and Schubert, G., 2002. Geodynamics. Cambridge University Press, Cambridge, 456 pp.

Veevers, J.J., 1971. Phanerozoic history of Western Australia related to continental drift. Journal of the Geological Society of Australia, 18(2): 87-96.

Veevers, J.J., 1988. Morphotectonics of Australia's northwestern margin-a review. In: P.G. Purcell and R.R. Purcell (Editors), The North West Shelf, Petroleum Exploration Society of Australia Symposium. Petroleum Exploration Society of Australia, Perth, pp. 19-27.

Veevers, J.J., 2000. Billion-year earth history of Australia and neighbours in Gondwanaland. GEMOC Press, Sydney, 388 pp.

Veevers, J.J. and Cotterill, D., 1976. Western margin of Australia: A Mesozoic analog of the East African rift system. Geology, 4(12): 713-717.

Veevers, J.J., Powell, C.M. and Roots, S.R., 1991. Review of seafloor spreading around Australia. I. synthesis of the patterns of spreading. Australian Journal of Earth Sciences: An International Geoscience Journal of the Geological Society of Australia, 38(4): 373 - 389.

Veevers, J.J. and Li, Z.X., 1991. Review of seafloor spreading around Australia. II. Marine magnetic anomaly modelling. Australian Journal of Earth Sciences, 38(4): 391-408.

Verhoef, J. and Collette, B., 1985. A geophysical investigation of the Atlantis-Meteor Seamount Complex. Proceedings of the Koninklijke nederlandse akademie van wetenschappen. Series B. Palaeontology, geology, physics, chemistry, anthropology, 88(4): 427-479.

Verhoef, J. and Collette, B., 1987. Lithospheric thinning under the Atlantis-meteor seamount complex (North Atlantic). Seamounts, Islands and Atolls, 43: 391-405.

Walcott, R.I., 1970. Flexure of the lithosphere at Hawaii. Tectonophysics, 9(5): 435-446.

Wallace, P.J., Frey, F.A., Weis, D. and Coffin, M.F., 2002. Origin and Evolution of the Kerguelen Plateau, Broken Ridge and Kerguelen Archipelago: Editorial. Journal of Petrology, 43(7): 1105-1108.

Watts, A.B., 1978. An analysis of isostasy in the world's oceans 1. Hawaiian-Emperor Seamount Chain. Journal of Geophysical Research, 83(B12): 5989-6004.

Watts, A.B., 2001. Isostasy and Flexure of the Lithosphere. Cambridge University Press, Cambridge, 458 pp.

Watts, A.B. and Cochran, J.R., 1974. Gravity Anomalies and Flexure of the Lithosphere along the Hawaiian-Emperor Seamount Chain. Geophysical Journal of the Royal Astronomical Society, 38(1): 119-141.

Watts, A.B., Cochran, J.R. and Selzer, G., 1975. Gravity anomalies and flexure of the lithosphere: A three-dimensional study of the Great Meteor Seamount, northeast Atlantic. Journal of Geophysical Research, 80(11): 1391-1398.

Watts, A.B., McKenzie, D.P., Parsons, B.E. and Roufosse, M., 1985. The relationship between gravity and bathymetry in the Pacific Ocean. Geophysical Journal International, 83(1): 263-298.

Watts, A.B. and Ribe, N.M., 1984. On geoid heights and flexure of the lithosphere at seamounts. Journal of Geophysical Research, 89(B13): 11152-11170.

Watts, A.B. and Taiwani, M., 1974. Gravity Anomalies Seaward of Deep-Sea Trenches and their Tectonic Implications. Geophysical Journal of the Royal Astronomical Society, 36(1): 57-90.

Weigel, W. and Grevemeyer, I., 1999. The Great Meteor seamount: seismic structure of a submerged intraplate volcano. Journal of Geodynamics, 28(1): 27-40.

Weis, D., Bassias, Y., Gautier, I. and Mennessier, J.-P., 1989. Dupal anomaly in existence 115 Ma ago: Evidence from isotopic study of the Kerguelen Plateau (South Indian Ocean). Geochimica et Cosmochimica Acta, 53(8): 2125-2131.

Weis, D., Frey, F.A., Saunders, A. and Gibson, I., 1991. Ninetyeast Ridge (Indian Ocean): A 5000 km record of a Dupal mantle plume. Geology, 19(2): 99-102.

Weissel, J.K., Anderson, R.N. and Geller, C.A., 1980. Deformation of the Indo-Australian plate. Nature, 287(5780): 284-291.

Wen, L., 2001. Seismic evidence for a rapidly varying compositional anomaly at the base of the Earth's mantle beneath the Indian Ocean. Earth and Planetary Science Letters, 194(1-2): 83-95.

Wen, L., 2006. A compositional anomaly at the Earth's core-mantle boundary as an anchor to the relatively slowly moving surface hotspots and as source to the DUPAL anomaly. Earth and Planetary Science Letters, 246(1-2): 138-148.

Wessel, P., Sandwell, D.T. and Kim, S.-S., 2010. The global seamount census. Oceanography, 23(1): 24-33.

Wessel, P. and Smith, W.H.F., 1991. Generic mapping tools. EOS Transaction, AGU, 72: 441.

Whittaker, J.M., Müller, R.D., Sdrolias, M. and Heine, C., 2007. Sunda-Java trench kinematics, slab window formation and overriding plate deformation since the Cretaceous. Earth and Planetary Science Letters, 255(3-4): 445-457.

Whittaker, J.M., Williams, S.E. and Müller, R.D., 2013. Revised tectonic evolution of the Eastern Indian Ocean. Geochemistry, Geophysics, Geosystems, 14: 1891–1909.

Wiens, D.A., DeMets, C., Gordon, R.G., Stein, S., Argus, D., Engeln, J.F., Lundgren, P., Quible, D., Stein, C., Weinstein, S. and Woods, D.F., 1985. A diffuse plate boundary model for Indian Ocean tectonics. Geophysical Research Letters, 12(7): 429-432.

Willbold, M. and Stracke, A., 2010. Formation of enriched mantle components by recycling of upper and lower continental crust. Chemical Geology, 276(3-4): 188-197.

Williams, S.E., Müller, R.D., Landgrebe, T.C. and Whittaker, J.M., 2012. An open-source software environment for visualizing and refining plate tectonic reconstructions using high-resolution geological and geophysical data sets. GSA Today, 22(4): 4-10.

Winterer, E.L., 1998. Cretaceous karst guyots: New evidence for inheritance of atoll morphology from subaerial erosional terrain. Geology, 26(1): 59-62.

Winterer, E.L. and Metzler, C.V., 1984. Origin and subsidence of Guyots in Mid-Pacific Mountains. Journal of Geophysical Research, 89(B12): 9969-9979.

Woodroffe, C.D., 2005. Late Quaternary sea-level highstands in the central and eastern Indian Ocean: A review. Global and Planetary Change, 49(1-2): 121-138.

Woodroffe, C.D. and Falkland, A.C., 1997. Chapter 31 Geology and hydrogeology of the Cocos (Keeling) islands. In: H.L. Vacher and M.Q. Terrence (Editors), Developments in Sedimentology. Elsevier, pp. 885-908.

Woodroffe, C.D., McLean, R.F. and Wallensky, E., 1994. Geomorphology of the Cocos (Keeling) Islands. Atoll Research Bulletin, 402: 1 -33.

Woodroffe, C.D., Veeh, H.H., Falkland, A., McLean, R.F. and Wallensky, E., 1991. Last interglacial reef and subsidence of the Cocos (Keeling) Islands, Indian Ocean. Marine Geology, 96: 137- 143.

Yue, H., Lay, T. and Koper, K.D., 2012. En echelon and orthogonal fault ruptures of the 11 April 2012 great intraplate earthquakes. Nature, 490: 245-249.

Zhao, D., 2004. Global tomographic images of mantle plumes and subducting slabs: insight into deep Earth dynamics. Physics of The Earth and Planetary Interiors, 146(1): 3-34.

Zijderveld, J., 1967. AC demagnetization of rocks: analysis of results. In: D.W. Collinson, K.M. Creer and S.K. Runcorn (Editors), Methods in paleomagnetism. Elsevier, Amsterdam, pp. 254-268.

Appendix 1

Table 1: Relative abundances summary showing the relative composition of different isotopes of Argon with percentage of $^{40}Ar(r)$ and $^{39}Ar(k)$ released in each step . The highlighted steps were used for constraining the age. The blue square boxes signify analyses included in age plateau calculation, red values are negative values, and summation (Σ) component at the bottom of the table is the sum of argon isotope used to calculate the total fusion age.

Winifred Beach

			36Ar	%1σ	37Ar	%1σ	38Ar	%1σ	39Ar	%1σ	40Ar	%1σ	Age (Ma)	± 2σ	40Ar(r) (%)	39Ar(k) (%)	K/Ca	± 2σ
2A20989D	63.00 W	■	0.0000736	11.561	0.0034778	90.960	0.0001067	8.085	0.0041874	0.790	0.0388094	0.540	4.91	± 1.52	42.61	3.15	0.518	± 0.942
2A20990D	64.00 W	■	0.0000501	17.656	0.0029307	105.573	0.0001268	6.654	0.0058973	0.963	0.0344915	0.654	4.07	± 1.12	55.96	4.43	0.866	± 1.828
2A21003D	65.50 W	■	0.0000239	32.059	0.0017304	190.090	0.0000891	11.836	0.0047929	0.856	0.0237330	0.924	4.27	± 1.20	69.35	3.60	1.191	± 4.529
2A21004D	67.00 W	■	0.0000842	10.450	0.0024069	139.812	0.0003560	4.603	0.0157488	0.728	0.0793261	0.346	4.30	± 0.42	68.59	11.83	2.813	± 7.867
2A21005D	68.00 W	■	0.0000705	11.747	0.0014126	224.006	0.0004918	2.915	0.0225866	0.603	0.1036895	0.251	4.56	± 0.28	79.81	16.97	6.875	± 30.801
2A21006D	69.00 W	■	0.0000908	8.976	0.0030458	104.768	0.0006022	1.743	0.0307808	0.527	0.1346900	0.228	4.36	± 0.20	80.07	23.12	4.345	± 9.105
2A21008D	70.00 W	■	0.0001004	8.855	0.0010750	317.362	0.0004113	3.731	0.0209499	0.641	0.0962265	0.324	3.94	± 0.32	68.95	15.74	8.379	± 53.186
2A21009D	71.50 W		0.0001587	7.826	0.0110515	28.288	0.0002916	3.799	0.0128173	0.620	0.0760524	0.317	2.87	± 0.72	38.91	9.62	0.498	± 0.282
2A21010D	73.00 W		0.0002293	5.738	0.1154115	6.164	0.0002645	4.028	0.0101739	0.933	0.0808562	0.291	2.73	± 0.98	27.36	7.58	0.038	± 0.005
2A21011D	80.50 W		0.0001161	7.550	0.1426941	5.843	0.0000966	10.109	0.0036511	1.123	0.0292381	0.751	2.31	± 1.91	22.50	2.66	0.011	± 0.001
2A21013D	82.00 W		0.0003117	4.516	0.4049945	5.475	0.0000779	10.649	0.0020201	1.404	0.0568216	0.459	1.55	± 6.68	3.77	1.30	0.002	± 0.000
		Σ	0.0013093	2.537	0.6739531	3.912	0.0029146	1.319	0.1336060	0.237	0.7539343	0.112						

Waterfall Spring

			36Ar	%1σ	37Ar	%1σ	38Ar	%1σ	39Ar	%1σ	40Ar	%1σ	Age (Ma)	± 2σ	40Ar(r) (%)	39Ar(k) (%)	K/Ca	± 2σ
2A20766D	68.00 W	■	0.0000587	14.556	0.0012380	325.101	0.0000272	35.737	0.0007883	2.395	0.0395555	0.460	34.67	± 8.18	55.96	2.21	0.273	± 1.778
2A20767D	68.50 W	■	0.0000685	13.860	0.0017230	235.441	0.0000185	51.420	0.0011138	1.880	0.0507215	0.274	33.71	± 6.41	59.94	3.13	0.278	± 1.307
2A20768D	69.00 W	■	0.0001226	6.953	0.0032921	122.702	0.0000614	15.692	0.0026510	1.035	0.1167381	0.154	37.41	± 2.49	68.87	7.45	0.346	± 0.849
2A20769D	69.50 W	■	0.0001047	9.275	0.0035008	115.359	0.0000666	14.379	0.0031217	1.161	0.1264824	0.111	37.73	± 2.45	75.51	8.77	0.383	± 0.884
2A20771D	70.00 W	■	0.0001210	9.611	0.0027578	144.437	0.0000792	12.710	0.0037939	0.861	0.1537036	0.127	38.28	± 2.34	76.65	10.66	0.591	± 1.708
2A20772D	70.80 W	■	0.0002434	4.300	0.0094751	43.908	0.0001479	7.646	0.0071863	0.745	0.2942151	0.100	38.15	± 1.21	75.57	20.19	0.326	± 0.286
2A20773D	71.60 W	■	0.0004225	4.624	0.0115631	35.665	0.0002116	5.925	0.0093676	0.629	0.4147650	0.137	38.12	± 1.60	69.82	26.32	0.348	± 0.248
2A20774D	72.40 W	■	0.0001381	7.729	0.0029488	137.340	0.0000659	14.562	0.0025670	1.401	0.1174375	0.198	36.74	± 3.22	65.10	7.21	0.374	± 1.027
2A20789D	80.20 W	■	0.0000316	26.867	0.0008176	140.880	0.0000149	30.177	0.0008226	1.413	0.0358564	0.252	39.45	± 7.58	73.53	2.31	0.433	± 1.220
2A20790D	82.00 W	■	0.0003483	4.772	0.0089804	13.978	0.0001211	6.286	0.0041818	1.038	0.2235943	0.098	35.54	± 3.00	53.82	11.74	0.200	± 0.056
		Σ	0.0016595	2.270	0.0446615	25.993	0.0008144	3.737	0.0355941	0.327	1.5730693	0.052						

Dolly Beach

			36Ar	%1σ	37Ar	%1σ	38Ar	%1σ	39Ar	%1σ	40Ar	%1σ	Age (Ma)	± 2σ	40Ar(r) (%)	39Ar(k) (%)	K/Ca	± 2σ
2A20302D	63.50 W		0.0002179	3.119	0.0015905	77.340	0.0000406	16.185	0.0002699	3.950	0.0735958	0.309	39.62	± 18.72	11.80	0.18	0.073	± 0.113
2A20303D	64.00 W		0.0001537	3.911	0.0011993	104.969	0.0000351	14.388	0.0005102	2.495	0.0633642	0.405	42.25	± 8.89	27.72	0.34	0.183	± 0.384
2A20304D	64.50 W		0.0000809	7.693	0.0004927	253.073	0.0000220	23.075	0.0005079	2.182	0.0392302	0.594	36.55	± 9.12	38.52	0.34	0.443	± 2.242
2A20306D	65.00 W		0.0001964	2.549	0.0001270	1094.630	0.0000479	13.199	0.0009057	1.533	0.0943561	0.245	48.22	± 4.30	37.84	0.60	3.067	± 67.134
2A20307D	65.80 W	■	0.0005842	2.619	0.0012899	105.459	0.0001345	5.672	0.0015199	1.185	0.2278268	0.115	43.16	± 7.37	23.49	1.01	0.506	± 1.068
2A20308D	66.30 W	■	0.0005347	2.239	0.0011454	109.442	0.0001252	7.449	0.0017762	1.484	0.2221563	0.140	43.21	± 5.06	28.19	1.18	0.666	± 1.459
2A20324D	66.80 W	■	0.0001146	5.555	0.0005720	168.357	0.0000216	18.228	0.0000939	9.377	0.0363663	0.159	27.33	± 49.56	5.76	0.06	0.071	± 0.239
2A20325D	67.30 W	■	0.0018646	1.945	0.0032249	31.095	0.0004018	2.791	0.0029230	0.851	0.6559791	0.062	41.77	± 9.03	15.17	1.94	0.389	± 0.242
2A20326D	67.80 W	■	0.0023497	1.764	0.0032876	31.335	0.0004927	2.948	0.0036242	1.593	0.8333267	0.040	44.66	± 8.40	15.85	2.40	0.474	± 0.297
2A20327D	68.20 W	■	0.0037607	1.633	0.0074105	13.633	0.0008250	2.730	0.0074991	0.521	1.4050842	0.050	46.21	± 5.95	20.14	4.97	0.435	± 0.119
2A20329D	68.40 W	■	0.0011635	2.229	0.0030600	34.730	0.0002504	4.391	0.0037310	1.038	0.4771398	0.038	42.72	± 5.11	27.25	2.47	0.524	± 0.364
2A20330D	68.60 W	■	0.0009993	1.953	0.0030007	33.451	0.0002379	3.212	0.0041065	0.545	0.4365578	0.054	41.35	± 3.48	31.72	2.72	0.588	± 0.394
2A20331D	69.00 W	■	0.0005837	1.799	0.0028420	33.688	0.0001452	5.846	0.0036387	0.975	0.3061114	0.118	44.48	± 2.27	43.15	2.41	0.550	± 0.371
2A20332D	69.60 W	■	0.0015954	1.807	0.0077503	13.744	0.0004183	3.454	0.0093939	0.760	0.8123352	0.049	43.92	± 2.32	41.44	6.22	0.521	± 0.143
2A20334D	70.20 W	■	0.0015528	1.815	0.0104230	11.205	0.0005170	2.864	0.0180723	0.465	1.1193133	0.053	44.51	± 1.20	58.66	11.97	0.745	± 0.167
2A20335D	70.50 W	■	0.0004779	2.463	0.0079545	12.700	0.0002461	2.524	0.0134491	0.675	0.6186326	0.047	43.43	± 0.86	77.05	8.91	0.727	± 0.185
2A20336D	70.80 W	■	0.0002462	2.873	0.0082454	13.227	0.0001584	4.601	0.0099788	0.664	0.4317450	0.049	44.08	± 0.78	83.13	6.61	0.520	± 0.138
2A20354D	71.30 W	■	0.0002278	6.437	0.0060891	22.648	0.0001772	3.406	0.0098462	0.603	0.4166584	0.049	43.46	± 1.20	83.80	6.52	0.695	± 0.315
2A20355D	71.90 W	■	0.0002926	5.883	0.0106410	13.317	0.0002166	4.312	0.0136827	0.563	0.5745278	0.035	43.71	± 1.03	84.95	9.06	0.553	± 0.147
2A20356D	72.50 W	■	0.0001905	6.705	0.0101409	12.966	0.0001697	3.849	0.0116326	0.642	0.4712389	0.096	43.75	± 0.97	88.11	7.70	0.493	± 0.128
2A20357D	80.00 W	■	0.0000749	17.756	0.0062306	21.452	0.0000810	7.125	0.0058911	0.775	0.2305517	0.077	43.43	± 1.77	90.53	3.90	0.406	± 0.174
2A20359D	82.00 W	■	0.0004612	3.195	0.0377608	5.772	0.0004264	3.786	0.0279341	0.454	1.1014869	0.093	42.46	± 0.55	87.79	18.49	0.318	± 0.037
		Σ	0.0177231	0.603	0.1330800	4.379	0.0051908	0.938	0.1509871	0.173	10.6475845	0.017						

Ethel Beach

			36Ar	%1σ	37Ar	%1σ	38Ar	%1σ	39Ar	%1σ	40Ar	%1σ	Age (Ma)	± 2σ	40Ar(r) (%)	39Ar(k) (%)	K/Ca	± 2σ
2A20931D	64.00 W	■	0.0003481	3.931	0.0012212	272.844	0.0001460	4.163	0.0040021	0.794	0.2279856	0.244	38.23	± 2.59	54.46	5.39	1.409	± 7.688
2A20932D	64.40 W	■	0.0002146	4.166	0.0037021	87.262	0.0001201	4.650	0.0044359	0.800	0.1955418	0.306	36.64	± 1.62	67.40	5.97	0.515	± 0.899
2A20933D	64.80 W	■	0.0001126	6.687	0.0019451	175.426	0.0000651	8.343	0.0032833	1.187	0.1320986	0.457	37.05	± 1.95	74.68	4.42	0.725	± 2.545
2A20934D	65.30 W	■	0.0000846	8.358	0.0028662	116.251	0.0000506	11.457	0.0028233	1.686	0.1146745	0.504	38.88	± 2.30	77.75	3.81	0.424	± 0.986
2A20936D	66.00 W	■	0.0001061	8.777	0.0015906	204.076	0.0000637	8.759	0.0030921	1.116	0.1274773	0.468	38.23	± 2.41	75.24	4.16	0.836	± 3.411
2A20937D	66.80 W	■	0.0001170	8.326	0.0048986	68.393	0.0000785	7.473	0.0032454	1.190	0.1317608	0.465	36.97	± 2.41	73.79	4.37	0.285	± 0.389
2A20938D	67.80 W	■	0.0001357	7.593	0.0028154	118.487	0.0000776	8.358	0.0041765	1.175	0.1684960	0.348	37.84	± 2.04	76.09	5.62	0.638	± 1.511
2A20939D	68.80 W	■	0.0004325	5.523	0.0088039	37.430	0.0002139	4.985	0.0083746	0.646	0.3824441	0.159	37.41	± 2.14	66.43	11.27	0.409	± 0.306
2A20982D	69.50 W	■	0.0003374	5.479	0.0103472	19.083	0.0001882	6.987	0.0087562	0.533	0.3587014	0.146	36.47	± 1.59	72.16	11.78	0.364	± 0.139
2A20983D	70.20 W	■	0.0001470	6.269	0.0070950	22.404	0.0001022	10.468	0.0046694	0.723	0.1793542	0.220	35.97	± 1.55	75.87	6.28	0.283	± 0.127
2A20984D	71.20 W		0.0001918	5.924	0.0091123	20.086	0.0000600	15.263	0.0026043	1.121	0.1176455	0.313	29.07	± 3.29	51.97	3.50	0.123	± 0.049
2A20985D	73.00 W		0.0003167	4.202	0.1053019	6.262	0.0001957	5.606	0.0080294	0.703	0.2965621	0.140	32.72	± 1.33	71.11	10.71	0.032	± 0.004
2A20987D	79.50 W		0.0000399	15.316	0.0162823	12.157	0.0000167	51.774	0.0008460	2.629	0.0334982	0.843	33.93	± 5.73	68.50	1.12	0.022	± 0.005
2A20988D	80.80 W		0.0004214	4.175	0.2896516	5.191	0.0003172	4.253	0.0162456	0.680	0.5287825	0.093	32.89	± 0.95	80.82	21.60	0.024	± 0.002
		Σ	0.0030054	1.600	0.4599012	4.190	0.0016955	1.957	0.0745842	0.248	2.9950226	0.066						

Sydney's Dale

			36Ar	%1σ	37Ar	%1σ	38Ar	%1σ	39Ar	%1σ	40Ar	%1σ	Age (Ma)	± 2σ	40Ar(r) (%)	39Ar(k) (%)	K/Ca	± 2σ
2A24273D	63.00 W		0.0233801	1.229	0.0016438	248.586	0.0047326	1.207	0.0084032	0.560	7.1724573	0.042	29.04	± 25.81	2.68	0.71	2.20	± 10.93
2A24274D	63.00 W		0.0031341	1.593	0.0005090	884.703	0.0006987	2.677	0.0072895	0.700	1.1632141	0.147	39.49	± 5.19	19.55	0.61	6.16	± 108.98
2A24275D	66.00 W		0.0546075	1.299	0.1713651	6.640	0.0116381	1.802	0.0788773	0.566	18.9938397	0.031	43.41	± 6.76	14.24	6.62	0.20	± 0.03
2A24276D	66.40 W	■	0.0064091	1.217	0.0002478	1685.545	0.0017085	1.788	0.0335673	0.374	3.0549422	0.070	42.99	± 1.78	37.36	2.82	58.26	± 1963.94
2A24279D	66.80 W	■	0.0104813	1.352	0.0073551	53.778	0.0028153	1.303	0.0539005	0.369	4.9417238	0.058	42.53	± 2.00	36.69	4.53	3.15	± 3.39
2A24280D	67.10 W	■	0.0099000	1.265	0.0045523	110.672	0.0027246	1.806	0.0556617	0.351	4.8695029	0.056	43.47	± 1.71	39.31	4.68	5.26	± 11.64
2A24281D	67.40 W	■	0.0051890	1.451	0.0066239	71.638	0.0015706	1.739	0.0380262	0.402	2.8318607	0.098	42.67	± 1.53	45.31	3.20	2.47	± 3.54
2A24282D	67.80 W	■	0.0046077	1.336	0.0011421	354.379	0.0014496	1.848	0.0384391	0.412	2.6894854	0.065	43.21	± 1.25	48.85	3.23	14.47	± 102.58
2A24284D	68.20 W	■	0.0050118	1.291	0.0042198	94.605	0.0015745	1.448	0.0440894	0.374	2.9866757	0.063	42.75	± 1.15	49.91	3.71	4.49	± 8.50
2A24285D	68.60 W	■	0.0042376	1.458	0.0026109	173.172	0.0014989	1.912	0.0445673	0.515	2.7841889	0.063	43.10	± 1.13	54.57	3.75	7.34	± 25.42
2A24286D	69.00 W	■	0.0052119	1.286	0.0089476	42.726	0.0019696	2.023	0.0687177	0.403	3.8473668	0.073	42.18	± 0.81	59.57	5.78	3.30	± 2.82
2A24287D	69.40 W	■	0.0031064	1.672	0.0095102	48.211	0.0013972	1.981	0.0551063	0.429	2.7802037	0.073	42.54	± 0.80	66.67	4.63	2.49	± 2.40
2A24303D	69.80 W	■	0.0039226	1.356	0.0024074	87.773	0.0021852	1.576	0.0945876	0.326	4.3473553	0.044	42.46	± 0.50	73.06	7.95	16.90	± 29.66
2A24304D	70.20 W	■	0.0024466	1.914	0.0056214	48.430	0.0016925	1.409	0.0835579	0.318	3.5298198	0.049	42.35	± 0.50	79.29	7.02	6.39	± 6.19
2A24305D	70.60 W	■	0.0019816	2.118	0.0003581	993.473	0.0015972	1.552	0.0887260	0.365	3.5349705	0.043	41.95	± 0.47	83.26	7.46	106.53	± 2116.70
2A24308D	71.40 W	■	0.0014359	2.209	0.0086745	27.364	0.0017857	1.769	0.1111900	0.353	4.0990520	0.040	41.76	± 0.36	89.56	9.35	5.51	± 3.02
2A24309D	71.80 W	■	0.0009751	2.636	0.0028283	101.764	0.0012528	1.550	0.0843647	0.347	3.0546281	0.049	41.43	± 0.37	90.48	7.09	12.83	± 26.10
2A24310D	72.20 W	■	0.0008000	3.514	0.0094123	27.596	0.0010713	1.784	0.0713487	0.378	2.5983385	0.054	41.84	± 0.43	90.84	6.00	3.26	± 1.80
2A24311D	72.20 W	■	0.0002691	4.584	0.0031158	69.945	0.0005240	3.041	0.0354638	0.359	1.2592347	0.105	42.05	± 0.41	93.64	2.98	4.89	± 6.85
2A24313D	79.00 W	■	0.0001344	9.882	0.0047889	79.690	0.0002194	4.136	0.0151033	0.659	0.5401321	0.053	41.91	± 0.86	92.65	1.27	1.36	± 2.16
2A24314D	81.00 W	■	0.0008485	2.569	0.0319861	15.475	0.0011909	2.057	0.0789314	0.358	2.8643402	0.046	41.89	± 0.36	91.25	6.63	1.06	± 0.33
		Σ	0.1480903	0.551	0.2701283	7.630	0.0452971	0.552	1.1899190	0.094	83.9433325	0.013						

Flying Fish Cove

			36Ar	%1σ	37Ar	%1σ	38Ar	%1σ	39Ar	%1σ	40Ar	%1σ	Age (Ma)	± 2σ	40Ar(r) (%)	39Ar(k) (%)	K/Ca	± 2σ
1.466	64.00 W		0.0001101	4.599	0.0004372	168.169	0.0000433	9.102	0.0015785		0.0781154	0.190	35.16	± 2.55	57.89	2.40	1.553	± 5.223
2A20281D	64.50 W		0.0000881	5.756	0.0003439	208.624	0.0000534	7.201	0.0024130	0.999	0.0979376	0.184	36.45	± 1.70	73.17	3.66	3.017	± 12.588
2A20282D	65.00 W	■	0.0000878	6.451	0.0005438	121.299	0.0000624	6.018	0.0031620	1.099	0.1236592	0.146	37.83	± 1.54	78.85	4.80	2.500	± 6.065
2A20283D	66.00 W	■	0.0000943	5.437	0.0024850	27.384	0.0000857	4.708	0.0042093	1.212	0.1612674	0.089	38.86	± 1.29	82.67	6.39	0.728	± 0.399
2A20285D	66.50 W	■	0.0000431	12.759	0.0001483	462.872	0.0000499	8.635	0.0025012	1.144	0.0899736	0.183	37.81	± 1.82	85.68	3.80	7.253	± 67.143
2A20286D	67.00 W	■	0.0000572	8.620	0.0017052	42.194	0.0000649	8.098	0.0032461	1.063	0.1189467	0.174	38.56	± 1.38	85.76	4.93	0.818	± 0.691
2A20287D	67.50 W	■	0.0000889	6.308	0.0030018	25.385	0.0000740	6.399	0.0038458	0.867	0.1464576	0.139	38.35	± 1.25	82.04	5.83	0.551	± 0.280
2A20288D	68.00 W	■	0.0001121	5.368	0.0053830	13.883	0.0000949	7.444	0.0047777	1.130	0.1832947	0.085	38.61	± 1.26	81.98	7.25	0.381	± 0.106
2A20290D	68.50 W	■	0.0001193	4.724	0.0038766	25.785	0.0001211	6.200	0.0059959	1.007	0.2225648	0.122	38.33	± 1.03	84.14	9.10	0.665	± 0.343
2A20291D	68.80 W	■	0.0001162	5.203	0.0036916	24.893	0.0000937	5.928	0.0051737	0.610	0.1980129	0.160	38.81	± 0.98	82.63	7.85	0.602	± 0.300
2A20292D	69.00 W	■	0.0000812	6.922	0.0024466	29.254	0.0000734	10.876	0.0038565	1.454	0.1482681	0.190	39.52	± 1.56	83.78	5.85	0.677	± 0.397
2A20293D	69.40 W		0.0000884	5.511	0.0018942	38.193	0.0000691	5.548	0.0031617	0.953	0.1227049	0.149	37.45	± 1.33	78.62	4.80	0.717	± 0.548
2A20296D	69.90 W		0.0001674	3.322	0.0022915	46.622	0.0000887	7.857	0.0035867	0.789	0.1564055	0.188	36.50	± 1.28	68.16	5.44	0.673	± 0.627
2A20297D	70.40 W		0.0001787	4.367	0.0037590	28.596	0.0000846	8.081	0.0034733	0.655	0.1485773	0.180	33.81	± 1.70	64.30	5.27	0.397	± 0.227
2A20298D	71.20 W		0.0001707	3.359	0.0036004	30.255	0.0000757	6.864	0.0025744	0.979	0.1097713	0.214	28.27	± 1.73	53.84	3.90	0.307	± 0.186
2A20299D	80.00 W		0.0002181	3.390	0.0053456	20.931	0.0000803	7.480	0.0022234	1.355	0.1121338	0.306	26.33	± 2.56	42.34	3.37	0.179	± 0.075
2A20301D	82.00 W		0.0006409	1.946	0.2716144	4.155	0.0002736	4.906	0.0103273	0.902	0.4247949	0.102	31.10	± 1.10	60.34	15.38	0.016	± 0.001
		Σ	0.0024626	1.067	0.3113970	3.787	0.0014888	1.756	0.0661063	0.267	2.6428855	0.039						

Appendix 2

Table 1: Major and trace element lower limit of detection analysed by XRF.

Major elements	Wt.%	Trace elements	ppm	Trace	ppm
SiO_2	0.01	**V**	1	**Mo**	0.2
TiO_2	0.01	**Cr**	0.3	**Cd**	0.2
Al_2O_3	0.03	**Co**	0.4	**In**	0.3
Fe_2O_3	0.01	**Ni**	0.3	**Sn**	0.4
MnO	0.01	**Cu**	0.3	**Sb**	0.5
MgO	0.02	**Zn**	0.3	**Te**	1.0
CaO	0.01	**Ga**	0.3	**I**	1.0
Na_2O	0.04	**Ge**	0.2	**Cs**	1.5
K_2O	0.01	**As**	0.3	**Ba**	1.5
P_2O_5	0.01	**Se**	0.2	**La**	2.0
		Br	0.3	**Ce**	3.0
		Rb	0.3	**Hf**	2.0
		Sr	0.2	**Tl**	0.7
		Y	0.2	**Pb**	0.2
		Zr	0.2	**Bi**	0.5
		Nb	0.2	**Th**	0.5
		Ta	2.0	**U**	0.5

Table 2: Results for BCR-2a, BIR-1 and BHVO-2 from LA-ICPMS conducted at Macquarie University.

Element	Mass	BCR-2a X1	BIR-1 X1	BHVO-2 X1
Li	7	7.90	3	4
Be	9	2.7	0.1	1.3
Sc	45	35	45	34
Ti	47	14282	5937	17266
V	51	410.2	322	309
Cr	53	17.0	356	249
Mn	55	1597	1380	1365
Co	59	38	53	46
Ni	60	14.0	183	131
Cu	65	27	123	139
Zn	66	127.3	66	105
Ga	71	21.5	15	21.3
Rb	85	47.8	0.19	9.74
Sr	88	332	110	395
Y	89	38.0	17.4	28.6
Zr	91	194	15.0	183
Nb	93	12.8	0.53	19.2
Mo	95	251	0.10	3.20
Cd	114	0.39	0.07	0.08
Cs	133	1.18	0.01	0.10
Ba	137	645	6.84	135
La	139	24.4	0.62	15.6
Ce	140	51.5	1.95	38.4
Pr	141	6.6	0.38	5.48
Nd	146	27.5	2.466	24.9
Sm	147	6.3	1.16	6.31
Eu	153	2.0	0.52	2.05
Tb	159	1.02	0.37	0.98
Gd	160	6.5	1.98	6.46
Dy	163	6.0	2.64	5.37
Ho	165	1.24	0.61	1.02
Er	167	3.46	1.80	2.61
Yb	173	3.09	1.68	2.00
Lu	175	0.46	0.25	0.28
Hf	178	4.48	0.60	4.40
Ta	181	0.71	0.04	1.16
Pb	208	9.7	4.61	2.83
Th	232	5.63	0.03	1.26
U	238	1.54	0.01	0.42

Table 3: Δ8/4, Δ7/4 Pb isotopic ratios for the combined Christmas Island sampling sites including those sampled and dredged (*) by Hoernle et al. 2011.

	Site Name	$^{206}Pb/^{204}Pb$	$^{207}Pb/^{204}Pb$	$^{208}Pb/^{204}Pb$	$^{207}Pb/^{204}Pb$ (NHRL)	$^{208}Pb/^{204}Pb$ (NHRL)	Δ7/4	Δ8/4
LVS	**Waterfall (CX--19A)**	18.8349	15.6113	38.9069	15.5327	38.3984	7.8602	50.8446
	Waterfall (CX--19B)	18.8742	15.6304	38.9764	15.5370	38.4460	9.3474	53.0446
	Ross Hill Pump (CX--21A)	18.8195	15.6123	38.8604	15.5310	38.3797	8.1245	48.0619
	Ross Hill Pump (CX--22A)	18.7917	15.6053	38.8529	15.5280	38.3462	7.7282	50.6699
	Golf Link (CX--26)	18.8173	15.6099	38.9904	15.5308	38.3771	7.9103	61.3272
	Dolly Beach (CX--30B)	18.8056	15.5585	39.0013	15.5295	38.3630	2.9015	63.8337
	Dolly Beach (CX--31)	18.7874	15.6417	39.0089	15.5276	38.3410	11.4172	66.7876
	Ethel Beach (CX--34)	18.8716	15.6051	38.9853	15.5367	38.4427	6.8424	54.2542
	Dale's (CX--40)	18.8347	15.6265	38.9819	15.5327	38.3981	9.3852	58.3822
	Dale's (CX--41)	18.9725	15.6402	39.1234	15.5476	38.5647	9.2603	55.8723
	Flying Fish Cove (CX--43)	18.8359	15.6136	38.9404	15.5328	38.3996	8.0747	54.0789
UVS	**Winifred (XM-33)**	18.8776	15.6225	38.9552	15.5373	38.4500	8.5201	50.5170
LVS	**SO199DR54-1***	19.2806	15.6473	39.2136	15.5810	38.9373	6.6262	27.6330
	SO199DR55-1*	19.5640	15.6475	39.5626	15.6117	39.2799	3.5755	28.2683
	SO199DR55-3*	19.5623	15.6467	39.5674	15.6116	39.2779	3.5129	28.9508
	CH5B*	18.9103	15.6380	39.1007	15.5409	38.4895	9.7103	61.1129
	CH6*	18.9676	15.6435	39.1616	15.5471	38.5588	9.6456	60.2729
	CH8*	18.6627	15.6532	38.9456	15.5140	38.1902	13.9149	75.5375
	CH98	18.8928	15.6061	38.9330	15.5390	38.4683	6.7146	46.4623
	CH11*	18.9364	15.6390	39.1476	15.5437	38.5211	9.5329	62.6507
	CH12*	18.8051	15.6455	39.0356	15.5295	38.3624	11.5981	67.3211
	CH13*	18.9351	15.6399	39.1617	15.5436	38.5195	9.6361	64.2197
UVS	**CH1A***	17.8674	15.5450	38.0317	15.4278	37.2286	11.7135	80.3020
	CH1B*	17.8692	15.5467	38.0352	15.4280	37.2309	11.8670	80.4339
	CH2*	17.8683	15.5461	38.0320	15.4279	37.2298	11.8146	80.2207
	CH3*	17.8680	15.5458	38.0316	15.4279	37.2294	11.7956	80.2198
	CH4*	17.8690	15.5461	38.0333	15.4280	37.2306	11.8124	80.2729
	CH7A*	17.8498	15.5471	38.0410	15.4259	37.2074	12.1224	83.3659

Appendix 3

Abstracts submitted at 2012 AGU Fall Meeting

Origin of seamount volcanism in northeast Indian Ocean with emphasis on Christmas Island

Rajat Taneja[1], Craig O'Neill[1], Tracy Rushmer[1], Simon Turner[1], Janne Blichert-Toft[2], Fred Jourdan[3], Mark Lackie[1]

The Northeast Indian Ocean has been a central point of research in the recent past due to its intraplate geophysical and geochemical characteristics. It is dominated by sub-aerial volcanic islands and submerged guyots and two islands, namely, Cocos (Keeling) Island and Christmas Island. Christmas Island, the focus of this study, consists of limestone and mafic intraplate volcanics. The origin of most of the features in northeast Indian Ocean is not fully understood. Christmas Island has experienced multiple stages of intraplate volcanic activity as previously established by $^{40}Ar/^{39}Ar$ radioisotopic analyses of basalts from the island (Hoernl et al., 2011). Here, we present new $^{40}Ar/^{39}Ar$ ages where the rock samples from Waterfall Spring (WS), Ethel Beach (EB) & Dolly Beach (DB) on the east coast of the island yielded plateau and mini-plateau ages of 37.75±0.77 Ma, 37.10±0.66 Ma and 43.37±0.45 Ma respectively, whereas a sample from Flying Fish Cove (FFC) in the north of the island yielded a minimum age of 38.6±0.5 Ma. All these units are part of the Lower Volcanics Series. The samples from the west coast (Winifred Beach, WB) are younger with an age of 4.32 ± 0.17 Ma, and are part of the Upper Volcanic Series. This confirms two stages of volcanism at the island with a gap of around 38 Ma.

The $^{40}Ar/^{39}Ar$ radioisotopic ages were overlayed on Gplates and seismic tomography models to determine its paleo motion. The present position of the island is 10.5°S, 105.5°E. During Eocene its reconstructed position was 30°S latitude. Seismic tomography models have highlighted a low velocity zone beneath the island during Eocene.

Geochemically, the two volcanic suites (Upper & Lower) are mostly similar in their major and trace element composition. The majority of localities (WS, EB, and WB) are basanites; whereas that from Dolly Beach is basaltic. The Dale's (west coast), are trachyte and appear evolved with high SiO_2. They also have low Ba and Sr ~25ppm, whereas those from east coast have 550 – 900 ppm Sr. Despite an age difference of more than 38 Ma, there is no significant difference between Hf, Nd and Pb isotopic signatures of the Upper Volcanic and Lower Volcanic series which show an enriched component, interpreted by Hoernle et.al (2011) to be due to contamination by continental material. This signifies a common homogenous source for a period of more than 40 Ma in contrast to many OIBs. Dale's do have a distinct isotopic character from the Lower Volcanic Series and this signature is still under study. These geochemical analyses from the island broadly lie within those sampled by Hoernle et al. (2011) from their regional study. Here, we are looking at the island in detail. We present geochronological, geophysical and geochemical data from the island which addresses this model using Christmas Island as an example.

Ref: Hoernle et al., 2011, Origin of Indian Ocean Seamount Province by shallow recycling of continental lithosphere, Nature Geoscience 4: 883-887

[1]Department of Earth and Planetary Sciences, CCFS ARC Centre of Excellence, Macquarie University, Sydney
[2]Ecole Normale Supérieure de Lyon, Laboratoire de Geologie de Lyon, Lyon, France
[3]Western Australian Argon Isotope Facility, JdL Centre & Department of Applied Geology, Curtin University

Conference abstract for talk presented at 34th International Geological Congress, Brisbane, August 2012.

Constraining paleo-latitudes of rocks from Christmas Island.

Rajat TANEJA[1], Craig O'NEILL[1],Phil SCHMIDT[2] and Tracy RUSHMER[1]

[1]Department of Earth and Planetary Sciences, Core to Crust Fluid Systems, ARC Centre of Excellence, Macquarie University, Sydney, Australia. Email: rajat.taneja@mq.edu.au;
[2]CSIRO Earth Science and Resource Engineering, North Ryde, NSW, Australia

The drifting of Australian landmass from Greater India around 136 Ma resulted in large volumes of volcanic eruptions in the Indian Ocean and surrounding continental margins. This was followed by later episodes of submarine eruptions. Evidence of this volcanism can be seen in the form of two exposed islands, Christmas Island and Cocos (Keeling) Island, and numerous submerged seamounts. Christmas Island is dominated by limestones and phosphates with some basalts and basanites. The island experienced three stages of volcanic activity the oldest one in Late Cretaceous followed by later phases in the Eocene and in the Miocene. Four sites were selected for paleomagnetic sampling, three on east and one on west coast. Samples were demagnetised using alternating field progressive demagnetisation with increments upto 70 mT. Characteristic Remanent Magnetisation was determined using PCA to remove low stability component. Fisherian statistical analysis gave two different mean inclinations (I_m) of 71° for Waterfall Spring & Dolly Beach and 55° for Winifred & Ethel Beach. The higher I_m of the former sites could be due to lightning strikes that disturbed the original magnetic character. These I_m were used to constrain the paleo-latitudes of the island using equation $\tan I_m = 2 \tan\lambda$. Steeper inclination gave a paleolatitude of 54°S whereas shallower inclination gave 36°S which lies in conformation with the position of island observed in plate reconstruction models at approximately 50–65 Ma.

Abstracts submitted at Biennial Conference of the SGGMP, Murramarang, 2011

Christmas Island has basanites to trachytes: Is it still just an OIB?

Rajat Taneja, Tracy Rushmer, Craig O'Neill

Department of Earth and Planetary Sciences, CCFS ARC Centre of Excellence, Macquarie University, Sydney

The late Jurassic spreading that lead to rifting of Australia from Greater Indian was accompanied by large amount of volcanic activity that covered both continental and oceanic areas. Two islands in Northeast Indian Ocean and a few submerged seamounts probably owe their origin to the submarine volcanism that occurred in Late Cretaceous and Eocene. Of the two islands, Christmas Island, a volcanic island cap, is an island rising 5500 m from the ocean. It lies 2000 km northwest of Perth. This study investigates the volcanic episodes erupted in the Christmas Island Seamount Province as they significantly impacted the thermal evolution of these margins. We are combining gravity modelling for submerged flat top seamounts and calculating palaeo-latitudes. This is complimented by geochemical studies of rocks from Christmas Islands. Rocks from Christmas Island show three ages of volcanic activity that range from Late Cretaceous and Eocene to more recent ones in around Pliocene.

Rock samples from 28 locations were collected, prepared and analysed for their major and trace elements geochemistry (Fig. 1). Prominent sites included; the western area (The Dale's), the north (Territory Day National Park, Flying Fish Cove) and three on the east coast (Waterfall Spring, Ethel Beach, and Dolly Beach). The former two sites on the east coast consist of fine grained black basalts that appear as sills. The Dolly Beach site, contains a basaltic dyke that protrudes through the surface containing phenocrysts of olivine. The TAS classifies the rocks as tephrite basanites to trachyte. Rocks on the east coast (Waterfall and Ethel Beach) and in north are tephrite basanite having low percentage of SiO_2 (45-50 wt.%) and alkali (4-5 wt.%). The samples from The Dales have a higher percentage of SiO_2 (60 wt.%) and alkali (12 wt.%), significantly lower MgO (0.5 wt.%) and are classified them as trachyte to trachydacite.

Figure 1: Geological Map of Christmas Island.

Trace elements for the samples from Christmas Islands have low concentration of Hf (< 2 ppm) and this applies to rocks from Waterfall Spring, Ethel Beach and Dolly Beach whereas the more evolved Dale's have relatively higher concentration between 15 – 20 ppm. The Dale's have one-third amount of Ba as compared to the rocks on the east coast and Sr concentration of the samples from The Dale's are anomalous, around 25ppm as compared to 550 – 900 ppm from east coast. This significant difference in trace elements and more importantly in Sr concentration could be due to fractionisation process or due to continental contamination left over by initial stage of rifting.

Abstracts submitted at 22nd ASEG Conference and Exhibition, Feb, 2012, Brisbane, Australia

Estimating the age of volcanism in Seamount Provinces of the Northeast Indian Ocean

Rajat Taneja
Department of Earth and Planetary Sciences,
Core to Crust Fluid Systems ARC Centre of Excellence
GEMOC ARC National Key Centre,
Macquarie University, Sydney,
rajat.taneja@mq.edu.au

Craig O'Neill
Department of Earth and Planetary Sciences,
Core to Crust Fluid Systems ARC Centre of Excellence
GEMOC ARC National Key Centre,
Macquarie University, Sydney
craig.oneill@mq.edu.au

SUMMARY

The breakup of Australian landmass from Greater India, part of the late dispersal of Gondwana, started around 136 Ma. Concurrent with this breakup was the eruption of significant volumes of volcanics, on both the continental margins of Australia and India, including the North-West shelf, and in the ocean basin separating the two. Later submarine volcanism occurred within the Christmas Island Seamount Province (ChrISP), or which Christmas and Cocos (Keeling) Islands are two subareal examples. These volcanic events significantly impacted the thermal evolution of these margins, but the ultimate cause for this disparate volcanism, and the relationship between margin volcanics and later submarine volcanic events, remains unclear. The study tries to establish a relation between the volcanic activities and look for any evidence of these volcanic episodes. The study uses gravity, magnetic, and subsidence modelling to attempt to constrain the structure and ages of seamount volcanism within the Christmas Island Seamount Province, including the Wharton Basin and Argo Abyssal Plain. Gravity modelling helps to determine the crustal structure and constrains the depth of limestone cap, which further helps in calculating when the seamount was sub aerially exposed and approximates the time since it was last exposure. The relationship between the volcanism observed in the ChrISP (Late Cretaceous to Eocene) and that recorded earlier on the NW shelf continental margin, remains ambiguous, and will be better constrained with forthcoming geochemical analysis. But the results presented here point to a rich and complex history of volcanism within the Indo-Australian plate.

Keywords: Seamounts, Cocos (Keeling) Islands, Christmas Island, Paleolatitude, Gravity Modelling

INTRODUCTION

The first sign of intercontinental rifting of Gondwana started in the Permian and Triassic and led to eventual rupturing of south-western Australia. Early Cretaceous saw the basaltic eruption of Bunbary Basalt (Western Australia) and Rajmahal Traps (Northeast India), associated with Kerguelen plume head, and the separation of India and Australia (Veevers, 1971). The presence of magnetic anomaly M25 [154.1 Ma] (Stagg *et al.* 1999; Heine and Müller, 2005) in the Argo and Gascoyne basin suggests seafloor spreading began in the Late Jurassic.

The eastern part of the Indian Ocean consists of seamounts whose origin is not well understood. Cocos (Keeling) Islands (CKI) and Christmas Island (CI) are the two seamounts in North East Indian Ocean that rise above the sea level, however, there are many seamounts in the area that are submerged. CKI is located in the Indian Ocean approximately 2,950 km north west of Perth, and consists of a circular coral atoll above a submerged volcano. CI is a limestone capped volcanic island located about 305 km south of Java. The island lies in the Wharton Basin off the western coast of Australia, and is moving northwards in to the Java Trench at around 70-80 mm/yr (Borissova, 1994). The rocks of the islands are of late Cretaceous to early Tertiary age and consist of intermediate to basic volcanics like basalts, andesites, and trachybasalts (Grimes, 2001). The bathymetry of the North-east Indian Ocean (Figure 1) demonstrates the existence of numerous flat-topped seamounts, or guyots. One such features is shown in the profiles in Figure 2. These features are generally thought to have weathered sub-areally, to acquire their morphology, suggesting that the seamount was once above sea-level and have been subjected to erosion and weathering processes.

METHODOLOGY AND RESULTS

This study utilises numerous geophysical approaches to constraining the age and history of the Christmas Island seamount province – including both CKI and CI. Gravity data has been used to model the thickness of limestone cover on CKI, which, together with coral deposition rates, can constrain the age of the islands. The depth below sea-level to submerged seamounts, together with a subsidence age-depth relation (Tucholke and Smoot, 1990), can be used to determine when the seamount was exposed above sea-level. Regional bathymetry data for the oceans have been employed to prepare profiles showing flat tops seamounts (Figure 2).

The ages obtained by these techniques were imported in Gplates to understand their movement over a global time scale. Gplates reconstructions are complemented with paleolatitudional calculations of drilled cores from CI in order to understand their evolution and movement on a global time scale.

Gravity Modelling: Gravity data was modelled for the CKI to determine the crustal structure of the oceanic realms and estimate the depth of limestone cover over the island. The regional gravity and bathymetry data sets were obtained from Scripps Institute of Oceanography, University of California. These are 1 minute grids and used in GMT to prepare gravity anomaly maps for the islands (Smith and Sandwell, 1997). The gravity data was modelled using gravity and magnetic modelling tool Modelvision version 8 by Encom. The data set in xyz format, consisting of distance (m) in X and Y coordinates and gravity anomaly values (gu), is imported in to the software to produce an observed gravity profile of the region. The ocean floor is then modelled to produce a calculated gravity profile that matches up with the observed profile. While modelling the ocean floor it was ensured

that the modelled crust matches with the bathymetry of the ocean floor. During modelling, a three layer crustal structure of the ocean floor has been assumed consisting of basalt, gabbro, and mantle. Watts, *et al*. (1985) computed gravity anomalies for the Hawaiian-Emperor seamount chain and proposed two models for deep crustal structure, one with thin oceanic crust under the ridge, and other with a normal oceanic crust.

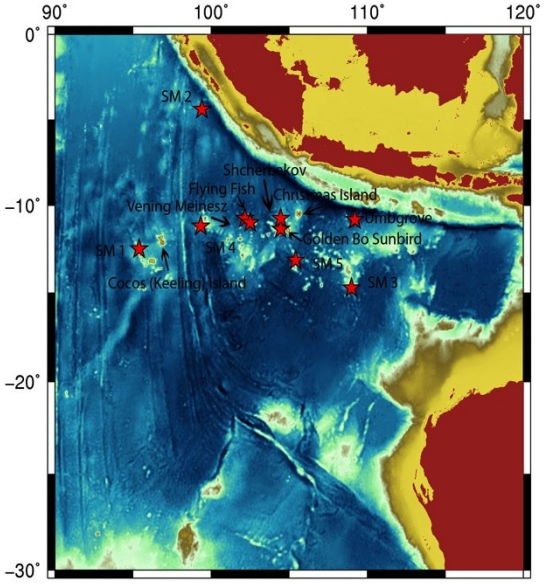

Figure 1: Map of the Northeast Indian Ocean displaying seamounts.

They have shown that the total crustal thickness is around 6.5 km beneath the Hawaiian arch and varies between 10.5 – 12.0 beneath the moat and 18.0 km under the ridge.
Similar crustal structure has been employed to our gravity analysis for CKI. The top layer of the islands consists of Pleistocene limestone. The depth of this layer is not known, however there are estimates for its depth based on dredging (IFM GEOMAR, 2009). The second layer beneath limestone is basalt. Its thickness has been assumed to be around 1.5 km according to Watts, *et al.* (1975) model. Basalts are underlain by gabbros, with thickness around 5 km. To compensate for the high gravity anomaly of the CKI, there has to be mass within the oceanic crust to balance the excess mass of the

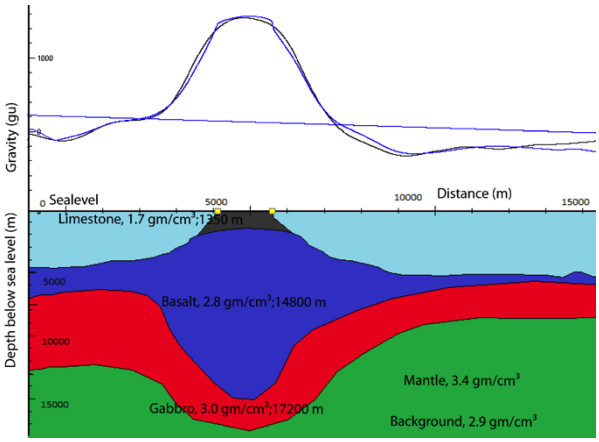

Figure 3: Gravity Modelling for Cocos (Keeling) Island at latitude 12.18°S, x-axis distance in m; positive y axis, gravity units; negative y axis depth below sea level;.

island above the ocean floor. This excess mass brings the crustal structure to deeper depths, the basaltic layers extends up to 15 km whereas the gabbro reaches up to 17 km depending on the density for these layers (Figure 3). The gravity modelling for CKI is presented in Figure 3. The depth of limestone is around 1,350 m when the density of the top layer is 1.7 gm/cubic cm and it becomes 1,500 m when the density is increased to 1.85 gm/cubic cm. If we assume fixed densities for limestone, gabbro and mantle (Table 1), but change the densities of basalt, we observe that the depth of limestone cover increases (Figure 4).

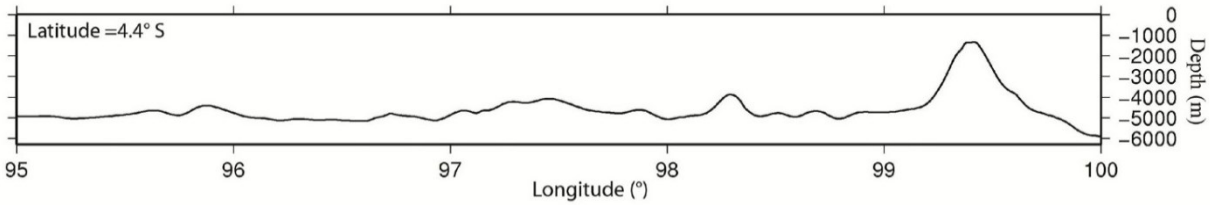

Figure 2: Profile of flat top of seamount, SM 2.

	Density (g/cm^3)	Depth to base (m)	Density (g/cm^3)	Depth to base (m)	Density (g/cm^3)	Depth to base (m)	Density (g/cm^3)	Depth to base (m)
Limestone	1.8	900	1.8	1100	1.8	1307	1.8	1800
Basalt	2.8	13700	2.85	14500	2.9	16400	2.95	17500
Gabbro	3.1	16000	3.1	16600	3.1	18500	3.1	19050
Mantle	3.3		3.3		3.3		3.3	
Background	2.88		2.88		2.88		2.88	

Table 1: Change in limestone thickness and crustal structure thickness with changing basaltic densities.

Name of the Seamount	Latitude(S)	Longitude	Depth below sea level (m)	Seamount Age, Ma (using the average age of crust as 94.4)	Seamount Age, Ma (Sea floor age, using GPlates age database)
SM 1	12.50	95.40	1537-1635	66.0-68.9	27.5-30.4 (55.9)
SM 2	4.40	99.42	1325- 1700	59.2-70.8	20.9-32.30 (55.9)
SM 4	11.20	99.34	1156-1470	53.1-63.9	42.4-53.1 (83.5)
SM 5	13.50	108.73	2182-2400	82.3-86.2	92.9-96.8 (105)
SM 3	14.75	108.99	3126-3300	93.7-94.3	126.0-126.6 (126.7)
Flying Fish	10.75	102.18	3057-3433	93.4-94.3	82.5-83.4 (83.5)
Golden Bo'Sunbird	11.38	104.46	294-552	15.6-28.1	26.2-38.7 (105)
Umbgrove	10.83	109.20	2334-2924	85.1-92.5	95.7-103.1(105)
Shcherbakov	10.75	104.83	1878-2242	75.4-83.4	80.0-89.0 (99)
Vening Meinesz	11.00	102.40	2065-2844	79.8-91.8	84.4-96.4 (99)

Table 2: Age Depth relation for flat topped peaks in East Indian Ocean.

This gives us age estimates of about 8 to 10 Myr for a growth rate of 0.08mm/yr; and between and 15 to 18 Myr for a growth rate of 0.1 mm/yr. Woodroffe *et al.* (1991) acknowledges that this growth rate is significantly faster than the rate predicted through thermal lithospheric models of that area, which is 0.0149 mm/yr (Marty and Cazenave, 1989) which would give an age in the range of 53 to 100 Myr.

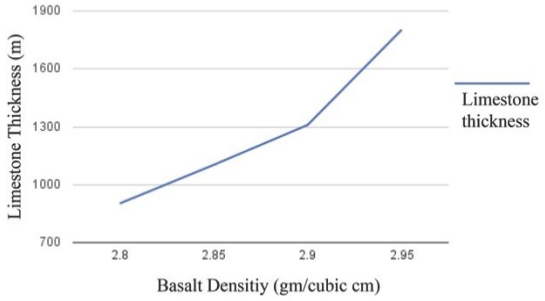

Figure 4: Increase in limestone cover thickness with increasing basaltic density.

Age Depth Relation: As the lithosphere moves away from the mid-oceanic ridge, it cools and begins to contract. The subsidence of the ocean floor is proportional to the square root of the age, however for larger ages it becomes exponential. This age-depth relations were further modified by Parsons and Sclater (1977) and they showed a break in the relation between 60 and 80 Ma ago, developing a 'plate' model to explain the behaviour of sea-floor of ages greater than 80Myr. Using this age-depth relation, we calculated the age when the seamount was sub aerially exposed and approximate their time of origin by back-tracking the feature from their present depth. The flat topped seamounts are evidence of the fact that they were subjected to erosion and weathering while they were exposed above the surface of the sea. We have used Parsons and Sclater (1977) and Tucholke and Smoot (1990) age-depth relation curve for the Atlantic Ocean with slight modification and used it on the Indian Ocean.

Modifying this relation for seamount subsidence in the North-East Indian Ocean we get,

$$(5900 - d_{sm}) = 2500 + 350 * t^{1/2},$$

$$\text{or, } t = \{((5900 - d_{sm}) - 2500)/350\}^2$$

Where; 5900 is the depth of the seafloor in the region, d_{sm} is the depth of the seamount, and t the age in Myr.

The age obtained from the above relation is subtracted from the age of the ocean crust, to get age the seamount was sub aerially exposed, which approximates - roughly - the age of the seamount. We did this in two ways, in the first example; we subtracted an average age of the crust which is depicted in column five in Table 2. Alternatively, we also extracted ages of the crust from the Gplates seafloor age database, to obtain seafloor ages for where that particular seamount lies, and this is depicted in column six. For this relation it is assumed that there is no other process acting to uplift or thermally reset the crust by any phase of volcanic activity (Tucholke and Smoot, 1990).

The ages obtained suggest around two stages of volcanic activity occurred in the region. The earliest was Early to Late Cretaceous; second one was Late Palaeocene to Early Eocene. This conforms with the dating of the volcanic activity on Christmas Island (Grimes, 2001), which suggested volcanic episodes in the Late Cretaceous, Early Eocene, and with the most recent one in Pliocene (Grimes, 2001).

Paleo- Latitude determination: Drilling was done on CI with the aim to determine the paleolatitudes of lava flows at the time of their formation. Four sites were selected for this purpose and on an average four to five samples were collected from each site. With the assistance of CSIRO, North Ryde, inclination and declination for each of the sample were determined by alternating-field demagnetisation..

Inclination, I of a sample can be used to calculate the paleolatitude by a simple relation,

$$\tan I = 2 \tan \lambda$$

where, λ, is the latitude of the paleosite.

Calculation of paleolatitudes from four samples at Christmas Islands gives us a mean latitude of -52°. However, using Gplates, we get a most southerly paleolatitude of -34°S for Christmas Islands at ~65 Myr (Figure 5). The discrepancy between latitudes is not yet reconciled.

Plate Tectonic Reconstruction: Seamounts picked from bathymetric plots were plotted in plate reconstruction software GPlates (Figure 5), that helps in visualizing the motion of these features in geological time from their past to present position on a global reference frame. In this the

seamounts with their present positions are reconstructed using a global rotation file, containing information about different plates and their evolution with time (Gplates rotation database). Each seamount is simply assigned an age of the plate it occupies. The reconstructed image of the Christmas Island seamount province, with respect to the (fixed) global tomography model of Becker and Boschi (2002) is shown in Figure 5.

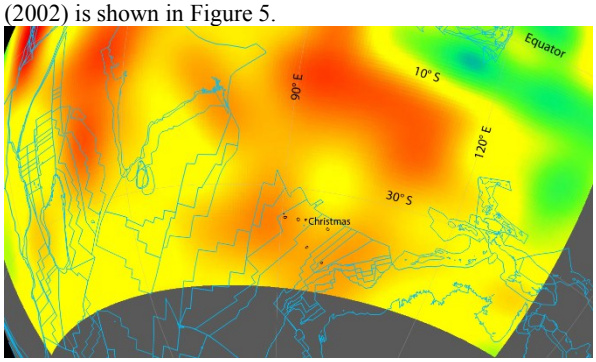

Figure 5: GPlates, plates tectonic reconstruction software, depicting paleo positions of seamounts at 60 Myr, overlying seismic tomography layer for present time (tomography model from Becker and Boschi, 2002, depth 450 km).

A distinct low velocity zone, centred around 37°S, is present in the Becker and Boschii (2002) model, which underlies the reconstructed position of the ChrISP. The low velocity anomaly is particularly prominent at the lower latitudes around the present positions these seamounts, suggesting a mantle contribution to their origin.

Conclusion:

The seamount province of the Northeast Indian Ocean indeed present a very rich and complex evolutionary history. The source for this volcanism is still presently not clear. Seismic tomography data analysed by Montelli *et al.* (2004) reveal the presence of an East Indian Ocean mantle plume, extending from the sublithosphere to 1900 km, with a radius of 400 km (Figure 5). We believe that this shallow mantle plume may power the seamount system in the Northeast Indian Ocean.

Gravity modelling for these islands helps us in understanding the crustal structure of the island and determines the depth of limestone. Our estimate of limestone depth for CKI of 800 to 1500m matches well with the depth ranges suggested by IFM-GEOMAR 2009. Using our age-depth techniques, stated above, we infer that the basalts were exposed around 19 Myr ago. This matches well with the subsidence age (15-19 Myr) obtained by coral accretion rates of 0.08 mm/yr by Woodroffe et al. (1991). We identified four flat top seamounts from the bathymetry data of the area, indicating they were once above sea-level and were subjected to erosion and weathering. Two of those have shallow depths in the range of 1300 to 1600m implying that they were above the surface in Early Oligocene to Early Miocene (32.3-20.9 Ma) for SM 2 and Early to Late Oligocene (30.4-27.5 Ma) for SM 1. SM 4 has an age of 53-42 Ma (Early to Middle Eocene) and SM 5 was exposed above sea-level during Late Cretaceous (93-97 Ma). This is concurrent with the earliest volcanic episodes (Late Cretaceous) on Christmas Island; subsequent events were dated as Eocene (35-40 Ma) and the most recent in Pliocene (3-5 Ma) by Grimes, 2001. Recent work by Hoernle *et al.* 2011 on Ar/Ar has shown a decreasing age trend from Agro Basin (136 Ma) in east to CKI (56-47 Ma) in the west, however, CI offsets this trend with ages of 44-4 Ma.

References:

Becker, T. W. and Boschi, L., 2002, A comparison of tomographic and geodynamic mantle models: Geochemistry, Geophysics, Geosystems, 3, 2001GC000168.

Borissova, I., 1994, Seafloor morphology and tectonics of the Christmas Island area, Indian Ocean: Australian Geological Survey Organisation, 1994/2.

Crawford, A. R., 1969, India, Ceylon and Pakistan: New Age Data and Comparisons with Australia: Nature 223, 380-384.

IFM-GEOMAR., 2009, Christmas Island seamount province and the Investigator Ridge: Age and causes of intraplate volcanism and geodynamic evolution of the south-eastern Indian Ocean: Liebniz Institute for Marine Sciences RV Sonne Cruise Report, SO199 CHRISP, Indonesia-Singapore: 2 August – 22 September 2008, 210 pp.

Grimes, K. G.,2001, Karst Features of Christmas Islands: Helictite 37, 41-58.

Heine, C. and Müller, R.D., 2005, Late Jurassic rifting along the Australian North West Shelf: margin geometry and spreading ridge configuration: Australian Journal of Earth Sciences: An International Geoscience Journal of the Geological Society of Australia, 52(1), 27 - 39.

Hoernle, K., Hauff, F., Werner, R., van den. Bogaard, P., Conrad, S., Gibbons, A., and Müller, D., 2011, The Christmas Island Seamount Province, Indian Ocean: Origin of intraplate volcanism by shallow recycling of continental lithosphere?: Goldschmidt 2011,Prague, Abstract,1032.

Marty, J. C. and Cazenave, A., 1989, Regional variations in subsidence rate of oceanic plates: a global analysis: Earth and Planetary Science Letters, 94(3-4), 301-315.

McElhinny, M.W. and Evans,M.E., 1968, An investigation of the strength of the geomagnetic field in the early precambrian: Physics of The Earth and Planetary Interiors 1(7), 485-497.

Montelli, R., Nolet, G., Dahlen, F. A., Masters, G., Engdahl, E., Robert Hung, Shu-Huei, 2004, Finite-Frequency Tomography Reveals a Variety of Plumes in the Mantle: Science, 303(5656), 338-343.

Parsons, B. and Sclater, J.G., 1977, An Analysis Of The Variation Of Ocean Floor Bathymetry And Heat Flow With Age: Journal of Geophysical Research, 82(5), 803-827.

Sandwell, D. T. and Smith, W.H. F., 1997, Marine gravity anomaly from Geosat and ERS 1 satellite altimetry: Journal of Geophysical Research, 102, 10039-10054.

Stagg, H. M. J., Wilcox, J.B., Symonds, P.A., O'Brein, G.W., Colwell, J.B., Hill P. J. A., Lee C-S., Moore A. M. G., Struckmeyer, I. M., 1999, Architecture and evolution of the Australian continental margin: AGSO Journal of Australian Geology & Geophysics, 17, 17 - 33.

Trueman, N. A.,1965, The phosphate, volcanic and carbonate rocks of Christmas Island (Indian Ocean): Journal of the Geological Society of Australia, 12(2), 261 - 283.

Tucholke, B. E. and Smoot, N.C., 1990, Evidence for Age and Evolution of Corner Seamounts and Great Meteor Seamount Chain From Multibeam Bathymetry: Journal of Geophysical Research, 95(B11), 17555-17569.

Veevers, J. J., 1971. Phanerozoic history of Western Australia related to continental drift: Journal of the

Geological Society of Australia, 18(2), 87-96.
Watts, A. B., Cochran, J. R., Selzer, G., 1975, Gravity Anomalies and Flexure of the Lithosphere: A Three-Dimensional Study of the Great Meteor Seamount, Northeast Atlantic: Journal of Geophysical Research, 80(11), 1391-1398.
Watts, A. B., ten Brink, U.S., Buhl, P., Brocher, T.M., 1985, A multichannel seismic study of lithospheric flexure across the Hawaiian-Emperor seamount chain: Nature, 315(6015), 105-111.
Woodroffe, C. D., Veeh, H. H., Falkland, A., McLean, R.F.,
Wallensky,E., 1991 Last interglacial reef and subsidence of the Cocos (Keeling) Islands, Indian Ocean: Marine Geology, 96, 137- 143.

Appendix